Experimental Investigation of Subcooled Flow Boiling Using Synchronized High Speed Video, Infrared Thermography, and Particle Image Velocimetry

by
Bren Andrew Phillips

B.S. Nuclear Engineering, University of Missouri–Rolla, 2005
S.M. Nuclear Science and Engineering, Massachusetts Institute of Technology, 2011

SUBMITTED TO THE DEPARTMENT OF NUCLEAR SCIENCE AND ENGINEERING IN PARTIAL FULFILLMENT OF THE REQUIREMENTS FOR THE DEGREE OF

DOCTOR OF PHILOSPOHY IN NUCLEAR SCIENCE AND ENGINEERING
AT THE
MASSACHUSETTS INSTITUTE OF TECHNOLOGY

JUNE 2014

Author: _____

Bren Phillips
Department of Nuclear Science and Engineering
May 15, 2014

Certified by: _____

Jacopo Buongiorno, Ph.D.
Associate Professor of Nuclear Science and Engineering
Thesis Supervisor

Certified by: _____

Emilio Baglietto, Ph.D.
Assistant Professor of Nuclear Science and Engineering
Thesis Reader

Certified by: _____

Thomas McKrell, Ph.D.
Research Scientist, Nuclear Science and Engineering
Thesis Reader

Certified by: _____

Despoina Chatzikyriakou, Ph.D.
Senior Engineer, Energy Research Group, Toyota Motor Europe
Thesis Reader

Accepted by: _____

Mujid Kazimi, Ph.D.
TEPCO Professor of Nuclear Engineering
Chair, Department Committee on Graduate Students

Experimental Investigation of Subcooled Flow Boiling Using Synchronized High Speed Video, Infrared Thermography, and Particle Image Velocimetry

by
Bren Andrew Phillips

Submitted to the Department of Nuclear Science and Engineering on
May 15, 2014
in Partial Fulfillment of the Requirements for the degree of

DOCTOR OF PHILOSOPHY
IN NUCLEAR SCIENCE AND ENGINEERING

Abstract

Subcooled flow boiling of water was experimentally investigated using high-speed video (HSV), infrared (IR) thermography, and particle image velocimetry (PIV) to generate a unique database of synchronized data. HSV allowed measurement of the bubble departure diameter. IR thermography allowed measurement of wall superheat (local distribution and surface-averaged values), heat transfer coefficient, nucleation site density, and bubble frequency. Particle image velocimetry allowed for the measurement of velocity profiles in the liquid phase for single bubble nucleation events. The tests were performed at pressures of 1.05, 1.5, and 2.0 bar and at subcoolings of 5, 10, and 15 °C. The mass flux values explored were 150-1250 kg/m^2/s. The heat flux values explored were 100-1600 kW/m^2. As expected, the heat transfer coefficients increased with increasing mass flux in the single-phase convection and partial boiling regions, and converged to a fully-developed boiling curve for high heat fluxes. The bubble departure diameter decreased with increasing mass flux and decreasing heat flux; in accordance with Sugrue's model. The nucleation site density increased with increasing superheat and decreasing mass flux, as predicted by Kocamustafaogullari and Ishii's model. The nucleation site density models under-predicted the nucleation site density for a given wall superheat. Wait time and frequency models did not reproduce the data accurately, and underestimated wait time by an order of magnitude. A new mechanistic model for calculating the wait time was developed that split the wall heat flux into the component that is transferred to the fluid, and the component that is transferred as sensible heat into the heater wall. Significant localized cooling was observed underneath bubbles sliding along the wall after departure from a nucleation site, an effect which should be considered in advanced models of subcooled flow boiling. The sliding bubble thermal effects were found to be insensitive to system conditions and were limited by the thermal conduction within the substrate. Bubble growth front velocities, and regions of flow influence of departing bubbles were measured with PIV. The database generated in this project can be used to inspire or validate mechanistic models and/or CFD simulations of subcooled flow boiling heat transfer.

Thesis Supervisor: Jacopo Buongiorno
Title: Assistant Professor of Nuclear Science and Engineering

Acknowledgements

First, I would like to thank my adviser Professor Jacopo Buongiorno for all of his support through all six of my years at MIT. You have provided excellent guidance, and had had great patience with all of my experimental setbacks. I truly would not have made it through without your help and support.

Secondly, Dr. McKrell has my deepest gratitude. You have helped me from my first day in the lab and were always there for any kind of problem I had. I would never have made it without your guidance. I will always remember the brainstorming sessions you, I, and Eric would have about various problems. I always found those interesting, fun, and stimulating.

Thanks to my readers Professor Emilio Baglietto and Dr. Despoina Chatzikyriakou, for all of their input over the years. Also, thank you to Professor Neil Todreas for agreeing to be my committee chair.

Thanks to Dr. Greg Dewitt who made this work possible by building the loop that I did all of my work on, and for teaching me how to run it.

A special thanks to Dr. Koroush Shirvan for running Fluent calculations for cross flow in my test section near the outlet transition.

Thesis preparation would have been much more difficult without all of the LaTeX help from Brian, Dusty, and Nick. The IAP class that Brian and Nick gave this year was very helpful for me.

I want to thank my family for all of the support they have given me during my time in graduate school, and putting up with the lack of time I had to talk and come visit. I owe a special thanks to my parents, because without their support and encouragement over the years, I would never have made it to grad school at MIT.

Thanks to Schlumberger for giving me my internship opportunity and for the use of the confocal microscope throughout my graduate career. Special thanks to Albert Perez for always hosting me when I came to use the microscope.

All of my fellow lab friends: Carolyn, Eric, Ethan, Melanie, Guanyu, Andrew, Matteo, Michael and Reza, thanks for all of your help on all those random things that come up in the lab.

The CMFD group: Alex, Despoina, Dusty, Enrique, Gustavo, and Riccardo, thanks for giving me all the comments and suggestions over the years.

MIT NSE would not function without the admins, so thanks for all of your hard work. I want to give a special thanks to Peter Brenton who has bailed me out of a jam on more than one occasion.

The support from all of my friends over the years has made my time at MIT enjoyable and memorable. Brittany, Eric, Koroush, and Lindsey, I will always remember all of the great times we had hanging out, and all of the long conversations we have had. Joe, Josh, and Nate, my office neighbors, thanks for always being up for a five minute conversation whenever I needed a break. Thanks to all my classmates, and especially those who have endured six years as a grad-student like me, you know who you are.

None of my Ph.D. would have been possible without funding from the Consortium for Advanced Simulation of Light Water Reactors (CASL) who provided funding throughout my PhD. Also, thanks to the National Science Foundation for funding through their graduate fellowship program that helped fund me for the first year and a half of my PhD.

Lastly, I want express my deepest love and gratitude to my fiancé Lindsey. You were always there for me, whenever I got stressed and frustrated, you always made life seem so much better. All of this time and effort for a Ph.D. would have little meaning if I did not have someone to share the rest of my life with, and I am so glad it is with you. I am looking forward to our lifelong adventure together....

Contents

List of Figures

List of Tables

Nomenclature

Notation	Description	Page List
A	Flow channel area (length^2)	46, 48
α	Advancing contact angle (angle)	57
a	Half thickness of the channel width (length)	115
α_f	Thermal diffusivity of the liquid (length^2 / time)	72
α_g	Aspect ratio of the test section (unitless)	115
α_λ	Radiation absorbance fraction of a surface (unitless)	27
α_w	Thermal diffusivity of the wall (length^2 / time)	72, 78
β	Receding contact angle (angle)	57
b	Half thickness of the channel thickness (length)	115
Bi	Biot number (unitless)	78
CHF	Critical heat flux (power / area)	26
C_m	Two phase friction multiplier (unitless)	48
δ	Thickness of the boundary layer (length)	46
$\delta\left(x\right)$	Momentum thickness of the boundary layer (length)	46
D^*	Hydraulic diameter divided by the axial position (unitless)	48
δ_1	Displacement thickness of the boundary layer (length)	46
δ_{beam}	displacement of beam under load (length)	39
D_d	Bubble departure diameter (length)	57, 63
D_h	Hydraulic diameter, $\frac{4A}{p_w}$ (length)	46, 63
$\Delta h_{sub,in}$	Subcooling enthalpy difference from saturation (energy / mass)	48
$\Delta X_{i,j}$	PIV particle displacement (length)	114
$\left(\frac{\partial P}{\partial z}\right)_{fric}$	Pressure gradient due to friction forces (pressure / length)	46
$\left(\frac{dp}{dz}\right)$	Total pressure gradient due to all forces (pressure / length)	115
$\Delta\rho$	The density difference between liquid and vapor phases (mass / volume^3)	48
δ_s	Viscous sublayer thickness (length)	45
Δt	The time delay between laser pulses (time)	114
ΔT_{sup}	Difference in wall temperature and saturation temperature (temp)	62
δ_w	Thickness of the heated wall (length)	78
d_w	Bubble foot diameter (length)	57
E	Modulus of Elasticity (force / area)	39
ϵ_1	Figure of merit for the error associated with the relative displacement of the particles (unitless)	114
ϵ_2	Figure of merit associated with the error of out-of-plane motion of the particles (unitless)	114

Notation	Description	Page List
ϵ_3	Figure of merit associated with the error from image displacement relative to particle image size (unitless)	114
$\mathbf{F}$	Vector sum of all forces (force)	25
f	Bubble departure frequency (time^{-1})	46
$\mathbf{F}_b$	Buoyancy force (force)	25, 56, 57
$\mathbf{F}_{cp}$	Contact pressure force (force)	25, 56
$\mathbf{F}_{du}$	Unsteady drag force (force)	25, 56
$\mathbf{F}_h$	Hydrodynamic pressure force (force)	25, 56, 57
Fo	Fourier number (unitless)	78
fps	Frames per second, (time^{-1})	27, 42, 43
$\mathbf{F}_{qs}$	Quasi-steady drag force (force)	25, 56
$\mathbf{F}_s$	Surface tension force (force)	25
f_s	Friction factor (unitless)	48, 115
$\mathbf{F}_{sL}$	Shear lift force (force)	25, 56
F_{sx}	Surface tension force x-component (force)	56
F_{sy}	Surface tension force y-component (force)	56
G	Mass flux (mass / area / time)	46, 63
g	Acceleration due to gravity (length / time^2)	57
G_s	Shear rate (unitless)	58
h	Heat transfer coefficient (power / temperature / length^2)	49, 78
h_{fg}	Enthalpy of vaporization (energy / mass)	48, 62, 63, 72
I	Moment of Inertia (length^4)	39
ITO	Indium Tin Oxide, a conductive oxide film that forms the active heater area	27, 35, 43, 87
k_e	Exit orifice coefficient (unitless)	48
k_f	Thermal conductivity of the fluid (power / length / temperature)	72
k_i	Inlet orifice coefficient (unitless)	48
k_w	Thermal conductivity of the wall (power / length / temperature)	72, 78
L	Length of a beam (length)	38
λ'	Cavity length scale, λ' = 2.50 x 10^{-6}m (length)	62
M	Mechanical moment about a point (force x length)	38
μ_c	Characteristic cone angle of nucleation site, typically 0.7 radians (angle)	62
μ_f	Dynamic viscosity of liquid (force x time / area)	63, 115
N''	Nucleation site density (sites / area)	24, 62
ν	Kinematic viscosity (length^2 / time)	45, 57
ONB	Onset of nucleate boiling, the point where two phase heat transfer begins to dominate (temperature)	26, 48, 103
P	Static pressure (force / area)	38
ϕ	Inclination angle of the bubble (angle)	56
P_h	The heated perimeter (length)	48
P_l	Pressure of liquid (force / area)	24, 63
P_v	Pressure of vapor (force / area)	24
p_w	Wetted Perimeter (length)	46
Q	Heat Generation Number (unitless)	78

Notation	Description	Page List
$q_w^{''}$	The wall heat flux (power / area)	48, 78
R	Instantaneous bubble radius (length)	57, 58
r^*	Critical radius (length)	24
R_c	Minimum cavity radius (length)	62, 72
Re	Reynolds number, $\mathrm{Re} = \frac{\rho v D}{\mu_f}$ (unitless)	13, 44, 115
$\mathrm{Re_b}$	Bubble Reynolds number (unitless)	57
$\mathrm{Re_{TP}}$	Two phase Reynolds number (unitless)	63
ρ_f	The density of the liquid phase (mass / volume)	48, 57, 58, 62, 63
R_g	Gas constant (energy / temp / mole)	62
ρ_g	The density of the vapor phase (mass / volume)	48, 57, 62, 63, 72
ρ	density of the fluid (mass / volume)	45
ρ_λ	Radiation reflection fraction of a surface (unitless)	27
R	The photographic spatial resolution (length)	114
RPP	Reactor prototypicality parameter (unitless)	21
r_r	Radius of curvature of the bubble (length)	57
RTDs	Resistance Temperature Detector	33
σ	Surface tension of the fluid, σ (force / length)	24, 57, 62, 63, 72
$[Sc_{Mod_K}]_{APP}$	Non-dimensional parameter of interest for RPP, applied value (PWR) (unitless)	21
$[Sc_{Mod_K}]_{EXP}$	Non-dimensional parameter of interest for RPP, experimental value (unitless)	21
Θ	Temperature ratio number (unitless)	78
ϑ	Angle of the test section with respect to horizontal (angle)	56
T_b	Bulk liquid temperature (temperature)	49, 72, 78
t_g	Bubble growth time (time)	25
T_i	Initial temperature (temperature)	78
τ_λ	Radiation transmission fraction of a surface (unitless)	27
T_n	Bubble nucleation temperature (temperature)	78
T_{sat}	Saturation temperature for the fluid at the local pressure (temperature)	25, 26, 62, 63, 72
T_w	Wall temperature (temperature)	49, 62, 72
τ_w	Shear stress at the wall (force / length)	45
t_w	Bubble wait time (time)	25, 72, 78
T_w^{0+}	Wall temperature after a bubble growth event (temperature)	72
U_∞	Uniform velocity that is found as approaching the middle of the channel in turbulent flow (velocity)	46
U	Flow velocity (velocity)	57, 58
$U_{i,j}$	Measured the velocity vector at position i,j (velocity)	114
v_{fg}	Specific volume change from liquid to vapor phase (volume / mass)	72
v_{fi}	Liquid inlet velocity (velocity)	48
w	distributed loading on a beam (force / length)	39
χ	Vapor quality (unitless)	63
x	Coordinate in the direction of flow (length)	46
x_g	Position in the channel in short dimension perpendicular to the flow (length)	115

Notation	Description	Page List
y	Position away from the wall perpendicular to the direction of the flow (length)	46
y_g	Position in the channel in long dimension perpendicular to the flow (length)	115
Z_B	Axial position of commencement of saturated boiling	26
Z_D	Axial position of the onset of significant voiding	25
z_d	Heated length to the site of interest (length)	48
Z_E	Axial position where equilibrium boiling occurs	26
Z_{NB}	Axial position of onset of nucleate boiling	25

1 Introduction

Subcooled flow boiling is a complicated phenomenon utilized in many industrial heat transfer applications, including conventional and nuclear power plants. It includes many heat transfer mechanisms, and is further complicated by the two phase flow and the non-equilibrium phenomena existing between the vapor and the liquid phases. Although it has been studied for many years, it is difficult to fully understand the underlying physics because of limitations on the parameters that can be simultaneously measured. A better understanding of subcooled flow boiling would allow for development of better codes and methods for predicting the flow characteristics in subcooled boiling heat transfer applications.

The development of better models for subcooled flow boiling would allow for better predictions of heat transfer in nuclear power plants. This would reduce time and costs involved in evaluating the boiling characteristics of two-phase heat transfer. New designs could also be more easily evaluated without the need for running of costly experiments. Better CFD modeling of two-phase heat transfer could also impact other technologies that utilize subcooled flow boiling such as two-phase heat exchangers and two-phase semiconductor cooling devices.

1.1 Objectives

The objective for the proposed work was to generate a new set of synchronized high-resolution data on subcooled flow boiling characteristics, including bubble departure diameter and frequency, temperature and velocity distributions of the liquid phase, and temperature profiles of the boiling surface. This data may be used to validate numerical models in Computational Fluid Dynamics (CFD) codes that model the two phase flow in the test section. Additionally, novel experimental observations presented here may inspire the development of more comprehensive mechanistic models of subcooled boiling. The approaches used in CFD include the Eulerian-Eulerian, two-fluid, six-equation model [1], and closure relations for the momentum and energy equations can be provided by models such as the heat flux partitioning model of Kurul and Podowski [2] and Kolev's bubble interaction model [3], which require bubble departure diameter, wait and growth times, and nucleation site density as input.

The approximate flow conditions of the experiment and how they compare to a typical Pressurized Water Reactor (PWR) are summarized in Table 1.2 along with parameter ranges for various other experimental works. While the flow conditions and geometry are not prototypical of the PWR core situation, they interrogate a sufficiently broad range of parameters to be used in the development of generally-applicable models and correlations for subcooled flow boiling heat transfer. Listed along with the reactor parameters is the reactor prototypicality parameter RPP, which is defined as [4].

$$RPP = \frac{[Sc_{Mod_K}]_{EXP}}{[Sc_{Mod_K}]_{APP}} \tag{1.1}$$

Where, $[Sc_{Mod_K}]_{EXP}$ is a parameter value from the experiment and $[Sc_{Mod_K}]_{APP}$ is a parameter value from the application (PWR in this case). The RPP values for the current work are shown in Table 1.2 along with the channel condition ranges for this work, previous works, and a PWR channel. All of the values are within range except for the pressure and density ratio, which are both due to the lower pressure in the

experiment.

Table 1.1 lists both the parameters that can be measured in the two phase flow loop and the method by which they were measured. These parameters will be measured while varying the mass flow rate, inlet subcooling, heat flux, and system pressure.

Table 1.1: Subcooled boiling parameters capable of being measured by the experimental setup.

Parameter	Measurement Method
Bubble Departure Diameter	HSV
Bubble Departure Frequency	HSV
Bubble Growth Time	HSV, IR
Bubble Wait Time	HSV, IR
Nucleation Site Density	IR
Point of Onset of Nucleate Boiling	HSV, IR
Heat Transfer Coefficient	IR
Bubble Sliding Velocity	HSV
Liquid 2D Velocity Field	PIV
Heater Surface 2D Temperature Profile	IR
Heat Flux	PI, EB
System Pressure	PT, PG
Inlet temperature	RTD, TC, TM
Outlet temperature	RTD, TC, TM
Flow Rate, Mass Flux, Re Number	FM

Abbreviation	Full Name
HSV	High Speed Video
IR	Infrared Imaging
PIV	Particle Image Velocimetry
RTD	Resistance Temperature Detector
TC	Thermocouple
TM	Thermistor
PT	Pressure Transducer
PG	Pressure Gauge
FM	Flow Meter
PI	Power Input
EB	Energy Balance

Table 1.2: Flow parameters in the current work and previous works compared with a PWR reactor subchannel at normal operating conditions.

	Current Work	PWR Range Range	Euh (2010)	Situ (2008)	Basu (2002)	Valle (1985)	Díaz (2005)	Typical RPP*
Reference #	N/A	[5]	[6]	[7]	[8]	[9]	[10]	[4]
Reynolds Number	6.7×10^3-9.0×10^4	2×10^5-5×10^5	1.75×10^4-1.78×10^6	3.2×10^4-6.1×10^4	8.45×10^3-1.14×10^5	5.50×10^2-3.94×10^4	8.00×10^1-1.13×10^3	0.20
Prandtl Number	1.1-6.2	0.9-1.2	1.22-1.83	1.78-2.23	1.89-3.76	2.23-7.01	~3	1.00
Froude Number	0.17-12.0	0-217	0.28-21.1	1.27-4.72	0.04-2.20	0.09-58.0	0.03-8.61	0.10
Boiling Number	0.03-3.64	0-0.25	0.015-0.506	0.03-0.20	0.012-3.41	0.06-13.0	0.03-5.94	1.00
Equilibrium Exit Quality	-0.03 to 0.0	-0.20 to -0.05	-0.05 to 0.09	-0.04 to 0.02	-.10 to -0.01	-0.16 to -.04	+	0.25
Water velocity (m/s)	0-1.3	2-5	0.23-1.98	0.48-0.93	0.13-0.92	0.8-2.0	0.03-3.54	0.20
Mass Flux (kg/m^2/s)	150-1250	1500-3500	214-1869	466-900	124-886	78-2000	25-350	0.43
Temperature (°C)	85-125	286-324	97.6-130.8	80-98.5	47.4-93.3	19.7-79.7	50	0.34
Pressure (kPa)	105-200	1.55×10^4	167-346	103	101	117	300	0.03
Density Ratio	836-1620	6	497-1017	1585	1610	1433	574	73.0
Inlet Subcooling (°C)	0-15	21-58	7.5-23.4	1.8-20.3	6.6-52.5	24-84	73	0.50
Hydraulic Diameter (mm)	16	12	19.1	19.1	39.2	7.1	1.5	1.25
Wetted Perimeter (mm)	110	30	179.6	179.6	1665.6	34	4.7	3.67
Heated Perimeter (mm)	15	30	60.0	60.0	42.0	10	4.7	0.50
Heat Flux (kW/m^2)	77-1600	0-450	61.3-238.0	60.7-206	25-963	300-4674	20-350	1.00
Channel Area (mm^2)	450	88	854	854	1633	60	1.76	5.11

* Nominal PWR conditions compared to current work

+ Not Reported

1.2 Background

1.2.1 Nucleate Boiling Fundamentals

Boiling on a surface requires that the surface have a superheat above the saturation temperature of the liquid. The heated wall conducts heat to the liquid next to the wall to a temperature above that of the bulk fluid and creates a thermal boundary layer. A bubble will preferentially form at a "nucleation site," which is a cavity on the heat transfer surface that has the proper shape to retain some non-condensable gases when the surface is flooded with the liquid. A typical conical cavity is shown in Figure 1.1.

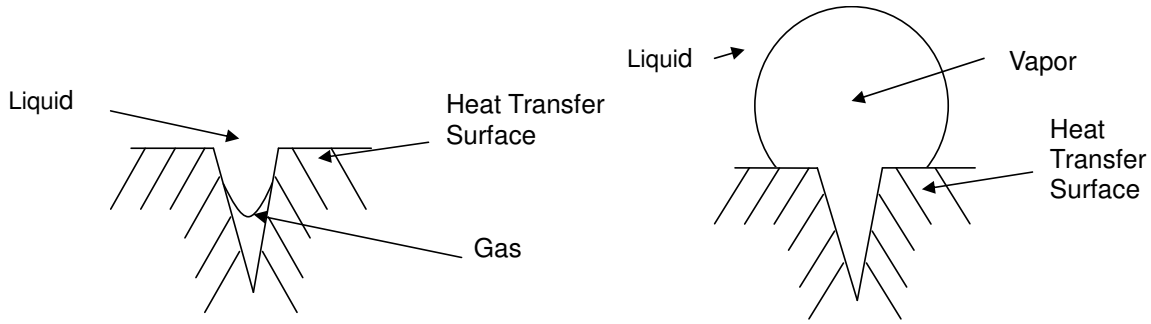

Figure 1.1: Example of typical active nucleation site (left), and bubble after growth (right)

Whether or not a cavity will retain entrapped gas is determined by the angle of the cavity compared to the contact angle of the liquid on the heat transfer surface. The contact angle of the liquid is defined by the angle a drop of the liquid makes on the surface of interest, and the static contact angle is shown in Figure 1.2. If the surface in Figure 1.2 was tilted and the drop began to roll on the surface, the angle the front of the drop makes with the surface is the advancing contact angle, and the angle of the back end of the droplet makes with the surface is the receding contact angle. A potential nucleation site will trap gas when the surface is flooded with liquid if the advancing contact angle of the liquid is greater than the cone angle of the cavity [11].

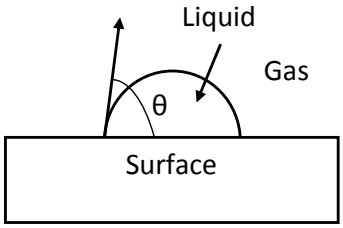

Figure 1.2: Contact angle made by a liquid on a solid surface.

When an adequate superheat has been reached, the bubble will begin to grow from liquid water vaporization. The condition when the bubble begins to grow is dependent upon the cavity mouth size, and is governed by the Young-Laplace equation (1.2) [12].

$$r^* = \frac{2\sigma}{P_v - P_l} \tag{1.2}$$

Where r^* is the critical radius σ is the surface tension of the fluid, P_v is the pressure of the vapor phase, and P_l is the pressure of the liquid phase. The number of active nucleation sites on the surface per unit area is referred to as the nucleation site density (N'').

The bubble will continue to grow until the forces pulling it from the surface are greater than the forces that are holding it on the surface. In the case of external flow there are several forces that act upon the bubble that dictate when it detaches from the wall. The bubble can either detach perpendicular to the wall (liftoff) or detach parallel to the wall (slide). In the case of a sliding bubble, there will usually be a small liquid film under the vapor of the bubble and the bubble remains close to the wall. The film may vaporize and cause the bubble to reattach and then once again break away from the wall. The forces acting on the bubble are shown in (1.3) [13, 14].

$$\sum \mathbf{F} = \mathbf{F}_s + \mathbf{F}_{qs} + \mathbf{F}_b + \mathbf{F}_{du} + \mathbf{F}_{sL} + \mathbf{F}_h + \mathbf{F}_{cp} \tag{1.3}$$

Where $\mathbf{F}$ is the vector sum of all forces acting on the bubble, $\mathbf{F}_s$ is the surface tension force that tends to hold the bubble on the surface, $\mathbf{F}_{qs}$ is the quasi-steady drag force caused by the drag of the flow around the bubble, $\mathbf{F}_b$ is the buoyancy force acting opposite of gravity, $\mathbf{F}_{du}$ is the unsteady drag force due to asymmetric growth, $\mathbf{F}_{sL}$ is the shear lift force caused by the velocity distribution next to the wall which tends to pull the bubble away from the wall, $\mathbf{F}_h$ is the hydrodynamic pressure force, and $\mathbf{F}_{cp}$ is the contact pressure force.

When the force balance is broken in either the vertical or parallel direction, the bubble will detach from the wall. The diameter of the bubble when it departs from the surface is referred to as the departure diameter. The model is described in more detail in section 3.3.1. As the bubble departs, water rushes onto the surface to fill the void the bubble left, and this turbulent motion will remove more heat from the surface, and is typically referred to as quenching.

The time from the start of the bubble growth to the detachment is called the growth time (t_g), and then the time from when the bubble departs until the next bubble begins to form is called the wait time (t_w). The sum of these two is the bubble period, and the inverse of the period is the bubble frequency as shown in (1.4).

$$f = \frac{1}{t_g + t_w} \tag{1.4}$$

A parameter that is often measured in tandem with the frequency is the nucleation site density. The nucleation site density represents the number of active nucleation sites per unit area for a given set of channel conditions. The sites may not all be active at a specific time, but if the system is in a quasi-steady boiling condition, the active sites will nucleate a bubble at some frequency determined by the characteristics of the specific site.

The frequency, nucleation site density, and bubble departure diameter are often used in mechanistic boiling models. Together they give an estimate of the energy removed from the surface from vaporization. However, in subcooled flow boiling, there is also a significant amount of condensation from the bubble as the bubble grows into the subcooled flow, which is a difficult quantity to experimentally measure.

1.2.2 Subcooled Flow Boiling

Consider a flow of single phase fluid within a channel with a heated wall as shown in Figure 1.3 (a). At some distance from the inlet, the temperature of the fluid near the wall becomes greater than T_{sat} and subcooled flow boiling begins. This is the onset of nucleate boiling, and the location is designated Z_{NB}. Note that the boiling begins prior to the bulk fluid reaching saturation temperature. At the onset of nucleate boiling the vapor bubbles do not leave the wall, as long as there is an equilibrium between evaporation at the bubble base and condensation at the bubble head due to cooling by the adjacent flow. As the temperature of the flow rises as the fluid travels through the heated channel, the bubbles may begin to grow larger and eventually detach, which marks the onset of significant voiding at the location Z_D. In subcooled boiling, the detached

bubbles may slide down the channel wall without moving into the bulk fluid because of condensation.

If the channel imparts enough energy to the flow, then the bulk fluid eventually becomes saturated and saturated boiling commences at the point Z_B. Since the bulk fluid is at T_{sat}, the bubbles can survive in equilibrium after entering the bulk fluid, thus further increasing the void fraction. Eventually, the channel will reach an equilibrium at the point Z_E where the flow cannot be distinguished from the flow of a channel that began with saturated boiling [15, 16]. More on subcooled boiling heat transfer and an estimation of the heat flux necessary for the test section can be found in Appendix B.

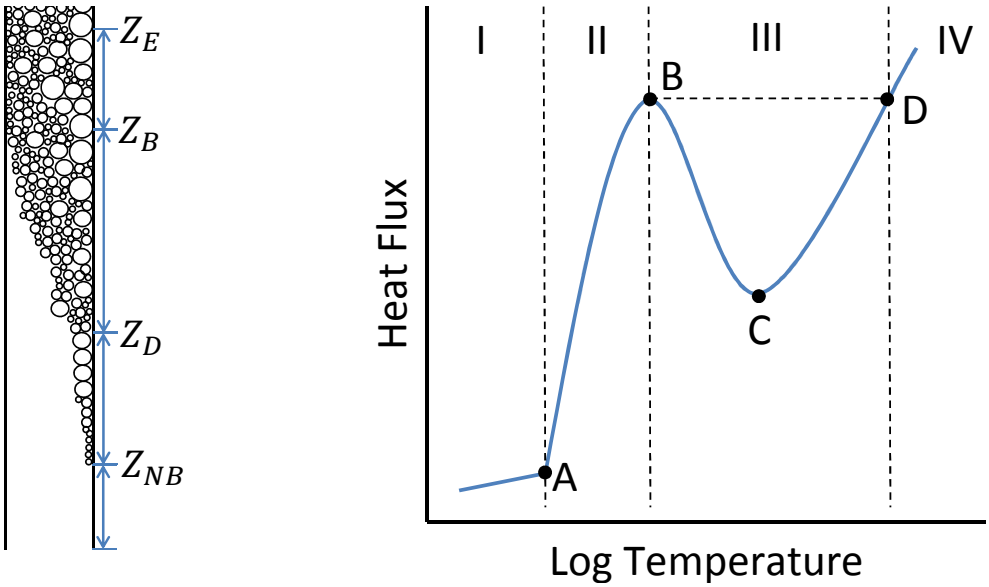

(a) Boiling channel

(b) Boiling curve

Figure 1.3: Boiling depicted by (a) development in a channel with a heated wall, and (b) a typical boiling curve.

Figure 1.3 (b) shows a typical boiling curve. There are four major regions in this curve. I: the single phase heat transfer regime, II: the nucleate boiling heat transfer regime, III: the transition boiling regime, IV: the film boiling regime.

For a given set of channel conditions of a fluid entering a heated channel, as the heat flux is increased, the wall temperature will increase to point "A," which is the onset of nucleate boiling (ONB) where nucleate boiling becomes dominant over single phase heat transfer and enhances the heat transfer. This reduces the wall temperature increase for a given increase in heat flux compared to single phase. As the heat flux increases, nucleate boiling continues until point "B" is reached, which is known as Critical Heat Flux (CHF). At this point, if the heat flux is further increased, the wall temperature will jump from point "B" to point "D" and there will be a drastic increase in wall temperature, usually resulting in the destruction of the surface due to the poor heat transfer characteristics of film boiling. Point "C" is known as the Leidenfrost point, and is the temperature below which the transition from film boiling back to nucleate boiling occurs.

Most heat transfer applications operate in regions "I" and "II", so boiling curves are typically only measured up to some point within region "II" below point "B" where CHF occurs.

1.2.3 Methods of Measurement

Particle Image Velocimetry

Particle image velocimetry (PIV) uses particles within a flowing fluid to determine the velocity vectors of the flow at various locations. This is accomplished by using a high speed video camera to image the flow over short time intervals and track how the particles in the fluid move. The particles are typically seeded into the fluid and are then highlighted by using a laser with cylindrical optics that disburse the laser beam into a "sheet." This sheet of light then highlights the particles in the plane of the laser and this image is captured by the high speed camera. This process is repeated to obtain a series of images over time.

These images can then be post processed to track the progression of the particles over time and thus calculate the velocity vectors within the laser plane sheet. This is accomplished by using two adjacent images, breaking them into a grid, and within each of these interrogation windows, the movement of the particle pattern is determined and a velocity vector is calculated. This method makes the assumption that the particles are moving at the same velocity as the fluid. Also, the components of the velocity vector within the light sheet plane are all that can be determined. The velocity component perpendicular to the plane cannot be determined by using a single camera [17, 18].

The PIV system used was a LAVision Flowmaster system using a Phantom V12.1 HSV camera. The camera has a resolution of 1280x800 and is capable of 6242 frames per second (fps) at full resolution, and tens of thousands of fps at reduced resolutions. With appropriate optics it can achieve a spatial resolution better than 7 μm.

Infrared Thermography

A high speed infrared (IR) camera was used to image a heater surface and obtain a 2D temperature profile of the heater surface. The infrared camera recorded counts of infrared radiation in the wavelength range of 3-5 μm and then this was used along with a calibration to determine the surface temperature. The materials for the heater were carefully chosen to allow for accurate determination of the surface temperature during the experiment. IR radiation can be absorbed (α_λ), reflected (ρ_λ), or transmitted (τ_λ) by a material. For a body at steady state, the absorbance must equal the emittance (emissivity) from the body. For a given wavelength of radiation these fractions must all sum to 1 as shown in Eq. (1.5) .

$$\alpha_\lambda + \rho_\lambda + \tau_\lambda = 1 \tag{1.5}$$

In the case of the heater design that is discussed in section 2.2, the heater substrate is made of a material that has very low absorbance and and a moderate reflectance and transmittance for the wavelengths of interest. The active heater itself is very thin (so it is in thermal equilibrium through its thickness) and is composed of a thin film of Indium-Tin Oxide (ITO). ITO is a conductive oxide that has almost a zero transmittance for the wavelengths of interest. Therefore, the radiation is either absorbed (then re-emitted) or reflected. The IR camera then only receives radiation from the ITO layer, and not from anything beyond the ITO. Thus emissions from the water are not observed, as well as reflections from the water. This information can then be used to determine the 2D temperature profile of the heater surface.

The reflections from the ITO from the environment are minimized by the test section design by keeping hot objects at angles so there is not a high visibility to the ITO. Also, proper camera alignment is necessary to keep reflections from interfering with the measurement. Even after taking precautions, there will still be some amount of reflected radiation, but with proper alignment, this is limited to the edge of the heater surface, which is then not used for measurements. Reflections from objects at room temperature have a very small intensity in the 3-5 μm range, and have a negligible effect on the measurement.

The cameras used for this work were a FLIR ThermoVision® SC6000 and an IR Cameras 806HS. Both of these cameras were 14-bit cameras with a maximum resolution of 640x512 pixels. However, the IRC camera was often used in a 13-bit mode that allowed for faster acquisition. The FLIR camera had a maximum capture rate of 50 Megapixels per second [19]. The IRC camera used a Santa Barbara Focal Plane sensor (SBF209) and had a maximum capture rate of 200 Megapixels per second [20]. The use of the proper optical setup and windowing the sensor, frame rates of up to 2500 Hz and spatial resolutions down to 15 μm were achieved. This provided a much higher spatial and temporal resolution than could be achieved by traditional thermocouple arrays which are limited by the physical size of the thermocouple and the response time of the thermocouple.

1.2.4 Mechanistic Modeling

Traditionally, the boiling phenomenon has been characterized empirically with correlations and very simple physical models. With the advent of new interrogation technologies, which have been discussed above, including high speed optical and infrared imaging as well as particle image velocimetry, the development of more accurate mechanistic models is possible. Bubble parameters can be measured such as nucleation site density, departure diameter, and frequency that are important as inputs to interfacial area transport models [1] and for semi-empirical models such as that of Podowski [21, 22]. The 2D temperature distribution of the surface during the ebullition cycle can also be measured and is needed for CFD methods based on interface tracking (see Appendix E) [23].

1.3 Previous Work

Subcooled flow boiling has been extensively studied; however, the work relevant are those that use the advanced flow characterization methods that were also used in this investigation. There is still a large body of data on this topic, but a representative sample is discussed that covers the previous work that has measured similar parameters with similar techniques.

Del Valle and Kenning [9] measured surface temperature and used high speed photography in subcooled flow boiling with water to examine nucleation site density in a rectangular channel. They calculated the heat removed through various processes including microlayer evaporation, quenching of the surface after bubble departure, and convection and compared the total values to the experimental heat flux. They found that for their 84K subcooled flow, quenching of the surface was the most important component of the heat transfer and the microlayer evaporation effect was negligible.

Basu et al. [8] measured the temperature distribution with thermocouples in a rod bundle. They developed a correlation for the onset of subcooled nucleate boiling based on the contact angle of the fluid with the surface, the local subcooling, and the axial location. Their correlation is for water and valid for contact angles from 1-85 °C, pressures from 1-137.5 bars, local liquid subcooling of 1.7-80 °C, and velocities from 0 m/s-17 m/s. They found that the nucleation site density depended only on contact angle and wall superheat.

Situ et al. [24] conducted subcooled flow boiling experiments with water in an annular channel. They measured bubble parameters such as departure diameter, nucleation site density, departure frequency, and velocity after departure with high speed photography. Situ et al. [7] went on to develop a correlation for bubble departure frequency.

Euh et al. [6] examined bubble departure in an annular channel during subcooled boiling. They varied the test conditions over a test matrix of 167-346 kPa, mass fluxes of 214-1869 $\frac{kg}{m^2-s}$, heat fluxes of 61-238 $\frac{kW}{m^2}$, and subcooling of 7.5-23.4 °C. They compared their data to the mechanistic models of Basu [25], Podowski et al. [21] and Situ et al.[7]. They found that the data fit Situ's model well, and developed a modified form of the model to better represent their data.

PIV has been applied to multiphase systems in the past. Hassan et al. [26] used PIV to measure the velocity of heavy mineral oil with air bubbles rising through the pool. The rise velocity of the bubbles was also determined from the high speed camera measurements. PIV has also been extended from simple two phase flows to study subcooled flow boiling. Estrada-Perez and Hassan [27] used particle tracking in subcooled boiling of refrigerant HFE-301 in a rectangular channel with a single heated wall. Estrada-Perez obtained velocity fields and turbulence intensities over a variety of Reynolds numbers and heat fluxes. They showed that particle tracking is a reliable method for determining velocities in the liquid phase during subcooled boiling. Estrada-Perez used his own particle tracking techniques that he developed [28] where he also showed that the errors in the velocities calculated by PIV increase with the mean particle size.

Thorncroft et al. [29] performed high speed camera analysis of upward and downward flow boiling of slightly subcooled FC-87 in a square test section equipped with a heating strip. They measured the heater surface temperature at various axial positions using thermocouples. They found that the dynamics were vastly different for upward and downward flow. They also concluded that a major mechanism of heat removal was the "sliding" of the bubbles along the surface prior to their departure. A bubble can either slide along the surface, or immediately depart into the bulk fluid and collapse [30]. Bubble sliding has been further investigated such as by Li et al. [31] and they found that the distribution of bubble sliding velocities and sliding diameters was quite large. They also identified two regimes of bubble sliding. The first is for bubbles with a short lifetime whose diameters fluctuate rapidly during sliding from rapid vaporization and condensation. The second type has a longer lifetime and the diameter changes more slowly. The interaction of nucleation sites can also have an influence on the departure diameter [32], in pool boiling the closer two sites are together tends to lower the departure diameter.

Chen et al. [33] investigated how bubble characteristics varied for R-407C in a narrow rectangular annular horizontal channel using HSV. They found that the heat transfer coefficient increased with a smaller gap. They also proposed correlations for nucleation site density and bubble frequency.

Recently, Sugrue et al. [34] conducted a systematic experimental investigation of bubble departure diameter in subcooled flow boiling over a range of mass fluxes, heat fluxes, inclination angles, pressures and subcoolings. Their data indicate that the bubble departure diameter increases with increasing heat flux, decreasing mass flux, decreasing subcooling, and decreasing pressure. Also, the bubble departure diameter increases with decreasing orientation angle, i.e. the largest bubbles are found to detach from a downward-facing horizontal surface.

High speed infrared cameras have been used to capture 2D temperature profiles of the surface during boiling. The data collected has been used to measure bubble parameters , the effect of nanofluids on bubble parameters, nucleation site density, and surface temperature during quenching [35–40]. There has been some work done with IR thermography to measure the wall temperature of a heater during flow boiling using very low frame rates that were unable to capture individual nucleation events [10].

Many researches have changed the surface characteristics in an attempt to enhance boiling heat transfer characteristics by coating surfaces with various micro-structured [41–43] and nanostructured surfaces including nanotubes [44–46], nanowires [47], and nanoporous structures [43, 48]. Most of these have shown enhancements in pool boiling heat transfer, but surface modifications for flow boiling have also been explored and shown to be capable of increasing heat transfer coefficient by up to 100% [49, 50] in pool boiling applications. Modifications to the surface chemistry to affect the wettability of the boiling surface in various patterns has also been explored in pool boiling, and in some cases showing increases in the heat transfer coefficient of up to 100% [51] and negligible enhancements in other cases [48].

The previous studies have measured various bubble parameters, but each experiment could not measure a vast number of them. Table 1.3 summarizes a sampling of the previous work and shows the large number of simultaneous parameters that are capable of being measured in this work that is discussed in the following sections. The multiple , and simultaneous measurement ability, allowed the development of a very detailed experimental database that can be used to validate the methods used in CFD codes as well as assist in the

development of mechanistic models for bubble growth, departure, and the mechanisms involved in two-phase heat transfer.

Table 1.3: Summary of parameters measured in previous research work and methods used versus those used in this work. Abbreviations are the same as those used and defined in Table 1.1.

Publications	Euh (2010)	Situ (2004, 2008)	Basu (2002)	Thorncroft (1998)	Del Valle (1985)	Estrada-Perez (2010)	Díez (2005)	Current Work
Reference #	[6]	[24] [7]	[8]	[29]	[9]	[26]	[10]	N/A
Departure Diameter	No	Yes, HSV	No	Yes, HSV	Yes, HSV	No	No	Yes, HSV, IR
Departure Frequency	Yes, HSV	Yes, HSV	No	Yes, HSV	No	No	No	Yes, HSV
Growth Time	Yes, HSV	Yes, HSV	No	Yes, HSV	Yes, HSV	No	No	Yes, HSV
Growth Rate	Yes, HSV	Yes, HSV	No	Yes, HSV	No	No	No	Yes, HSV
Wait Time	Yes, HSV	Yes, HSV	No	Yes, HSV	No	No	No	Yes, HSV
Sliding Velocity	No	No	No	Yes, HSV	No	Yes	No	Yes, IR, HSV
Nucleation Site Density	No	No	Yes	No	Yes, HSV	No	No	Yes, IR, HSV
Onset of Nucleate Boiling	No	No	Yes, HSV, PI	No	Yes, HSV, PI	Yes	Yes	Yes, IR, PI
Heat Transfer Coefficient	No	No	No	No	No	No	Yes, IR, PI	Yes, IR, PI
Liquid 2D Velocity Field	No	No	No	No	No	Yes, PIV	No	Yes, PIV
Heater 2D Temperature Profile	No	No	No	No	No	No	Yes	Yes, IR
Heat Flux	Yes	Yes	Yes	Yes	Yes	Yes	Yes	Yes
System Pressure	Yes, PG	Yes, PG	Yes, PT	Yes, PT	Yes	No	Yes	Yes, PT
Inlet temperature	Yes, TC	Yes, TM	Yes, TC	Yes, TC	Yes, TC	Yes	Yes	Yes, TM
Outlet temperature	Yes, TC	Yes, TC	Yes, TC	Yes, TC	Yes, TC	Yes	Yes	Yes, TM
Flow Rate, Mass Flux	Yes, FM	Yes, FM	Yes, FM	Yes, FM	Yes, FM	Yes	Yes	Yes, FM

2 Experimental Setup

2.1 Flow Loop

A flow loop was modified for this work that was previously designed and built by the Dr. Greg Dewitt and is located in the MIT Green Lab, NW13-253. Detailed information about the loop can be found in [52]. The loop is composed of 304 and 316 stainless steel. The loop consists of a variable speed pump, a turbine flow meter, a preheater (used to maintain constant subcooling), a stainless steel heat exchanger, an accumulator with a nitrogen gas over pressure, a fill and drain tank, various temperatures are measured via resistance temperature detectors RTDs, and pressures are measured with pressure transducers. The temperatures are measured via RTDs located at the condenser inlet and outlet and the test section inlet and outlet. System pressure is measured by pressure transducers located at the inlet and outlet of the pump and the inlet and outlet of the test section. Pressure gauges are also installed throughout the loop, including the gas side of the accumulator, the outlet of the heat exchanger, and the inlet to the loop from the fill and drain tank. The schematic of the flow loop is shown in Figure 2.1.

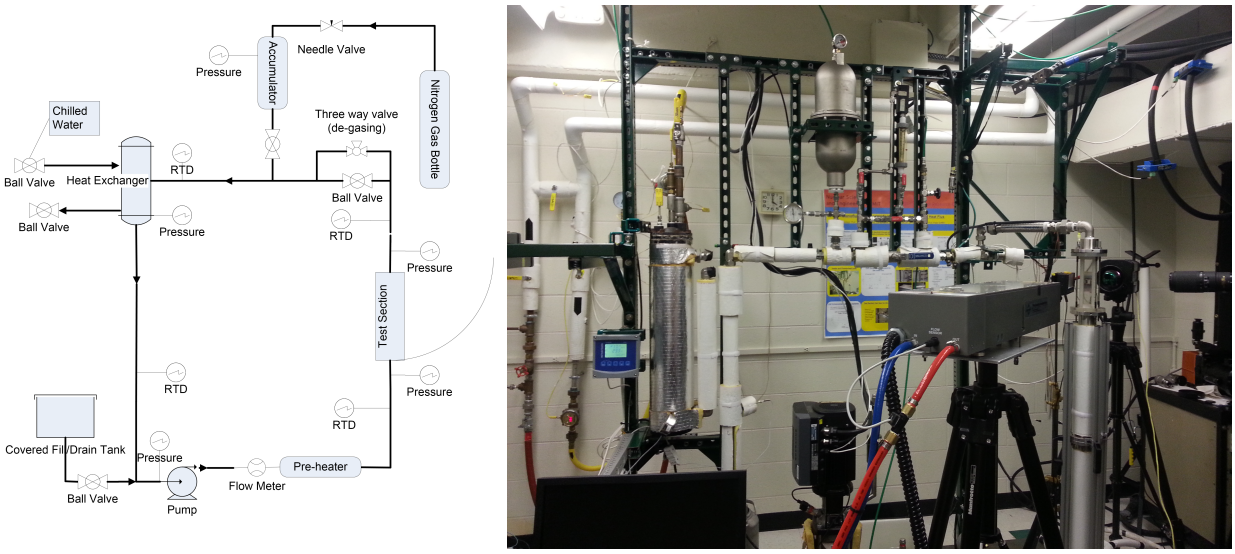

(a) Loop schematic

(b) Loop picture

Figure 2.1: (a) Schematic and (b) picture of the experimental flow loop, schematic courtesy of Gregg Dewitt.

2.2 Test Section and Heater

A customized test section was designed and manufactured to replace the previous test section in the flow loop described in section 2.1. The test section and heater had a variety of design requirements that are summarized in Table 2.1. The most important functions of the test section are that the test cell must be able to achieve subcooled flow boiling, be capable of being imaged by the HSV and IR cameras, and be compatible with the PIV system.

Table 2.1: Flow loop, flow cell, and heater design requirements .

Requirement	Basis
The cell must have visible access from a minimum of two sides that are at 90° angles.	There must be optical access for the high speed camera and the PIV laser.
The visible accesses should be flat and composed of a uniformly thick transparent material.	Prevent optical distortion from curved or variable thickness windows.
The cell must have IR access from the back side of the heater.	Provide an appropriate surface and substrate for the IR camera to get the 2D temperature profile on the surface.
The heater must be capable of reaching a heat flux which leads to bubble departure for a 40°C subcooling with 1000 kg/m^2/s flow.	There must be sufficient heat flux available to get bubble departures for imaging.
The heater must be a minimum of 1 cm x 1 cm in size.	Provides a sufficiently large heater area for imaging multiple bubble formations and departures.
The flow crossing the heater must be hydrodynamically fully developed.	Ensure fully developed flow across the heater to simplify the theoretical modeling and simulation of the flow.
The heater must be flush with the flow channel and any deviation must be quantifiable.	Minimize the flow disturbance from the edge of the heater.
The cost of the experimental section and the heaters must be within budget.	Stay within budgetary constraints.
The cell and heater must be able to operate from room temperature to 150 °C.	Accommodates the heat and thermal expansion without failure or leakage.
The windows must extend a minimum of 3 cm upstream of the heater and 3 cm downstream the heater.	Allows for measuring velocity fields at the inlet to the heater and outlet of the heater.
Electrical connections to the heater must be made outside the flow.	Prevent flow disturbances from electrical connections and minimize electrochemical corrosion of metal on the heater surface.
The heater must be sufficiently restrained to prevent vibration.	The heater must be fixed in a single location.
The flow cell and heater must withstand a differential pressure of a minimum of 2 bars.	Prevent mechanical failure of the test section due to loop pressure.
The heater corrosion must be minimized.	Prevent fouling of the flow loop or heater surface, and ensure an adequate lifetime of the heater.

Figure 2.2 shows a diagram of the quartz test section; the complete manufacturing drawings for the test section and associated components can be found in Appendix H. The test section has about 6 L/D values of quartz upstream and downstream of the heater recess, and then has flanges attached so that the section mated easily with the stainless steel loop on either side. On the inlet side, the cell was mated with a stainless steel conduit that had the same dimensions as the quartz flow channel, and the flanges were joined via a face-to-face seal with an O-ring, so that there was no flow disturbance at the inlet. The stainless steel entrance region had a length of nearly 64 times the equivalent diameter of the test section.

A hole in one side of the test section was designed for the heater cartridge to be fit with an O-ring groove to create a water tight seal with the heater cartridge. The O-ring groove and bolt holes were machined in a separate piece of $^1/_4$-inch quartz to prevent any crack propagation from the machined features into the channel wall of the test section. The bolt holes in the test section were fitted with 2-56 helical coils (McMaster-Carr # 91732A204), and were secured in place with Duralco™ 4463 epoxy. The helical coils were installed by placing a bolt coated in mold release (Dow Corning Molykote® 7) in the helical coil and then filling the holes with epoxy. The bolt with the helical coil was then placed in the hole and removed. The hole was then refilled with epoxy and the bolt with the helical coil was placed back into the hole. The bolt was then secured to ensure it was setting perpendicular to test section. The excess epoxy was cleaned off of the test section. After the epoxy cured, the bolts were backed out of the inserts.

Four 14 mm long 2-56 size bolts passed through bolt holes in the heater cartridge and mechanically secured the heater cartridge to the flow channel, compressed the O-ring, and passed electrical current to the heater.

The entrance region was constructed of 316L stainless steel to match the rest of the test loop. The first entrance component was a transition piece that transitioned the flow from 1 inch piping to the rectangular flow channel of the test section. This piece had an O-ring groove to seat against one side of the entrance assembly that had no O-ring groove. Each entrance assembly was 19 inches long, so two of these were placed end to end to surpass 64 L/D values to ensure that fully developed hydrodynamic flow was achieved. The second face of the second entrance assembly (which had an O-ring groove) mated with the entrance side of the quartz test section. Then at the top of the quartz test section was another National Pipe Thread (NPT) transition piece that transitioned the flow back to a 1 inch pipe. Drawings of the entrance region and NPT transition can be found in Appendix H.3.

The heater consisted of a 20 mm x 20 mm x 1 mm sapphire substrate with a 10 mm x 20 mm active Indium-Tin Oxide (ITO) heater area. The ITO was a thin film < 1 μm thick. The ITO was then wrapped around the side of the heater and 2.5 mm onto the back to allow attachment of the electrodes to the heater with conductive epoxy. The ITO resistance was minimized to 2.5 Ω/square to minimize the voltage drop across the heater and the heater had a nominal resistance of 5 Ω. To ensure that the ITO did not have large resistances on the corners of the sapphire, the corners were filleted with an approximate radius of 500 μm, and this necessitated the thicker sapphire of 1 mm. The ITO on the back of the heater was covered with silver pads to ensure good electrical connections with the electrodes. The electrodes and insulator had a shelf on which the sapphire heater sat that extended 2.5 mm under the sapphire. The graphite portion of the shelf had small semi-cylindrical cutouts that allowed for excess epoxy from the heater installation process to drain away from the heater and not block IR access. This approach had the disadvantage of blocking the IR access to the 2.5 mm on the two edges of the ITO heater adjacent to the electrodes. The heater and frame were designed to be placed into the flow cell in an orientation where the electrodes were at the top and bottom of the heater instead of at the sides. The orientation of the heater was to ensure that nucleation of bubbles on the intersection between the electrodes and sapphire did not interfere with the HSV camera. The heater is shown in Figure 2.5.

Between the electrodes on the edge of the heater there are Macor® insulators that make up a frame for the sapphire heater to be placed in and affixed to. The Macor® and the graphite are bolted and epoxied together to form a water tight seal between the graphite and the Macor®. This frame is then be placed into the glass

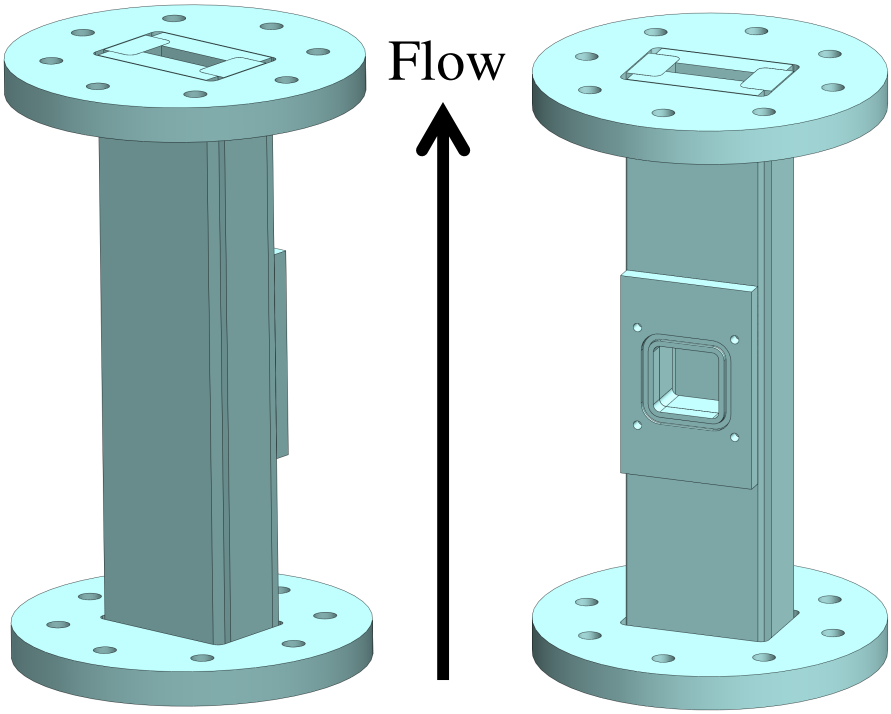

(a) Back view (b) Front view

Figure 2.2: Model of the quartz flow channel.

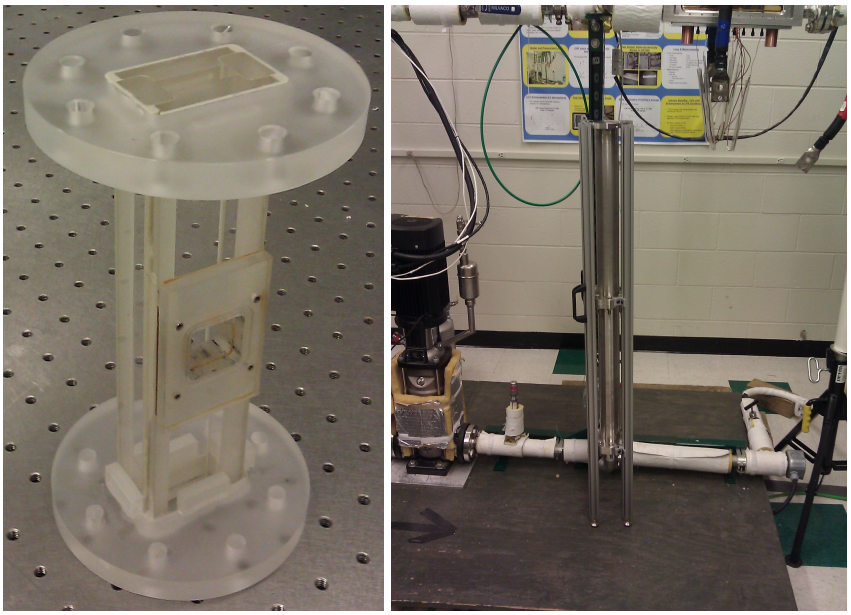

Figure 2.3: Picture of completed test section (left). Picture of assembled entrance regions (right).

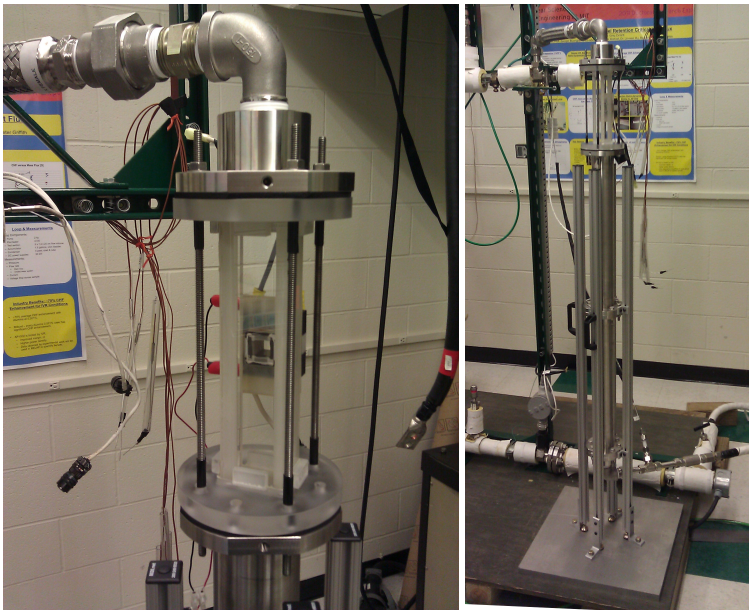

Figure 2.4: Picture of completed test section installed with entrance regions (left). Picture of complete test assembly (right).

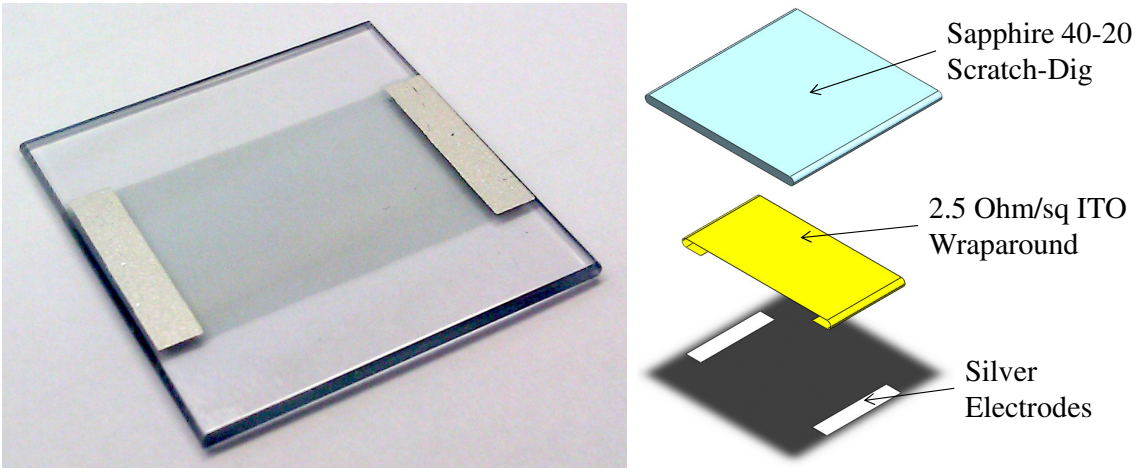

(a) Heater picture

(b) Heater exploded

Figure 2.5: ITO coated sapphire heater, (a) picture, and (b) exploded view.

flow boiling cell with a $^1/_{16}$-inch soft Viton® O-ring to make a water tight seal. The electrical connections are made using bolts that run through the electrodes and into the inserts in the quartz test section. The heater is placed in the heater cartridge shown in Figure 2.6, and pictures of the heater cartridge with and without the heater installed are shown in Figure 2.7. The procedure for the installation of the heater into the cartridge is in Appendix C.

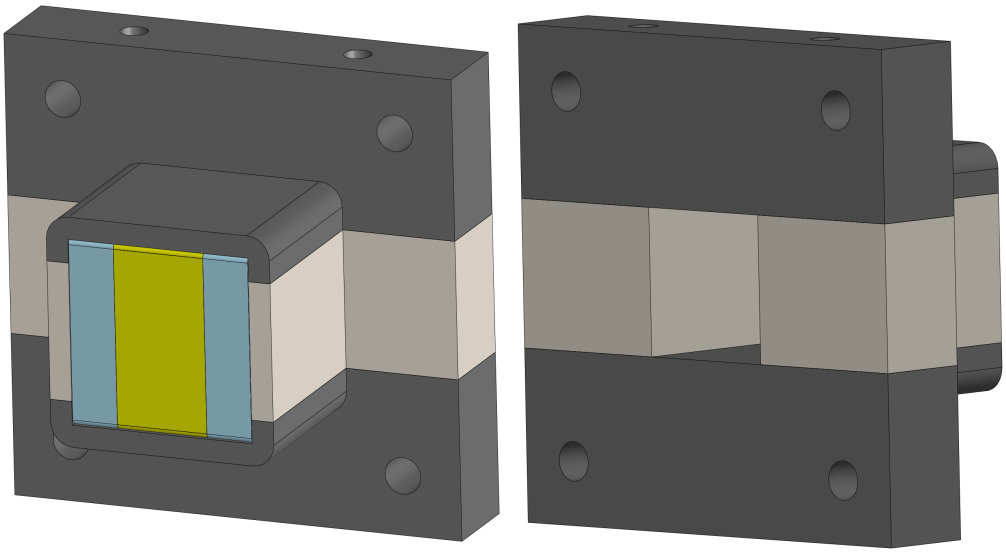

(a) Front view (b) Back view

Figure 2.6: Model of the ITO heater cartridge, (a) front view and (b) back view.

The resistance of the heaters should be approximately 7.5 Ω prior to installation into the cartridge, and approximately 5.0 Ω after installation into the cartridge where the sides get an electrical connection to the graphite. The uninstalled resistance ranged from 7.5-10.0 Ω on all of the heaters except for one which had a resistance of over 25 Ω. This is likely a problem with the coating on one of the edges. This high resistance heater was used as a test piece and to assist with the manufacturing of the heater cartridge.

2.2.1 Heater Stress and Deflection Calculation

The heater was supported on all sides so the stress field created from the pressure inside the channel had components in all three dimensions. However, to help bound the bending moments, stress, and deflection it was assumed that it was a simple beam that was supported on two opposite sides. The heater is supported on four sides, but two of the sides have a compliant gasket which is not a rigid support. Thus, the actual stresses will be between the simple beam stresses and the stresses created by a plate supported on for sides. The internal pressure of the flow loop creates a uniform force distribution across the heater. To be conservative, it was assumed that the heater was supported on the very edge. Summing the moments of the beam, the moment created is shown in equation (2.1).

$$M = \frac{PL^3}{4} \tag{2.1}$$

M is the moment, P is the internal pressure, and L is the length of the heater. The maximum deflection of the heater for a uniformly loaded beam with a rectangular cross section is given by (2.2) [53].

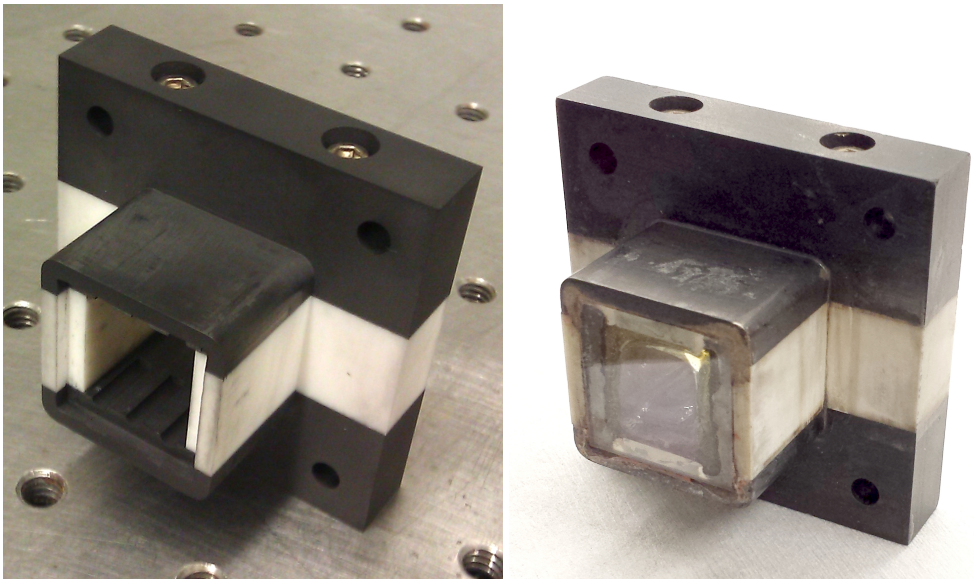

(a) Heater not installed (b) Heater installed

Figure 2.7: Picture of completed heater cartridge (a) without sapphire heater, and (b) with sapphire heater.

$$\delta_{beam} = \frac{5wL^4}{384EI} \tag{2.2}$$

δ_{beam} is the deflection, w is the distributed load (force/length), E is the modulus of elasticity, and I is the moment of inertia.

In Figure 2.8, the stress in the heater is shown with a conservative value for the ultimate tensile stress for sapphire. The stress is plotted assuming the stress that would result in a simply supported beam [53] and from a look-up table for a square plate supported on all 4 sides [54]. The value of the ultimate tensile strength of sapphire was taken as a conservative value at 500 °C. The maximum deflection of the heater is shown versus pressure in Figure 2.9.

2.2.2 Epoxy Selection

Different epoxy selections were made for the test section, one was for the assembly of the flow cell, and the second was for the heater cartridge. The epoxy selected for the flow cell was Cotronics Duralco™ 4463 and the selection for the heater cartridge was Cotronics Duralco™ 4703. The properties are compared to the requirements in Table 2.2.

Epoxy Bond Tests

Samples were made to determine the bond strength of the Duralco™ 4463 low expansion epoxy that was used for assembling the flow cell. Two types of samples were prepared – one with and one without the overlap of the epoxy onto the quartz as shown in Figure 2.10. The second sample is also shown in Figure 2.10, and has a bond area of $^1/_{16}$ in^2. A third sample was also created to test the bond thickness of the epoxy when clamped as shown in Figure 2.11. The approximate size of the bond was 5 mils.

Two of the samples with the the bond area of $^1/_{16}$ in^2 were tested. One side of both samples failed during curing. The other side was then tested to failure. The strength results were consistent, and ~2000 psi strength

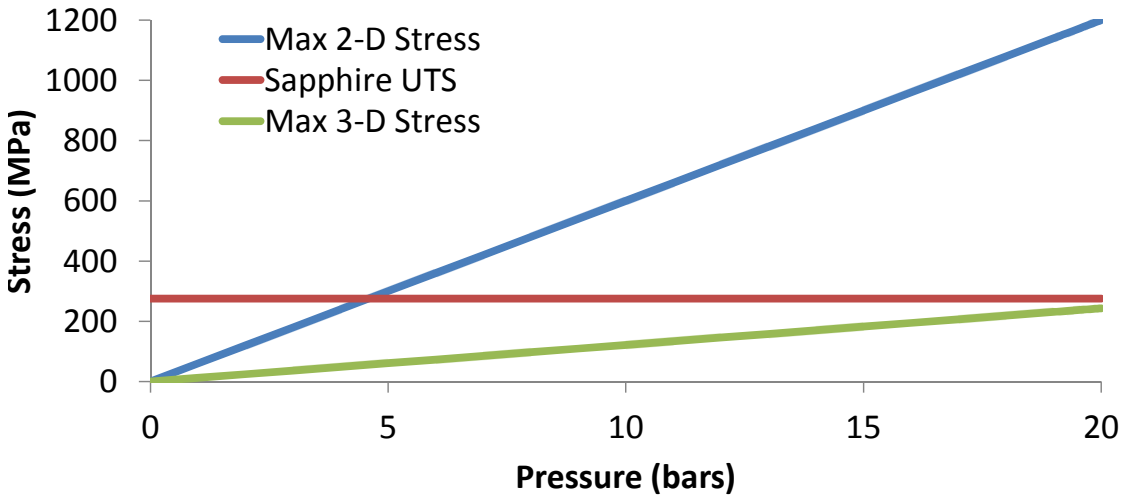

Figure 2.8: Stress of the sapphire heater versus internal loop gauge pressure.

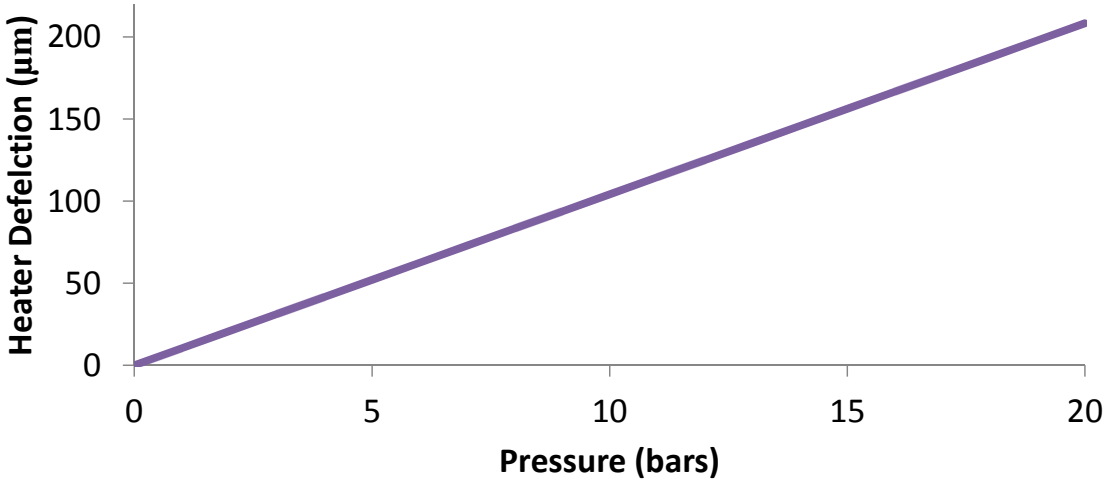

Figure 2.9: Sapphire heater deflection versus internal loop gauge pressure.

that was the design requirement for the test section. The strength is likely less than the reported strength of the epoxy due to the fact that the face of the quartz failed rather than the epoxy itself. The bond thickness test sample had a bending moment placed on the bond until it failed to observe the failure mechanism. The bond did not fail, instead the quartz failed, and this is shown in Figure 2.11.

Table 2.2: Flow cell and heater cartridge epoxy required properties and Cotronics Duralco™ 4463 and 4703 properties.

Flow cell requirement	Duralco™ 4463 Epoxy [55]
UTS greater than 2000 psi	UTS of 7000 psi
Stable to 150 °C	Stable to 260 °C
Stable in water	Stable in water
Bonds well to quartz	Bonds well to quartz
Highly rigid	2% strain to failure
Thermal expansion coeff. $\sim 0.5 \times 10^{-6}$/°C	Thermal expansion coeff. 2.0×10^{-5}/°C

Heater cartridge requirement	Duralco™ 4703 Epoxy [56]
UTS greater than 1000 psi	UTS of 11,800 psi
Stable to 250°C	Stable to 340 °C
Stable in water	Stable in water
Bonds well to quartz and Macor®	Bonds well to quartz and Macor®
Highly rigid	2% strain to failure
Thermal expansion coeff. $\sim 6.0 \times 10^{-6}$/°C	Thermal expansion coeff. 3.9×10^{-5}/°C

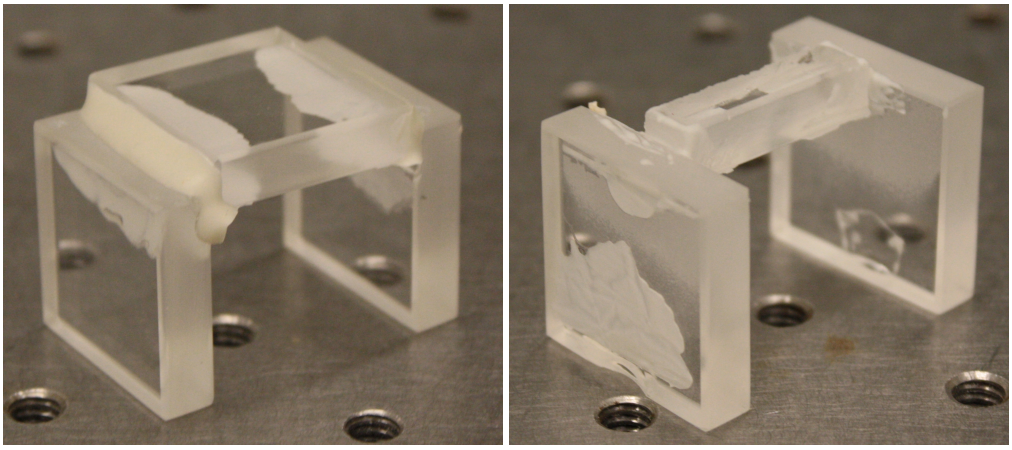

(a) 1-inch sample (b) $1/4$-inch sample

Figure 2.10: Strength test of quartz on quartz bonding with Duralco 4463 low expansion epoxy, (a) 1-inch sample, and $1/4$-inch sample with no epoxy overlap on top of the quartz.

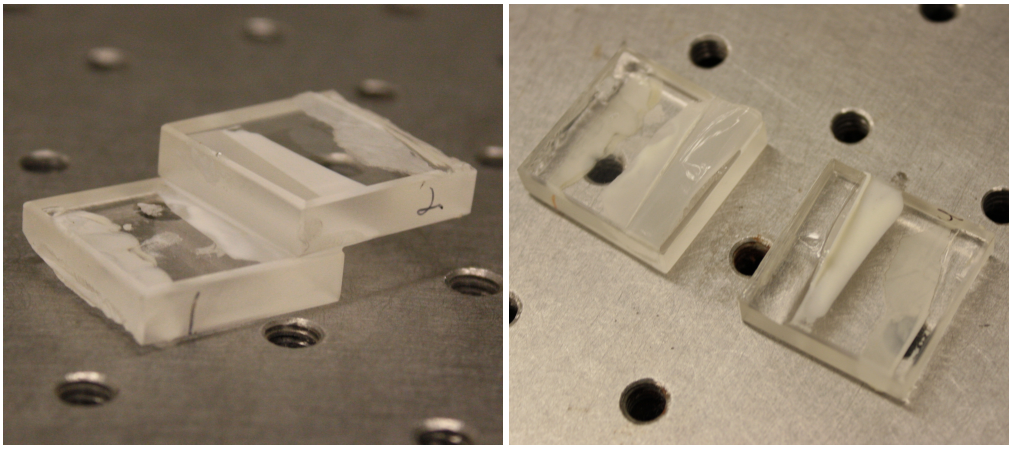

(a) Bond thickness sample (b) Bond thickness sample failed

Figure 2.11: Sample used to measure the bond thickness of Duralco 4463 epoxy (a) before testing, and (b) after failure from an applied moment.

2.3 Experimental Procedure

The loop was filled with deionized water from the fill/drain tank using nitrogen gas to pressurize the fill tank to approximately 5 psig. The pump was then started and non-condensable gasses were vented out of the system while makeup water was added through the fill tank. The preheater was then started to raise the temperature of the liquid, which lowered the solubility of non-condensable gases. When the fluid reached ~40 °C the mass flux was increased to 500 kg/m^2/s, and the test section heater was energized to allow for nucleate boiling to assist in degassing. When the fluid temperature reached 60 °C the temperature was stabilized by adjusting the power of the preheater and the degassing line was cycled. The degassing line valve was cycled every 10 minutes until no more bubbles emerged from the degassing line. The dissolved oxygen (DO) probe was installed and flow was aligned to the DO probe. A low reading of dissolved oxygen (5 ppm or less) confirmed that the loop was degassed. The loop bulk temperature was then raised to the desired temperature for the test.

The high speed video camera and the high speed IR camera were set up, and each were configured as described below. The optical setup is shown in Figure 2.12. The FLIR SC6000 camera is shown in the setup, although almost all of the data was taken with the IRC806HS high speed IR camera instead.

The HSV camera settings for the HSV/IR data collection included a Nikon 200 mm lens with 68 mm of extension rings, 15 µs exposure, 2500 fps, f/8 aperture, 1280x800 sensor resolution with the 1280 pixels in the flow direction, and 245 mm distance from the edge of the test section to the lens casing. For the PIV/IR data collection, the HSV camera was setup similarly, but with 204 mm of extension rings, 5 µs exposure, 720x720 resolution, and 161 mm distance from the test section to the front of the casing of the laser filter. For the PIV tests, the camera was also mounted on a support device that allowed for supporting the very long lens using the second from the front $^1/_4$-20 mounting hole on the camera, with the support pushed all of the way forward. This balanced the camera reasonably well over the tripod. The camera angle was checked using a level to ensure it was perpendicular to the test section.

A LED light with adjustable intensity was placed on the opposite side of the test section to take shadowgraphy images. In the case of the HSV/IR data, the light was adjusted to use the full 12-bit range of the camera without saturation of pixels. For the PIV/IR data, the light was adjusted so that the background reading uses less than 250-300 of the 4096 counts, and the rest of the dynamic range was reserved for the PIV particles. Care was also taken to make the background illumination as uniform as possible, as this

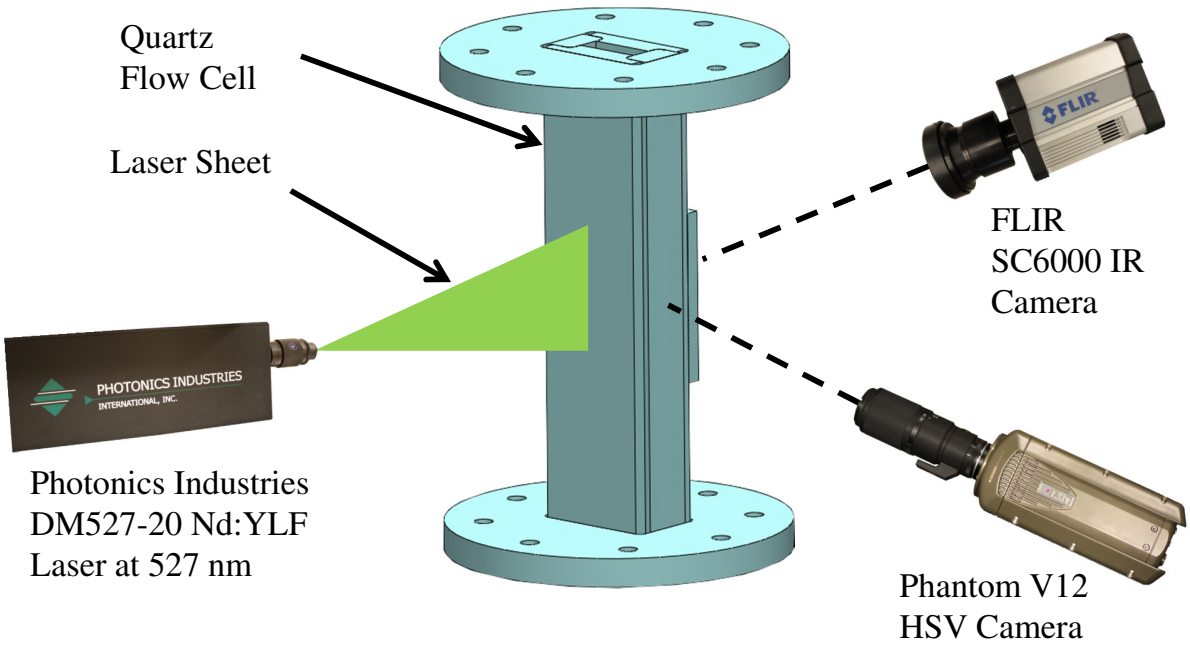

Figure 2.12: Arrangement of cameras and laser for HSV/PIV/IR data collection.

helped with the ease of creating the masks for the PIV vector calculations as discussed in Section 4.4.1. The HSV camera was spatially calibrated using a reticule with 0.1 mm division on it to get the size per pixel. The calibration was done over as large of a range of the sensor as possible, a minimum of half the sensor.

The temperature of the surface was determined via IR thermography. For the HSV/IR data the IRC camera was setup with a 50 mm lens, 1.0 inch of extension rings, 0.5 ms integration time, 1250 fps, 3-5 µm filter (filter 2), 85.0 mm from the back of the cartridge to the lens casing, low temperature correction at room temperature, and a high temperature correction at 95 °C. For the PIV/IR data the IR camera setup was a 50 mm lens, 2.5 inches of extension rings, 0.39 ms integration time, 2500 fps, 3-5 µm filter (filter 2), 31.7 mm from the back of the cartridge to the lens casing, low temp correction at room temperature, and a high temp correction at 100 °C.

The correction was a two point non-uniformity correction that used a blackbody simulator that compensated for non-uniform response in the pixels. The IR camera signal was calibrated before the experiment by imaging the heater with a thermocouple on the surface to read the average temperature. This data was used to construct a temperature versus signal calibration curve. The average temperature on the surface was then determined using a custom MATLAB script that averaged the temperature across the heater both spatially and temporally. The IR camera calibration was checked one more time in situ against the loop temperature, before the test section heater was energized. There was a slight shift from the dry calibration to the in situ conditions and the calibration curve was adjusted by shifting the dry calibration curve down to match the data points taken during heat-up. An example of the IR calibration curve is shown in Figure 2.13. The IR camera was spatially calibrated by either using the same method as discussed above for the HSV camera, or it was calibrated based on the known distance from one side of the ITO to the other.

When the loop temperature was stable the mass flux was adjusted to the desired value. Then the heat flux of the heater was adjusted to the desired value, and 5 minutes were allowed to pass for the heater to reach equilibrium. Then simultaneous HSV/PIV and IR images were acquired using a trigger signal that sent a +5 volt signal to both the PIV system's "Trigger" and to the IRC camera's "SYNC I/O" port.

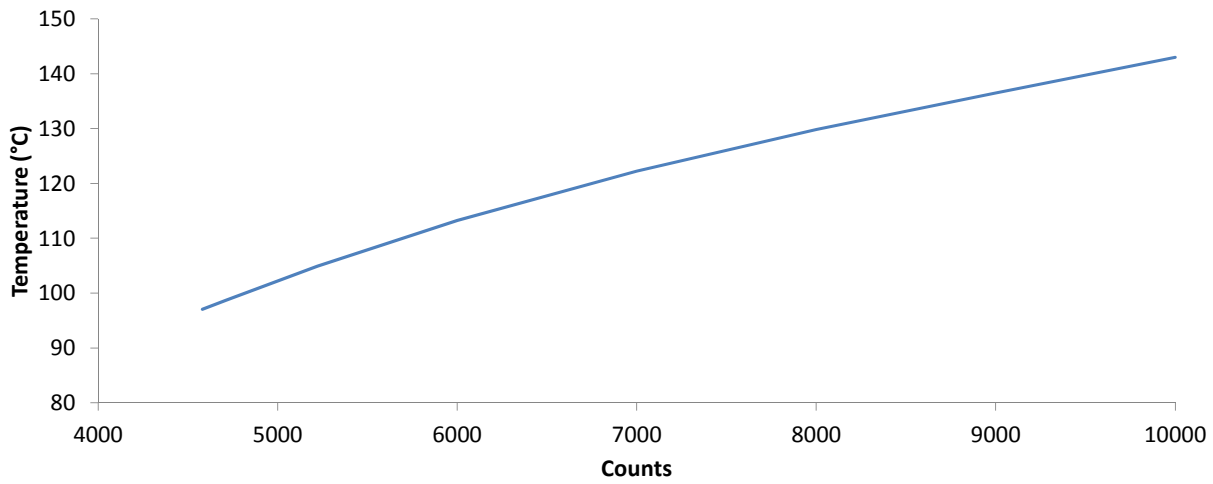

Figure 2.13: Typical temperature calibration curve for IR camera.

2.4 Cross Flow at Test Section Exit

To estimate how far downstream the flow lines were affected by the transition from a square channel, to round channel two Fluent calculations were run by Dr. Koroush Shirvan. One at $\mathrm{Re}{=}1{\times}10^5$ and one at $\mathrm{Re}{=}1{\times}10^6$. In Figure 2.14 the velocities in the x- and y-directions (perpendicular to the flow) for all of the flow lines are shown as a function of the z position (the direction of flow). There are no changes in the x- and y-velocities until 4 cm or less from the transitions, and since in the flow channel design there was $>$6 cm between the heater and the transition, there should not be any affect at the location of the heater due to the transition. The 0 location on the x-axis is the point where the transition between the rectangular and circular cross-sections occurs. The figures labeled wide are in the 30 mm direction and the figures labeled narrow are in the 10 mm direction.

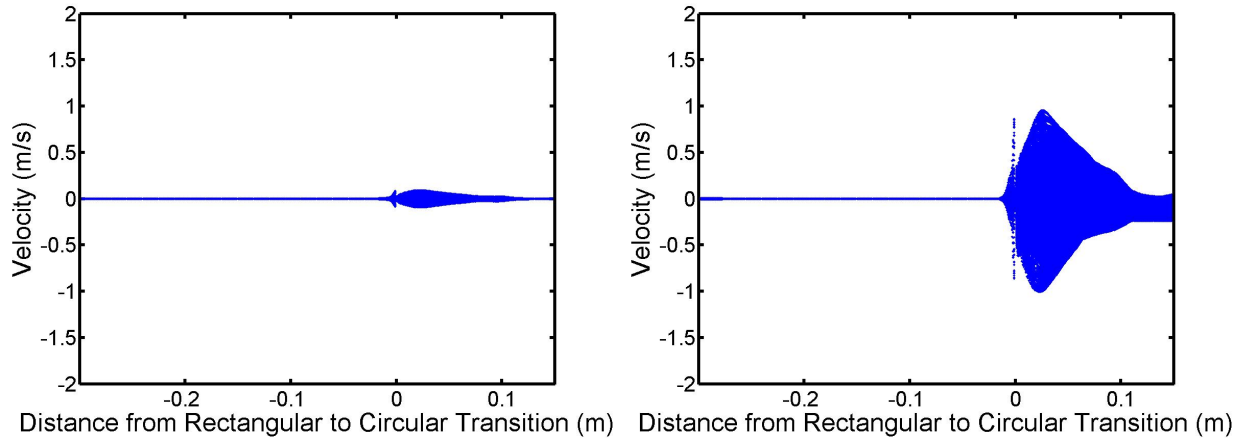

(a) Narrow, Re = 1×10^5

(b) Narrow, Re = 1×10^6

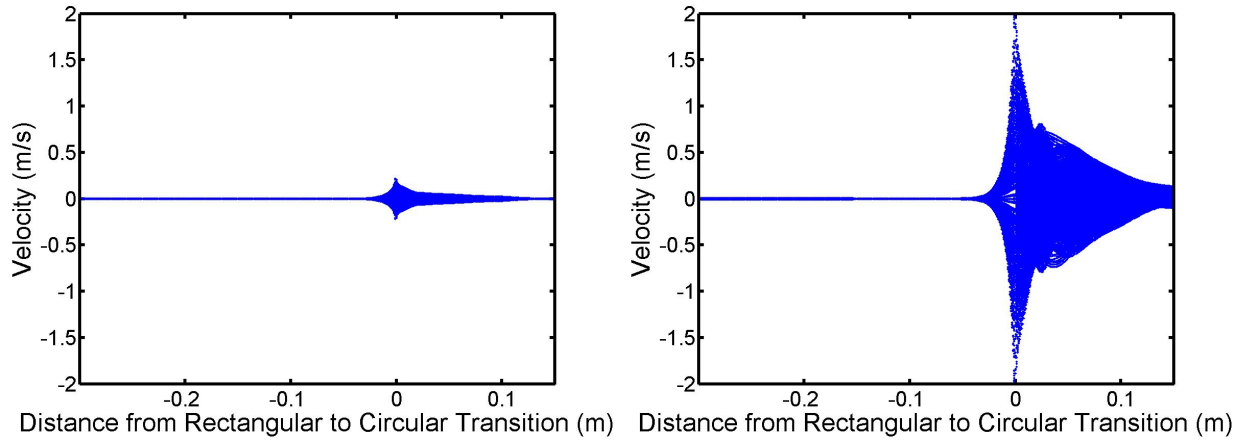

(c) Wide, Re = 1×10^5

(d) Wide, Re = 1×10^6

Figure 2.14: Velocities from Fluent simulation of test section for all of the flow lines in both the narrow and wide directions.

2.5 Boundary Layer Thickness

The boundary layer thickness was of interest in designing the test section to determine the tolerances needed along the wall to not affect the flow. As long as defects along the wall does not extend past the boundary layer, they have a minimal influence on the flow. The viscous sublayer can be approximated by Eq. (2.3) [57] [58].

$$\delta_s = 5\frac{\nu}{u^*} \tag{2.3}$$

and

$$u^* \approx \left(\frac{\tau_w}{\rho}\right)^{\frac{1}{2}} \tag{2.4}$$

Where δ_s is the thickness of the viscous sublayer, ν is the kinematic viscosity, τ_w is the shear stress at the wall, and ρ is the density of the fluid. The shear stress can be estimated from an anticipated pressure

gradient from a smooth pipe for the flow conditions.

$$\left(\frac{\partial P}{\partial z}\right)_{fric} = \frac{\tau_w p_w}{A} = \frac{f}{D_h}\frac{G^2}{2\rho} \tag{2.5}$$

$$\left(\frac{\partial P}{\partial z}\right)_{fric} = \left(\frac{0.12}{0.016}\right)\left(\frac{2000^2}{2 * 1000}\right) = 15\ \frac{\text{kPa}}{\text{m}} \tag{2.6}$$

$$\tau_w = A\frac{\left(\frac{\partial P}{\partial z}\right)_{fric}}{p_w} = \frac{4.5 \times 10^{-4} * 15 \times 10^3}{0.110} = 61.4\ \text{Pa} \tag{2.7}$$

Where $\left(\frac{\partial P}{\partial z}\right)_{fric}$ is the pressure gradient, p_w is the wetted perimeter, A is the channel area, f is the friction factor, D_h is the hydraulic diameter, and G is the mass flux Then from Eq. (2.4) u^* can be calculated and from Eq. (2.3) the viscous sublayer size can be calculated.

$$u^* \approx \left(\frac{\tau_w}{\rho}\right)^{\frac{1}{2}} = \left(\frac{61.4}{1000}\right)^{\frac{1}{2}} = 0.248\ \frac{\text{m}}{\text{s}} \tag{2.8}$$

$$\delta_s = 5\left(\frac{9 \times 10^{-7}}{0.248}\right) \approx \boxed{0.02\ \text{mm}} \tag{2.9}$$

The full turbulent boundary layer using the $^1/_7{}^{th}$ power law for the velocity distribution yields Eq. (2.10) for the velocity distribution along a flat plate.

$$\frac{u}{U_\infty} = \left(\frac{y}{\delta}\right)^{\frac{1}{7}} \tag{2.10}$$

Where U_∞ is the uniform velocity that is found as approaching the middle of the channel, y is the position away from the wall perpendicular to the direction of the flow, and δ is the thickness of the boundary layer. Then using the shear stress at the wall and expression for the displacement thickness and momentum thickness Eq. (2.11) can be developed for the boundary layer thickness.

$$\delta\left(x\right) = 0.37x\left(\frac{U_\infty x}{\nu}\right)^{-\frac{1}{5}} \tag{2.11}$$

Where $\delta\left(x\right)$ is the momentum thickness of the boundary layer, x is the coordinate in the direction of flow, and δ_1 is the displacement thickness. The displacement thickness which represents the distance that the streamlines are shifted because of the existence of the boundary layer is given by Eq. (2.12).

$$\delta_1 = \frac{\delta\left(x\right)}{8} \tag{2.12}$$

For the values in the designed test section the displacement thickness is on the order of 1 mm.

3 HSV/IR Results

The data were collected at 1.05, 1.5, and 2.0 bar at constant subcoolings of 5 °C, 10 °C, and 15 °C. The mass flux values tested were 150, 250, 500, 750, 1000, and 1250 kg/m^2/s. The heat flux values explored were 100, 200, 400, 600, 800, 1000, 1200, 1400, and 1600 kW/m^2. For each combination of the above variables, the average heat transfer coefficient, bubble departure diameter, bubble departure frequency, and nucleation site density were measured. Estimates of the experimental uncertainties for all reported data are presented in section 5. The experimental setup is discussed in section 2.

3.1 Test Matrix

The test matrix was developed to explore the full range of mass fluxes available in the test loop. The heat flux increments were chosen such that there were several points where the nucleation site density could be accurately measured between the onset of nucleate boiling and the point where the number of active nucleation sites was too high to measure, this upper nucleation site density is discussed in sections 3.4.2-3.4.4. The highest heat flux was chosen to be well above that that of interest in a PWR, while still low enough that two-phase flow instabilities would not occur. The test matrix for the HSV/IR work is shown in Table 3.1

Table 3.1: HSV/IR test matrix.

Heat Flux $\left(\frac{kW}{m^2}\right)$	**Mass Flux** $\left(\frac{kg}{m^2-s}\right)$					
	150	**250**	**500**	**750**	**1000**	**1250**
100	x	x	x	x	x	x
200	x	x	x	x	x	x
300	x	x	x	x	x	x
400	x	x	x	x	x	x
500	x	x	x	x	x	x
600	x	x	x	x	x	x
700	x	x	x	x	x	x
800	x	x	x	x	x	x
1000	x	x	x	x	x	x
1200	x	x	x	x	x	x
1400			x	x	x	x
1600					x	x

The Subcooling number verses Zuber number map for the test matrix is shown in Figure 3.1. The subcooling number and Zuber number are defined in (3.1) and (3.2) respectively [59, 24].

$$N_{sub} = \frac{\Delta h_{sub,in}}{h_{fg}} \frac{\Delta \rho}{\rho_g} \tag{3.1}$$

$$N_{Zu} = \frac{q''_w P_h z_d}{A v_{fi} h_{fg}} \frac{\Delta\rho}{\rho_g \rho_f} \tag{3.2}$$

$\Delta h_{sub,in}$ is the subcooling enthalpy difference from saturation, h_{fg} is the heat of vaporization, $\Delta\rho$ is the density difference between liquid and vapor phases, ρ_g is the density of the vapor phase, ρ_f is the density of the liquid phase, q''_w is the wall heat flux, P_h is the heated perimeter, z_d is the heated length to the site of interest, A is the flow area, and v_{fi} is the liquid inlet velocity. An approximate formulation of stability from density wave oscillations was proposed by Ishii [59] and given in (3.3).

$$N_{Zu} - N_{Sub} < \frac{2\left[k_i + \frac{f_s C_m}{2D^*} + k_e\right]}{1 + \frac{1}{2}\left(\frac{f_s C_m}{2D^*} + 2k_e\right)} \tag{3.3}$$

f_s is the single phase friction factor, C_m is the two phase friction multiplier, k_i is the inlet orifice coefficient, k_e is the exit orifice coefficient, and D^* is the hydraulic diameter divided by the axial position.

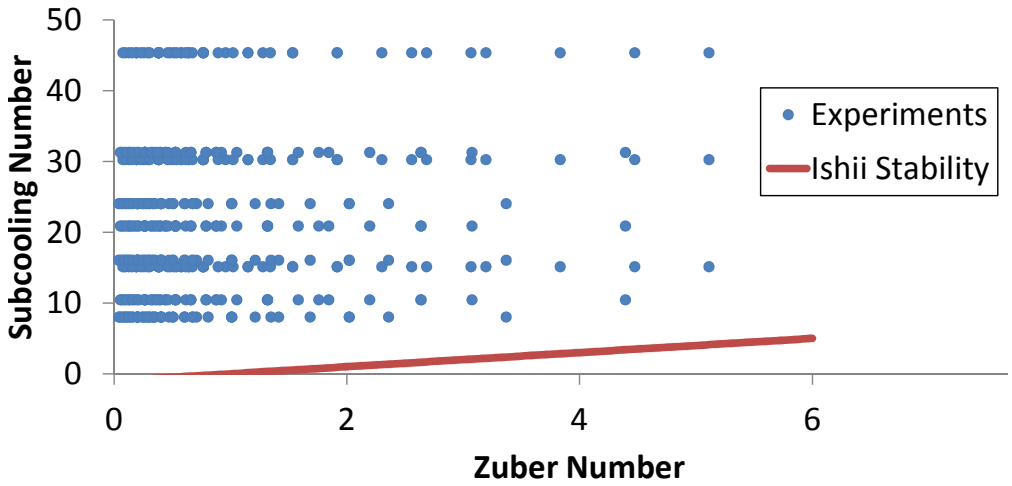

Figure 3.1: Subcooling number versus Zuber number for the test matrix in Table 3.1, plotted with the density wave oscillation stability line approximation proposed by Ishii [59].

3.2 Boiling Curves and Heat Transfer Coefficients

The boiling curves for 1.05 bar, 1.5 bar, and 2.0 bar are plotted in Figures 3.2, 3.3, and 3.4 respectively. The boiling curves show the classic trends of nucleate flow boiling [60], there is a linear behavior in the single phase heat transfer region. The wall superheat is reduced as the mass flux increases, pressure increases, and heat flux decreases. For a fixed subcooling, the temperature of the fluid is higher at higher pressures, and decreases the viscosity. The decreased viscosity increases the Re number as pressure increases for a constant subcooling. This causes a higher single phase heat transfer coefficient as the pressure increases. The wall superheat at ONB increases with increasing mass flux. At ONB the boiling curve slope increases indicating a rise in the heat transfer coefficient. This rise in the heat transfer coefficient allows for a larger

heat flux to pass through the surface for a given increase in wall superheat. As the heat flux and wall superheat increase, the boiling becomes more pronounced and eventually becomes fully-developed and the heat transfer coefficients converges to a single curve, essentially insensitive to changes in mass flux. At this point the disruption of the thermal boundary layer and the turbulence caused by the bubbles departing are a more dominant heat transfer mechanism than the flow rate of the bulk fluid.

The heat transfer coefficients for 1.05 bar, 1.5 bar, and 2.0 bar are shown in Figures 3.5, 3.6, and 3.7 respectively. The heat transfer coefficients follow the expected trends as well. The heat transfer coefficient increases with increasing mass flux, and is relatively constant for a given mass flux with respect to heat flux in the single phase heat transfer regime. Then as boiling begins, heat transfer increases significantly, and eventually the different mass flux curves merge together to a single line. The heat transfer coefficient is defined by the heat flux and the temperature difference from the wall to the bulk temperature shown in (3.4).

$$h = \frac{q''}{T_w - T_b} \tag{3.4}$$

The bulk inlet temperature is used for T_b to calculate the heat transfer coefficient, since the heater is short in length and there is little variation in the bulk temperature along the length of the heater. Typically for a longer channel, T_b would be the bulk temperature at the same axial location that the wall temperature was measured. h represents the heat transfer coefficient and T_w is the temperature of the heated wall which is measured via IR Thermography. The wall temperature is averaged over the middle of the heater. The area is centered in the middle of the heater and is approximately an area of 6 mm wide and 5 mm tall.

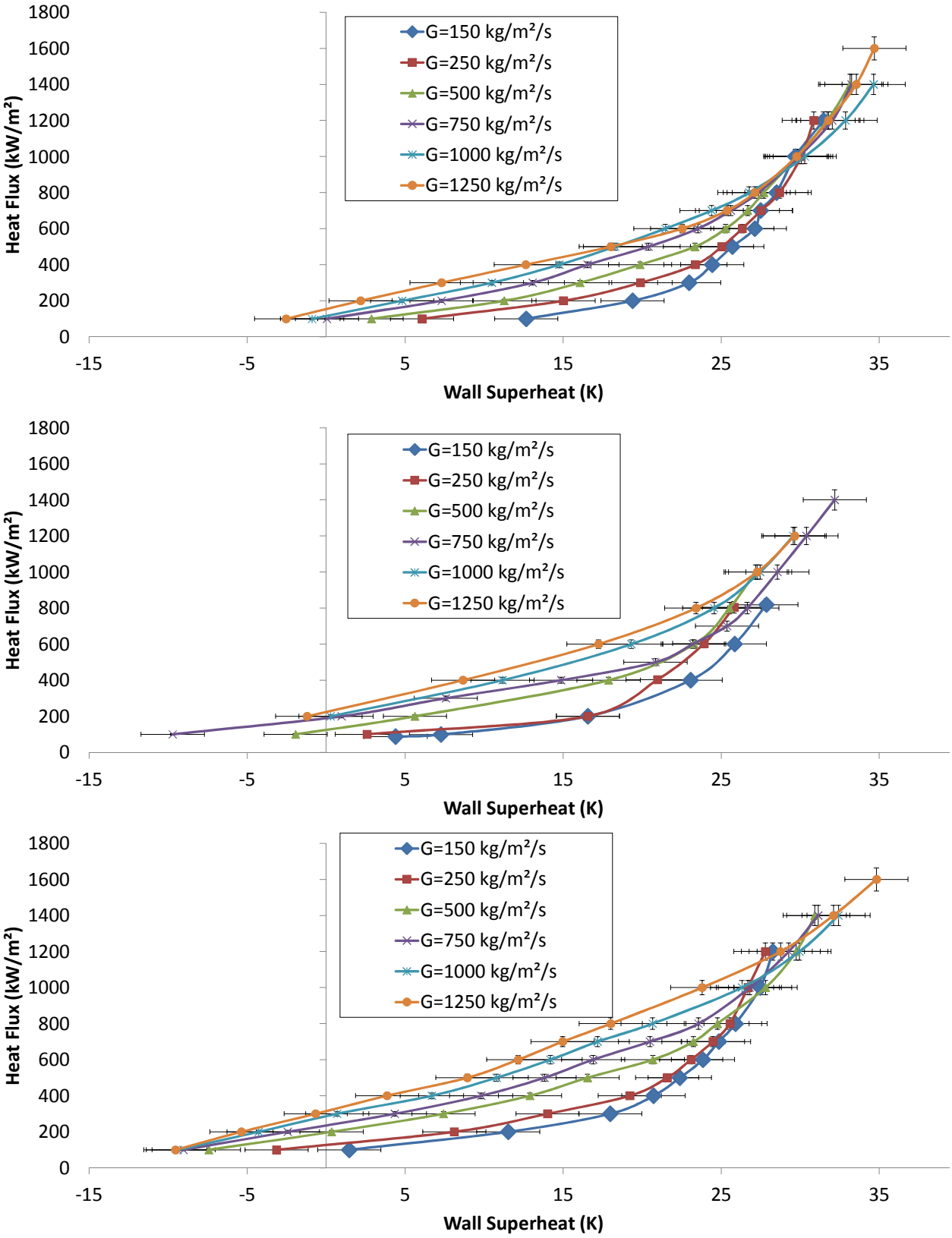

Figure 3.2: 1.05 bar boiling curves for subcoolings of 5 °C (top), 10 °C (middle), and 15 °C (bottom)

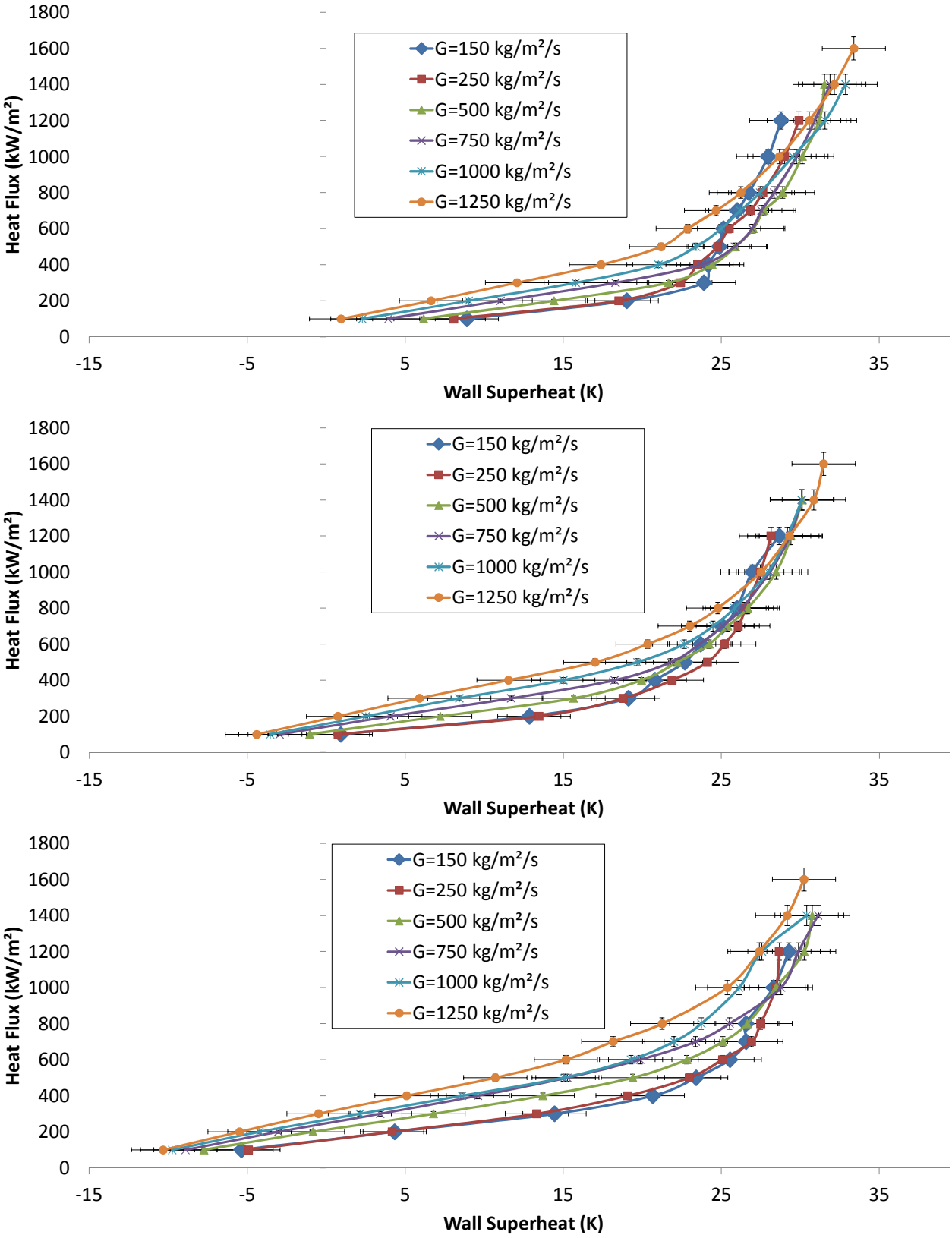

Figure 3.3: 1.5 bar boiling curves for subcoolings of 5 °C (top), 10 °C (middle), and 15 °C (bottom)

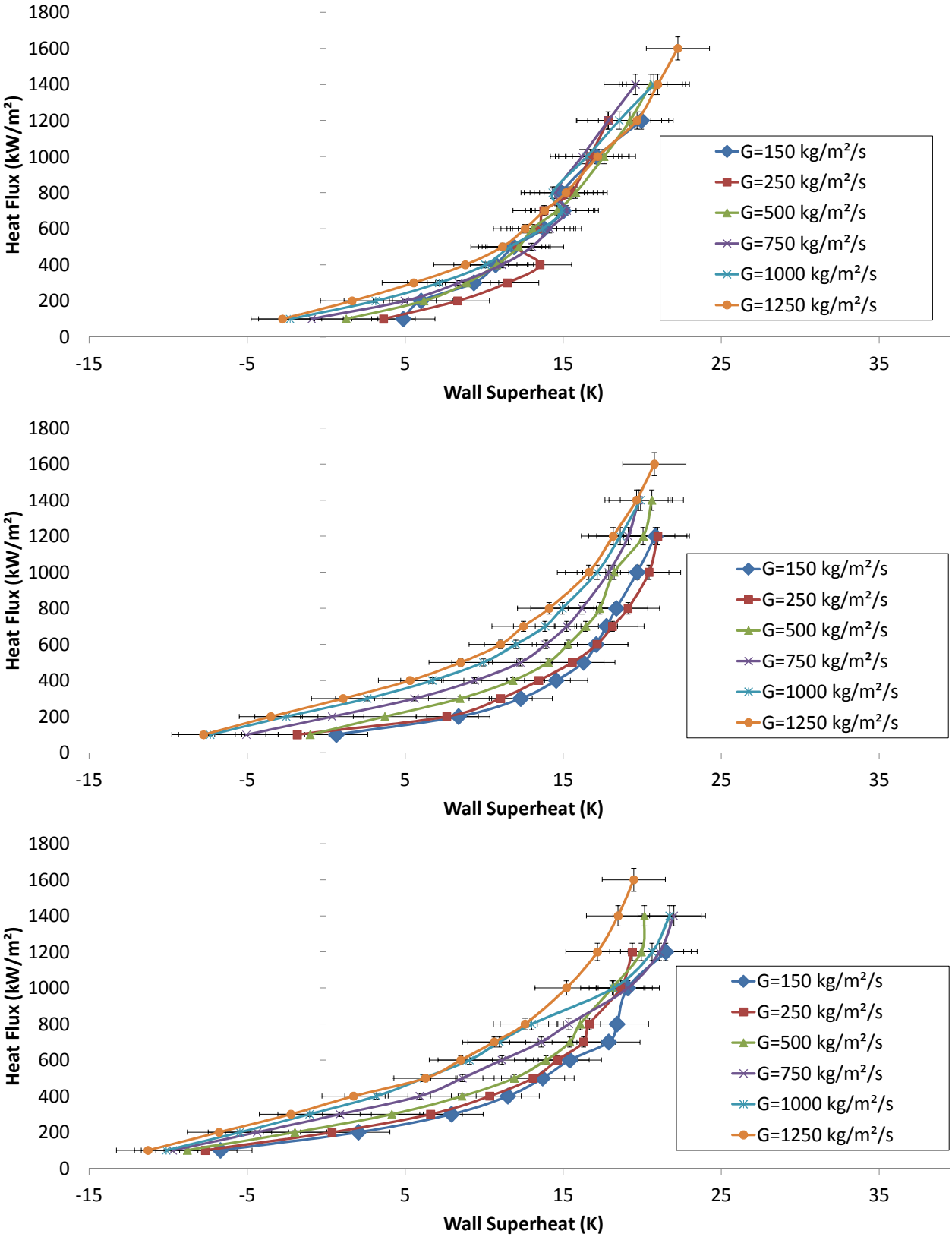

Figure 3.4: 2.0 bar boiling curves for subcoolings of 5°C (top), 10°C (middle), and 15°C (bottom)

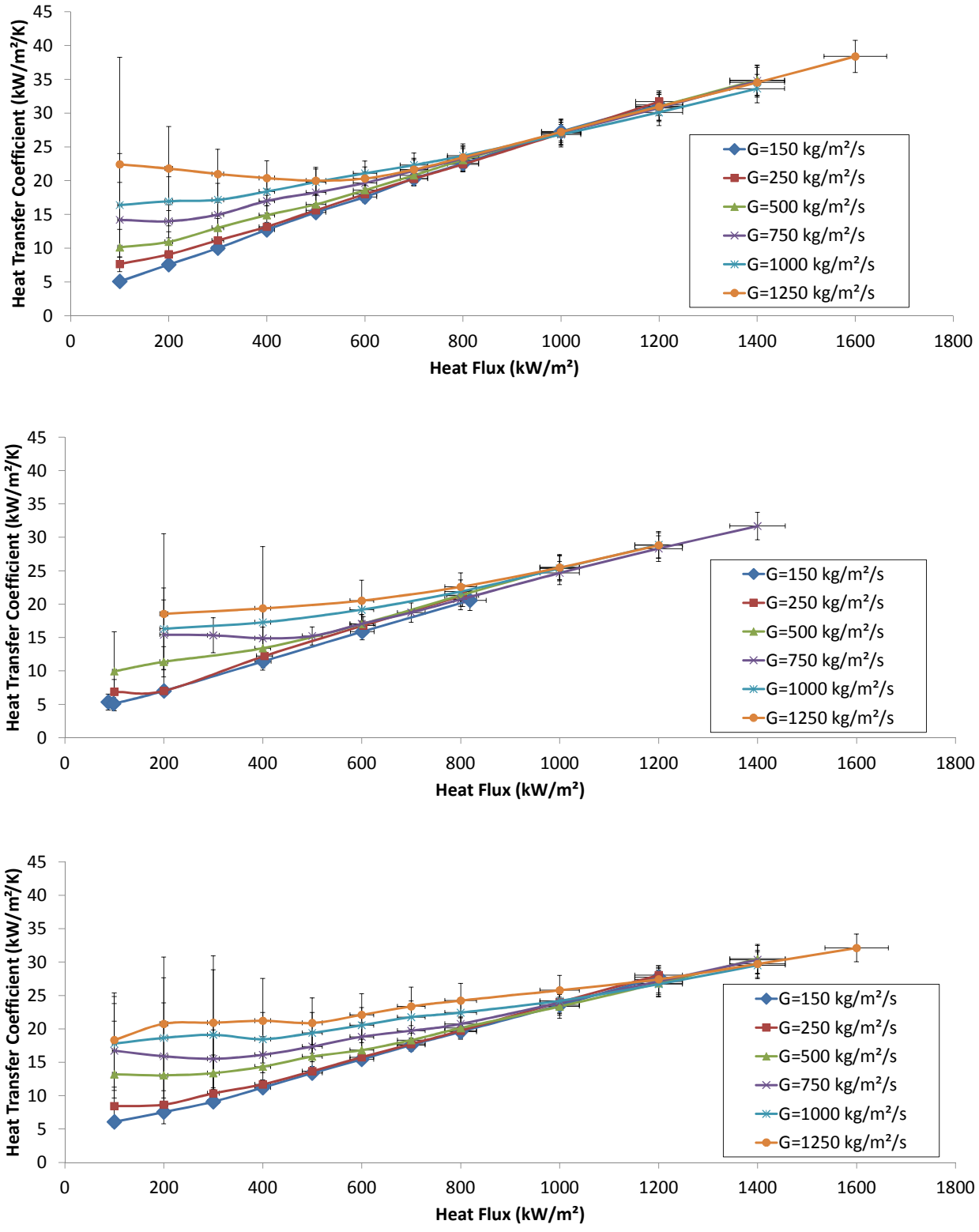

Figure 3.5: 1.05 bar heat transfer coefficients for subcoolings of 5 °C (top), 10 °C (middle), and 15 °C (bottom)

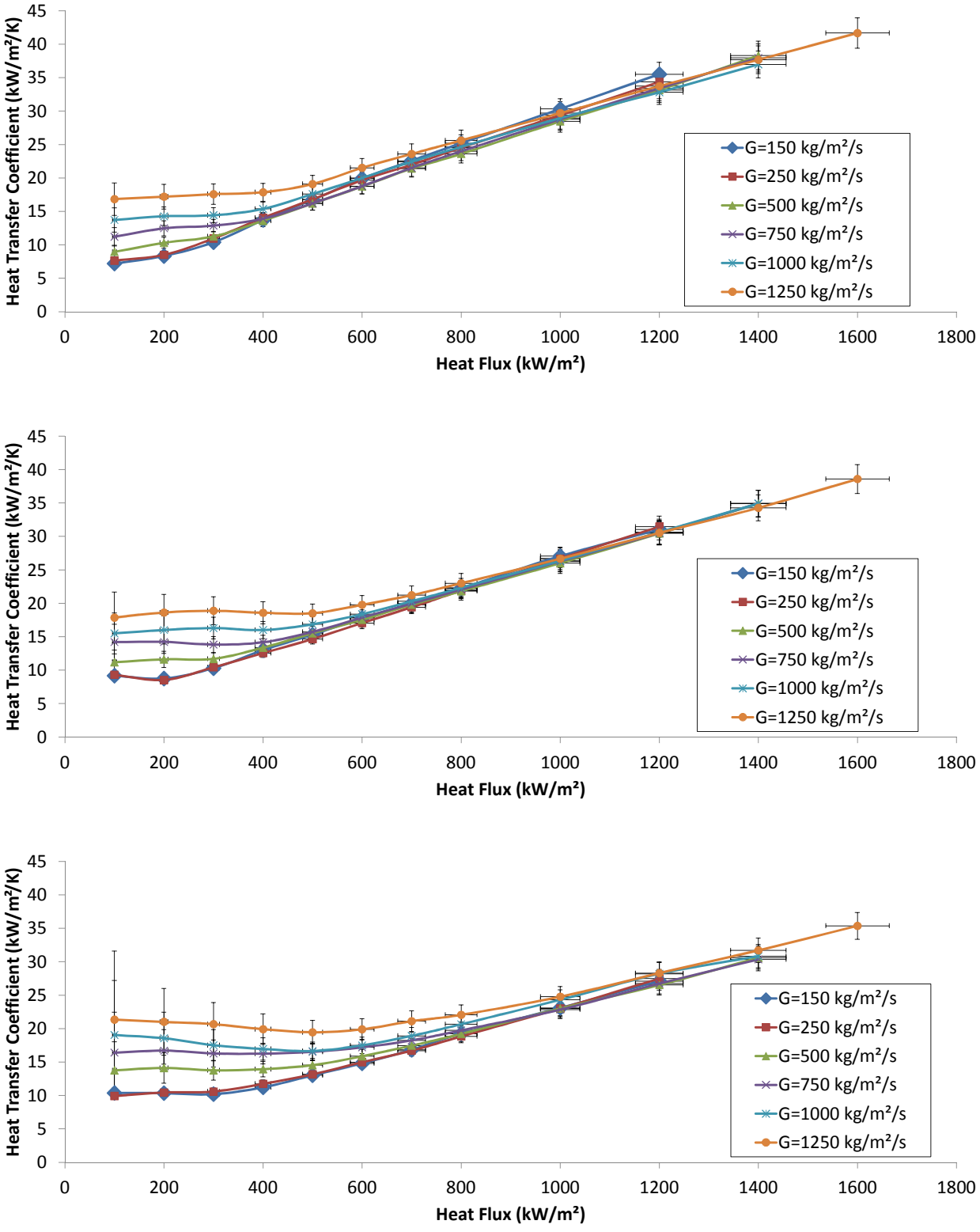

Figure 3.6: 1.5 bar heat transfer coefficients for subcoolings of 5 °C (top), 10 °C (middle), and 15 °C (bottom)

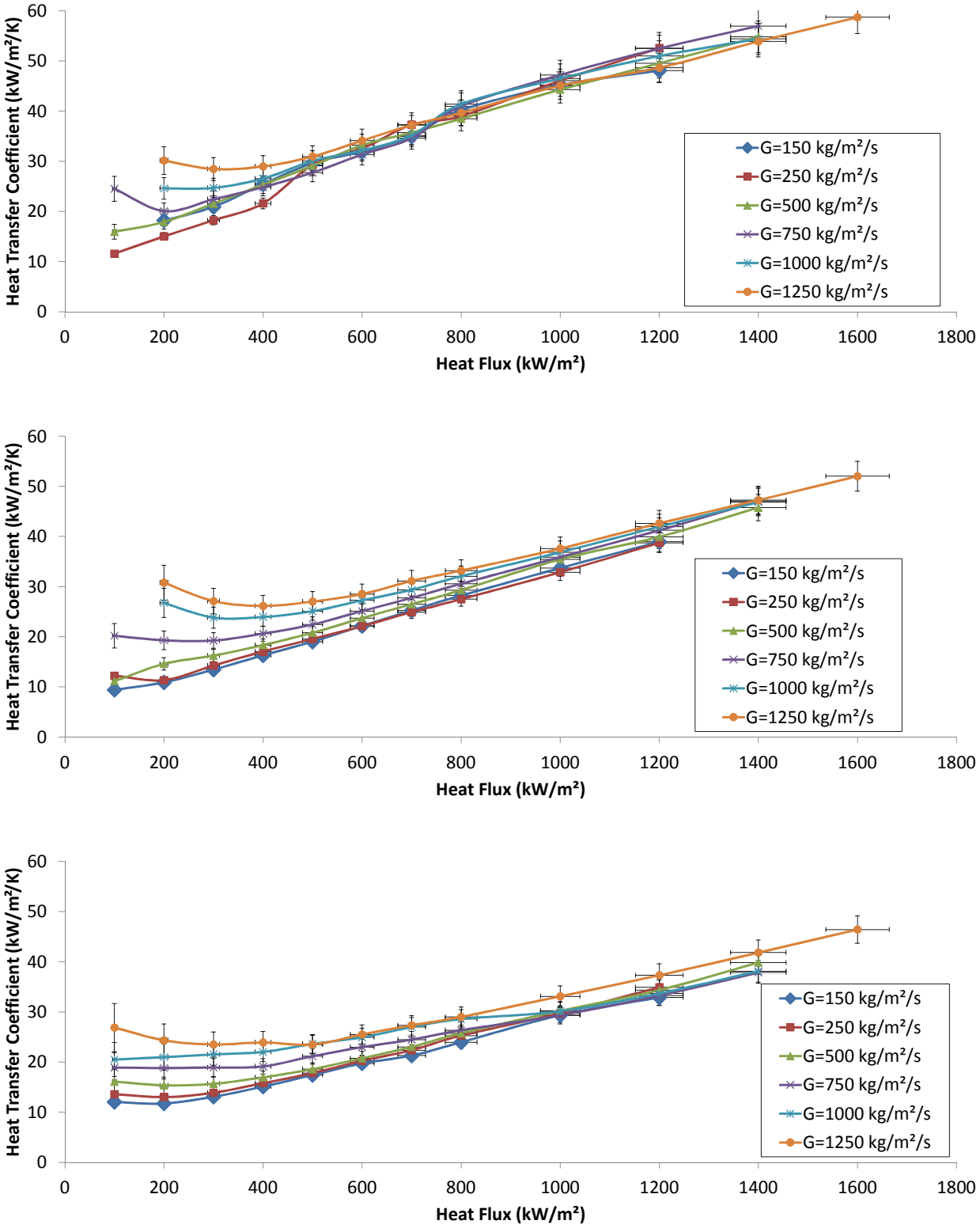

Figure 3.7: 2.0 bar heat transfer coefficients for subcoolings of 5 °C (top), 10 °C (middle), and 15 °C (bottom)

3.3 Bubble Departure Diameter

3.3.1 Bubble Departure Diameter Model

The bubble departure diameter results are compared to a mechanistic bubble departure diameter model first developed by Klausner et al. [13] and then modified by Sugrue et al. [14] that was introduced in section 1.2.1. This model sums the forces acting on the bubble in the direction perpendicular and parallel to the flow. When the force balance is broken in the direction parallel to the flow, the bubble will slide, and when the balance is broken perpendicular to the flow the bubble will lift off. The forces are broken down into their components, so starting with the vector sum from (1.3), the x and y-components of the force vectors are shown in (3.5) and (3.6) respectively. A diagram of the forces acting on the bubble are shown in Figure 3.8. To accommodate computational error, the net force must exceed 1×10^{-15} N in either the x or y-direction for the bubble to be considered to depart. The x-direction is in the direction of the flow, the y-direction is perpendicular to the flow and away from the wall.

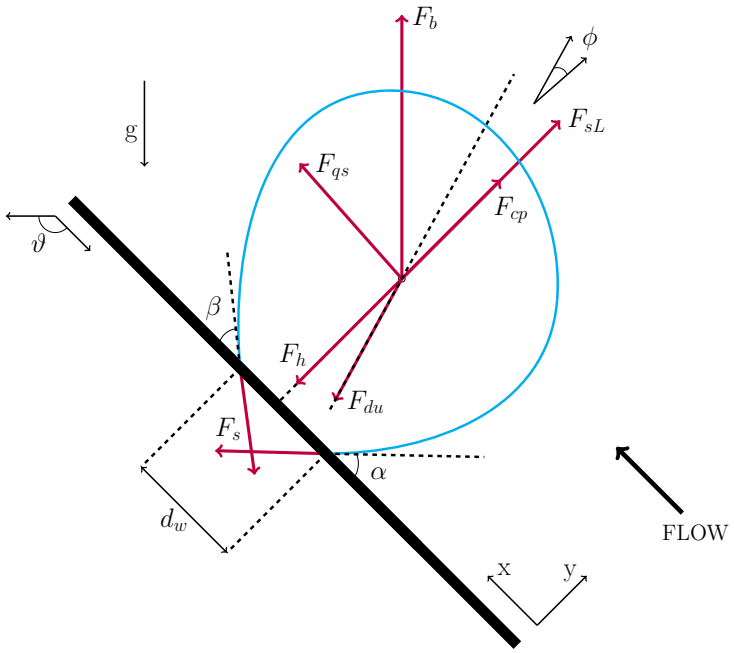

Figure 3.8: Force balance model for Sugrue et al. bubble departure diameter model. Graphic courtesy of Rosie Sugrue [14].

$$\Sigma F_x = F_{sx} + F_{qs} - F_b \sin\vartheta + F_{du} \sin\phi \tag{3.5}$$

$$\Sigma F_y = F_{sy} + F_{sL} - F_b \cos\vartheta - F_h + F_{cp} + F_{du} \cos\phi \tag{3.6}$$

ϑ is the angle the heater makes with the horizontal, and ϕ is the angle of bubble growth with respect to the y-axis, and for the vertical test section this is assumed to be $\pi/18$. The forces are the same as described in 1.2.1, but broken into their x and y components. The x-components are F_{sx}, which is the surface tension force, $\mathbf{F}_{qs}$ is the quasi-steady drag force, $\mathbf{F}_b$ is the buoyancy force, and $\mathbf{F}_{du}$ is the unsteady drag force. The y-components are F_{sy}, which is the surface tension force, $\mathbf{F}_{sL}$ is the shear lift force, $\mathbf{F}_b$ is the buoyancy force, $\mathbf{F}_h$ is the hydrodynamic pressure force, $\mathbf{F}_{cp}$ is the contact pressure force, and $\mathbf{F}_{du}$ is the unsteady drag force.

The contact angle of the liquid with the surface affects the surface tension force. Specifically, it is dependent on both the advancing and receding contact angles, and the forces in the x and y direction is shown in (3.7) and (3.8) respectively.

$$F_{sx} = -1.25 d_w \sigma \frac{\pi(\alpha - \beta)}{\pi^2 - (\alpha - \beta)^2} \tag{3.7}$$

$$F_{sy} = d_w \sigma \frac{\pi}{\alpha - \beta} [\cos\beta - \cos\alpha] \tag{3.8}$$

α is the advancing contact angle, β is the receding contact angle, and σ is the surface tension. d_w is the bubble foot diameter, which is the contact of the bubble with the wall, and was modified from previous mechanistic models to that defined in (3.9) to better fit experimental data. D_d is the bubble departure diameter.

$$\frac{d_w}{D_d} = \frac{1}{40} \tag{3.9}$$

The quasi-steady drag force is is derived from a uniform flow over a spherical bubble and is shown in (3.10).

$$F_{qs} = 6\pi\nu\rho_l U R \left[\frac{2}{3} + \left[\left(\frac{12}{\mathrm{Re_b}} \right)^n + 0.796^n \right]^{-1/n} \right] \tag{3.10}$$

ν is the kinematic viscosity, n is 0.65, and R is the bubble radius at a given time. U is the flow velocity at the bubble's center and thus it is dependent on the size of the bubble. The velocity near the wall is assumed to follow turbulent single phase relations proposed by Reichardt and given by Hinze [61] shown in (3.11). $\mathrm{Re_b}$ is the bubble Reynolds number and is calculated using this velocity and the bubble diameter.

$$\frac{U(y)}{u^*} = \frac{1}{\kappa} \ln\left(1 + \kappa y^+\right) + c \left[1 - \exp\left(-\frac{y^+}{\chi_d} \right) - \frac{y^+}{\chi_d} \exp\left(-0.33 y^+\right) \right] \tag{3.11}$$

$U(y)$ is the velocity distribution near the wall, u^* is the area averaged velocity, y^+ is the dimensionless distance from the wall equal to $\frac{y u^*}{\nu}$, κ is 0.4, χ_d is 11, and c is 7.4.

The buoyancy force acts in opposition to gravity, and in the case of this work, acts in the positive x direction, the force is shown in (3.12).

$$F_b = \frac{4}{3}\pi R^3 \left(\rho_f - \rho_g\right) g \tag{3.12}$$

g is acceleration due to gravity, $\mathbf{F}_b$, R, ρ_f, and ρ_g are as defined previously. The hydrodynamic force is calculated treating the bubble as a sphere in a flow field and shown in (3.13).

$$F_h = \frac{9}{8}\rho_f U^2 \frac{\pi d_w^2}{4} \tag{3.13}$$

$\mathbf{F}_h$, ρ_f, U, and d_w are as defined previously. The contact pressure force is shown in (3.14)

$$F_{cp} = \frac{\pi d_w^2}{4} \frac{2\sigma}{r_r} \tag{3.14}$$

r_r is the radius of curvature and the value of the radius of curvature used was $r_r = 5R$, as proposed by Klausner [13]. The shear shear lift force is given in (3.15).

$$F_{sL} = \frac{1}{2}\rho_f U^2 \pi R^2 \left[3.877 G_s^{1/2} \left[{\mathrm{Re_b}}^{-2} + \left(0.344 G_s^{1/2} \right)^4 \right]^{1/4} \right] \tag{3.15}$$

$$G_s = \left| \frac{dU}{dy} \right| \frac{R}{U} \tag{3.16}$$

G_s is the dimensionless shear rate and is given in (3.16). ρ_f, R, and U are as defined previously. The unsteady force is due to the bubble growing asymmetrically due to being distorted by the channel flow and is shown in (3.17).

$$F_{du} = -\rho_f \pi R^2 \left(R\ddot{R} + \frac{3}{2}\dot{R}^2 \right) \tag{3.17}$$

$\dot{R}$ is the growth rate is determined by the Zuber [62] growth model shown in (3.18).

$$R(t) = \frac{2b}{\sqrt{\pi}} \mathrm{Ja} \sqrt{\eta_l t} \tag{3.18}$$

The non-spherical nature of the bubble is represented by b with a typical value of 1.56.

3.3.2 Bubble Departure Diameter Experimental Data

The bubble departure diameter was measured using HSV, the spatial resolution was 15 μm per pixel, and an area of 1280x800 pixels was imaged at a rate of 1000-5000 Hz as appropriate for the flow conditions, and The HSV acquisition frequency was multiple of the IR camera acquisition frequency, so that the two cameras could be synchronized (i.e. 2500 Hz on the HSV camera and 1250 Hz on the IR camera). The bubble departure diameter is defined here as the diameter of the bubble at the time of lift off (detachment perpendicular to the wall) or sliding (detachment parallel to the wall), whichever comes first. The diameter was only measured for flow regimes in which individual bubbles could be identified and were not greatly influenced by other bubbles during their growth (i.e. no bubble coalescence on the surface, and no bubbles passing a departing bubble). The bubbles were measured at the location of the onset of boiling on the heater surface.

The distribution of the bubble departure diameters was much larger than the measurement uncertainty of 15 μm, and the error bars on the plot in Figures 3.9, 3.10, 3.11 represent the standard deviation of the distribution. Klausner's force-balance model [13] modified by Sugrue et al. [34, 14] is shown as a comparison to the experimental data. This model tracks with the data well, although it tends to under predict the departure diameter at high mass fluxes. The data shows increasing departure diameters with increasing heat flux, decreasing mass flux, and decreasing subcooling as expected. These same trends were observed also by Sugrue et al.

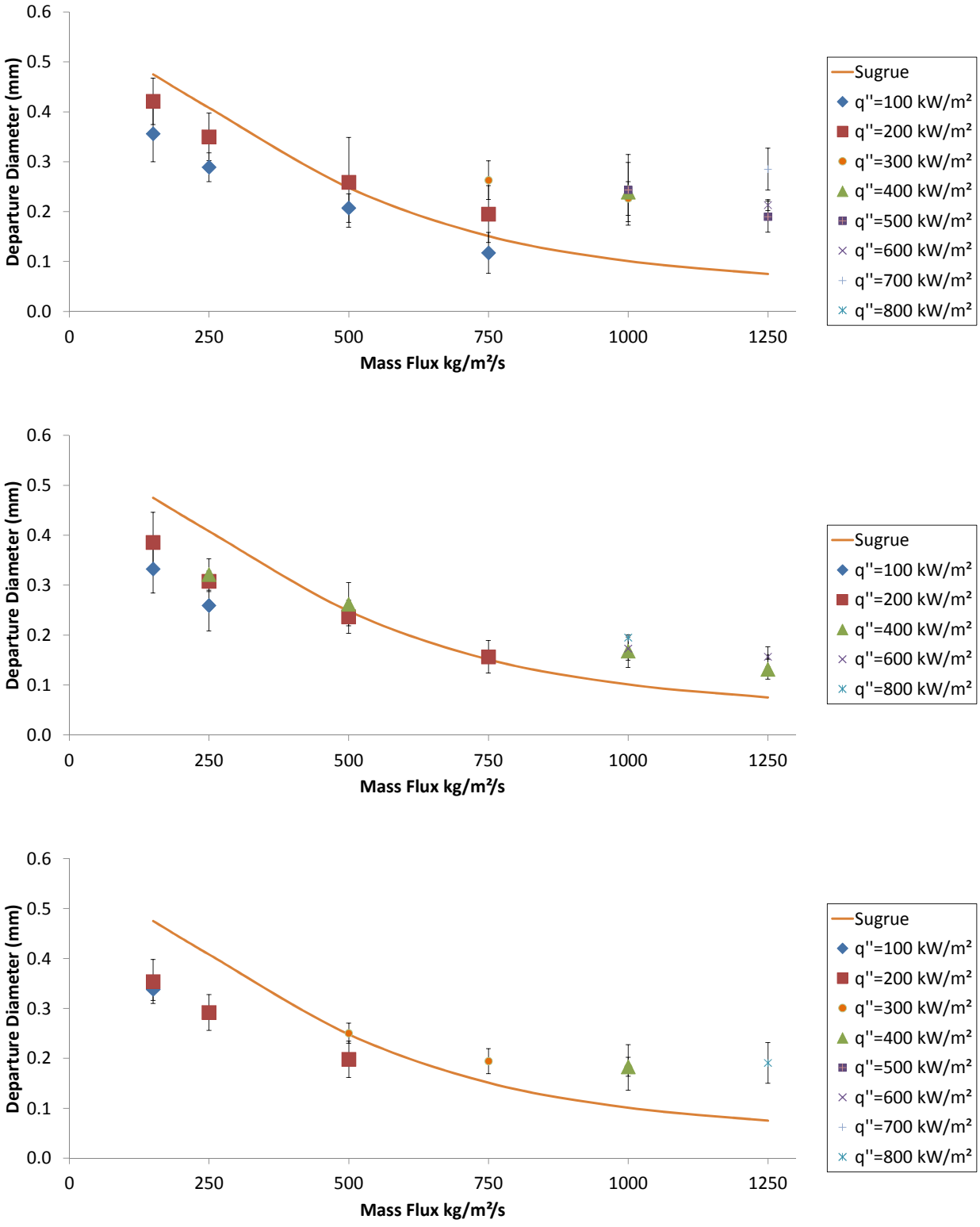

Figure 3.9: 1.05 bar bubble departure diameters for subcoolings of 5 °C (top), 10 °C (middle), and 15 °C (bottom).

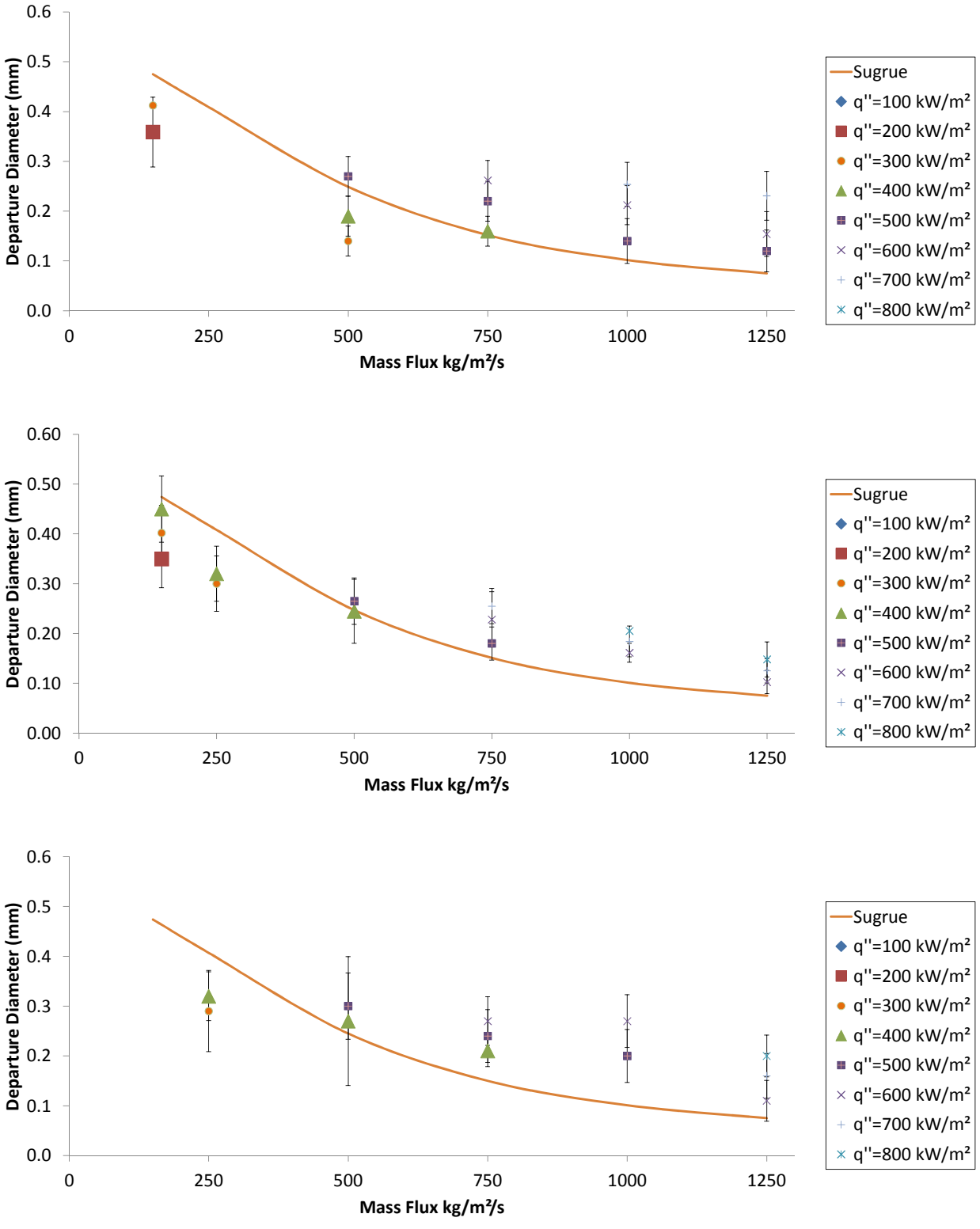

Figure 3.10: 1.5 bar bubble departure diameters for subcoolings of 5 °C (top), 10 °C (middle), and 15 °C (bottom).

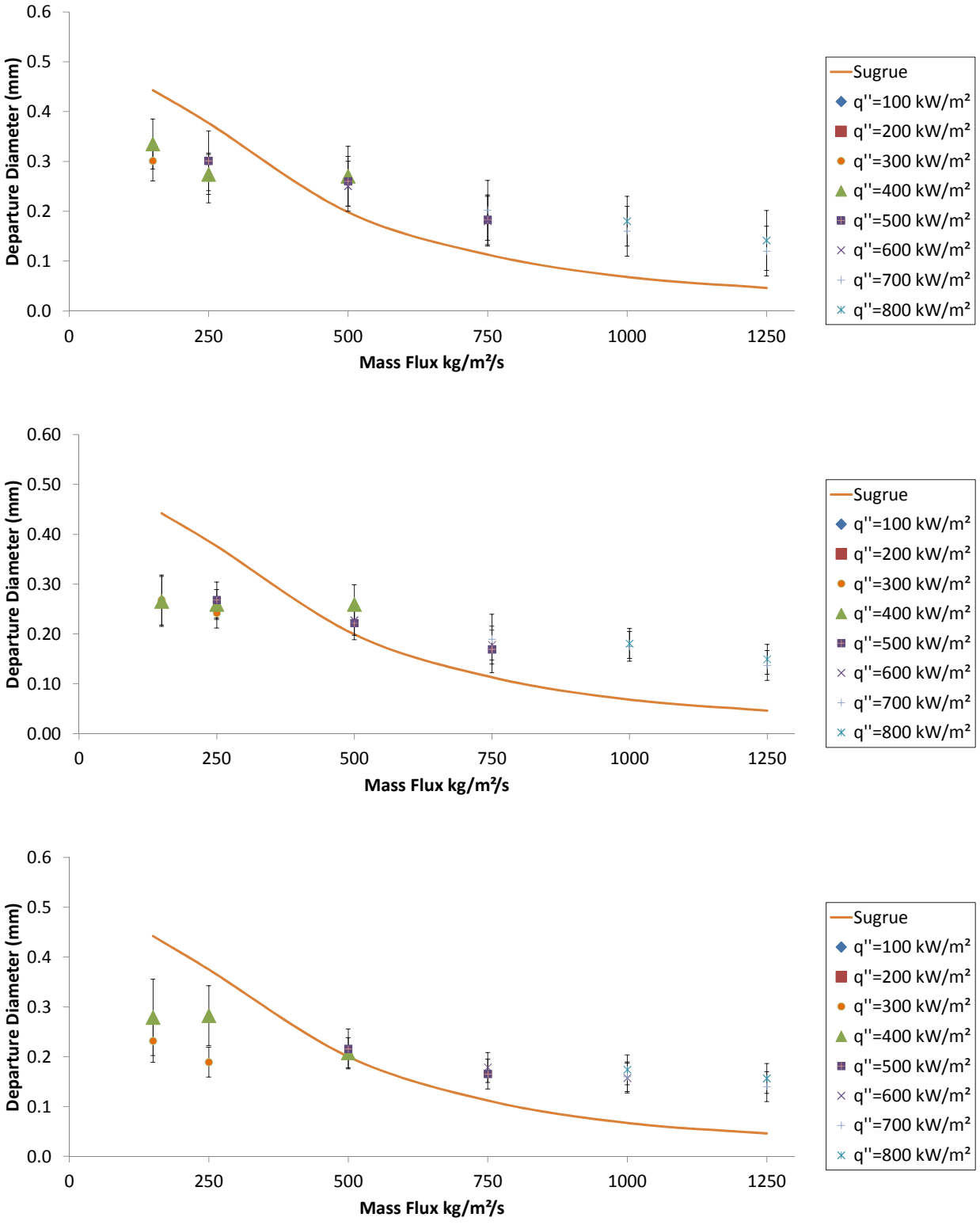

Figure 3.11: 2.0 bar bubble departure diameters for subcoolings of 5 °C (top), 10 °C (middle), and 15 °C (bottom).

3.4 Nucleation Site Density

3.4.1 Existing Nucleation Site Density Correlations and Models

Many nucleation site density models exist, and they predict a wide range of results for a given set of conditions. Many were developed for pool boiling and are not very accurate when extended to flow boiling. In this section, a few of the relevant models will be presented.

The Lemmert-Chawla nucleation site density correlation [63] is widely used and the formula is shown in (3.19). The typical values for m and p are 185.0 and 1.805.

$$N'' = (m\Delta T_{sup})^p \tag{3.19}$$

N'' is the nucleation site density and ΔT_{sup} is the wall temperature minus the saturation temperature.

The Hibiki-Ishii nucleation site density model incorporates a dependence on the contact angle of the surface with the fluid, as well as being dependent on the system pressure, and both have a strong influence on nucleation site density [64]. The contact angle is incorporated since this is an important parameter to determine whether a site contains trapped gasses, which determines whether the site is active or not, see section 1.2.1. The model is given in (3.20),

$$N'' = \overline{N''}\left(1 - \exp\left(-\frac{\theta^2}{8\mu_c^2}\right)\right)\left[\exp\left(f(\rho^+)\frac{\lambda'}{R_c}\right) - 1\right] \tag{3.20}$$

where $\overline{N''}$ is the reference nucleation site density of 4.72 x 10^5 sites/m^2, μ_c is a characteristic cone angle scale for a nucleation site, ρ^+ is given in (3.21) - (3.22), λ' is the cavity length scale and is set equal to 2.50 x 10^{-6}m, θ is the static contact angle, R_c is the minimum cavity radius, and is given in (3.23).

$$\rho^+ = \log\left(\frac{\rho_f - \rho_g}{\rho_g}\right) \tag{3.21}$$

$$f(\rho^+) = -0.01064 + 0.48246\rho^+ - 0.22712{\rho^+}^2 + 0.05468{\rho^+}^3 \tag{3.22}$$

$$R_c = \frac{2\sigma\left\{1 + (\rho_g/\rho_f)\right\}/p}{\exp\left\{h_{fg}(\Delta T_{sup})/(R_g T_w T_{sat})\right\} - 1} \tag{3.23}$$

R_g is the gas constant based on the molecular weight of the fluid, σ, ρ_g, ρ_f, h_{fg}, T_w, T_{sat}, and ΔT_{sup} are as defined before.

The nucleation site model proposed by Kocamustafaogullari and Ishii [65, 64] is shown in (3.24)-(3.31).

$$N'' = N''^*/D_d^2 \tag{3.24}$$

$$N''^* = f(\rho^*)R_c^{*-4.4} \tag{3.25}$$

$$\rho^* = (\rho_f - \rho_g)/\rho_g \tag{3.26}$$

$$f(\rho^*) = 2.157\text{x}10^{-7}\rho^{*-3.2}(1 + 0.0049\rho^*)^{4.13} \tag{3.27}$$

$$R_c^* = \frac{R_c}{D_d/2} \tag{3.28}$$

$$\Delta T_e = S\Delta T_{sat} \tag{3.29}$$

$$S = \frac{1}{1 + 1.5\text{x}10^{-5}\text{Re}_{\text{TP}}} \tag{3.30}$$

$$\text{Re}_{\text{TP}} = \frac{G(1-\chi)D_h}{\mu_f} \tag{3.31}$$

N'' is the nucleation site density, R_c^* is the effective critical cavity size, ρ_g is the density of the vapor, ρ_f is the density of the liquid, D_d is the departure diameter, σ is the surface tension, P_l is the liquid pressure, h_{fg} is the heat of vaporization, R is the gas constant, ΔT_e is the effective wall superheat, T_g is the vapor temperature, T_{sat} is the saturation temperature, G is the mass flux, χ is the vapor quality, D_h is the hydraulic diameter, μ_f is the dynamic viscosity of the fluid, F=1 for cases where the Martinelli parameter is $>$10, and Re_{TP} is the two phase Reynolds number.

3.4.2 Measurement of Nucleation Site Density

An automatic algorithm for calculating the nucleation site density was developed. The detection algorithm took an average value from each pixel across time and subtracted this mean value from the current frame. This deviation from the mean highlighted specific sites, and then a signal cutoff value was applied that removed highlighted areas that were not sites. Clusters of pixels were then identified and their centroids calculated. The size of the temperature footprint of the nucleation site was determined, if the thermal footprint was too large ($>$0.12 mm^2), the site was rejected to prevent counting nucleation sites late in the ebullition cycle. The centroids were then rounded to whole pixel values, and this coordinate was compared to previously recorded sites. A site was only counted as a new site if there was not a previous site in the exclusion zone of a previous nucleation site.

Tables 3.2 and 3.3 are two schemes for exclusion zones for rejecting adjacent nucleation sites, showing the closest that two adjacent sites can be without being considered the same site. Each box represents a camera pixel, and the "x" represents unique site locations. The tables show the maximum packing of nucleation sites for each scheme. Table 3.2 corner pixels are not allowed to be counted as a new nucleation site, while in Table 3.3 diagonal pixels from an already counted site are allowed to be counted as a unique site. At low heat fluxes the choice of scheme only affects the nucleation site density by an increase in the number of sites that are double counted. However, at higher heat fluxes the scheme can have an effect on the value determined as nucleation site density increases because of the maximum number of sites that can be counted differs for each scheme. The scheme in Table 3.2 imposes a theoretical maximum of 3080 sites/cm^2 for the resolution of the FLIR camera (90 μm), while the scheme in Table 3.3 imposes a theoretical maximum of 6160 sites/cm^2 for the FLIR camera. For the IRC camera outfitted with a 50 mm lens and 1" extension ring (37 μm resolution), the scheme of Table 3.2 yields a theoretical maximum of 18,250 sites/cm^2 and the scheme of Table 3.3 imposes a theoretical maximum of 36,500 sites/cm^2. However, if the density gets to a moderate percentage of the maximum, sites will start to be missed. To maintain consistency between data of different spatial resolutions, a constant area of an exclusion zone was implemented of 0.073 mm^2, which corresponds to Table 3.2 for a spatial resolution of 90 μm/pixel, and this is discussed more in detail in sections 3.4.3 and 3.4.4.

A convergence criterion was imposed to minimize the counting of noise as nucleation sites. For example, if an infinite number of frames were counted, the nucleation site count would slowly increase as spurious points were counted, even if all the sites had been identified. There are several potential forms of error in this methodology. The first is from the choice of the heuristics for selecting a site. These include the signal cutoff value, the convergence criteria, and the maximum site size. These three values were varied to explore

Table 3.2: No Adjacent Nucleation Site at Corners.

x		x		x		x	
	x		x		x		x
x		x		x		x	
	x		x		x		x

Table 3.3: Adjacent Nucleation Site at Corners.

x		x		x		x	
	x		x		x		x
x		x		x		x	
	x		x		x		x
x		x		x		x	
	x		x		x		x
x		x		x		x	
	x		x		x		x

the sensitivity to the total number of nucleation sites counted, and within the reasonable range of possible choices these parameters affected the outcome by about 6%. The cutoff value has to be restrictive enough to be able to distinguish between nucleation events and the thermal effects of a sliding bubble, but not so restrictive that sites are missed. There is also the error associated with camera spatial resolution. As the site density gets higher, there will be more missed sites because of the increased likelihood of sites overlapping that are closer together than the resolution of the camera. The automatic MATLAB-based counting algorithm was validated by comparing it to manual counting and found to agree within 10%. However, the automatic site counter was consistently larger, and would identify sites missed during the hand counting. An example of the sites located for a small area of the heater (approximately 60x60 pixels) is shown in Figure 3.12. The left figure shows the IR image with black crosses over the identified sites. The right image shows the binary clusters of pixels that were identified by the algorithm for which the centroids were calculated.

3.4.3 Nucleation Site Density - Monte Carlo

A Monte Carlo method was used to compare the measured nucleation site density to how many would be missed with that density based on the imposed exclusion zone around a counted site. The script worked by creating a matrix with each element representing a pixel of the sensor of the camera. Then a random location on the sensor was chosen from a uniform distribution. If the location met the requirements of being a new site (i.e. two sites cannot be in adjacent pixels), then the matrix was updated showing that location had a nucleation site and both the measured and actual nucleation site counter was incremented by one. If the randomly picked location was not a new site, then only the actual site counter was incremented by one. This process continued until the measured site counter was equivalent to the number of sites measured from the experimental data. There were two counts, the measured site count which matched the experimental data, and the actual site count, which included those that would have been missed by the experimental nucleation site counting method. This gives an estimate of how many sites would be missed for different nucleation site densities.

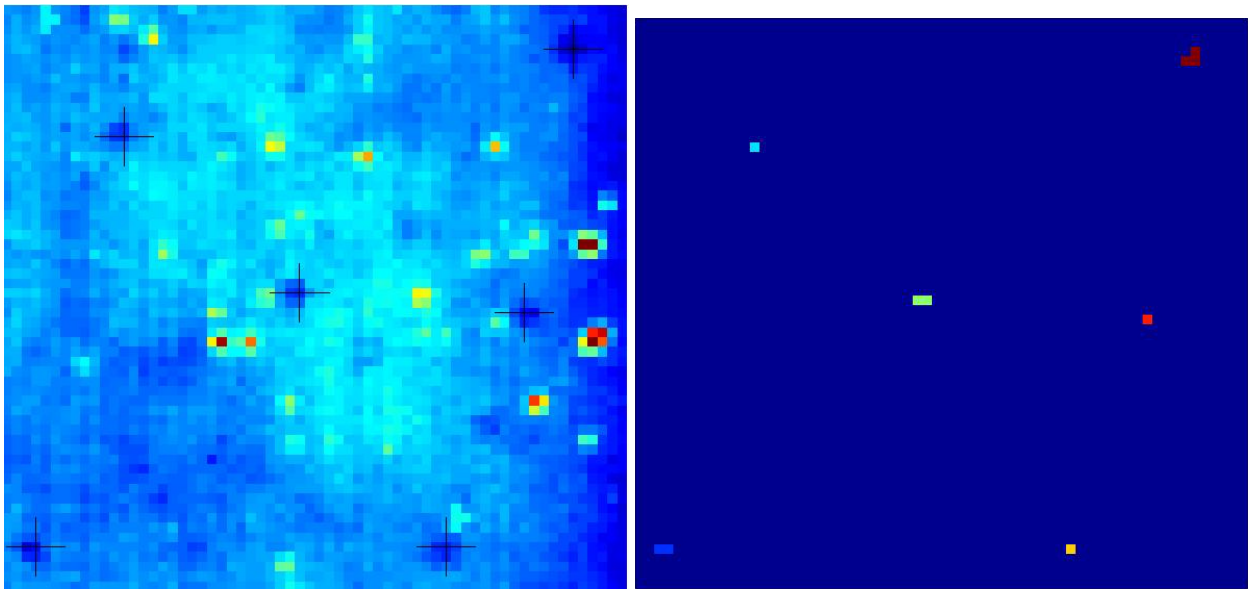

Figure 3.12: Example of nucleation site algorithm output, IR image (left) and pixel clusters (right). The localized red spots on the left image are regions of high emissivity where the temperature cannot be measured.

Then the the nucleation site matrix was cleared and the process started over to get the actual site counter value to converge, and the process was repeated until the average of the actual site density over all the histories changes less than 0.1 sites per iteration. Then this process was done for a variety of measured nucleation site densities. This was completed for the 90 μm per pixel spatial resolution of the FLIR Camera. Figure 3.13 shows the plot of the actual site density versus the measured site density with a y=x line also plotted. As the nucleation site density increases the actual value becomes progressively larger than the measured value. If the random sites are allowed to be adjacent to each other (curve labeled Actual 0 μm), at 500 sites/cm^2 the actual value is 20% higher than the measured value, at 1000 sites/cm^{2}the actual value is 60% higher, and at 1350 sites/cm^2 the actual value is 100% higher. If the sites are not allowed to be adjacent to each other and have an exclusion area of 100 μm, then these differences are nearly halved. This allows for statistical correction of measured nucleation sites if desired. It also gives information for choosing a cutoff for the maximum nucleation site density so that the results do not need statistical correction.

3.4.4 Influence of Exclusion Zone

The spatial resolution of the data taken with the IRC camera was approximately 37 μm/pixel compared to the the 90 μm/pixel of the data taken with the FLIR camera. Thus, a comparison on using different exclusion zones for counting or not counting an adjacent site was performed. The different exclusion zones are the number of pixels that are within the exclusion zone for a specific site. A 9 pixel exclusion zone is the same as shown in Table 3.2, a 25 pixel exclusion zone means that another site cannot be in a 5 x 5 pixel square with the nucleation site in the middle, and a 49 pixel zone means that another site cannot be in a 7 x 7 pixel box with the site at the middle of the square.

The results in Figure 3.14 show that as long as the nucleation site density is below ~2100 sites/cm^2 for a 37 μm resolution, the exclusion zone does not influence results, and is consistent regardless of the exclusion zone. Thus, this value is chosen for the maximum cutoff for reporting nucleation site densities. The 90 μm/pixel resolution data is consistent with the higher resolution data if it is statistically corrected using the

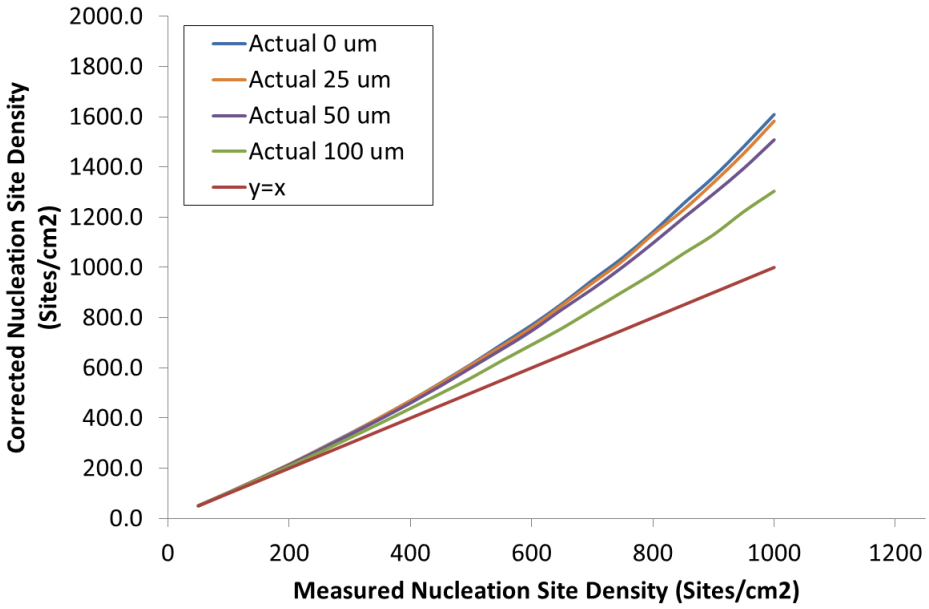

Figure 3.13: Actual site density for various minimum distances between random sites versus the measured site density.

Monte Carlo method discussed in section 3.4.3.

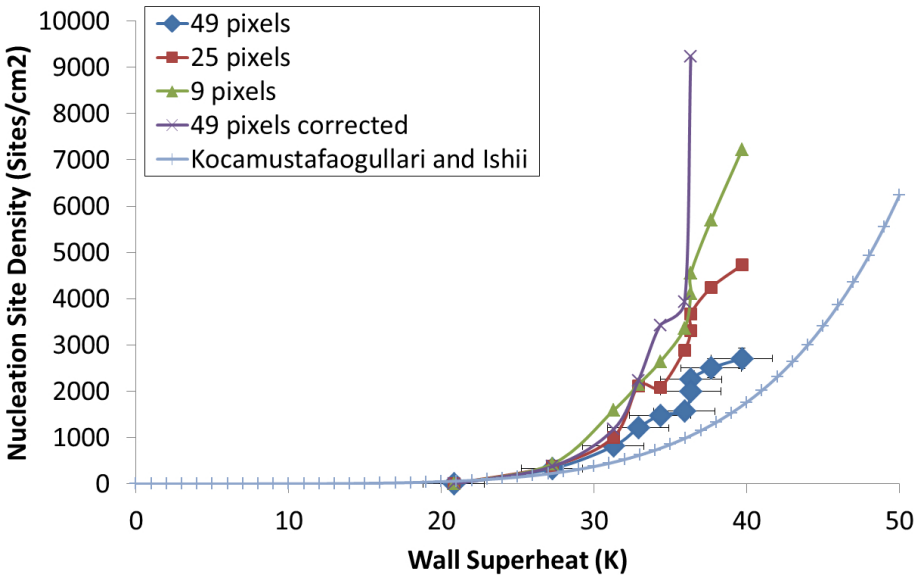

Figure 3.14: Nucleation site density for 5 °C subcooling for various exclusion zone sizes for the 37 µm per pixel data.

3.4.5 Nucleation Site Density Results

The experimental results of the nucleation site densities for 1.05, 1.5, and 2.0 bar are shown in Figures 3.16, 3.17, and 3.18 respectively. The nucleation site densities follow the expected trends. The nucleation site density decreases for a given wall superheat as mass flux increases, and as the pressure increases.

The Kocamustafaogullari and Ishii, the Lemmert-Chawla, and the Hibiki-Ishii models that were presented in section 3.4.1 are shown in Figure 3.15 for 1.05 and 2.0 bar for as a comparison.

The models tend to underpredict the nucleation site density for a given wall superheat. The Kocamustafaogullari and Ishii model, which attempts to calculate an effective wall superheat based on the fluid flow results in a too strong of a dependence on the mass flux. The other models are mostly affected by water property changes due to pressure.

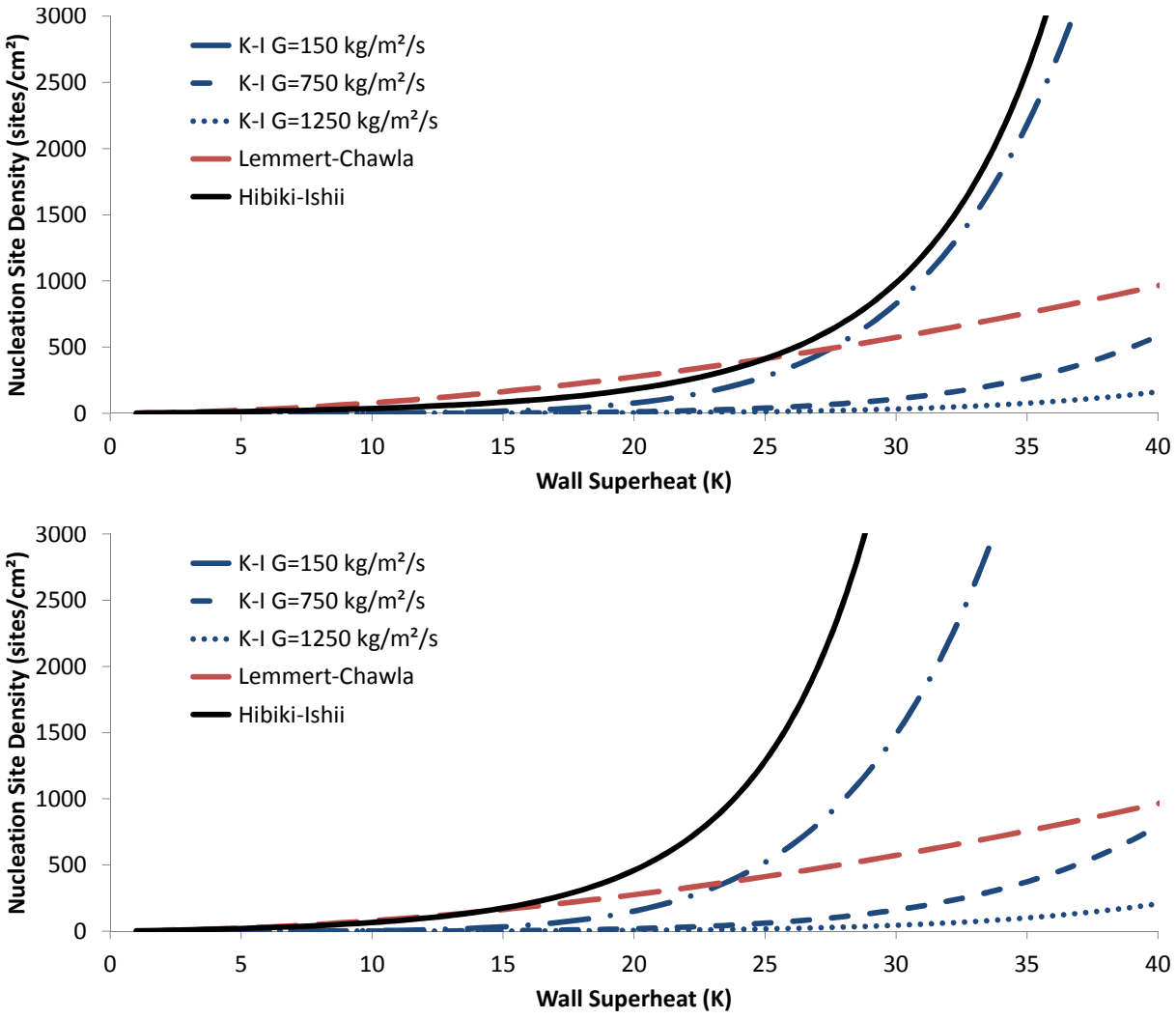

Figure 3.15: Nucleation site density models for 1.05 bar (top) and 2.0 bar (bottom).

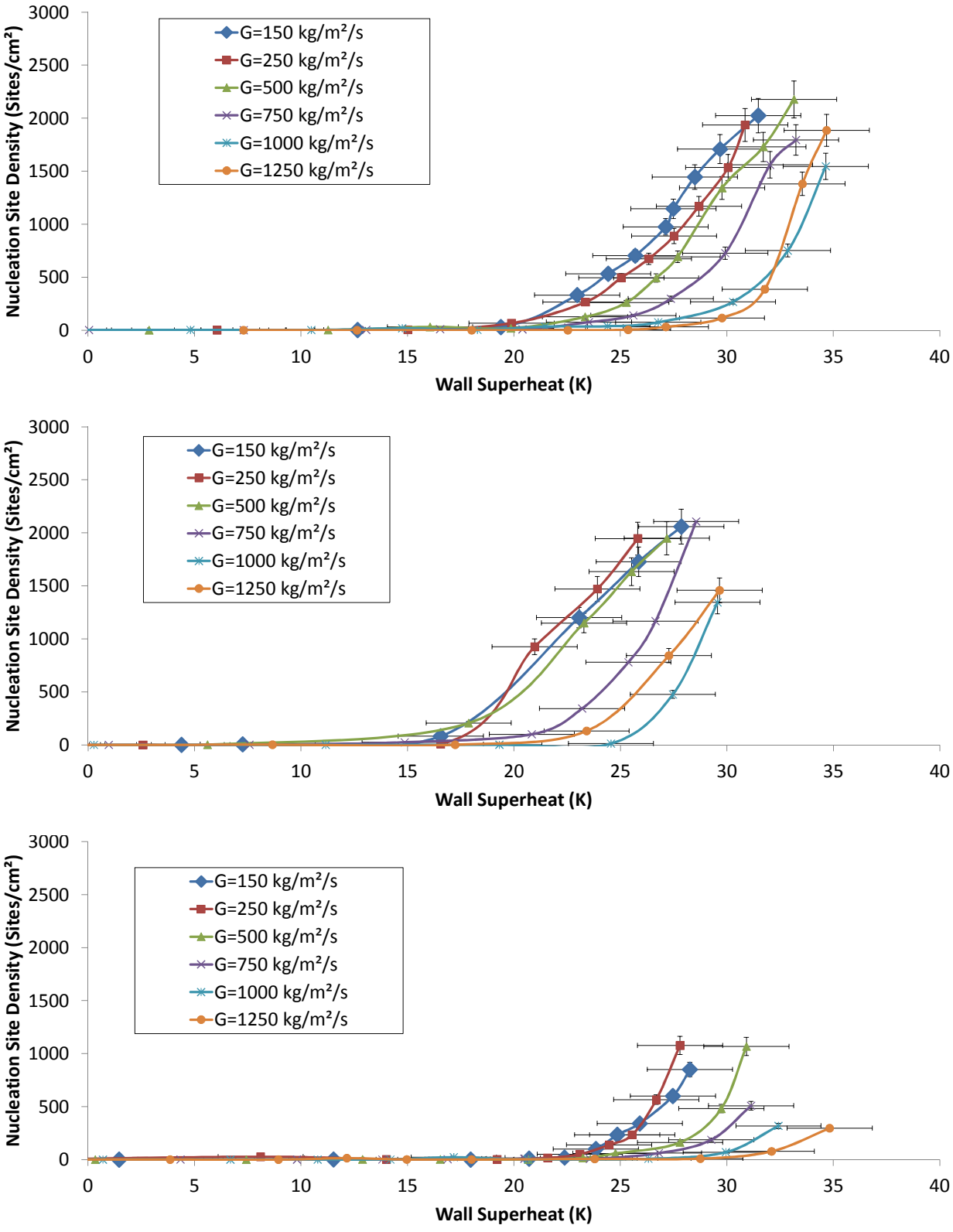

Figure 3.16: 1.05 bar nucleation site densities for subcoolings of 5 °C (top), 10 °C (middle), and 15 °C (bottom)

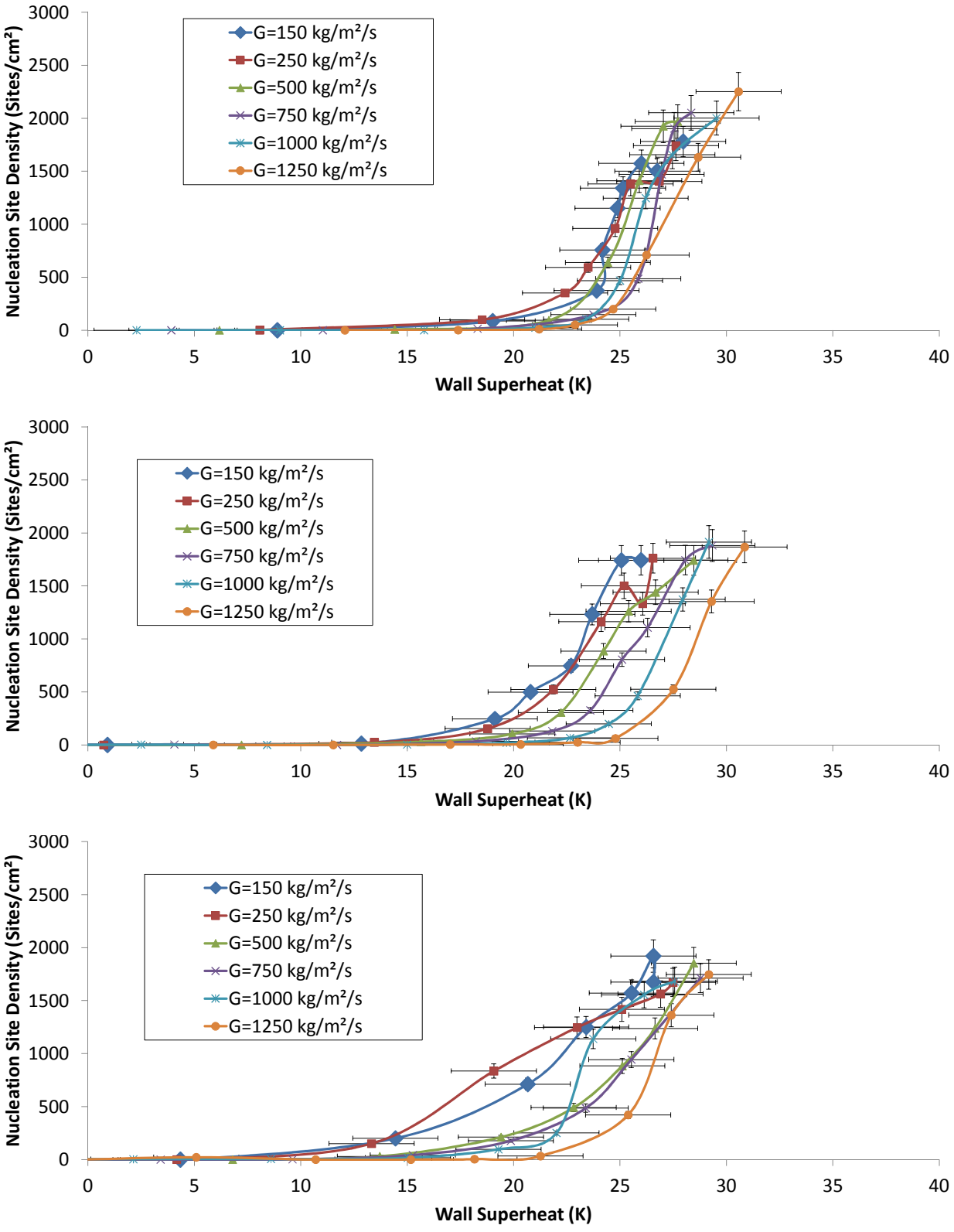

Figure 3.17: 1.5 bar nucleation site densities for subcoolings of 5 °C (top), 10 °C middle), and 15 °C (bottom)

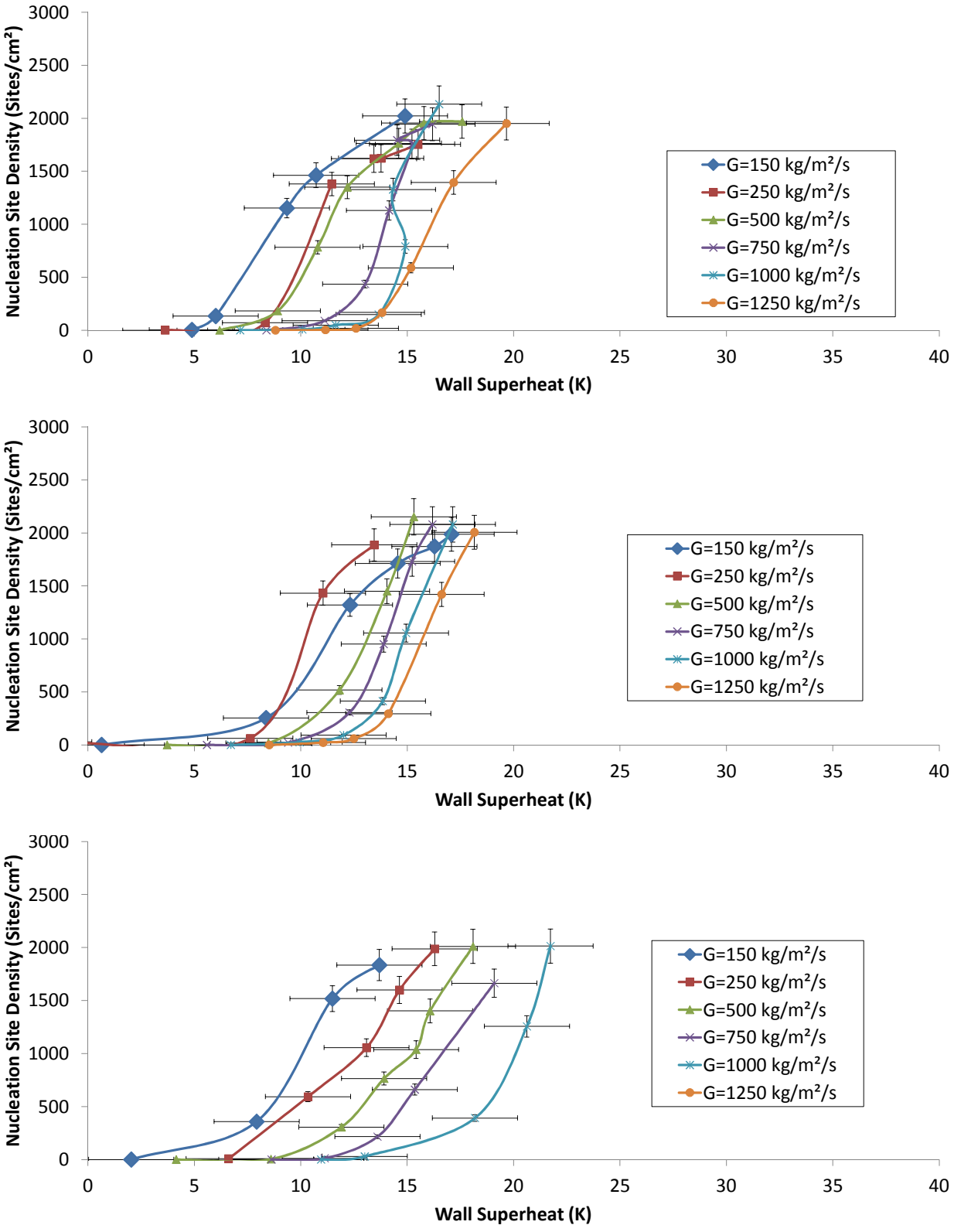

Figure 3.18: 2.0 bar nucleation site densities for subcoolings of 5 °C (top), 10 °C (middle), and 15 °C (bottom)

3.5 Frequency

3.5.1 Existing Frequency Correlations and Models

More recently developed frequency models are based on a more mechanistic approach than older models. Han and Griffith [66] developed an analytical model for the wait time shown in (3.32).

$$t_w = \frac{9}{4\pi\alpha_f}\left[\frac{(T_w - T_b)\,R_{c,approx}}{T_w - T_{sat}\left[1 + (2\sigma/R_{c,approx}\rho_g h_{fg})\right]}\right]^2 \tag{3.32}$$

$$R_{c,approx} = \frac{2\sigma T_{sat}}{\rho_g h_{fg}\Delta T_{sup}} \tag{3.33}$$

t_w is the wait time, α_f is the thermal diffusivity of the liquid, T_w is the wall temperature, T_b is the bulk fluid temperature, T_{sat} is the saturation temperature, σ is the surface tension, ρ_g is the vapor density, h_{fg} is the enthalpy of vaporization, and $R_{c,approx}$ is the minimum critical cavity radius and is shown in (3.33). Typically, for this model the wait time is considered to be three times the growth time for calculation of the frequency.

The wait time model of Yeoh and Tu [67], which is similar to that of Han and Griffith (1965) [66], except that it does have correction factors to take into account the heater surface contact angle. The model is shown in (3.34) - (3.36).

$$t_w = \frac{1}{\pi\alpha_f}\left[\frac{(T_w - T_l)R_c C_1}{(T_w - T_{sat}) - 2\sigma T_{sat}/C_2 R_c \rho_g h_{fg}}\right]^2 \tag{3.34}$$

$$C_1 = \frac{(1 + \cos(\theta))}{\sin(\theta)} \tag{3.35}$$

$$C_2 = \frac{1}{\sin(\theta)} \tag{3.36}$$

R_c is the minimum cavity radius, and θ is the contact angle of the liquid with the surface.

Podowski [22] proposed a wait time model shown in (3.37). The model utilizes the heat flux, thermal properties of the fluid and heater, as well as the surface temperature and bulk liquid temperature.

$$\frac{2q''/\sqrt{\pi}}{k_w/\sqrt{\alpha_w} + k_f/\sqrt{\alpha_f}}\sqrt{t_w} - \frac{\left[T_w^{0+} - T_b\right]R_c}{\sqrt{\pi\alpha_f t_w}} + T_w^{0+} - T_{sat} - \frac{q''R_c/k_f}{1 + (k_w/k_f)\sqrt{\alpha_f/\alpha_w}} - \frac{2\sigma}{R_c}\frac{T_{sat}v_{fg}}{h_{fg}} = 0 \tag{3.37}$$

α_w is the thermal diffusivity of the wall, α_f is the thermal diffusivity of the liquid, k_w is the thermal conductivity of the wall, k_f is the thermal conductivity of the liquid, T_w^{0+} is the wall temperature after a bubble departure, and v_{fg} is the specific volume change from the liquid to the vapor phase.

The model by Hatton and Hall [66] is shown in (3.38). It takes into account the heat capacity of the wall but uses a volumetric heat generation rate H that is difficult to quantify with a thin film heater, thus this model is not useful for comparing to this work.

$$t_w = \frac{\rho_w C_w \delta_w \delta_f}{k_f} \ln \left[\frac{1}{1 - \frac{(T_{sat} - T_\infty) + 2\sigma T_{sat}/R_c \rho_g h_{fg}}{H \delta_w \delta_f / k_f} \left(\frac{1}{1 - c_1 R_c / \delta_f} \right)} \right] \tag{3.38}$$

The simple empirical model by Basu is shown in (3.39). The growth time is based off of the departure diameter of the bubble and the Jakob number and is shown in (3.41).

$$t_w = 139.1 \left(\Delta T_{sup}^{-4.1} \right) \tag{3.39}$$

$$\frac{D_d^2}{\alpha \mathrm{Ja} t_g} = 45 \exp\left(-0.02 \mathrm{Ja}_{\mathrm{sub}}\right) \tag{3.40}$$

$$\mathrm{Ja}_{\mathrm{sub}} = \frac{\rho_l c_{pl} \Delta T_{sub}}{\rho_g h_{fg}} \tag{3.41}$$

3.5.2 Method of Measurement

The frequency measurement algorithm started with a similar mechanism to the nucleation site counter to identify the sites. However, slightly different heuristics needed to be applied. To attribute a nucleation to a specific site, a site had to have a minimum of two pixels between it and an adjacent site so that the nucleation was attributed to a specific site unambiguously. Table 3.2 shows the closest packing of nucleation sites allowed for the nucleation site counting, and Table 3.4 shows the maximum packing proposed for the wait time determination. Once the sites were identified, the frequency was determined from the sharp decrease in the temperature at the site.

Table 3.4: Maximum packing for nucleation sites for wait time determination.

x			x			x	
x			x			x	
x			x			x	

Figure 3.19 is the histogram for the measured frequencies for the case of 1.05 bar, 10 °C subcooling, 1000 kg/m^2/s mass flux, and 800 kW/m^2 heat flux. The mean bubble period (1/f) for this case with the current parameters is 60.8 ms. The distributions are quite wide, but this example was cut off after 200 ms to show the distribution better because the probability for a period of over 200 ms is very low. Each bin is 1 ms wide.

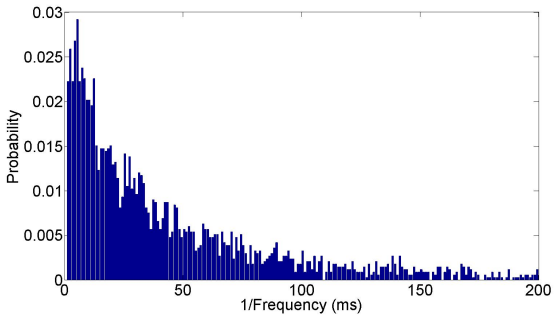

Figure 3.19: Probability of wait + growth times for a sample set of data.

3.5.3 Frequency Results

The experimental results for the bubble frequencies for 1.05, 1.5, and 2.0 bars are shown in Figures 3.20, 3.21, and 3.22. All of the results are plotted along with the Basu period correlation. The 1.05 bar, 15 °C subcooling has several other models discussed in section 3.5.1 plotted as well.

As can be seen from the results, the models vary over an order of magnitude, but the period results from this study are on an order of magnitude or more longer time scale than the models. This is attributed to the correlation of bubble frequency to the wall superheat. The surface used in this study is smooth compared to a typical engineering surface as discussed in section 4.6, and thus will tend to have higher superheats than a typical engineering surface. The growth time models do a reasonable job of predicting growth times, and are on the order of 0.1-1.0 ms for most of the conditions in this study. However, the wait time was observed to be much longer than predicted by the models. This implies that the physical phenomena involved are not being captured by the wait time models. Most do not account for the thermal properties of the heater, or the heat flux of the heater, and none accurately account for heat transfer to the bulk fluid. Furthermore, heat generation for this experiment is a planar heat source on the heat transfer wall, which will have a different temperature distribution compared to that of a heater with a volumetric heat generation. A mechanistic wait time model based on a planar heat source is proposed in section 3.5.4.

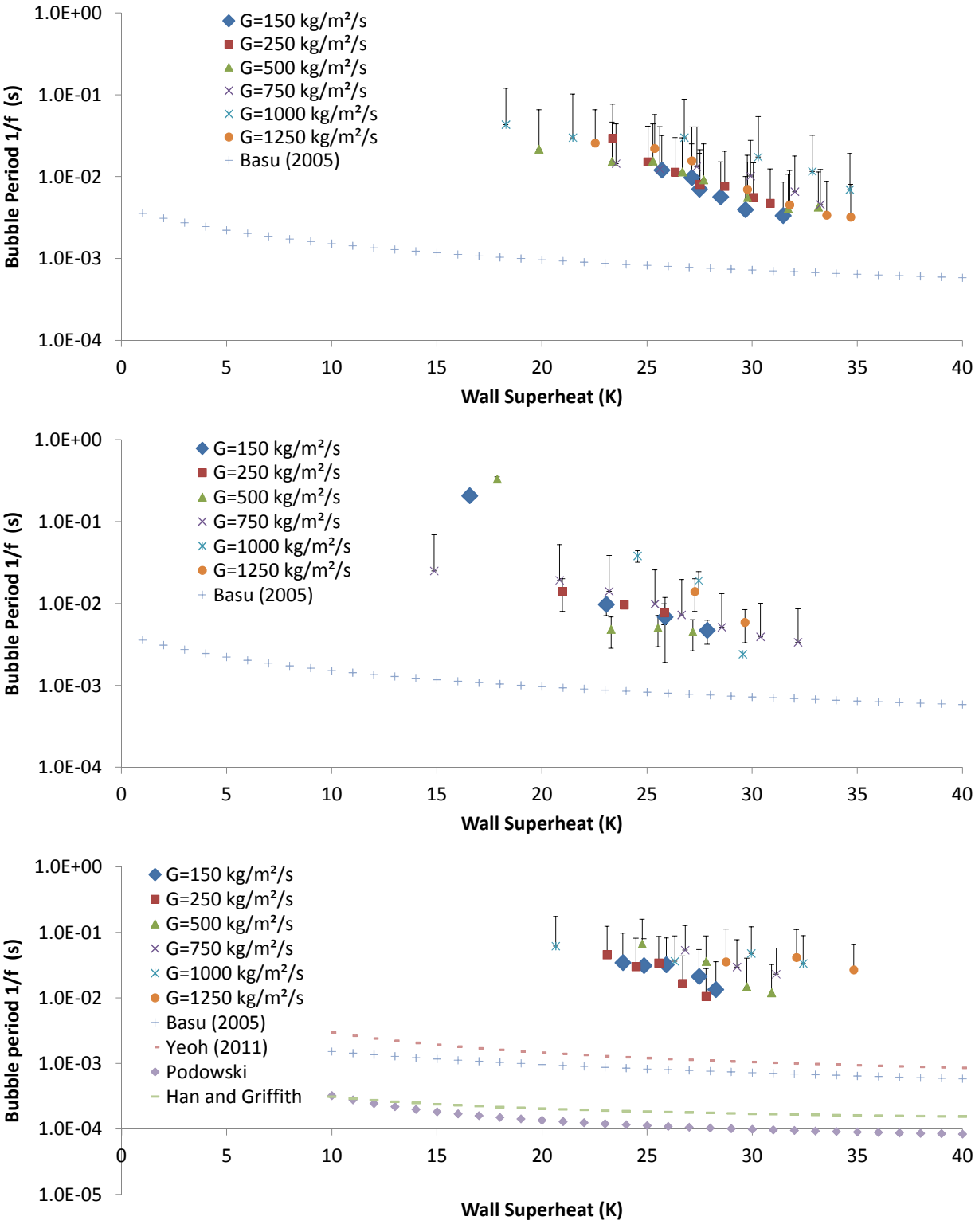

Figure 3.20: 1.05 bar bubble periods for subcoolings of 5 °C (top), 10 °C (middle), and 15 °C (bottom).

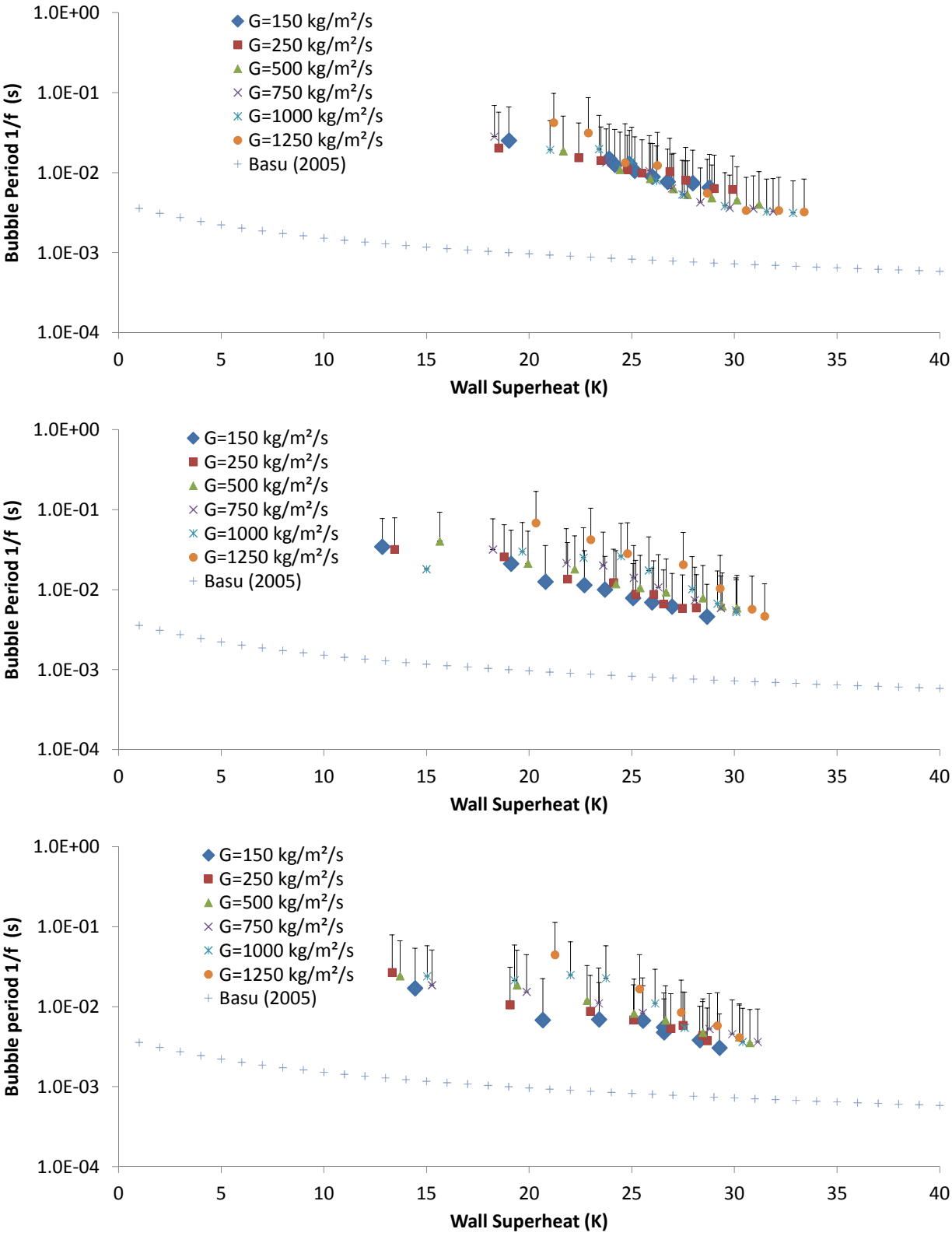

Figure 3.21: 1.5 bar bubble periods for subcoolings of 5 °C (top), 10 °C (middle), and 15 °C (bottom).

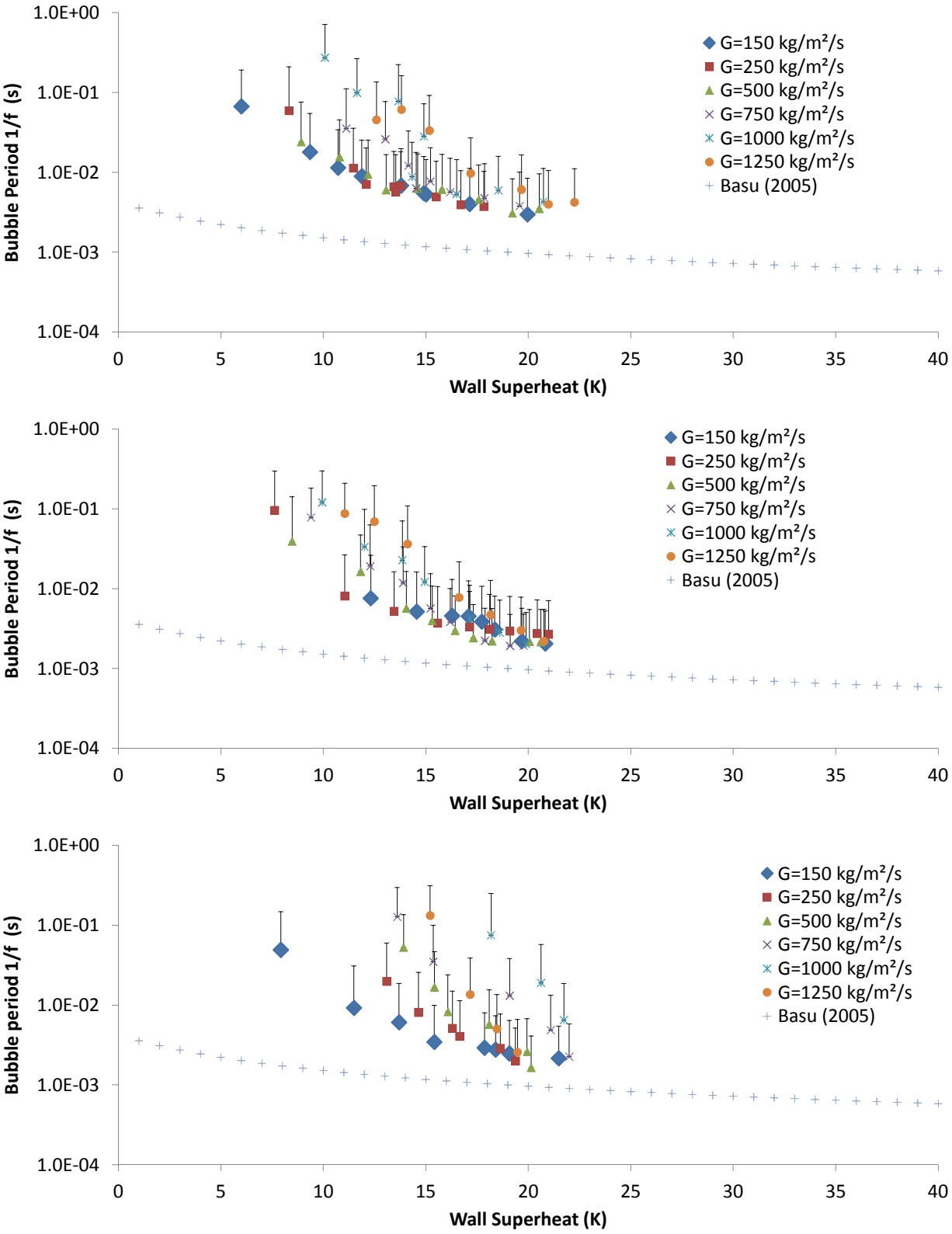

Figure 3.22: 2.0 bar bubble periods for subcoolings of 5 °C (top), 10 °C (middle), and 15 °C (bottom).

3.5.4 Proposed Wait Time Model

The proposed wait time model is based on the idea that for a specific nucleation site there is a specific nucleation temperature at which a bubble will grow. Thus, if the nucleation temperature for a site is known, as well as the temperature drop caused by a bubble nucleating, then the wait time can be calculated. The model assumes that there is a planar heat generation on the surface of the heater, just like in the heater for this work, and that this heat flux is split between the substrate and the environment based on a heat transfer coefficient h. The substrate starts out at a uniform temperature T_i, and the flowing liquid has a bulk temperature of T_b. When the wall temperature reaches the nucleation temperature, T_n, the bubble would nucleate and this is the wait time t_w.

Table 3.5: Parameters for wait time model, definitions, and units.

Parameter	Definition	Units
t_w	Wait time	time
$q_w^{''}$	Total heat flux	mass x time^{-3}
h	Heat transfer coefficient	mass x time^{-3} x temperature^{-1}
δ_w	Substrate thickness	length
k_w	Substrate thermal conductivity	mass x length x time^{-3} x temperature^{-1}
α_w	Substrate thermal diffusivity	length^2 x time^{-1}
T_n-T_i	Temperature rise to nucleation	temperature
T_i-T_b	Temperature difference from substrate to fluid	temperature

There are 8 parameters that are involved in the model, that are shown in Table 3.5 along with their fundamental units. There are four different fundamental units: length, mass, time and temperature. Using the dimensional analysis, this means there can be determined $8 - 4 = 4$ independent pi-groups to simplify the analysis. A set of these are shown in (3.42)-(3.45). The Buckingham-Pi theorem assures that these 4 pi-groups are related by a unique function.

$$\frac{\alpha_w t_w}{\delta_w^2}, \quad \text{Fourier number, Fo} \tag{3.42}$$

$$\frac{h\delta_w}{k_w}, \quad \text{Biot number, Bi} \tag{3.43}$$

$$\frac{T_n - T_i}{T_i - T_b}, \quad \text{Temperature ratio, } \Theta \tag{3.44}$$

$$\frac{q^{''}\delta_w}{k_w\left(T_i - T_b\right)}, \quad \text{Heat generation number, Q} \tag{3.45}$$

To find this unique function that relates the dimensionless terms, the heat equation can be solved for a given set of boundary conditions and initial conditions. The heat equation is written in one spatial dimension and time and is shown in (3.46).

$$\frac{\partial T}{\partial t} = \alpha_w \frac{\partial^2 T}{\partial x^2} \tag{3.46}$$

α_w is the thermal diffusivity of the substrate, t is time, and T is temperature. The initial condition is that the substrate is at a uniform initial temperature at $t = 0$.

There are two cases for the physical model that will be considered. The first case involves a semi-infinite

wall, and the second case involves a finite wall that is adiabatic on one side. Both physical setups are shown in Figure 3.23.

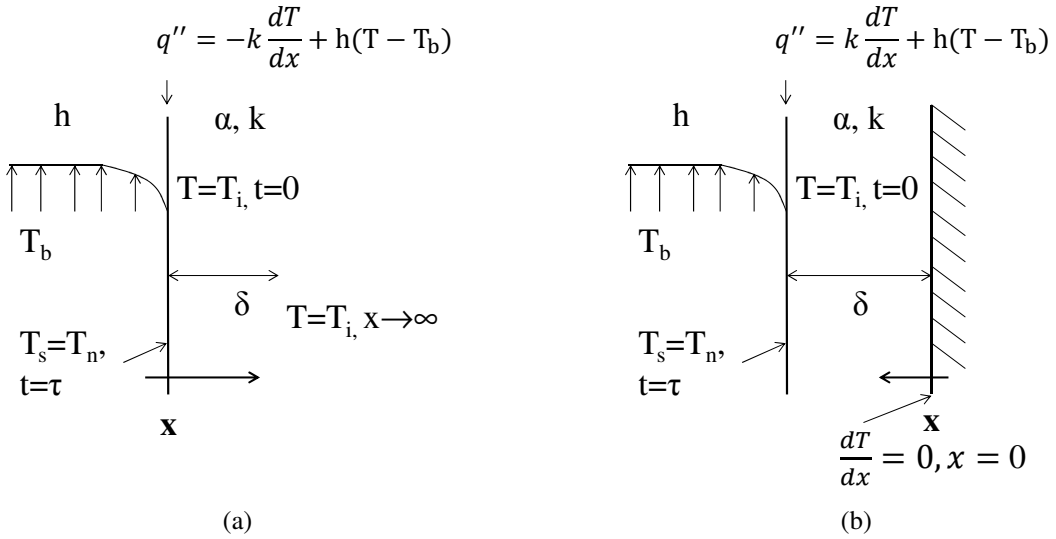

Figure 3.23: Wait time model physical setup (a) for semi-infinite wall, and (b) for adiabatic finite wall.

For the semi-infinite wall setup, the first boundary condition is that the temperature goes to T_i at $x \to \infty$. The first condition implies the wall is infinitely thick in the positive x-direction. The second boundary condition is that the heat flux is split between the fluid based on the single phase heat transfer coefficient at $x = 0$, and the substrate based on the ΔT between the wall and the bulk temperature. The initial condition is shown in (3.47), and the boundary conditions are shown in (3.48) and (3.49).

$$T = T_i, \text{ at } t = 0, \text{ for } x \geq 0 \tag{3.47}$$

$$T = T_i, \text{ as } x \to \infty, \text{ for all } t \geq 0 \tag{3.48}$$

$$q'' = -k\frac{\partial T}{\partial x} + h(T - T_b), \text{ at } x = \delta, \text{ for } t \geq 0 \tag{3.49}$$

For the finite wall setup, the first boundary condition is that the temperature derivative is zero at $x = 0$. The first condition implies that the back wall of the heater is adiabatic. The second boundary condition is that the heat flux is split between the fluid based on the single phase heat transfer coefficient at $x = \delta$, and the substrate based on the ΔT between the wall and the bulk temperature. The initial condition is shown in (3.50), and the boundary conditions are shown in (3.51) and (3.52).

$$T = T_i, \text{ at } t = 0, \text{ for } 0 \leq x \leq \delta \tag{3.50}$$

$$\frac{\partial T}{\partial x} = 0, \ x = 0 \text{ for all } t \geq 0 \tag{3.51}$$

$$q'' = k\frac{\partial T}{\partial x} + h(T - T_b), \text{ at } x = \delta, \text{ for } t \geq 0 \tag{3.52}$$

Solving the heat equation 3.46 with the initial and boundary conditions for the semi-infinite wall problem, obtained using the Laplace transform method, is shown in (3.53).

$$\frac{T(x,t)-T_b}{T_i-T_b}=1 + \frac{\mathrm{Q}-\mathrm{Bi}}{\mathrm{Bi}}\left[-\exp\left(\frac{hx}{k_w}+\frac{h^2\alpha_w t}{k_w^2}\right)\operatorname{erfc}\left(\frac{h}{k_w}\sqrt{\alpha_w t}+\frac{x}{2\sqrt{\alpha_w t}}\right)\operatorname{erfc}\left(\frac{x}{2\sqrt{\alpha_w t}}\right)\right] \tag{3.53}$$

Substituting in for the nucleation temperature, $T=T_n$, at the wall, $x=0$, yields equation (3.54).

$$\Theta = 1+\frac{\mathrm{Q}-\mathrm{Bi}}{\mathrm{Bi}}\left[-\exp\left(\frac{h^2\alpha_w t_w}{k_w^2}\right)\operatorname{erfc}\left(\frac{h}{k_w}\sqrt{\alpha_w t_w}\right)+1\right] \tag{3.54}$$

If $\frac{h}{k}\sqrt{\alpha_w t_w}$ <<1, then a first order Taylor expansion yields an approximate result shown in (3.55).

$$\mathrm{Fo}\approx\frac{\pi}{4}\left(\frac{\Theta}{\mathrm{Q}-\mathrm{Bi}}\right)^2 \tag{3.55}$$

This can also be expressed in terms of the wait time shown in (3.56)

$$t_w=\frac{\pi}{4}\frac{\delta_w^2}{\alpha_w}\left(\frac{\Theta}{\mathrm{Q}-\mathrm{Bi}}\right)^2 \tag{3.56}$$

This yields a functional form for the wait time model. Comparing this model to the experimental data shows that a fitting parameter of 5 is appropriate to fit the data from these experiments, and is shown in (3.57).

$$t_w=\frac{5\pi}{4}\frac{\delta_w^2}{\alpha_w}\left(\frac{\Theta}{\mathrm{Q}-\mathrm{Bi}}\right)^2 \tag{3.57}$$

The fitting parameter is necessary since the assumption of the initial temperature profile in the sapphire being uniform is not actually true, because there is some temperature distribution within the sapphire at $t=0$. The model with the fitting paramter of 5 is plotted along with the 1.05 bar, 5 °C data in Figure 3.24.

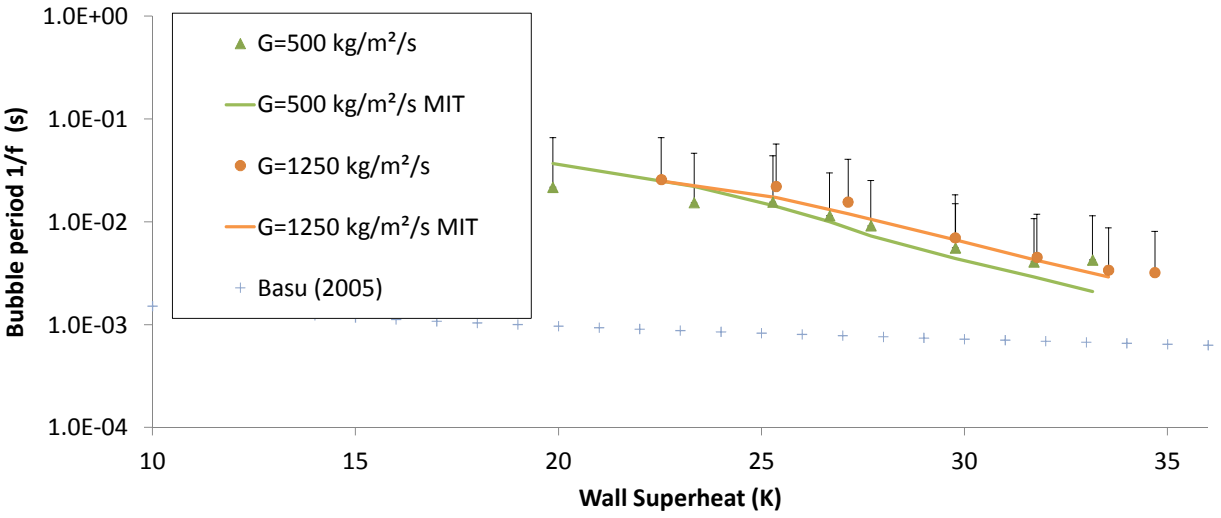

Figure 3.24: Wait time model with fitting parameter applied plotted against 1.05 bar, 5 °C subcooling data.

The limitations of this model are listed below.

- Semi-infinite slab assumption must hold, $\sqrt{\mathrm{Fo}} << 1$.
- Truncation to first order Taylor expansion to eliminate the error function complement must hold, $\mathrm{Bi}\sqrt{\mathrm{Fo}} << 1$.
- Wall temperature must be increasing, $\mathrm{Q} > \mathrm{Bi}$.
- Single phase heat transfer must be representative during the wait time.
- The heat generation must be a planar source on the heat transfer surface.

This model was developed using the assumption of a planar heat source on the wall since this replicates the physical setup of the experiment for which the data was gathered. Thus, this limits the models applicability. However, the method of the heat flux being split between single phase heat transfer to the liquid and to heating up the wall is a general approach that could be applied to more typical heater setups. For example, the problem could be solved for a heater with volumetric heat generation rate.

The solution to the finite wall problem with $x = \delta$ and $T = T_n$ is shown in (3.58).

$$\Theta = \frac{\mathrm{Q}}{\mathrm{Bi}} + \sum_{i=1}^{\infty} \left(1 - \frac{\mathrm{Q}}{\mathrm{Bi}}\right) \frac{4 \sin(\lambda_n) \cos(\lambda_n) \exp\left(-\lambda_n^2 \mathrm{Fo}\right)}{2\lambda_n + \sin(2\lambda_n)} \tag{3.58}$$

The eigenvalues λ_n are defined by (3.59).

$$\lambda_n \tan \lambda_n - \mathrm{Bi} = 0 \tag{3.59}$$

Unfortunately, for short wait times, several terms in the infinite series are significant. Since the wait time is in each term of the series, this makes solving for the wait time a cumbersome process. Furthermore, the eigenfunction shown in (3.59) is a transcendental equation, and makes solving for the wait time also cumbersome. These complications would make the implementation of the semi-infinite wall model in a CFD code not very practical. Therefore, since the limitations of the semi-infinite wall solution are satisfied for the conditions in the experimental data, the semi-infinite form was used for comparison.

3.6 Sliding Bubbles

3.6.1 Sliding Bubble Example

If the force balance on a bubble attached to the wall is broken in the direction of the flow before it is broken perpendicular to the flow, the bubble will slide along the surface and remove heat from the wall while sliding. An example of a sliding bubble is shown in Figure 3.25, as a time series, and Figure 3.26 as a video. This case is at a low heat flux of 130 kW/m^2/s, a mass flux of 200 kg/m^2-s, and 10 °C subcooling at 1.05 bar. A single bubble was examined as it slid along the surface of the heater. The HSV image was taken with the HSV from the front. Both images are spatially scaled to the scale bar shown in the HSV images. The flow goes from the bottom to the top of the image.

The temperature profile along the path the bubble slides is shown in Figure 3.27. A slight increase in the temperature along the heater surface in the direction of the flow can be seen prior to the bubble sliding over the heater surface. As the bubble slides over the surface, the temperature lowers, and after the bubble passes, the temperature is still depressed from prior to bubble sliding over the surface. After approximately 80 ms, the temperature profile returns to near the equilibrium values that existed prior to the bubble crossing the surface.

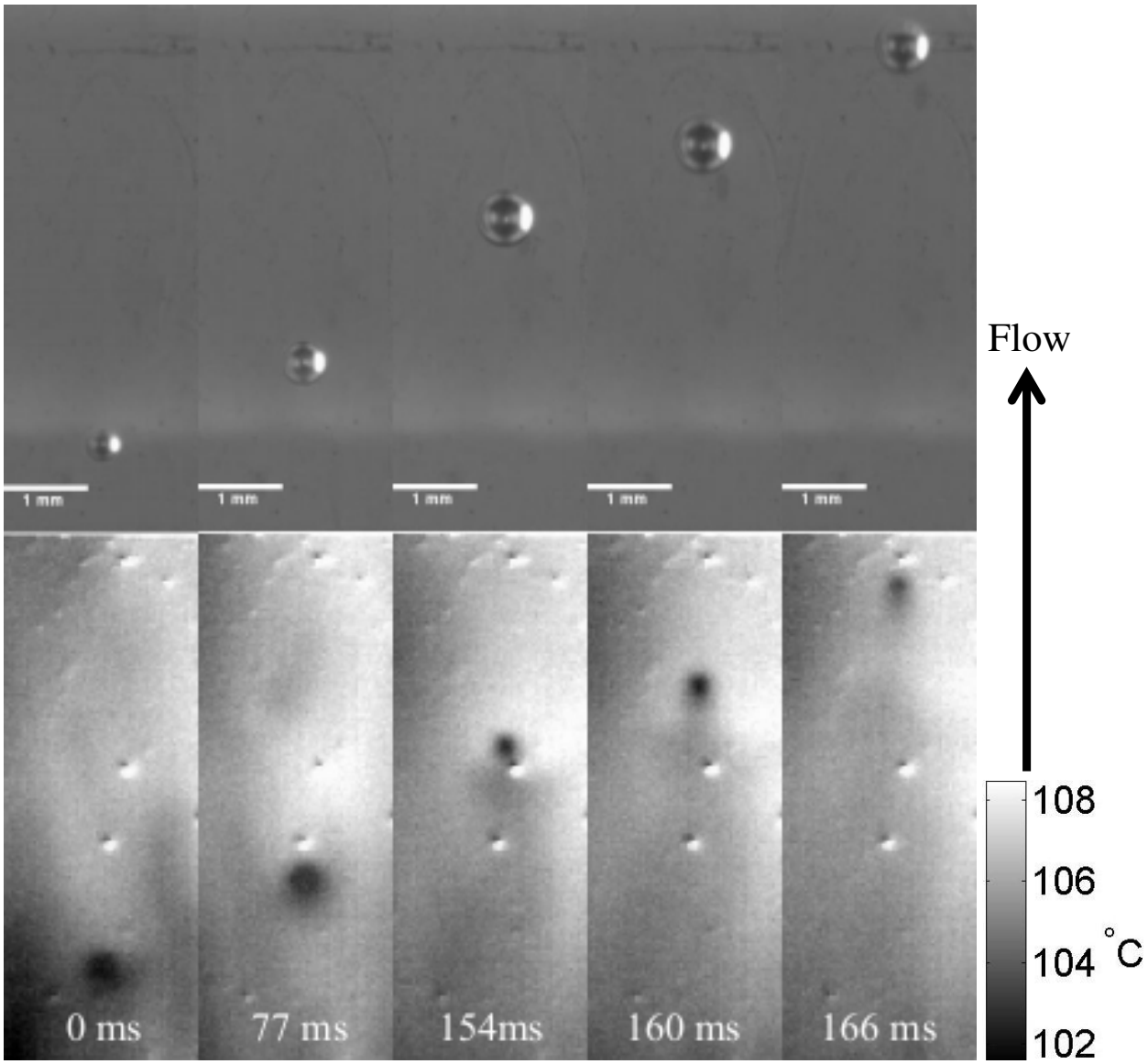

Figure 3.25: HSV (top) and IR (bottom) of a bubble from the start of sliding (t=0 ms) to it reaching the edge of the frame (t=166 ms).

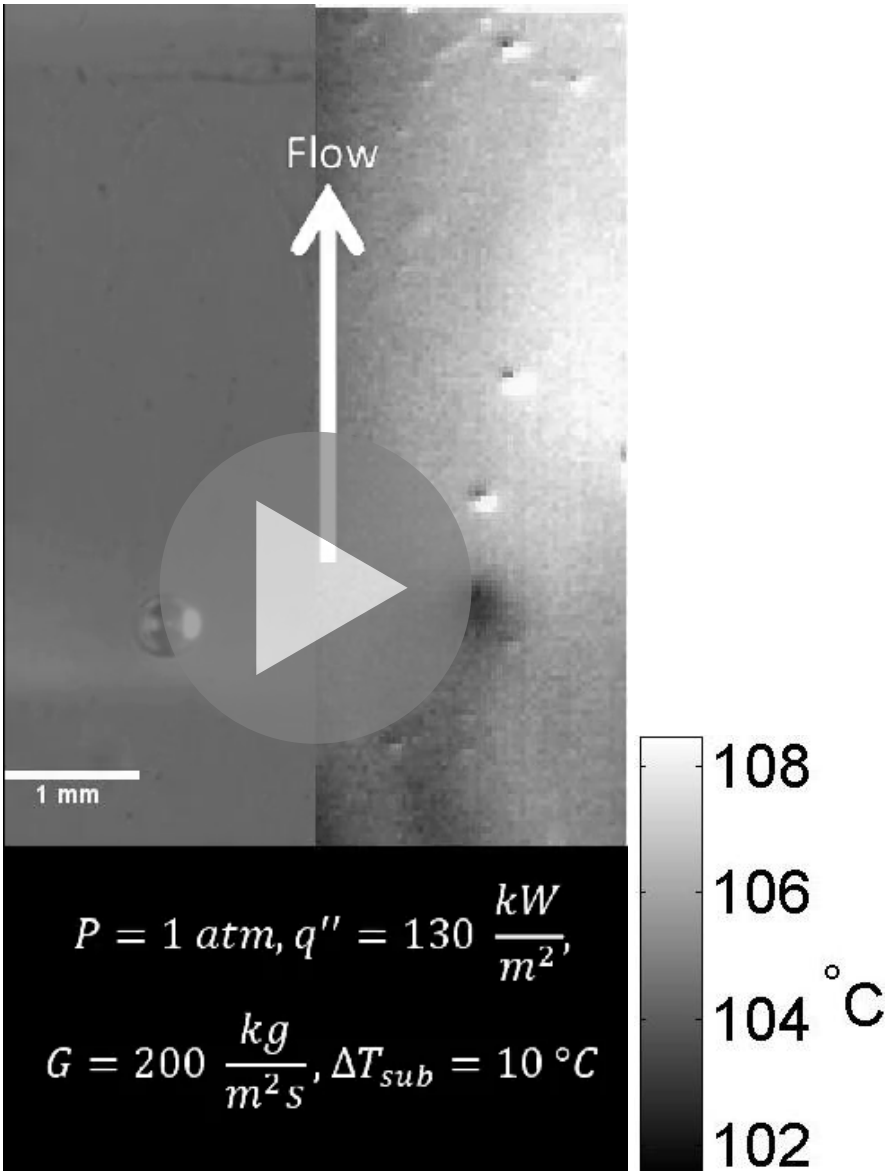

Figure 3.26: Video of sliding bubble, HSV (left) and IR Temperature (right).

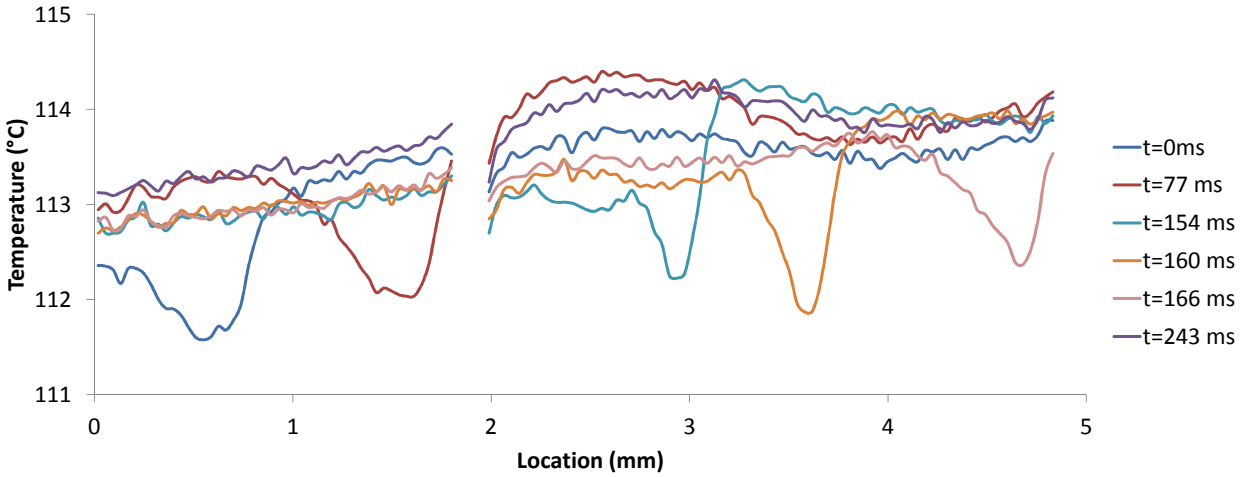

Figure 3.27: Temperature profile across the bubble sliding path for various time steps. t=0 is just before the bubble begins sliding. The gap in the data is from the bubble traversing a non-uniformity in the heater where the temperature could not be read accurately.

3.6.2 Bubble Sliding Velocities and Temperatures

Bubble sliding velocities were calculated from the IR images. The beginning location of the sliding bubble was marked, and then the end of the sliding of the bubble was marked. The velocity was calculated based on the bubble displacement divided by the time between the frames times the number of frames it takes to travel that distance. To keep the measurements consistent, the following heuristics were applied to picking bubbles for measuring:

1. The path length of the sliding bubble has to be a minimum of 0.5 mm and span a minimum 3 frames. In some cases, 2 adjacent frames were used to calculate the velocity if the bubble center is not well defined at one of the endpoints (i.e. the bubble is departing), but the sliding bubble must be evident in a 3rd frame. This is to ensure that there is sufficient time to get an adequate average velocity, and to minimize the effect of the acceleration of the bubble upon departing.

2. The bubble formation has to be observed on the surface. This ensures the bubble was formed on the surface and has not detached and reattached

3. Bubble should not be hydrodynamically affected by other bubbles (this basically limits the measurement to ~1000 sites/cm^2).

The thermal effect of the bubble on the surface was also quantified. Bubbles chosen for sliding velocity measurement were also used to measure the thermal effects on the surface. The cooling underneath the bubble was determined by finding the maximum cooling underneath the bubble while it was sliding. This was reported as a deviation of the temperature under the bubble compared to the average temperature for that location.

Measuring sliding velocities was only feasible between nucleation site densities on the order of 100 sites/cm^2 to 1000 sites/cm^2. Below this range there were very few bubbles nucleating and sliding in the time frame the data was taken. Above that range, there were too many nucleation sites and the bubbles were coalescing.

The bubble sliding velocities are shown in Figure 3.28 and the sliding bubble ΔT values are shown in Figure 3.29.

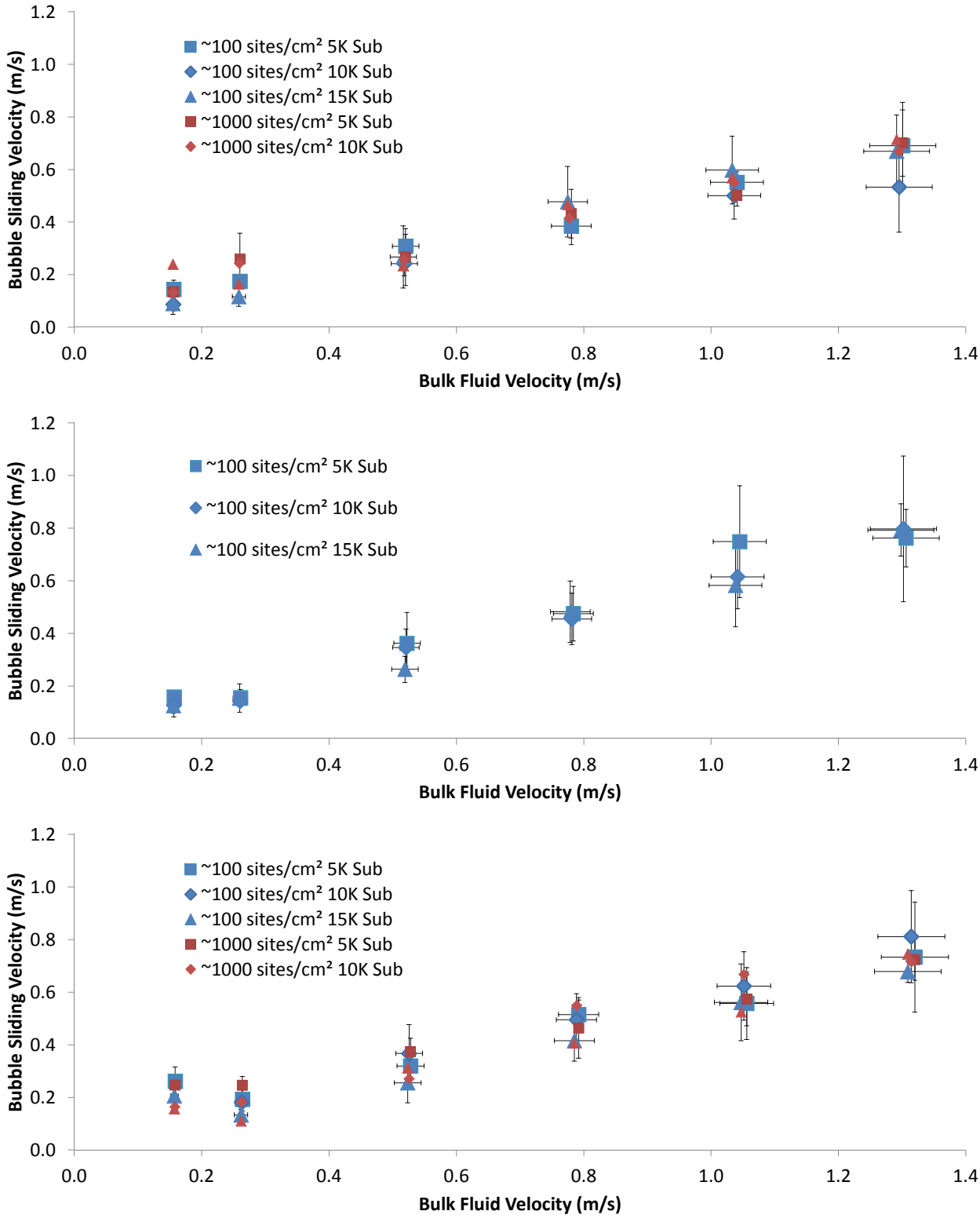

Figure 3.28: Sliding bubble velocity data, 1.05 bar (top), 1.5 bar (middle), 2.0 bar (bottom).

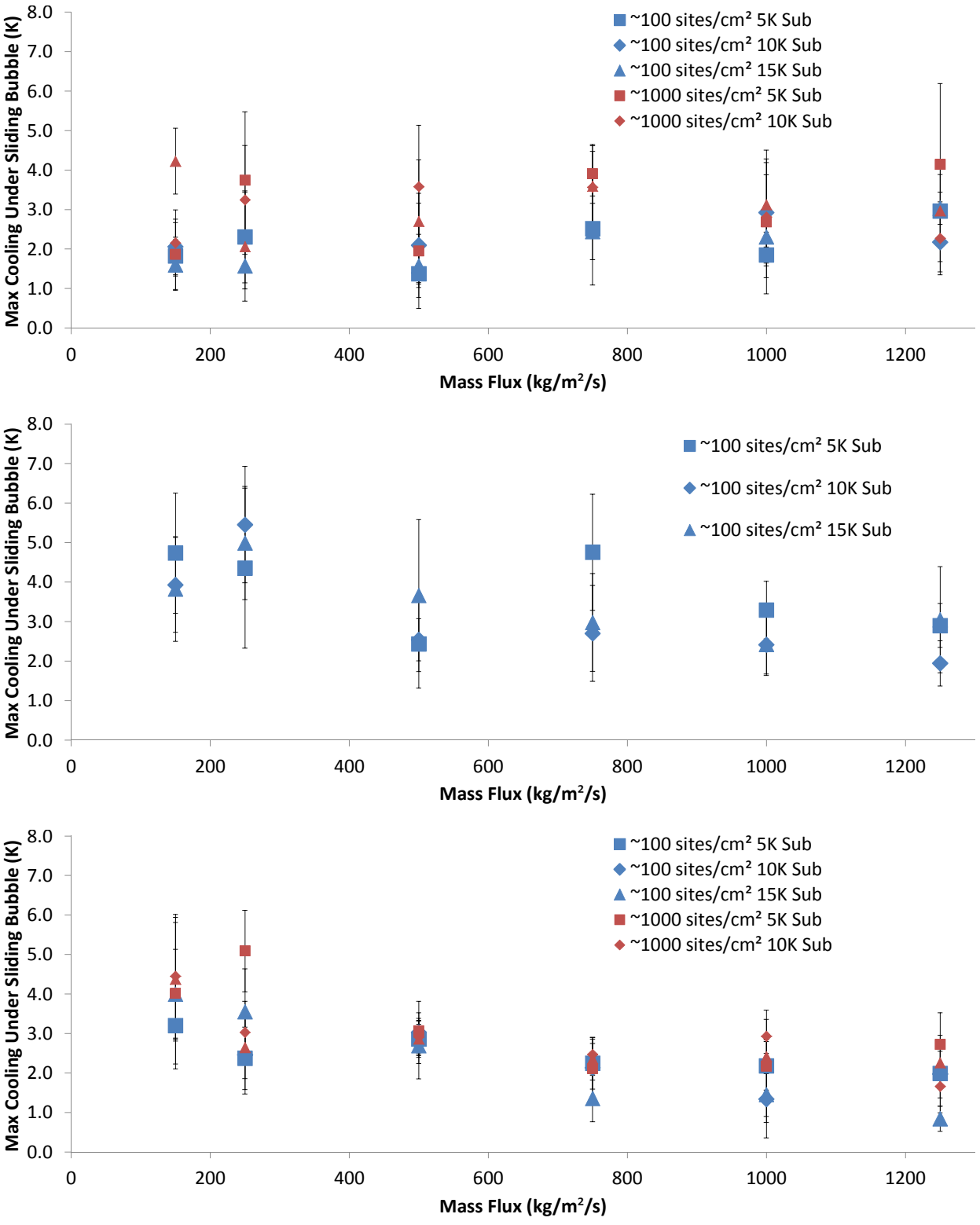

Figure 3.29: Sliding bubble ΔT values, 1.05 bar (top), 1.5 bar (middle), 2.0 bar (bottom).

3.6.3 Bubble Sliding Thermal Effect Timescales

The temperature depression of a sliding bubble was found to be relatively constant based on the experimental data, and have little dependence on pressure, mass flux, heat flux, and subcooling . To understand this phenomenon the effect of conduction on bubble sliding thermal phenomenon was analyzed by solving the heat equation in axisymmetric cylindrical coordinates. The PDE toolbox in MATLAB was used to solve the equation. The model included a 10 mm diameter cylinder that was 1 mm thick composed of sapphire. The axis of symmetry, the back bottom boundary, and the outer radius boundary all had adiabatic boundary conditions. The top 25 µm of the sapphire had a volumetric heat generation rate that was equivalent to 200 kW/m^2 of heat flux to simulate the ITO heater. The bulk temperature on the top surface was set to 95 °C. A 0.5 mm diameter region in the center of the top face of the cylinder had an imposed heat transfer coefficient that was varied from 20,000 - 200,000 W/m/K to simulate a sliding bubble, and the rest of that surface had a heat transfer coefficient of 10,000 W/m-K, which would the heat generation rate for that area. The model is shown in Figure 3.30. The results of the 100,000 W/m-K heat transfer coefficient case are shown in Figure 3.31 and in a video in Figure 3.32.

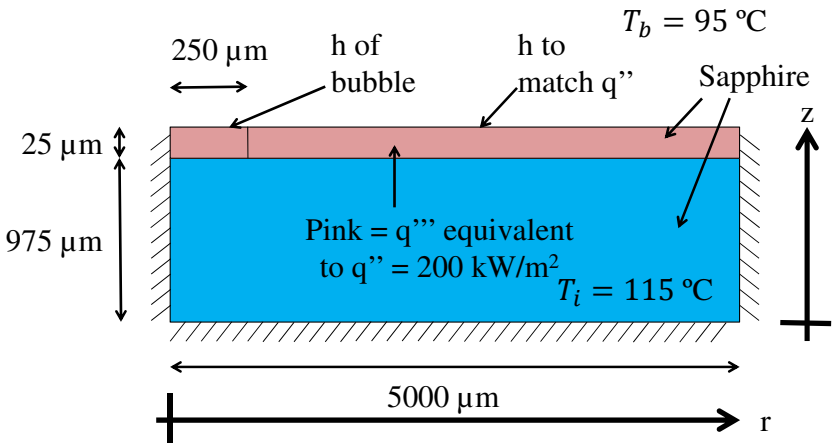

Figure 3.30: Physical model used for sliding bubble timescale analysis.

Plots of the minimum temperature under the bubble (bubble center) is plotted in Figure 3.33. This plot demonstrates that for a given heat transfer coefficient of the bubble, the surface temperature hits a quasi-equilibrium due to conduction from the substrate within about 1 ms. There are some special cases for the 100 kW/m^2/K heat transfer coefficient. The high q" case has a heat generation rate equivalent to 1000 kW/m^2 instead of the 200 kW/m^2 for the rest of the cases. The heat transfer coefficient for the high q" case was increased to match the heat generation rate for the area outside the simulated sliding bubble. The low Tb case has the bulk temperature reduced to 85 °C, the heat transfer coefficient of the low Tb case was reduced to match the heat generation rate for the area outside the simulated sliding bubble.

Measured sliding bubble velocities ranged from ~0.1 ms to ~0.8 m/s. For a 0.5 mm diameter bubble, it would have a residence time over a single location of ~0.6 ms to ~5.0 ms. Referencing Figure 3.33, the maximum temperature difference between these two times from any one of the curves is ~4 °C. The more realistic cases for heat transfer coefficients for the sliding bubble region of the sliding bubble region are closer to 1-2 °C. Furthermore, this method would tend to overestimate the temperature drop from a sliding bubble since the bubble is essentially being modeled as "stuck" at a point and drawing heat from a single location. Thus, all other things being equal, a maximum difference of a couple of degrees would be expected between two bubbles based on sliding velocity alone. This is consistent with the temperature measurements of sliding bubbles from section 3.6.2, that regardless of the sliding velocity, the bubbles had similar cooling effects on the heated surface. However, there are other influencing effects such as the local heat transfer

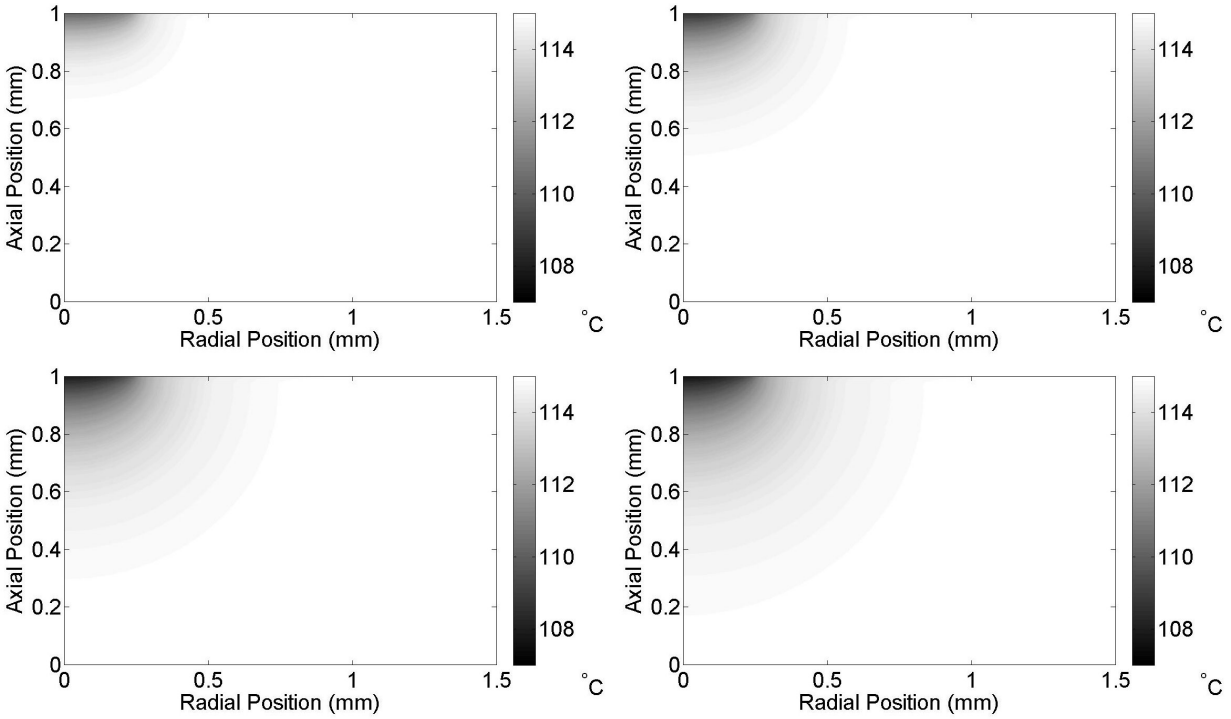

Figure 3.31: Temperature profile of the sapphire with a simulated bubble on the surface at 1 ms (top left), 3 ms (top right), 7 ms (bottom left), and 10 ms (bottom right).

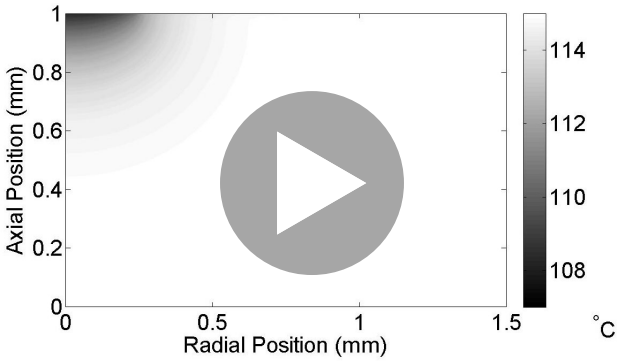

Figure 3.32: Temperature profile of the sapphire with a simulated bubble on the surface for t = 0-10 ms.

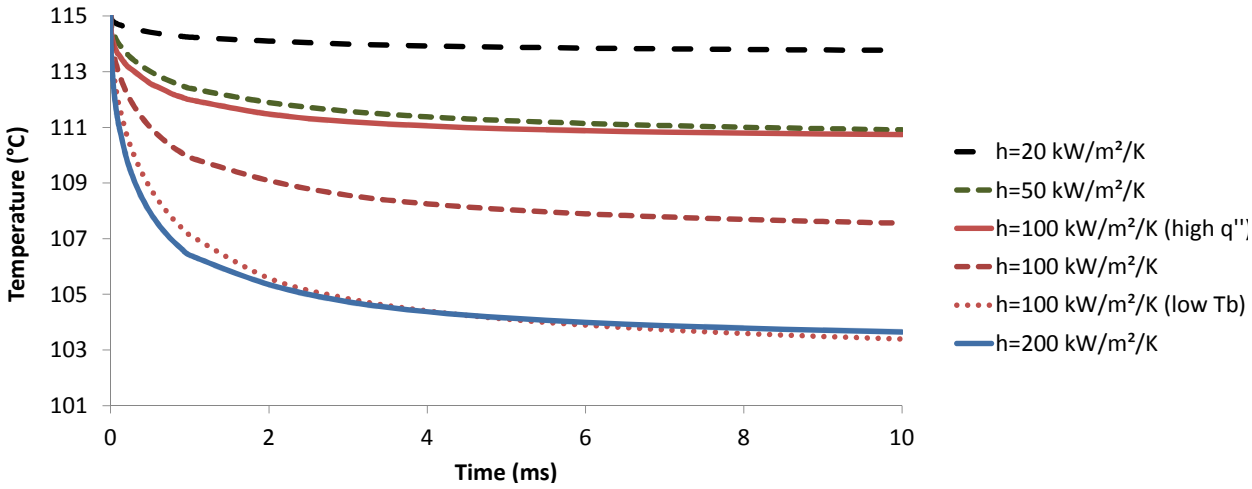

Figure 3.33: Time dependent temperatures under a simulated sliding bubble.

coefficient, which could vary in time based on parameters such as the liquid film thickness under the bubble and local wall superheat.

4 Single Bubble PIV/IR

4.1 Test Matrix

The experimental conditions for the PIV/IR data are shown in Table 4.1. Three subcoolings and three mass fluxes were explored. At each condition, data for a minimum of 3 bubble cycles was taken at ONB. To accompany this, data for the adiabatic condition, and for a heat flux just prior to the onset of nucleate boiling was also collected. The maximum mass flux was 350 kg/m^2/s due to the fact that at the high magnification used, the particle displacement was approaching the limit of PIV for mass fluxes exceeding this value.

Table 4.1: Conditions for single bubble tests, 9 total conditions.

File #	Subcooling (°C)	Mass Flux (kg/m^2/s)	Heat Flux (kW/m^2)
480	5	133	77.8
485	5	250	112.2
492	5	350	154.2
494	10	209	159.7
502	10	250	172.5
511	10	350	213.1
468	15	192	159.7
473	15	250	172.5
476	15	350	213.1

4.2 Experimental Setup

4.2.1 Camera Setup

The optical setup was modified from that of the high speed video, and IR experimental data, to get a higher resolution of vectors for PIV. The PIV setup increased distance between the rear element of the lens, and the sensor to 204 mm. This increased the spatial resolution to 6.8 μm compared to the HSV/IR setup of approximately 15 μm, a little more than double the spatial resolution. Adding another set of extension rings (68 mm) would only increase the spatial resolution by a little over a μm per pixel. Thus, 204 mm of extension rings was the practical limit of magnification achievable with the 200 mm lens. The sensor was windowed down to 720 x 720 pixels to increase the temporal resolution of the camera to 10,000 Hz, which was the maximum pulse rate of the Photonics laser. The red filter for filtering out the laser light on the end of the lens was at a working distance of 161 mm from the face of the test section. A f/8 aperture was used to bring the entire laser sheet into focus and allow the particles to be properly sized on the sensor of ~4 pixels per particle.

The new optical setup needed structural support since the lens was too heavy when placed so far from the camera, so a support system was added to the camera mount. The support system allowed for the tripod to

bear some of the weight and moment created by the long lens. The new optical setup along with the support structure is shown in Figure 4.1.

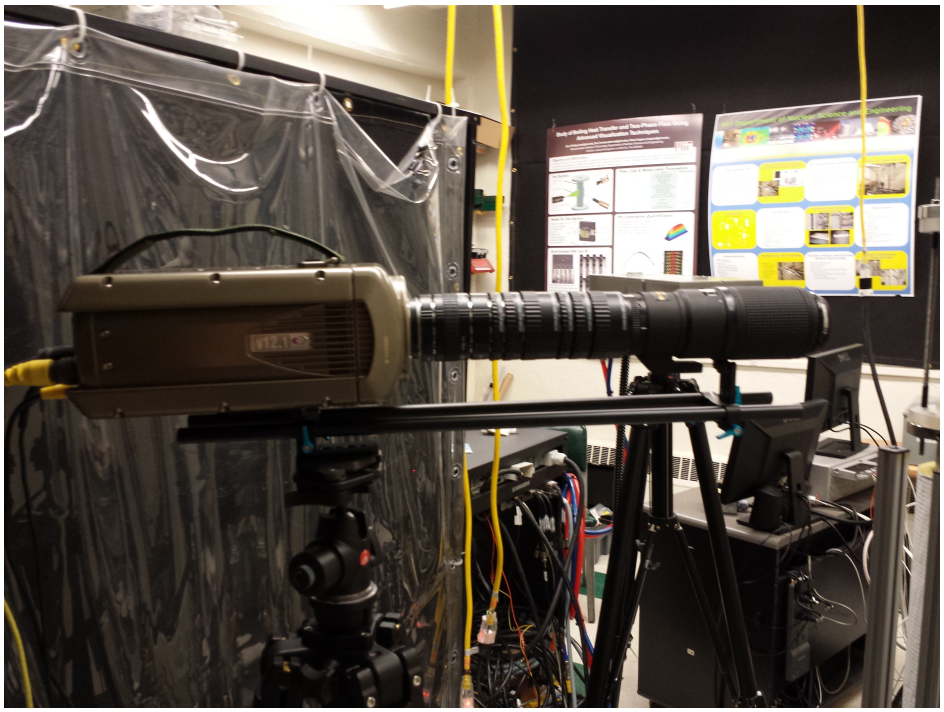

Figure 4.1: High speed camera optical setup with structural support for PIV.

There were a few drawbacks to the PIV optical setup compared to the HSV/IR setup that are listed below.

1. The light gathering from the lens was reduced.
2. Vignetting increased significantly.
3. Imperfections/contaminants on the lens were in focus and affected image quality because of the increased focal distance.
4. The field of view was reduced significantly to a little less than 5 x 5 mm.
5. The depth of focus was reduced to a point where keeping the entire laser sheet in focus was challenging.
6. Shorter working distance.

Of the above concerns, the only one that caused significant problems was the imperfections and contaminants on the lens being visible. This created locations on the image where no signal can be recorded. This can create an issue with the PIV processing algorithm if the areas are too large, since particles disappeared as they crossed these regions.

The optical setup of the IRC camera was modified to use a 50 mm lens, with 2.5 inches of extension rings. This yielded a spatial resolution of 14.8 µm/pixel, compared to about 37 µm/pixel from the HSV/IR tests. The acquisition rate for the IR was 2500 Hz instead of 1250 Hz, and the integration time was reduced from 0.5 ms to 0.39 ms. The IR camera only took one picture for every 4 pictures taken by the high speed camera. The camera's field of view was only 512 x 96 pixels, with 96 pixels in the direction of flow, or about 1.4 mm. The two point non-uniformity correction was performed at room temperature and at 100 °C.

4.2.2 PIV Particle Injection

Particle seeding density decreased with time as particles fell out of solution. Therefore, the fluid could not be seeded a single time and stay at the proper concentration. A method of online seeding had to be incorporated into the loop. This was accomplished with a stainless steel syringe, with a compression fitting to pipe it into the loop. The syringe was placed in a syringe pump to inject the particle solution into the loop. The syringe held 50 cm^3 this allowed for an adequate dilution of the particle solution prior to injection, so that the volume of the $^1/_{16}$-inch tubing was not a significant volume compared to the syringe volume. This was important so the dead volume between the syringe and the flow loop did not hold a significant number of particles that would not make it into the flow. The syringe was rated to 1500 psig, and was obtained from Harvard Apparatus as part #7022255, and the replacement Viton® O-rings were part #722473. The syringe was piped into the loop right after the preheater before the flexible hose that leads into the entrance region. $^1/_{16}$-inch tubing connected to the syringe, which was connected to a $^1/_{16}$-inch to $^1/_4$-inch tubing adapter. The adapter attached to a $^1/_4$-inch needle valve that then was attached to the loop. The setup is shown in Figure 4.2.

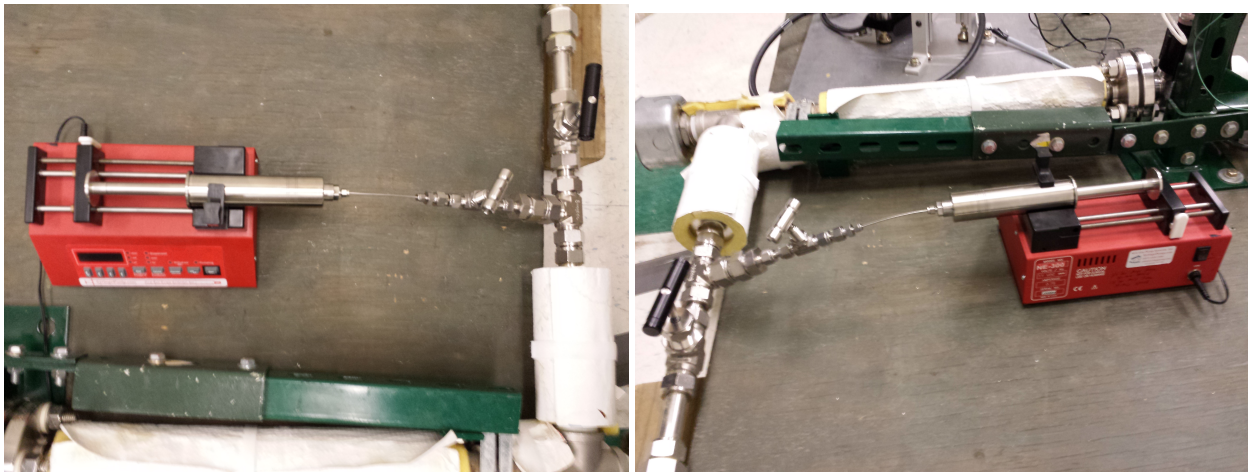

Figure 4.2: Harvard Apparatus 50 cm^3 stainless steel syringe, with $^1/_{16}$-inch fitting, and installed in a syringe pump to allow for PIV particle injection into the loop.

The injection procedure was to fill the syringe with a dilute PIV particle solution and then bleed the air out of the syringe. The valve was cracked open then closed to allow the leg of $^1/_{16}$-inch tubing to fill with water. The syringe was then installed into the syringe pump and connected to the $^1/_{16}$-inch leg of pipe. The valve was then opened, and the syringe pump was started to begin injection. The first injection of particles was done when the loop was at the desired operating conditions and was done at a fast rate of 20 mL/min. After the desired seeding density is obtained, the injection rate could be lowered to 1-3 mL/min to maintain a constant seeding density. The target ideal seeding density was ~0.02 particles/pixel. However, the more typical seeding density obtained was ~0.006 particles/pixel, but this is still sufficient to give reliable vector calculation as discussed in section 5.12.

4.3 Particle Selection

4.3.1 Hollow Glass Spheres

Hollow glass spheres are commonly used in water applications due to their density being between 1.05 and 1.10 g/cc, which is just above that of water, and being very inexpensive. Glass spheres do tend to have a large

size distribution, which usually is a detriment, since there is a larger spectrum of intensities of the particle that the camera has to capture. Also, the size distribution creates different drag forces on different sized particles. However, in the application of this experiment, glass spheres were not a viable option, because they rely on the refraction and reflection of direct laser light. Due to the two-phase application, the intensity of a lens flare from a bubble could cause damage to the sensor, so particles that directly use laser light to illuminate were not an option.

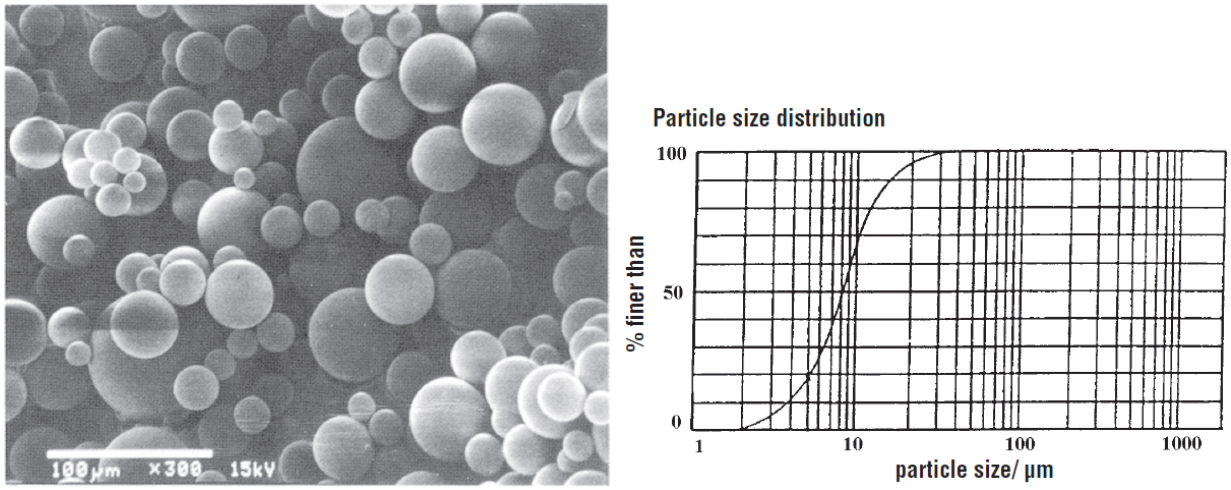

Figure 4.3: SEM images of hollow glass spheres (left) and CDF of size distribution (right) (reprinted with permission from LaVision) [68].

4.3.2 Polystyrene Particles

Polystyrene particles that fluoresce have been successfully used in pool boiling applications [69]. They are ideal for water because of the density of 1.05 g/cc, which is similar to water. However, polystyrene has a glass transition temperature of ~90 °C, which is the temperature at which the particles begin to soften. When this temperature is reached the particles soften and become "sticky;" the particles will then aggressively agglomerate and stick on the wall. The seeding density was observed to decrease quickly when at temperatures near 90 °C. Clumps of particles will also break off the wall when the mass flux is increased creating large particles in the flow which were not ideal for PIV.

4.3.3 Melamine Particles

A new type of particle was selected for PIV at higher temperatures, because of the instability of the polystyrene particles above 90°C. The new particle was derived from a melamine resin, had temperature stability beyond 200 °C, was available in sizes of 1-12 µm, was mono-dispersed with a standard deviation of 0.15 µm, and was marked with Rhodamin B to fluoresce from laser light. The fluorescence was in the red region which allowed filtering of the green laser light, and protected the HSV camera from reflected and refracted laser light.

The melamine particles had a higher specific gravity of 1.51 compared to 1.05 of the previously used polystyrene particles. This raised the question of particle settling and its effect on results. The settling terminal velocity was calculated using Stokes Law shown in (4.1), and the values for the new melamine particles were compared to the old polystyrene particles as shown in Figure 4.4.

$$w = \frac{2\left(\rho_p - \rho_f\right) g r^2}{9\mu_f} \tag{4.1}$$

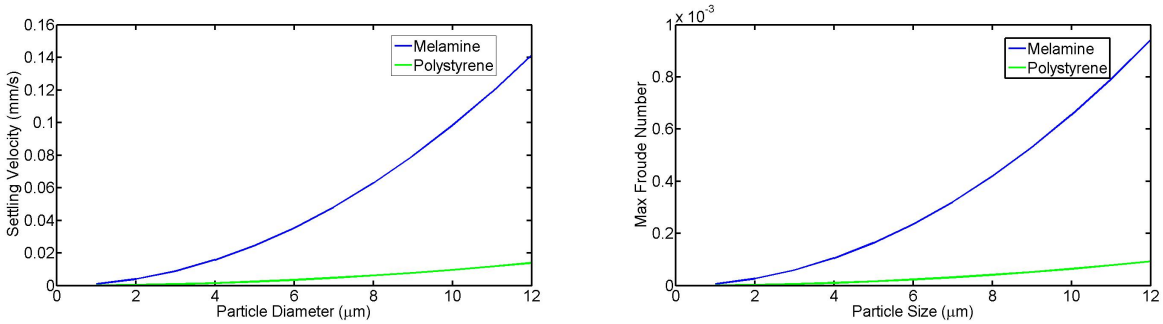

Figure 4.4: Settling velocity (left) and accompanying Froude number (right) for the melamine particles compared to the previously used polystyrene particles.

For a 4 μm particle, the melamine settling terminal velocity was ~0.015 mm/s. At 10,000 Hz frame separation time is 0.1 ms. Thus, the particle will settle 0.0015 μm between each frame pair, which is equivalent to 2.2×10^{-4} pixels. As discussed in section 5.12, even the most optimistic claims of PIV subpixel resolution are around 1.0×10^{-2} pixels. Thus, the settling velocity is 2 orders of magnitude smaller than the resolution of PIV, and can be neglected.

SEM images of the melamine particles and the absorption/emission spectra for Rhodamin B is shown in Figure 4.5.

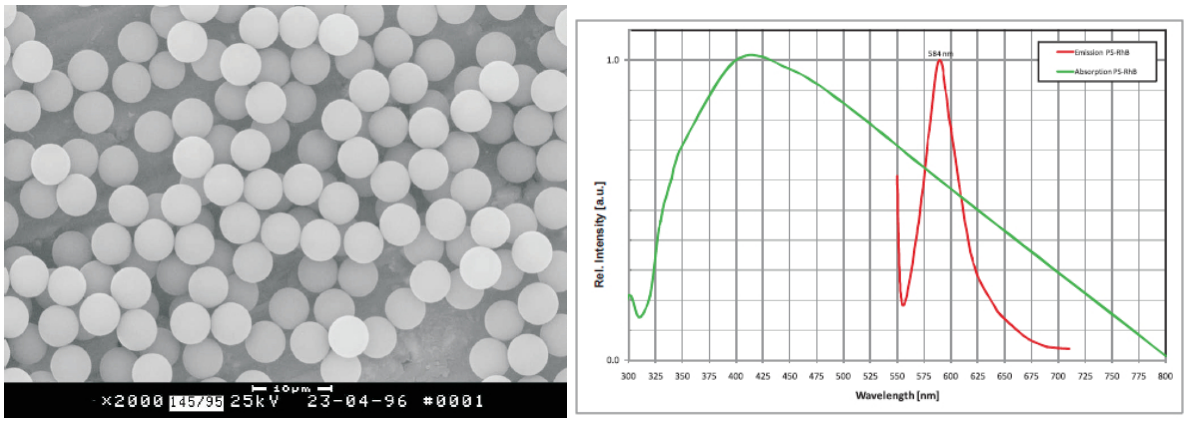

Figure 4.5: SEM images of melamine particles (left) and absorption/emission spectra from Rhodamin B (right) (Reprinted with permission from LaVision) [70].

4.3.4 Particle Intensity

The melamine particles fluoresce, but the intensity for 5 μm particles was observed to be similar to that of the 3 μm particles made of polystyrene that had been used previously. However, the intensity was acceptable, and could even be reduced if necessary, and particles sizes as low as 2 μm could be used and still maintain a signal to noise ratio well above the minimum of 2:1 as shown in Table 4.2. However, a signal of noise ratio of greater than 10 is ideal, so 4 μm particles were chosen as an acceptable compromise between size

and signal. This higher signal to noise ratio increases the sub-pixel resolution of PIV, and also allows for simultaneous shadowgraphy images to be taken utilizing the lower dynamic range of the camera.

Table 4.2: Melamine particle parameters for various sizes.

Particle Size (μm^2)	Particle Area (μm^2)	Relative Area	Relative Intensity at Max Power	Estimated Signal / Noise at Max Power
1.0	0.8	0.0	0.1	0.9
2.0	3.1	0.2	0.4	3.6
3.0	7.1	0.4	0.8	8.0
4.0	12.6	0.6	1.4	14.2
5.0	19.6	1.0	2.2	22.3
6.0	28.3	1.4	3.2	32.0
7.0	38.5	2.0	4.4	43.6
8.0	50.3	2.6	5.7	57.0
9.0	63.6	3.2	7.2	72.1
10.0	78.5	4.0	8.9	89.0
11.0	95.0	4.8	10.8	107.7
12.0	113.1	5.8	12.8	128.2

4.3.5 Particle Settling, Deposition, and Agglomeration

The water used to fill the loop was seeded with the melamine particles, and then injected into the loop. During heat-up using the preheater at full power of 2 kW (~300 kW/m^2), the particle seeding density dropped. This is shown in Figure 4.6 that shows the initial seeding density, and the final seeding density after reaching 85 °C, where the seeding density has dropped an order of magnitude. The time between the start of heat-up to reaching 85 °C was approximately 90 minutes. The flow was kept at a constant 500 $kg/m^2/s$.

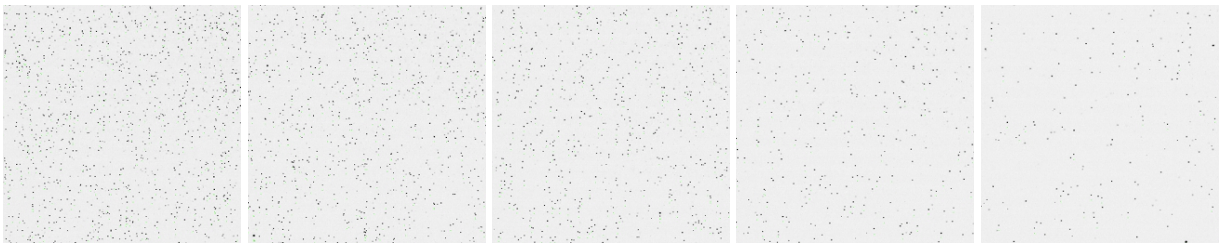

Figure 4.6: Particle density during heat-up. From left to right 25, 40, 55, 70, and 85 °C.

After reaching 90 °C, the pump was run up to full speed for about 10 seconds and seeding was restored to near the original concentration, also there was no apparent agglomeration of particles. This process was repeated several times over the course of 30 minutes. The particle seeding density did slightly decrease after each attempt as shown in Figure 4.7.

Even with the preheater secured, there is a decrease in particle seeding density as shown in Figure 4.8.

Figure 4.7: Particle density after pump shifts at 90 °C. Time evolves from left to right over approximately 30 minutes.

Figure 4.8: Particle density with preheater secured over 20 minutes, time evolves from left to right.

4.4 PIV Image Processing

4.4.1 Masking PIV regions using HSV

The dynamic range of the HSV camera was split and used to take simultaneous high speed shadowgraphy and PIV. Then the shadowgraphy was used to mask off the image going through the PIV routine so as to not to calculate vectors in regions with a bubble. The routine was based upon an edge detection algorithm, that then used some image processing to fill in the rest of the bubble region. The processing of the masks was done within MATLAB and then the images were input into DaVis as a mask for vector calculation. The algorithmic mask was also used to mask out the wall to prevent vector calculations in the wall area where there was no flow. Similar masking concepts have been implemented before [71].

First, a high pass filter was used to only allow particles and the brighter background to pass as an unmasked region and this also bi-linearized the image as to only include pixels as either 0 or 1. Then a median filter was applied, which goes through the image on a defined pixel scale size, and replaces each region with the median of the nearest neighbor regions. This completed the edge detection; however, a bubble may have a lens flare in the middle that is also detected as an edge. This would mean that a spot in the middle of the bubble was still unmasked. This was removed by taking any unmasked regions that were fully encompassed by a masked off region and adding them to the masked region. The results of the various masking stages are shown in Figure 4.9.

Each data set needed to have specific parameters tweaked for the specific lighting conditions and bubble sizes for that case to get an appropriate mask. The specific mask settings for each file are shown in Table 4.3.

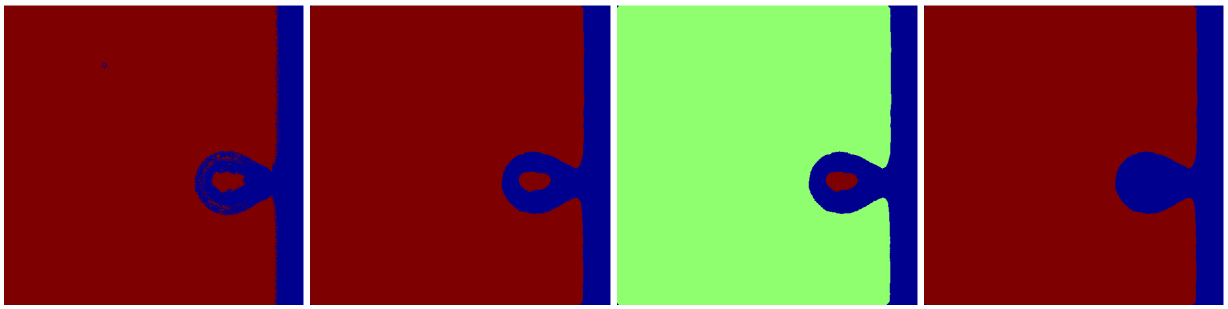

(a) High pass (b) Median (c) Enclosed (d) Final

Figure 4.9: Visual results of the various mask processing stages.

Table 4.3: Mask settings for each PIV file.

File Name	Sub-cooling (°C)	Mass Flux (kg/m^2/s)	High Pass Cutoff	Median Filter N Pixels	Cluster Minimum Pixels
480	5	133	110	20	4
485	5	250	130	15	4
492	5	350	130	15	4
494	10	209	110	10	4
502	10	250	110	10	4
511	10	350	110	10	4
468	15	192	140	15	4
473	15	250	150	15	4
476	15	350	150	10	4

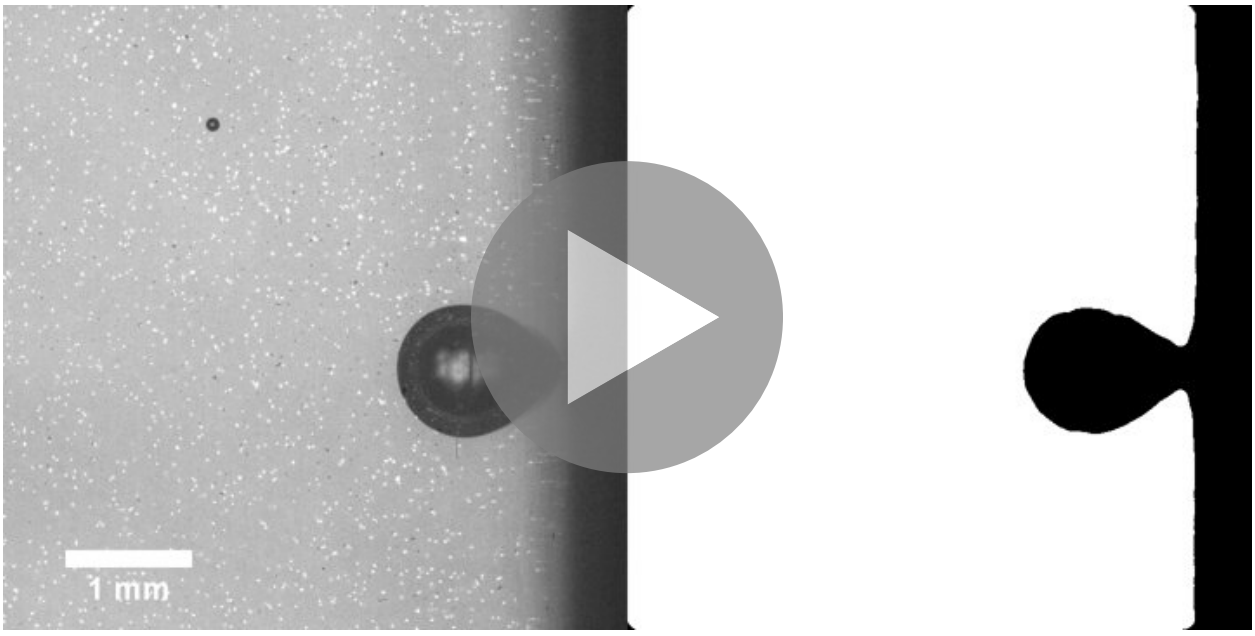

Figure 4.10: Example video of masking with source image (left) and the mask applied to PIV vector calculations (right).

4.4.2 PIV Vector Processing Parameters

The PIV vector processing parameters used in DaVis 8.2 to calculate the vectors are discussed in this section. The ”PIV time-series” operation was used as the single operation in the operation list. Time series cross-correlation was set to use the previous result as a reference shift, and was restricted to 5 pixels.

Image pre-processing was performed to subtract sliding background on a 4 pixel length scale. Then 20 counts were subtracted to remove the background noise from unmasked regions. Particle intensity was normalized on a 4 pixel scale. 4 pixels were used as the size scale since this is the size scale of particles. The value of 20 counts was subtracted as this was observed to remove the background lighting levels.

Masks were defined as a geometric mask, and a mask loaded from disk. The geometric mask was used to mask out the wall, and the first full first pass vector from being calculated (32 pixels from the wall). This first vector was masked because it has a large uncertainty that is difficult to quantify, so it was omitted. The mask set to mask the bubble that was created in MATLAB and discussed in section 4.4.1 was applied as a mask loaded from disk. The masks were applied to all images. Advanced Mask settings were disabled.

The vector calculation parameters were set to use the defined masks. Cross-correlation was employed to calculate time resolved vectors for each image pair (1-2, 2-3, 3-4, etc.). Advanced data source settings were disabled. Multi-pass iterations were used with a first pass of a 32 x32 square pixel window with a 50% overlap of interrogation windows and 2 passes. The second pass was a 16 x 16 square pixel window, with a 50% window overlap and one pass. Image correction was disabled and high-accuracy mode for final passes was enabled. GPU processing was disabled. For multi-pass options the initial window shift was set to 0 pixels in both directions. The standard correlation function was used for both initial and final passes. Symmetric shift deformed interrogation windows were used. Multi-pass post processing was employed to use a 1x median filter to remove and replace vectors if the difference to average was >2 standard deviation of neighbors, groups of <3 vectors were removed, empty spaces were filled with interpolation, and a one time 3x3 smoothing filter was applied.

The vector post processing was enabled. The allowable vector range limit was disabled. Vectors were deleted if the peak Q <1.3. A two time median filter of strongly remove and iteratively replace vectors was used to remove the vector if the difference to average was >2 standard deviations of the neighbors and to reinsert if the difference to average was <2 standard deviations of the neighbors. Groups with less than 5 vectors were removed. Empty spaces were filled with interpolation, but “Fill-up all” was disabled. A two time 3x3 smoothing filter was applied. “Make mask permanent” was disabled.

4.5 Single Bubble PIV/IR Results

Videos of synchronized PIV and IR images for a minimum of 3 bubble cycles for the 5, 10, and 15 °C subcooling cases are shown in Figures 4.11, 4.12, and 4.13 respectively. The video must be clicked once to activate, and then clicked again (or the play/pause clicked) to start playing the video. The different mass fluxes may be selected by clicking the appropriate button to switch to the desired mass flux.

The scale of the IR video is set to match that of the PIV scale on the x-axis. Vector magnitude for the PIV is shown by the color scale on the right of the video, IR temperature is shown by the scale to the right of the IR image overlay. Water flow is from the bottom of the image to the top of the image. The playback speed is 10 Hz, while the recording rate was 10,000 Hz, so the videos are played back at $^1/_{1000}{}^{\text{th}}$ of real time. The recording rate of the IR images was at 2,500 Hz, thus 4 identical frames of IR data are seen for every frame of PIV data.

The 5 °C subcooling and 133 kg/m^2/s data are shown as a time series in Figure 4.14. Time = 0 was the initial bubble nucleation event. The initial growth phase proceeded very quickly and reached speeds of ~0.5 m/s and the bubble had more than doubled in diameter in the first 0.2 ms. By 0.5 ms the temperature effects of the bubble were seen. The IR camera took an image every 0.4 ms compared to the 0.1 ms of the high

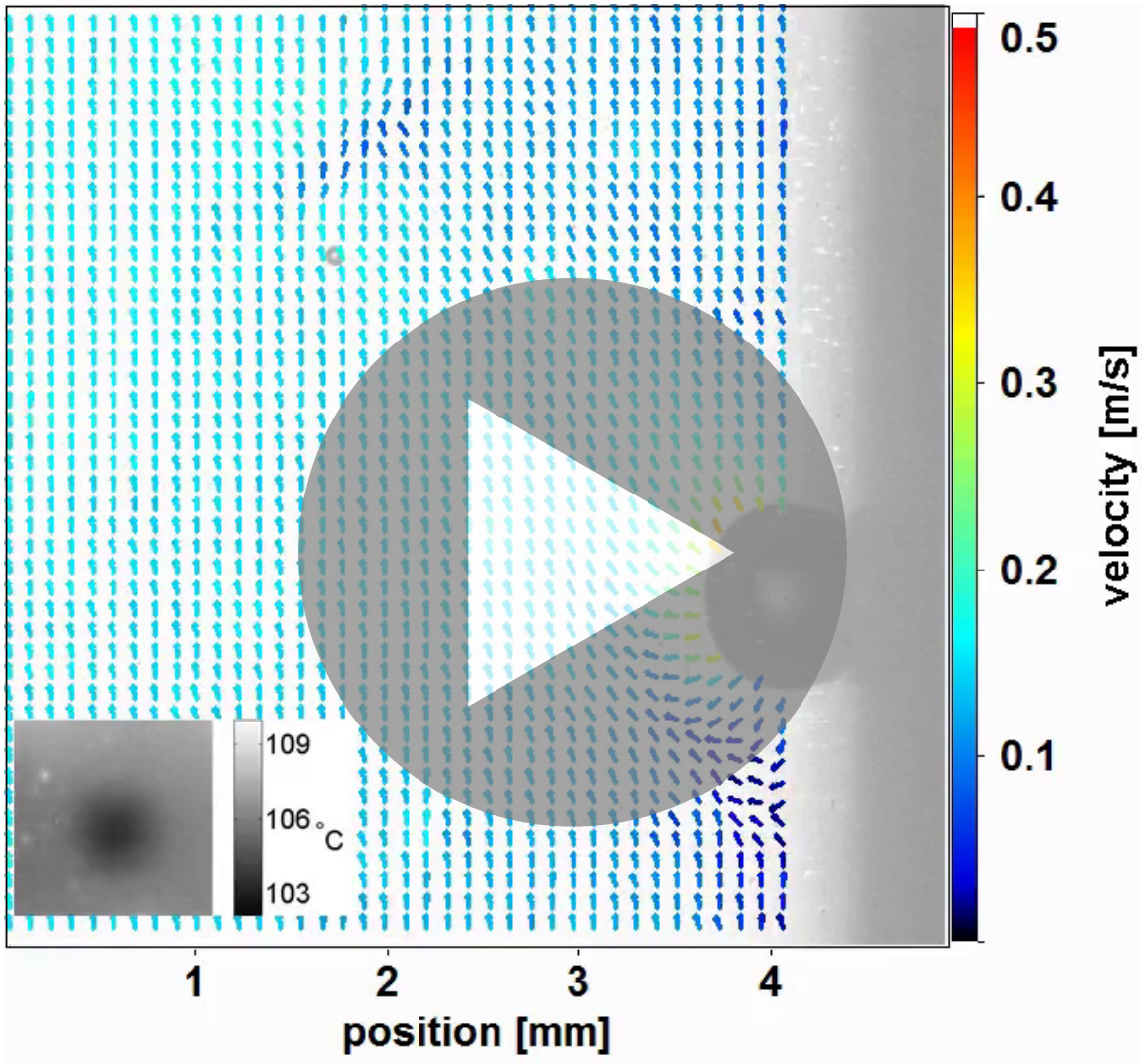

Play/Pause	G = 133 kg/m^2/s	G = 250 kg/m^2/s	G = 350 kg/m^2/s	G = 133 kg/m^2/s, Differential

Figure 4.11: Single bubble PIV videos for 1.05 bar, 5 °C subcooling, for 133, 250, and 350 kg/m^2/s.

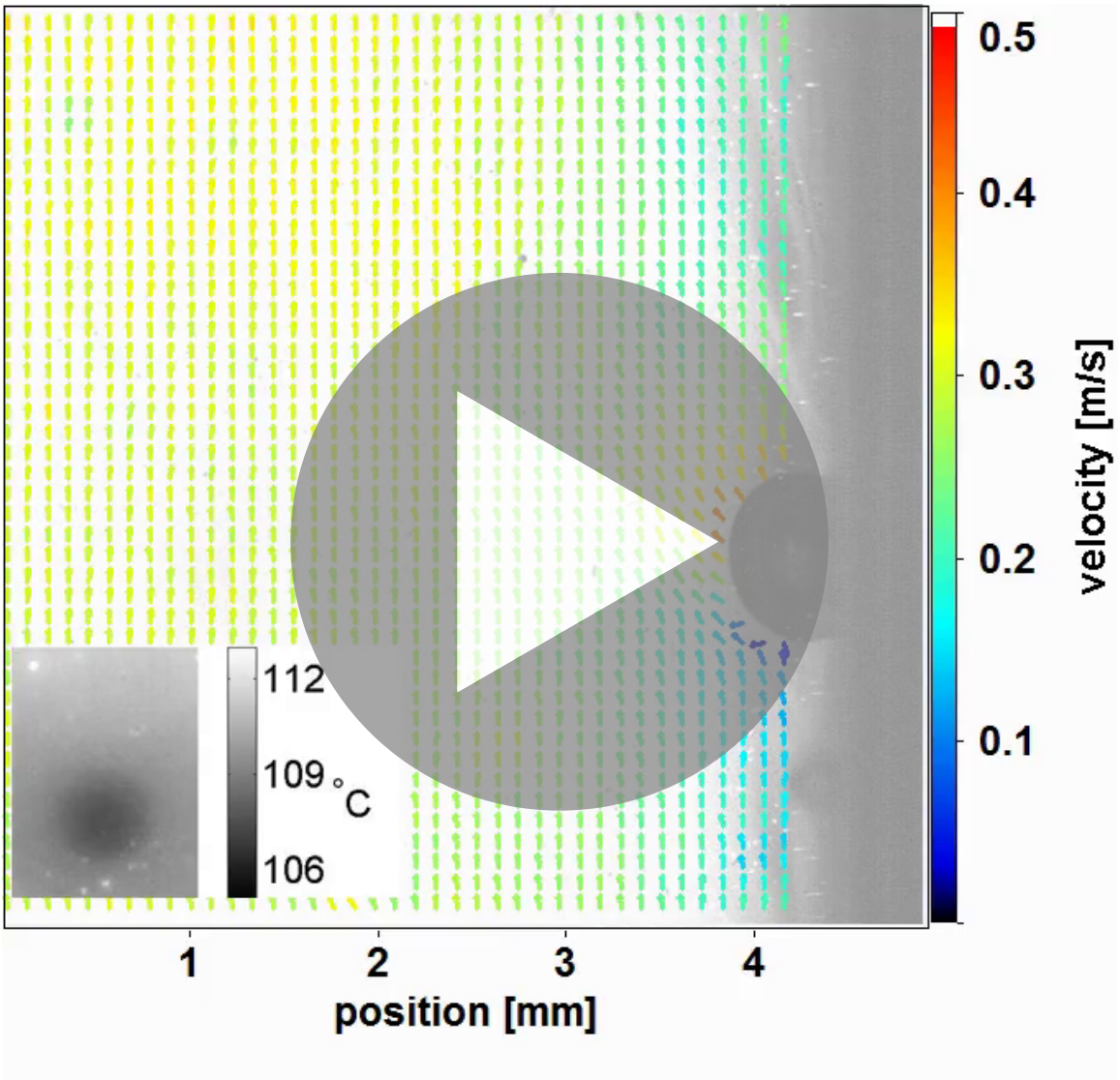

Play/Pause	G = 209 kg/m^2/s	G = 250 kg/m^2/s	G = 350 kg/m^2/s

Figure 4.12: Single bubble PIV videos for 1.05 bar, 10 °C subcooling, for 209, 250, and 350 kg/m^2/s.

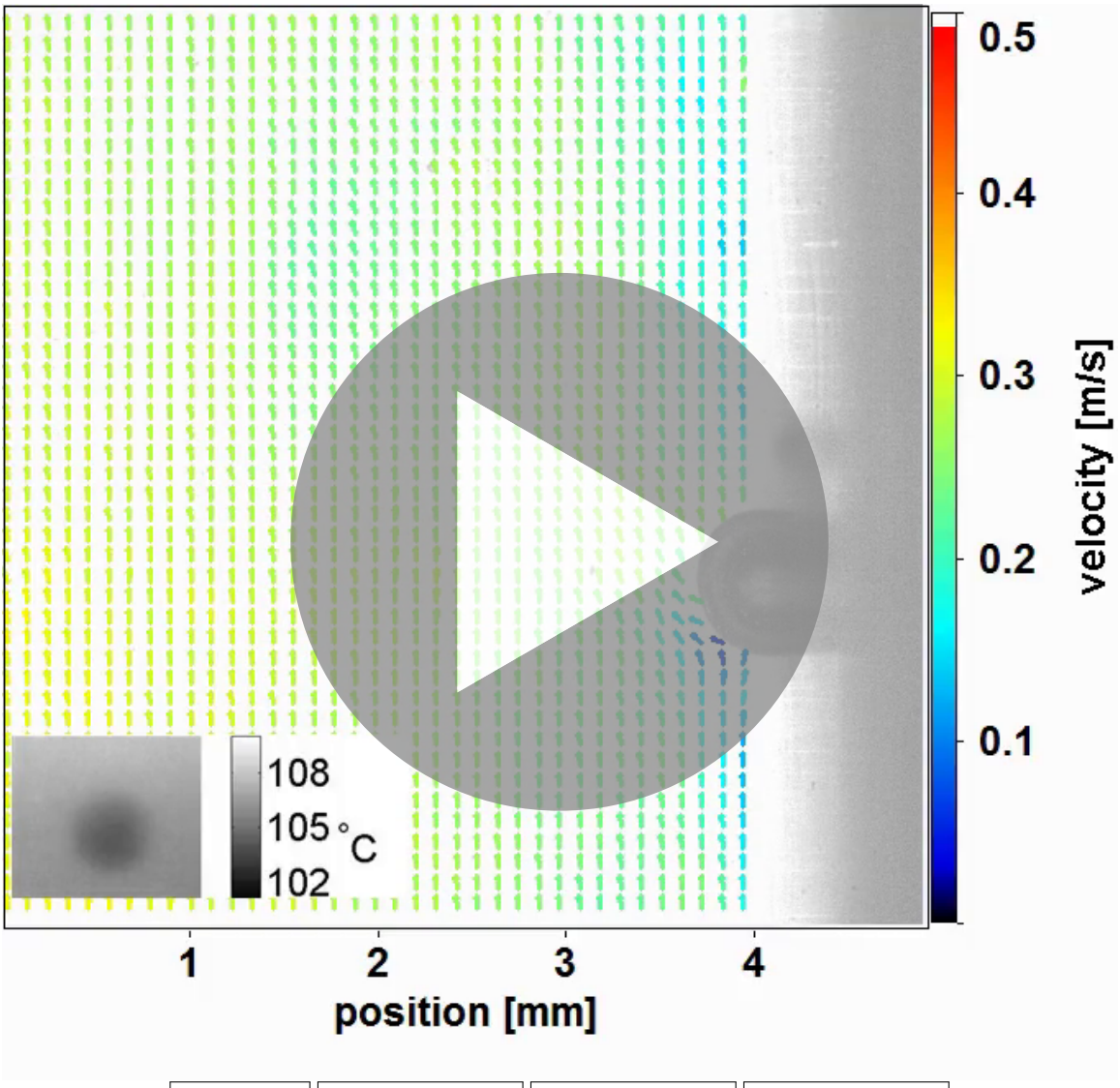

Play/Pause	G = 192 kg/m^2/s	G = 250 kg/m^2/s	G = 350 kg/m^2/s

Figure 4.13: Single bubble PIV videos for 1.05 bar, 15 °C subcooling, for 192, 250, and 350 kg/m^2/s.

speed camera. At 0.7 ms the bubble continued to grow and approximately doubled in diameter again. By 1.1 ms, the temperature underneath the bubble had dropped ~3 °C. By 1.5 ms the middle of the thermal footprint had begun to heat-up as the microlayer under the bubble evaporated and the triple contact line of the vapor, liquid, and the wall moved out away from the center of the bubble footprint. This left a dry region region in the middle of the bubble footprint that had poor heat transfer. The bubble growth rate was also slowing, and instead of pushing liquid away from the bubble, the bubble was acting as quasi-stagnant obstacle and the flow was forced around the bubble. The bubble was also extending into the bulk fluid, which was subcooled. Thus, condensation was occurring on the outer interface, which also slowed the bubble growth. At 2.4 ms the bubble had started to neck at the wall as the shear lift force became dominant, and began to pull the bubble away from the wall. Also during this time, the bubble footprint had shifted up in the direction of flow due to drag forces on the bubble. An asymmetric thermal footprint was also created as the bubble was pushed upwards. The bubble continued to neck at the wall and departed at 3.4 ms. The wall began to heat back up to the bubble's nucleation temperature of ~105.9 °C. The bubble departed, entered the bulk fluid, and then rapidly collapsed due to the subcooled fluid. The collapse initiated at the bottom hemisphere of the bubble that was being impinged by subcooled liquid. The collapsing front was ~0.5 m/s at its peak.

The temperature profile underneath the bubble is shown in Figure 4.15. Each point in the line profile was averaged over 3 pixels in the direction normal to the profile line to smooth the data. The shift in the bubble in the direction of flow can be seen in the asymmetry of the the temperature profile as time evolves. This asymmetry differs from pool boiling where the bubble tends to have a very symmetric footprint as it grows and departs [69].

Initially, the profile is nearly flat and symmetric. There was a slight increase in temperature in the direction of the flow as would be expected as the fluid heats as it travels over the heater. Then the bubble nucleated and the temperature dropped under the bubble as vaporization occurred. The temperature under the bubble reached a minimum value due to thermal diffusion from the substrate to the surface. This is a similar phenomenon to the sliding bubble as discussed in section 3.6.3. Then the bubble growth was slowed as it extended past the thermal boundary layer and condensation occurred on the surface of the bubble protruding into the bulk flow. During this time the bubble was shifted slightly in the direction of the flow due to drag forces, and caused additional wall cooling to take place downstream of the bubble. The bubble then departed and the temperature of the surface began to rise until the nucleation temperature was reached once again, and the cycle repeated.

Figure 4.11 has an additional video of the 5 °C subcooling and 133 kg/m^2/s mass flux case where the time averaged velocity profile without bubble growth and departure was subtracted from the instantaneous velocity vectors for flow with a bubble. The time average profile without a bubble was calculated by the velocity field for conditions just below ONB. In the case of the 5 °C subcooling and 133 kg/m^2/s mass flux, the prior to ONB data was taken at a heat flux of 56.7 kW/m^2 compared to the 77.7 kW/m^2 for the case with the bubble nucleation. The time averaged values for the no bubble case along with the time averaged profile for with a bubble are shown in Figure 4.16. The case with a bubble was averaged over 30+ bubble cycles, and includes the entire bubble cycles.

The spot of lower velocity in Figure 4.16 (b), was due to a contaminant on the lens that was inside the packaged lens, and could not be cleaned. Normally, this would not be in focus, but because of the use of extension rings to increase magnification, it is both in focus and magnified. However, the spot is present in both data sets – the one without the bubble and the one with the bubble – and thus the error should cancel when performing the subtraction of the instantaneous velocities from the averaged velocities.

The instantaneous velocities for a bubble nucleation had the average velocity profile subtracted from them, and this shows the velocity deviations caused by the bubble relative to the developed flow. The vectors in this case are close to zero if the bubble is not influencing the fluid flow at a given location. To give a better visual indication of the bubble influence on the fluid flow, vectors in this case had their size scaled to their velocity as well as having a color scale for velocity. This information can be used to determine the bubble

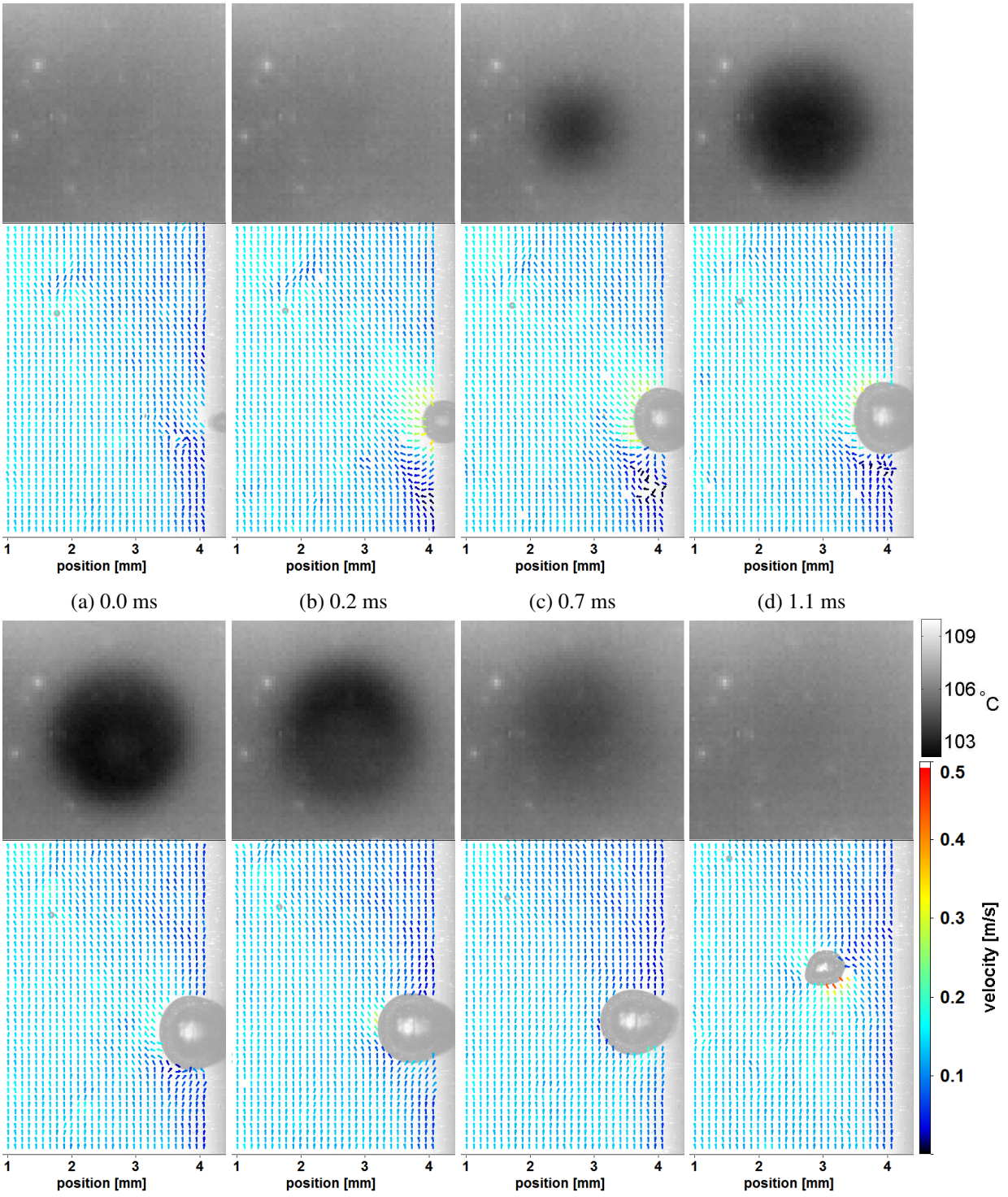

(a) 0.0 ms (b) 0.2 ms (c) 0.7 ms (d) 1.1 ms

(e) 1.5 ms (f) 2.4 ms (g) 3.4 ms (h) 7.4 ms

Figure 4.14: Single bubble PIV time series for 1.05 bar, 5 °subcooling, and 133 kg/m^2/s. The PIV has the scale below, and the IR image is 1 x 1 mm.

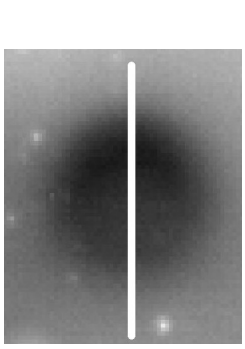

(a) Profile Line

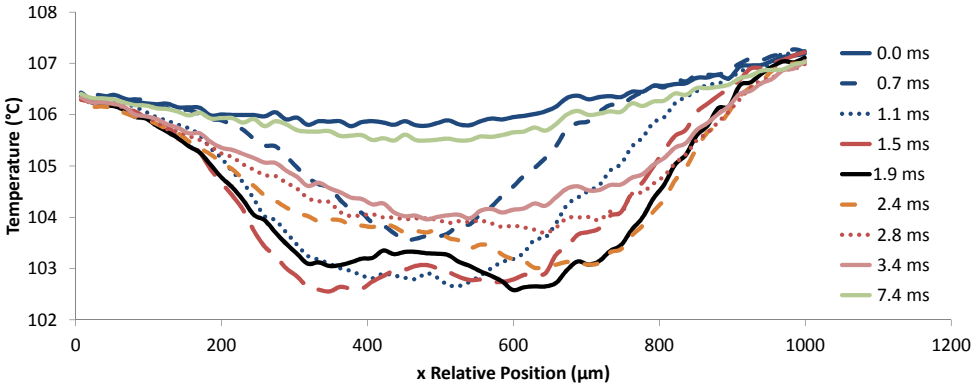

(b) Temperature Plot

Figure 4.15: Temperature profile under the first bubble evolved in time for 1.05 bar, 5 °subcooling, and 133 kg/m^2/s. The white line in (a) shows the profile line for the chart. In the IR image, flow is from the bottom to the top, and in the chart, the direction of flow is in the direction of increasing x.

growth front velocity and to see the range of influence during a bubble nucleation.

The change in the average velocity profile shown in 4.16 (c) with and without bubble nucleation shows the dramatic influence that bubble growth and departure has on the liquid velocities near the wall around the bubble. The area of influence of the bubble along the wall extends upstream beyond the 1.5 mm imaged prior to the nucleation site, where the flow is slowed due to the bubble being an obstacle. The influence extends down stream and away from the wall as the bubble departs and moves into the bulk flow.

The bubble front velocity was calculated by taking the average of the magnitude of the vectors at the bubble front. The velocity was then smoothed with a moving average filter with a span of 5 values. The velocity for the 5 °C subcooling and 133 kg/m^2/s mass flux case is shown in 4.17. Time = 0 was the bubble nucleation and the velocity is plotted as a function of time until bubble departure. The bubble front velocity peaked at ~0.5 m/s at ~0.6 ms. The bubble front velocity began to slow as the bubble extended past the thermal boundary layer and condensation occurred at the outer edge of the bubble. The velocity front for all three bubble cycles was consistent.

The single bubble growth and wait times and the standard deviation of the distribution of the values are listed in Table 4.4. The seemingly odd trend in the wait time with increasing mass flux was due to the fact that the heat flux changed between mass fluxes. The heat flux is adjusted at each condition to give ONB conditions for a single nucleation site with a specific nucleation temperature. At higher mass fluxes the bubble departed earlier and removed less heat from the wall, and thus the wall required less time to reach the nucleation temperature and resulted in a shorter period. There is a competing effect of the increased heat transfer from the increased mass flux, but the decreased two-phase heat transfer, and increased heat generation dominates.

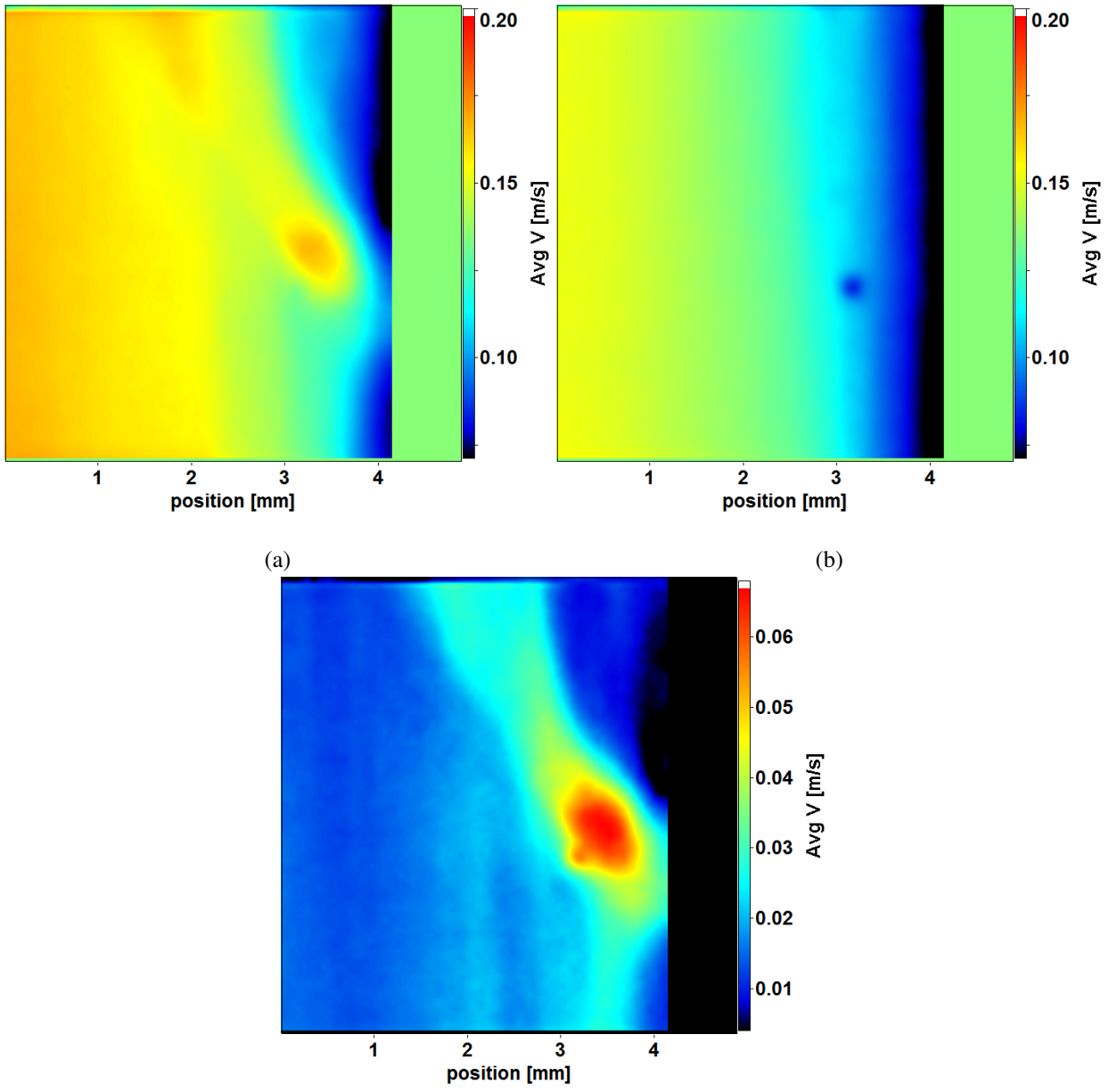

Figure 4.16: Average velocity magnitudes over time for 5 °C subcooling and 133 kg/m^2/s for (a) case with bubble nucleation, (b) case with heat flux just below bubble nucleation, and (c) Difference of case a - case b.

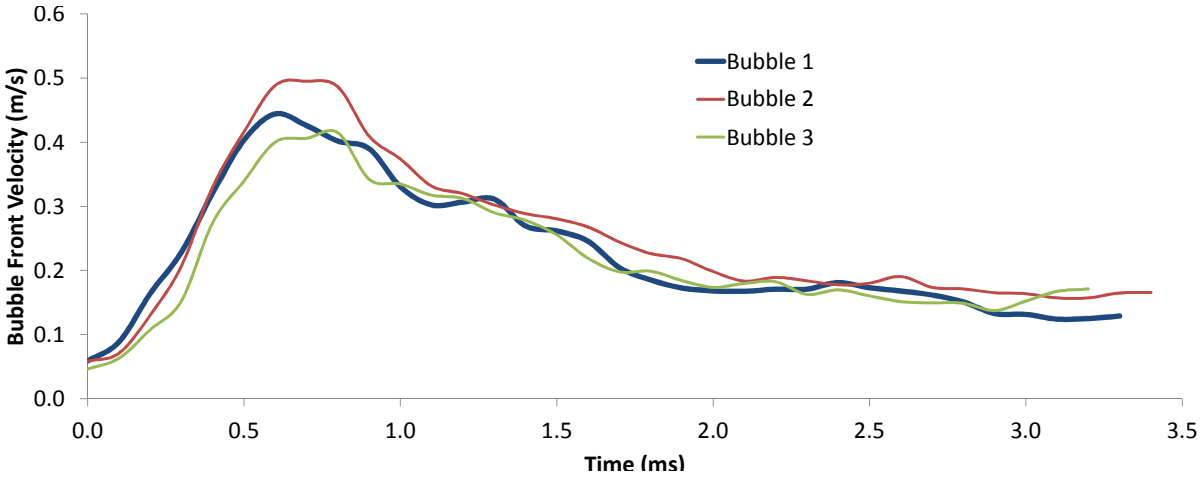

Figure 4.17: Bubble front velocity versus time for 1.05 bar, 5 °C subcooling, and 133 kg/m^2/s.

Table 4.4: Growth time, wait time, and period in ms.

	Growth	Wait	Period	Growth Stdev	Wait Stdev	Period Stdev
5 °C Sub						
133	1.40	10.0	11.6	0.79	0.73	0.58
250	0.68	5.15	5.88	0.15	0.24	0.31
350	0.36	2.68	2.98	0.17	0.22	0.24
10 °C Sub						
209	1.06	7.48	8.50	0.19	1.68	1.85
250	1.38	6.68	8.00	0.30	0.76	0.70
350	0.84	3.33	4.10	0.18	0.35	0.45
15 °C Sub						
192	1.10	7.95	9.20	0.53	0.30	0.47
250	0.90	2.85	3.80	0.16	0.17	0.22
350	0.54	2.28	2.85	0.17	0.15	0.17

4.6 Heater Surface Characterization

4.6.1 Heater Wettability

The influence of PIV particle deposition on the heater surface was investigated. During PIV testing, particles fell out of solution, and also preferentially deposited on the heater surface during boiling. The duration of the tests where the heater was boiling was only a few hours, and the heater was cleaned with acetone after each day's testing. The contact angle of the surface with PIV particles on it was measured and compared to the contact angle of the heater in other conditions. The contact angle has a strong affect on the bubble nucleation on a surface. The higher the contact angle the less free energy it takes to nucleate a bubble on the surface [12]. Also, the contact angle of the surface affects what nucleation sites are active when the surface is flooded. The higher the contact angle, the larger the number of active nucleation sites on the surface.

Wettability measurements were taken on a new heater cleaned with acetone (New Heater), PIV particle coated heater (PIV Particles), PIV particle coated heater after setting in air for ~2 weeks (PIV Aged), PIV particle coated heater after acetone cleaning (PIV Cleaned), a used heater never exposed to PIV particles after setting air for ~2 months (No PIV Aged), a used heater never exposed to PIV particles after acetone cleaning (No PIV Clean), and a used heater never exposed to PIV after setting in air for ~4 months (No PIV Aged). These cases are shown in Figure 4.18.

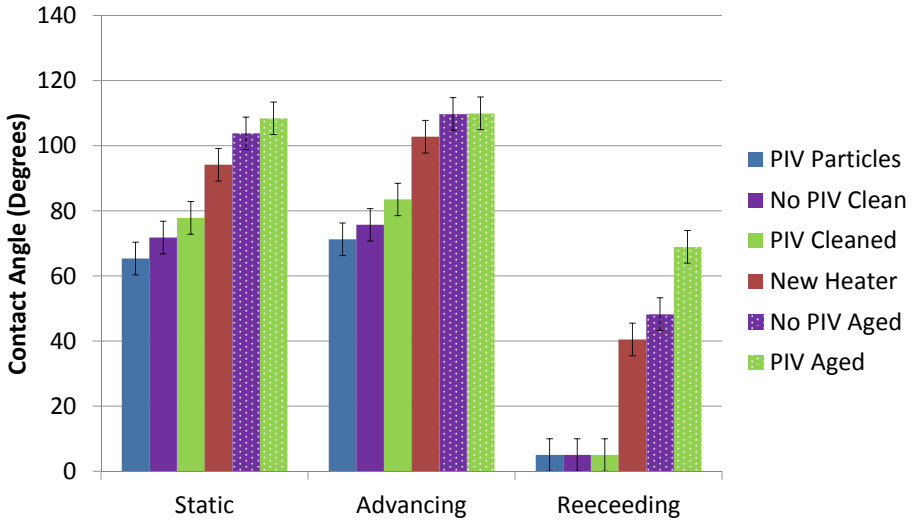

Figure 4.18: Contact angles for PIV particle coated heater and heaters in various other conditions.

There was a shift to lower contact angles after a heater was used from ~95° to ~70°. This was presumably from the change in the stoichiometry of the ITO after having a current passed through it in an oxidizing environment. Likely, the ratio of oxygen relative to indium and tin was increased, and lowered the contact angle. Then as the heater sat after being cleaned, the contact angles went up slightly (due to hydrocarbon absorption [72]) . After being cleaned with acetone, and the hydrocarbon buildup was removed, the contact angle dropped back to the lower contact angle that existed before the hydrocarbon adsorption. The contact angle of the heater surface for one with PIV particles and one after it has been cleaned of PIV particles were very close to the same value of the contact angle of a used heater that has been cleaned. This implies that there is little effect on wettability based on PIV particle deposition.

4.6.2 PIV particle Coating Thickness

The deposition of PIV particles onto the surface was quantified by taking a heater after a day of PIV testing and taking confocal microscope measurements using an Olympus LEXT OLS3000 Confocal Scanning Laser Microscope at Schlumberger-Doll Research. A fine point was used to wipe away a streak of the PIV particles, and then the surface was imaged with the confocal microscope. The height difference was measured from the results to quantify the thickness. The layer was measured to be 0.9 µm thick. Since the particles were 4 µm in diameter this implied that there was less than one monolayer of particles on the surface, and that deposited particles did not form a multilayer on the surface. Multiple layers of small particles can form a porous structure that can have a large influence in boiling characteristics [73]. An image of the depth measurement is shown in 4.19.

The roughness of a clean heater was also measured and the SRa was 0.081 µm +/- .015 µm for a bare heater. The roughness of the heater with PIV particles could not accurately be measured due to the particles interfering with the measurement, and yielding noisy data from reflections and fluorescence of the particles.

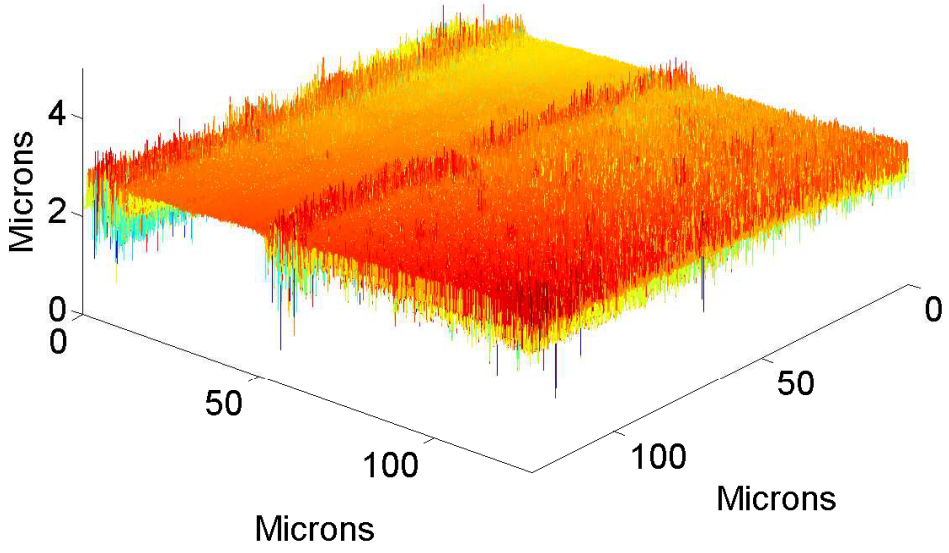

Figure 4.19: Image of PIV particle coated heater with scratch in the coating.

4.6.3 Boiling Curves

The effect of PIV particle deposition on boiling heat transfer was investigated. This was performed by starting with a clean heater and taking boiling curve measurements for 1.05 bar and 10 °C for mass fluxes of 500 and 1000 kg/m^2/s. Then a series of PIV measurements were taken, and then the boiling curve experiments were repeated with a PIV coated heater. The results are shown in Figure 4.20. The curves were within the experimental error, showing that there was not a significant change in the two phase heat transfer characteristics due to PIV particle deposition.

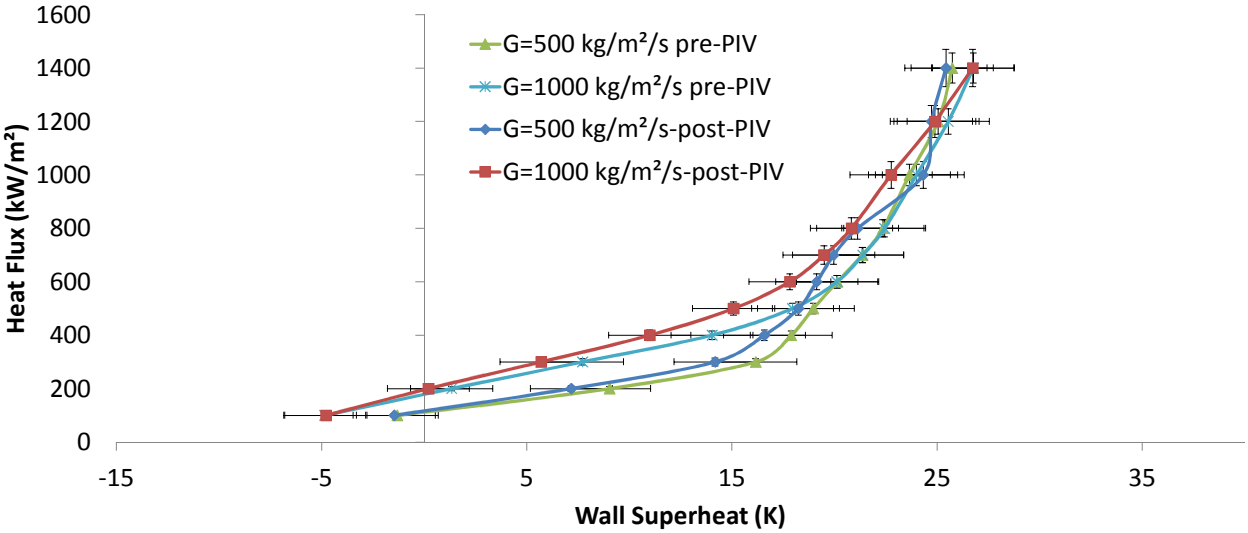

Figure 4.20: Boiling curves for pre-PIV particle depositon and post-PIV particle deposition

5 Uncertainty Analysis

5.1 Heat Flux

The heat flux is determined by measuring the current and voltage to the heater, and then calculating the heat input over the active heater area. The primary source of uncertainty is the uncertainty in the measured current, voltage, and the heater area. The uncertainty for the current as measured by the shunt resistor is 0.005 A, the uncertainty in the voltage is 0.005 V. The uncertainty in the area is due to measurement error as well as an uncertainty in the length of the heater due to the unique wrap around design, and the high thermal conductivity of the graphite electrodes. The error of the width is taken to conservatively be 0.1 mm, and the error of the length is taken to be conservatively 0.5 mm.

Propagating the uncertainty in the dimensions leads to an area uncertainty of 2.7%. For the smallest heat flux of 100 kW/m^2, which has the largest relative uncertainty, the measured current is 1.8 A, and the voltage is 11.1 V. Propagating the uncertainty for all three values leads to an uncertainty of 2.8%. The worst case heat loss from the back of the heater from natural convection of the air has been estimated to be 0.6 kW/m^2 for a heat flux of 100 kW/m^2, which is a 0.5% bias error. For 300 kW/m^2 and above, the bias error is estimated to be $<$1%.

5.2 Mass Flux and Velocity

The uncertainty of the mass flux comes from the Omega FTB-1422 turbine flow meter volumetric uncertainty. The meter was calibrated in lab and has a stated accuracy of 1.0% of reading as stated by the manufacturer. The uncertainties associated with fluid properties are taken to be negligible, so the only other uncertainty is the uncertainty in the area of the channel. The dimensions are known to better than 0.1 mm and are uniform within this range. Thus the uncertainty from the channel area is 1.05%. The propagated uncertainty is then 1.8%. The velocity is calculated from just the mass flux plus the water density, whose uncertainty may be ignored so the bulk velocity also has an uncertainty of 1.8%

5.3 Heat Transfer Coefficient

The heat transfer coefficient uncertainty is dependent on the uncertainty from the heat flux, the inlet temperature, and the average wall temperature from the IR. Propagating the uncertainty of the temperature yields an uncertainty in the ΔT of 2.24 °C. Taking a typical ΔT of 20 °C and propagating the uncertainty with the heat flux uncertainty yields a characteristic value of 11.5%. Specific uncertainty values for each case are reported in the heat transfer coefficient plots.

5.4 Inlet Temperature

The inlet temperature is measured with calibrated Omega 4-wire RTDs, model # PR-11-3-100-1/8-6-E, which are accurate to 0.35 °C. The inlet temperature was held constant within 0.5 °C during the experiments. Thus, a reasonable estimate of the inlet uncertainty is less than 1.0 °C.

5.5 Pressure

The Omega pressure transducers installed in the loop are accurate within 0.035 bar.

5.6 Bubble Departure Diameter

The two main sources of uncertainty in the bubble departure diameter measurement come from uncertainty in the calibration of the spatial resolution of the camera and the selection of the pixels to mark the diameter.

The spatial calibration of the camera is carried out by setting up the optics to a wide aperture of f/4 on a 200-mm lens, with 68-mm of extension rings. This creates a very narrow plane of focus, that can be used to ensure the optics are perpendicular to the plane being imaged. A known distance is measured using the camera and can be selected within about 5 pixels of 600, or approximately 0.8%. There is also an uncertainty with the camera being not quite perpendicular with respect to the interrogation plane. Based on the depth of field of approximately 2 mm, the distance from target to the focal plane of approximately 30 cm, and the vertical field of view of 25 mm, the maximum uncertainty is about 0.02 mm out of 25 μm or, approximately 0.1%.

The bubble diameter can reasonably be measured within 1 pixel, which is an uncertainty of 15 μm. For a bubble diameter of 200 μm this is an uncertainty of 7.5%, which is larger than the above mentioned alignment uncertainties, and can be taken to be the uncertainty in the measurement. However, the distribution of bubble diameters far exceeds this value, so the distribution standard deviation (stochastic uncertainty) is shown in the error bars in the plots instead of the uncertainty.

5.7 IR Surface Temperature

The IR Cameras have a precision that is typically better than 0.1 °C. However, the cameras are calibrated in-situ to a surface temperature from an Omega K-type thermocouple with a stated accuracy of 1.1 °C. On top of the thermocouple uncertainty is the uncertainty associated with the (often) non-linear calibration curve, and the variation from the polynomial fit, or the uncertainty from interpolation. This error is observed to be less than 0.8 °C. These errors all stack for an estimated error of 2.0 °C.

However, since the camera has a precision of better than 0.1 °C, and the uncertainty from the calibration and thermocouple measurement are minimal for a ΔT, the uncertainty of a ΔT within an IR recording has been observed to be 0.5 °C or better.

5.8 Nucleation Site Density

There are several potential forms of error in the methodology to determine the nucleation site density. The algorithm for site identification is discussed in detail in section 3.4.2. The first is from the choice of the heuristics for selecting a site. These include the signal cutoff value, the convergence criteria, and the maximum site size. These were varied to explore the sensitivity, and within the reasonable range of possible choices affected the outcome by about 8%. The cutoff value has to be restrictive enough to be able to distinguish at low heat fluxes between nucleation events and the thermal effects of a sliding bubble, but not so restrictive that sites are missed. There is also the uncertainty associated with camera spatial resolution. The spatial resolution of the pixels is 90 μm for the FLIR camera, and 36 μm for the IRC camera. As the site density gets higher, there will be more missed sites because of the increased likelihood of sites overlapping that are closer together than the resolution of the camera. Site densities are only reported if they are less than 2100 sites/cm^2 so that this effect is minimized.

The automatic MATLAB-based counting algorithm was validated by comparing it to manual counting and found to agree within 15%, the value reported as error bars in the plots.

5.9 Bubble Departure Frequency

The bubble departure frequency is determined directly from identifying nucleation sites using the previously discussed automated routine, and then examining each site across time to determine when it nucleates again. There are all the same input parameters that can be varied as there are to the nucleation site density routine, plus an additional parameter as to how far from a given identified nucleation site is treated as the same site for frequency determination.

Varying these parameters over a reasonable range of values has shown that the frequency will vary by around 10%. The automated routine has been compared for a small number of frames to hand determination of the bubble departure period, and for proper selection of the input parameters, the two methods are within 17%.

5.10 Bubble Sliding Velocity

The bubble sliding velocity is determined from the IR temperature distribution, and is calculated from the maximum cooling to the maximum cooling location. The IR camera temperature profile is used to calculate velocity since it is easy to do concurrently when determining sliding temperatures. This method also gives a 1:1 correspondence to a measured sliding temperature. When imaging with HSV from the side, it is not possible at moderate heat fluxes and higher to get a 1:1 correspondence between a sliding bubble on the IR and HSV. It is nearly impossible to determine sliding velocities on HSV at the heat fluxes that correspond to 1000 sites/cm^2.

The uncertainty in the spatial calibration is negligible as discussed in section 5.6 and can be ignored. The uncertainty in determining the distance is 1 pixel. The timing error of the camera is very small and can be neglected so the uncertainty is just one pixel (36 μm) divided by the path length (minimum of 400 μm) or $<$9%. The typical error is less than 9% since a typical path length is approximately 1 mm so a more typical error is 3.6%.

5.11 Camera Timing

The desynchronization and timing uncertainty of the HSV and IR cameras has been measured using an interference pattern created by pulsing IR and visible LEDs. The timing uncertainty of the cameras has been measured to be less than 1 μs/s. The desynchronization of the cameras has been measured to be ~300 μs for PIV, and $<$10 μs for HSV. For more details on measuring the camera timing uncertainty and the full results see Appendix F.

5.12 PIV Uncertainty

There are a few methods that have been used to quantify PIV uncertainty. One is to use laminar flow between 2 parallel plates and compare the measured velocity profile with the analytic solution as done by Adeyinka et al. [74]. Although this test section cannot be assumed to be a set of parallel plates, there is also a theoretical solution to laminar flow in a rectangular duct. Adeyinka et al. [74] had an aspect ratio was very high of 47.6 the dimensions of the channel was 12.6 mm x 600 mm and this situation is very close to infinite parallel plates.

Another method of Adeyinka et al. [74] was a free convection cell heat transfer cell that was heated on one side and cooled on another to set up a natural convection flow. The dimensions were 39 mm x 39 mm x 59 mm.

There are also theoretical formulations to estimate the uncertainty. The maximum velocity uncertainty at can be estimated as determined by Luff [75].

$$U_{i,j} = \frac{\Delta X_{i,j}}{R_p \Delta t} \tag{5.1}$$

$$\delta \Delta X_{i,j} = \left[(\epsilon_1)^2 + (\epsilon_2)^2 + (\epsilon_3)^2 \right]^{\frac{1}{2}} \tag{5.2}$$

$$\delta U_{i,j} = \left\{ \left[\left(\frac{\Delta X_{i,j}}{R_p \Delta t} \right) \delta \Delta X_{i,j} \right]^2 + \left[\left(\frac{\Delta X_{i,j}}{R_p^2 \Delta t} \right) \delta \Delta R_p \right]^2 + \left[\left(\frac{\Delta X_{i,j}}{R_p \Delta t^2} \right) \delta \Delta t \right]^2 \right\} \tag{5.3}$$

Where $U_{i,j}$ is the velocity at position i,j, $\Delta X_{i,j}$ represents the particle displacement, R is the photographic spatial resolution, and Δt is the time delay between laser pulses, ϵ_1 is figure of merit for the error associated with the relative displacement of the particles, ϵ_2 is a figure of merit associated with the error of out-of-plane motion of the particles, ϵ_3 is a figure of merit associated with the error from image displacement relative to particle image size. The above represents worst case errors and for typical PIV setups are ~7%.

Beresh used stereoscopic PIV [76] in multiple configurations to compare the results for a single flow case to verify uncertainty estimates. Hariharan et al. [77] performed the same nozzle experiment with the same conditions at three different laboratories and for typical turbulent flow conditions the inter-laboratory error was ~10%. This was only achieved after developing a set of standard operating procedures and best practices for PIV experiments.

In general PIV uncertainty estimates have been lowered as new processing algorithms have been developed. The estimates on error with newer processing techniques claim to have reduced errors from around one tenth of a pixel to as low as one one hundredth of a pixel [78, 79].

5.12.1 PIV Experimental Error Quantification

To verify the PIV setup and to get an estimate of the uncertainty in the PIV measurements for the setup, PIV was used to measure laminar flow conditions in the experimental loop. There is an analytic solution for fully developed laminar flow in a rectangular duct and this can be used to calculate the velocity profile. The equations for a rectangular duct are shown in (5.4)-(5.6) [80].

$$u = -\frac{16}{\pi^3} \left(\frac{dp}{dz} \right) \frac{a^2}{\mu_f} \sum_{n=1,3\ldots}^{\infty} \left[\frac{(-1)^{(n-1)/2}}{n^3} \left(1 - \frac{\cosh(n\pi y_g/2a)}{\cosh(n\pi b/2a)} \right) \cos\left(\frac{n\pi x_g}{2a} \right) \right] \tag{5.4}$$

$$u_m = -\frac{1}{3} \left(\frac{dp}{dz} \right) \frac{a^2}{\mu_f} \left(1 - \frac{192}{\pi^5} \left(\frac{a}{b} \right) \sum_{n=1,3\ldots}^{\infty} \left[\frac{1}{n^5} \tanh\left(\frac{n\pi b}{2a} \right) \right] \right) \tag{5.5}$$

$$f_s \mathrm{Re} = \frac{24}{\left(1+\frac{1}{\alpha_g}\right)^2 \left(1 - \frac{192}{\pi^5 \alpha_g} \sum_{n=1,3\ldots}^{\infty} \left[\frac{\tanh \frac{n\pi\alpha_g}{2}}{n^5}\right]\right)} \tag{5.6}$$

Where a and b are the half thickness of the channel dimensions, y_g and x_g are the locations within the channel in each direction, f_s is the friction factor, Re is the Reynolds number, α_g is the aspect ratio of the channel, μ_f is the fluid dynamic viscosity, and $\left(\frac{dp}{dz}\right)$ is the pressure gradient along the channel.

Equations (5.4) and (5.5) are developed from the derivation done by Marco and Han [81]. The equation for the velocity profile reported by Marco and Han is shown in (5.7).

$$u = -\frac{16}{\pi^4 \mu_f}\left(\frac{dp}{dz}\right) \sum_{m=1,3\ldots}^{\infty} \sum_{n=1,3\ldots}^{\infty} \frac{\sin\frac{m\pi x_g}{2a} \sin\frac{n\pi y_g}{2b}}{mn\left(\frac{m^2}{4a^2}+\frac{n^2}{4b^2}\right)} \tag{5.7}$$

The only assumptions are:

- Constant physical properties
- Velocity at the wall is zero

This can be applied to the test section used in these experiments to get the analytic solution for the flow. Figure 5.1 is the plot of (5.4)-(5.6) [80] for a rectangular duct of 10 mm x 30 mm which is the nominal size of the subcooled flow boiling test section.

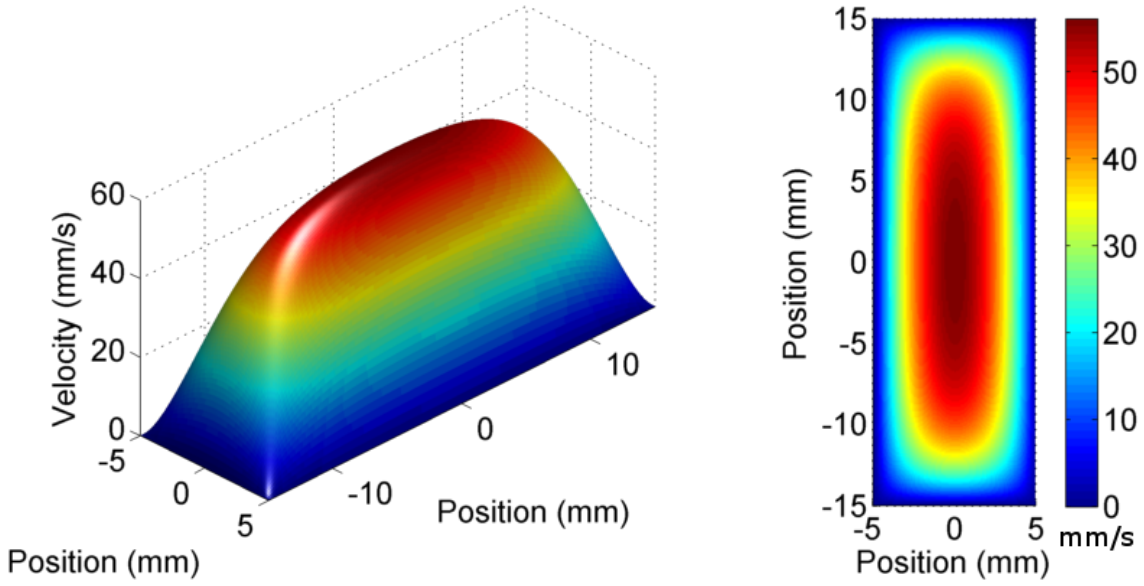

Figure 5.1: Velocity profile for rectangular channel of the quartz test section 10 mm x 30 mm Re=500, isometric view (left) and top view (right).

The loop was reconfigured to perform the PIV uncertainty quantification experiments, the reconfigured loop for these experiments is shown in Figure 5.2. Two solenoid valves were used to divert the flow and

collect the water in the reservoir. The mass of water in the bag, and the time to fill was used to calculate the flow rate for a given pump setting and valve configuration.

The seeding density for the experiments was approximately 0.5 ml, 1 wt% polystyrene particles per 1 gallon of water. The loop normally holds around 3 gallons, so that is about 1.5 ml per water change. The PIV uncertainty quantification experiment will has a large reservoir, holding at ∼10 gallons, so to seed that experiment, it took ∼7 ml.

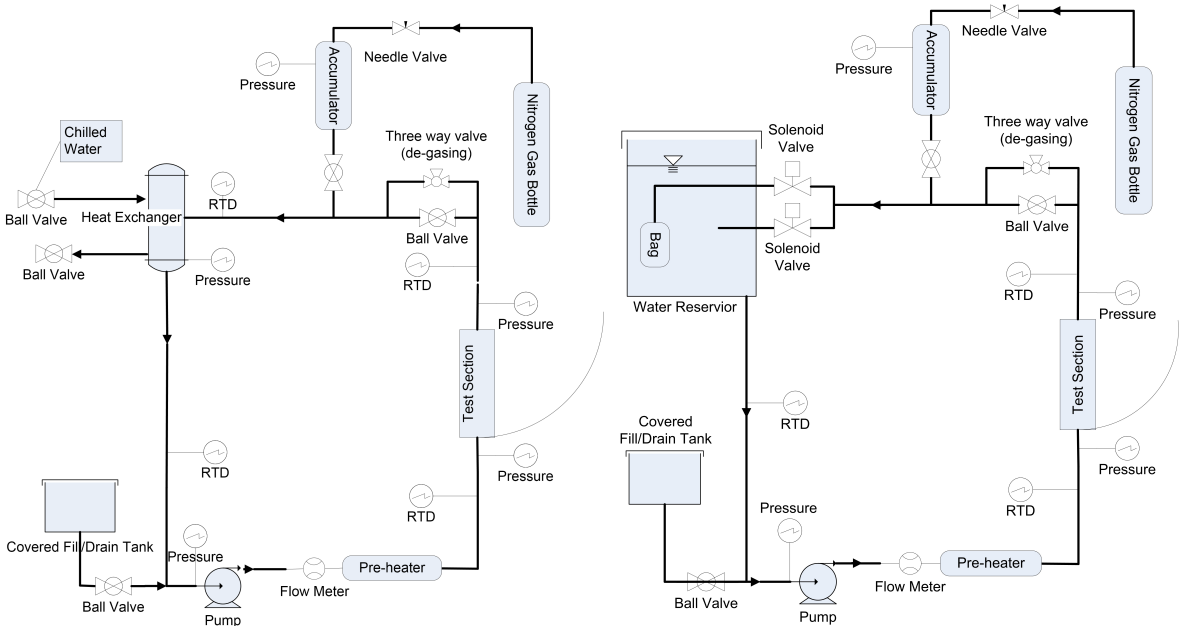

Figure 5.2: Diagram of the Loop in the configuration for running normal experiments (left) and for running PIV uncertainty quantification experiments.

The loop as modified is shown in Figure 5.3. The additions include the tank where the flow measurement occurs, 2 solenoid valves to redirect the flow, and PIV system. The solenoid valves either direct the flow into the tank, or into a bag that is under water within the tank. Both connections to the tank are at the same elevation. The solenoids are hooked up to a toggle switch so that one valve is always open (energized) while the other is closed (de-energized). The flow into the bag is timed and then weighed.

The bag was modified to have a bulkhead fitting through the bag that was attached to the outlet of one of the solenoid valves. The bag was then heat sealed so that the bulkhead fitting was the only entrance into the bag. The bag was weighed to get a reference weight for the bag and fitting. A stopper was placed into the inside hole of the bulkhead fitting from the outside of the bag. The dead leg of pipe on the bulkhead valve was then filled with water, and the bag was attached to the coupling inside of the reservoir.

When flow conditions were set as desired, the solenoid valves switched positions to direct flow into the bag, and the timer was started. After an appropriate amount of time (∼2 minutes) to fill the bag but not overfill it the timer was stopped and the solenoid positions were switched again to redirect flow into the reservoir.

The bag then had a stopper placed in it once again, and was removed from the reservoir. The dead leg of pipe was dumped back into the reservoir so that the only water in the bag was from the flow into the bag. The bag was then dried on the outside to remove all water weight that was not in the bag. Then the bag was weighed, and the net weight of the water was calculated, the corresponding flow rate was calculated, which was then converted to a Reynolds number and corresponding velocity profile.

The water from the bag was returned to the reservoir and PIV data was taken for the flow condition. Then

after the collection of PIV data, the flow rate was measured again using the same method to ensure the flow rate had not changed.

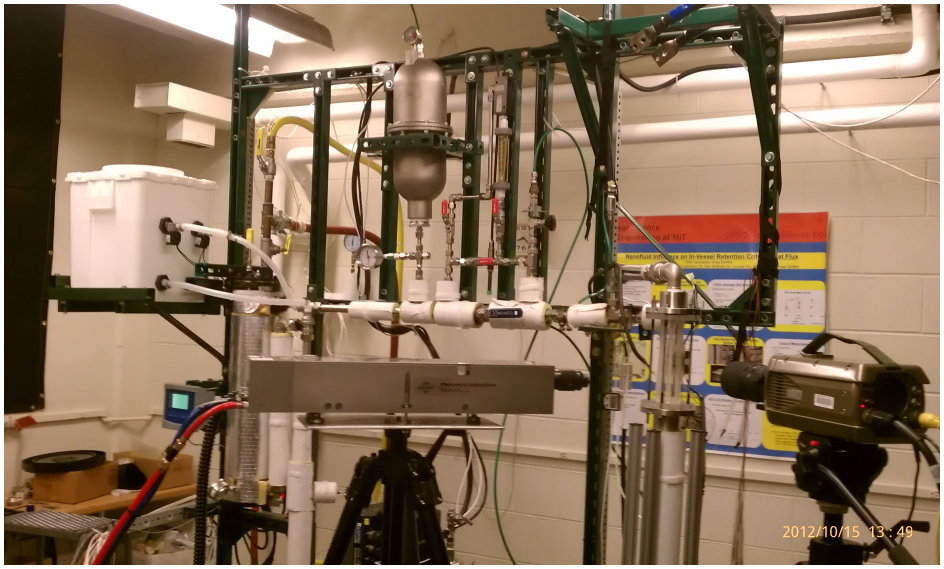

Figure 5.3: A characteristic velocity profile from the experimental data compared to the theoretical values.

Data was taken using the PIV for a flow rate of 0.318 gpm, this corresponds to a Reynolds number of 1058.

At a first attempt at taking the data, the error was found to be about 5% for the full scale velocity. Various experimental parameters were improved and tweaked. Laser alignment, camera alignment, focus was improved, and laser intensity was optimized. Also, improved masking for the velocity calculations. The camera was not perfectly aligned, but the angular offset was measured and the scale was adjusted accordingly. The laser alignment turns out to not be very crucial because the profile is fairly constant over more than 1.5 mm. This is also far more than the laser sheet width (~0.5 mm) so a constant velocity of the particles was observed without the laser perfectly centered on the channel. The error for the theoretical measurement is about 1.6% from the propagated error from temperature uncertainty and flow uncertainty. The experimental error is shown in Figure 5.5 and is ~4% of full scale.

However, all of the results are within 4% of the full scale value. Low velocities, especially near a wall are difficult to capture accurately because of the small pixel displacement of the particles. Thus, if the spatial resolution is 1/10 of a pixel, and the pixels next to the wall only move 1/10 of a pixel, this yields a 100% error. The results are shown in Figures 5.4 and 5.5, and error for theoretical value is represented by the line thickness, and for the Experimental is represented by the dot size.

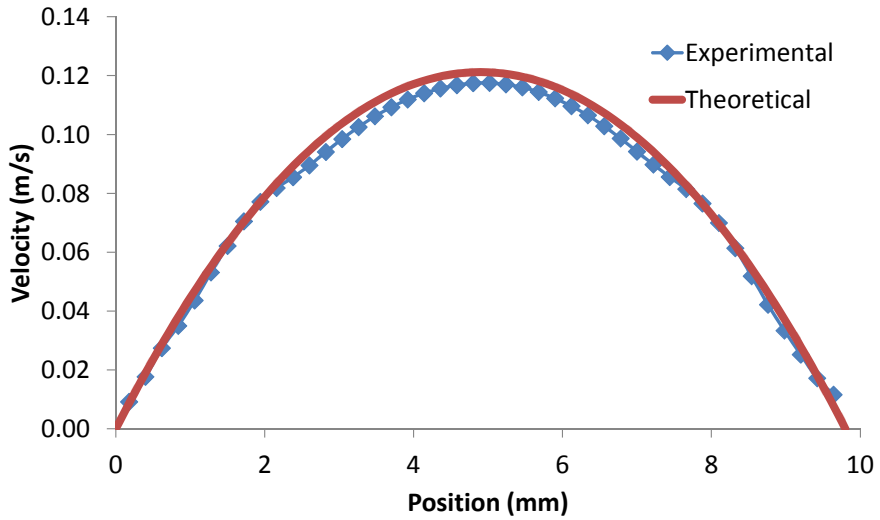

Figure 5.4: A characteristic velocity profile from the experimental data compared to the theoretical values for a Reynolds number of 1070.

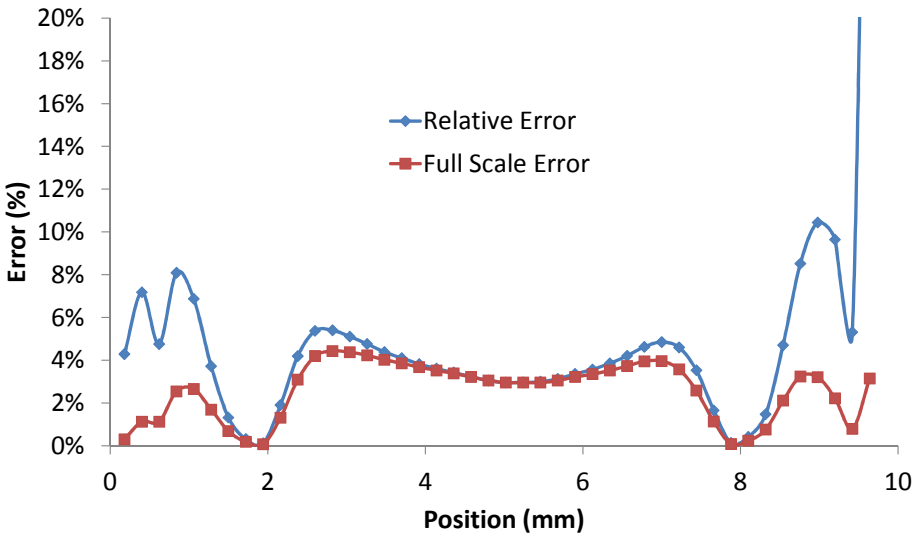

Figure 5.5: Error for velocity from theoretical for Figure 5.4.

5.12.2 PIV of Synthetic Images

Circular Shear Zone

To test the PIV processing algorithms used on the single bubble PIV data synthetic images were created. The images were created using DaVis 8.1.2 . The first set of images involves a circular shear zone that is shown in the video in Figure 5.6. This involves a circular zone in the middle spinning counter clockwise, while the fluid outside of this region is spinning clockwise. The width of the shear zone was varied to different pixel widths. This width is how many pixels it takes for the flow to reverse directions. The quicker the reversal occurs the more challenging the PIV processing is.

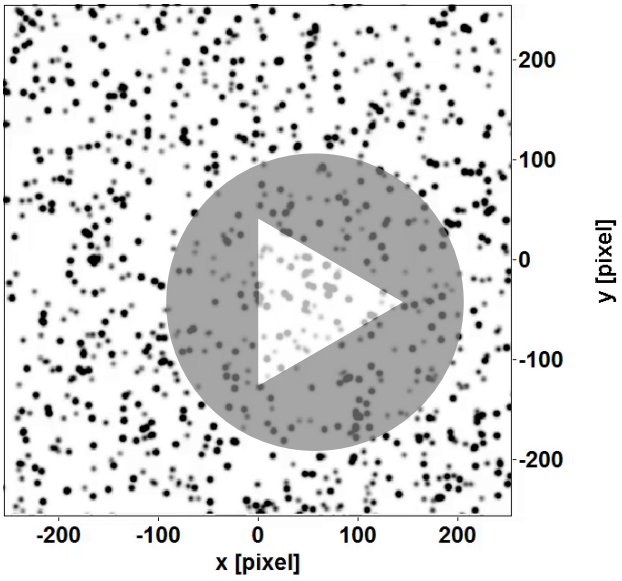

Figure 5.6: Video of synthetic image with circular shear zone, black dots are particles.

All of the other parameters were kept the same which are representative of the experimental conditions observed for the PIV single bubble. The displacement of the pixels was in the range of 5 pixels, particle size was 4 pixels, the particle seeding density was random at 0.0065 particles/pixel, the dynamic range of the particle intensities was 10-bit, the size of the image was 512x512 pixels, the reference vector grid was 16 pixels. The PIV processing parameters were the same as those used in the single bubble PIV data discussed in section 4.2.

The source vectors and calculated vectors for a 128 pixel wide shear zone is shown in Figure 5.7. The differences between source and solution for both a 128, 32, 16, and 8 pixel wide shear zone and are shown in Figures 5.8, 5.9, 5.10, and 5.11 respectively.

As the width of the transition zone decreases the error begins to climb, and when the shear zone transition becomes smaller than the interrogation window size as shown in Figure 5.11, the error will exceed 2 pixels in the region of the transition, which is ~30% error of full scale. However, when the transition zone is the same size scale of the interrogation window, error is ~10% of the full scale velocity.

Angular error of the vectors at the velocity reversal locations can be as much as 180°if the pixel displacement is ~⅕ of a pixel. For displacements that are ~1.0 pixel the angular error is bounded $<1°$.

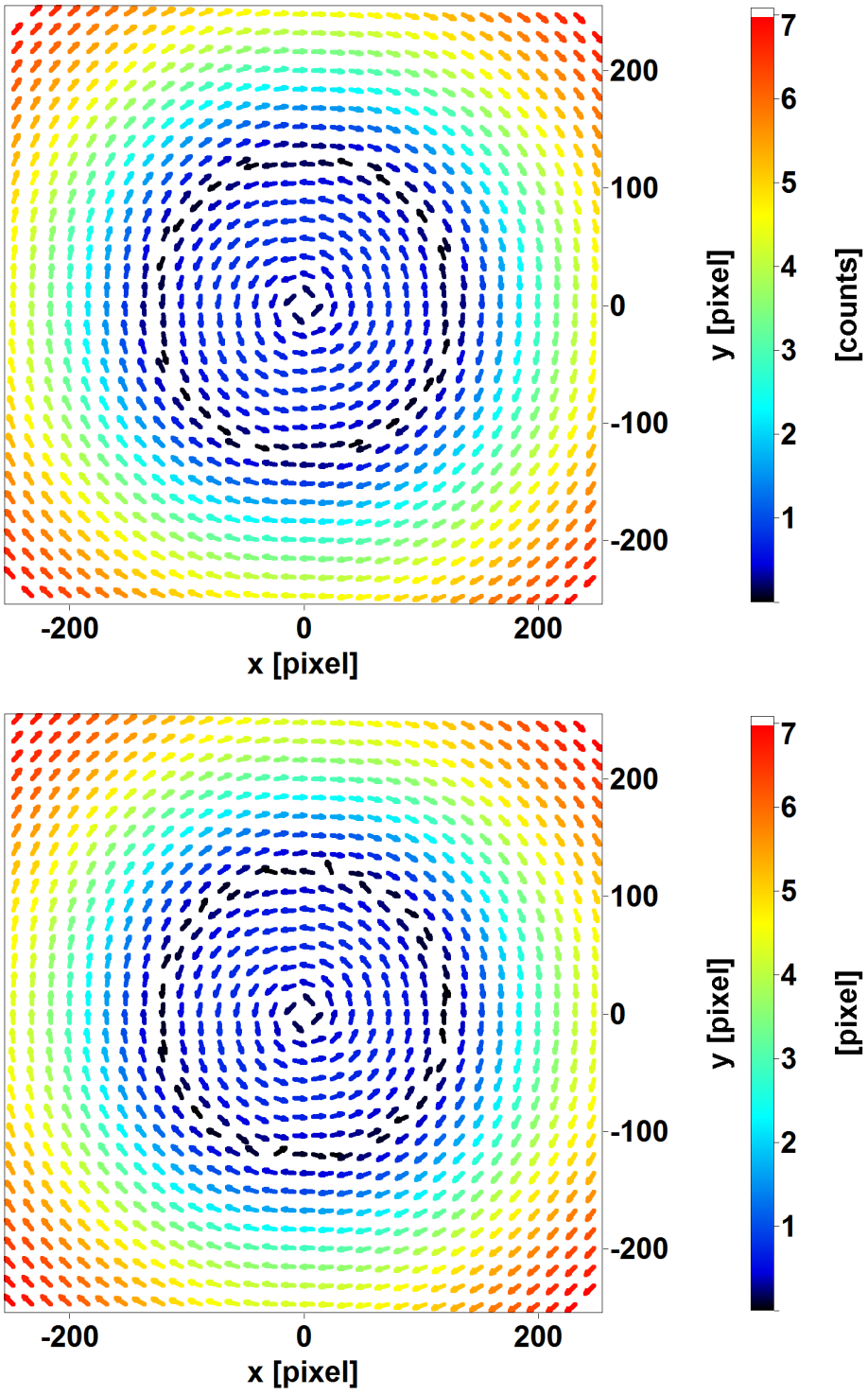

Figure 5.7: 128 pixel wide shear zone, source vectors (top), and calculated vectors (bottom).

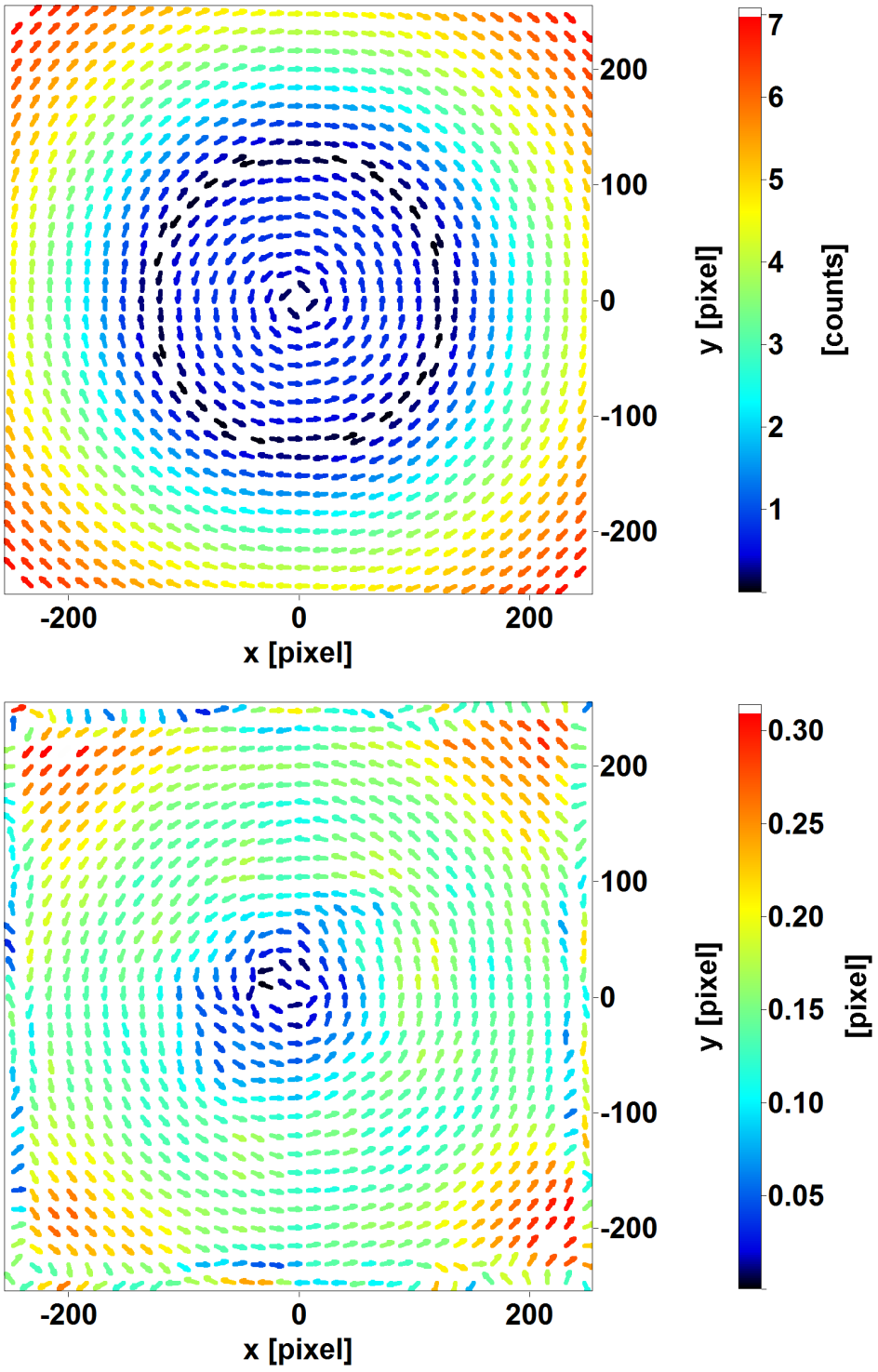

Figure 5.8: 128 pixel wide shear zone, source vectors (top), and difference from calculation (bottom).

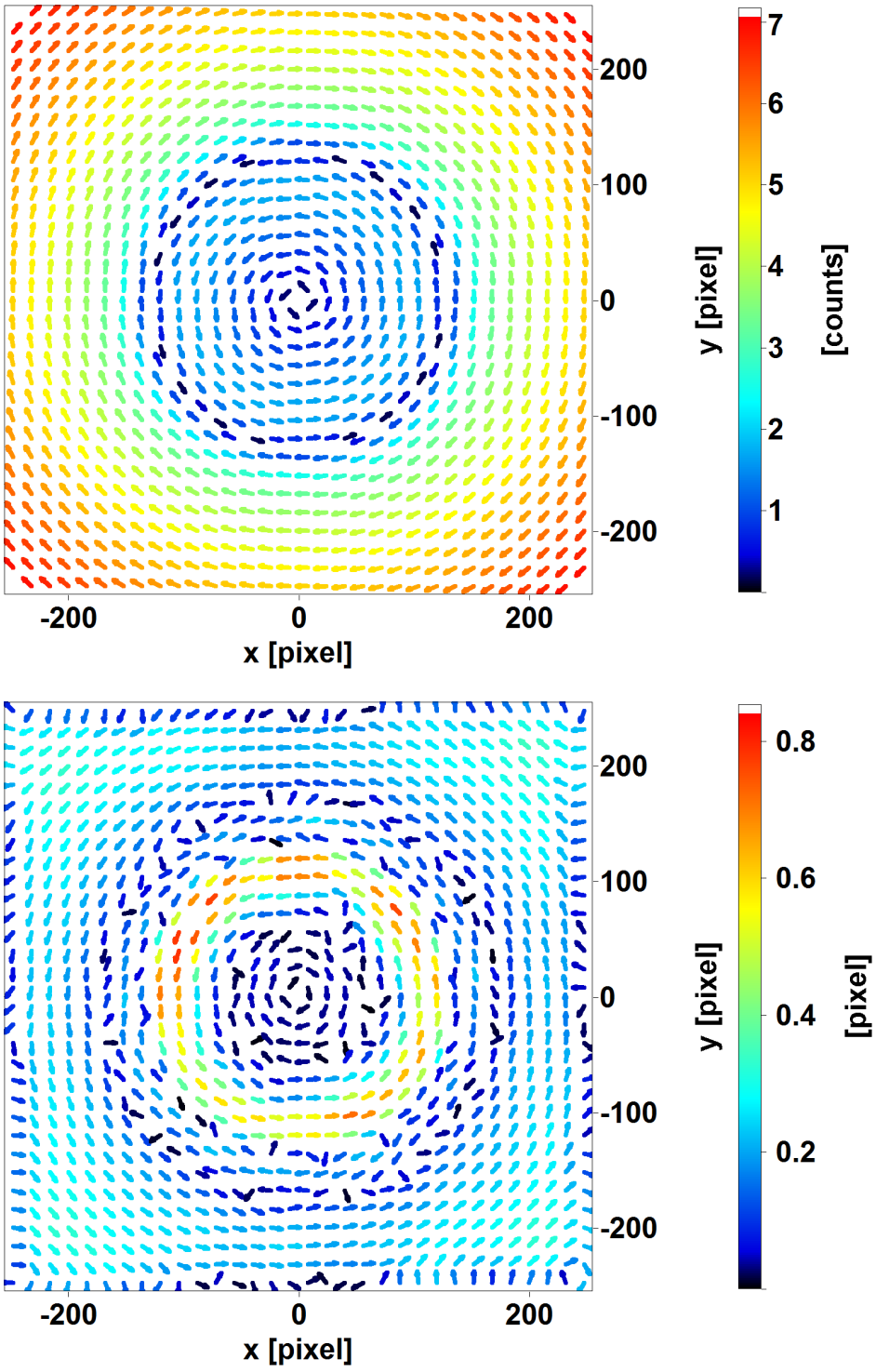

Figure 5.9: 32 pixel wide shear zone, source vectors (top), and difference from calculation (bottom).

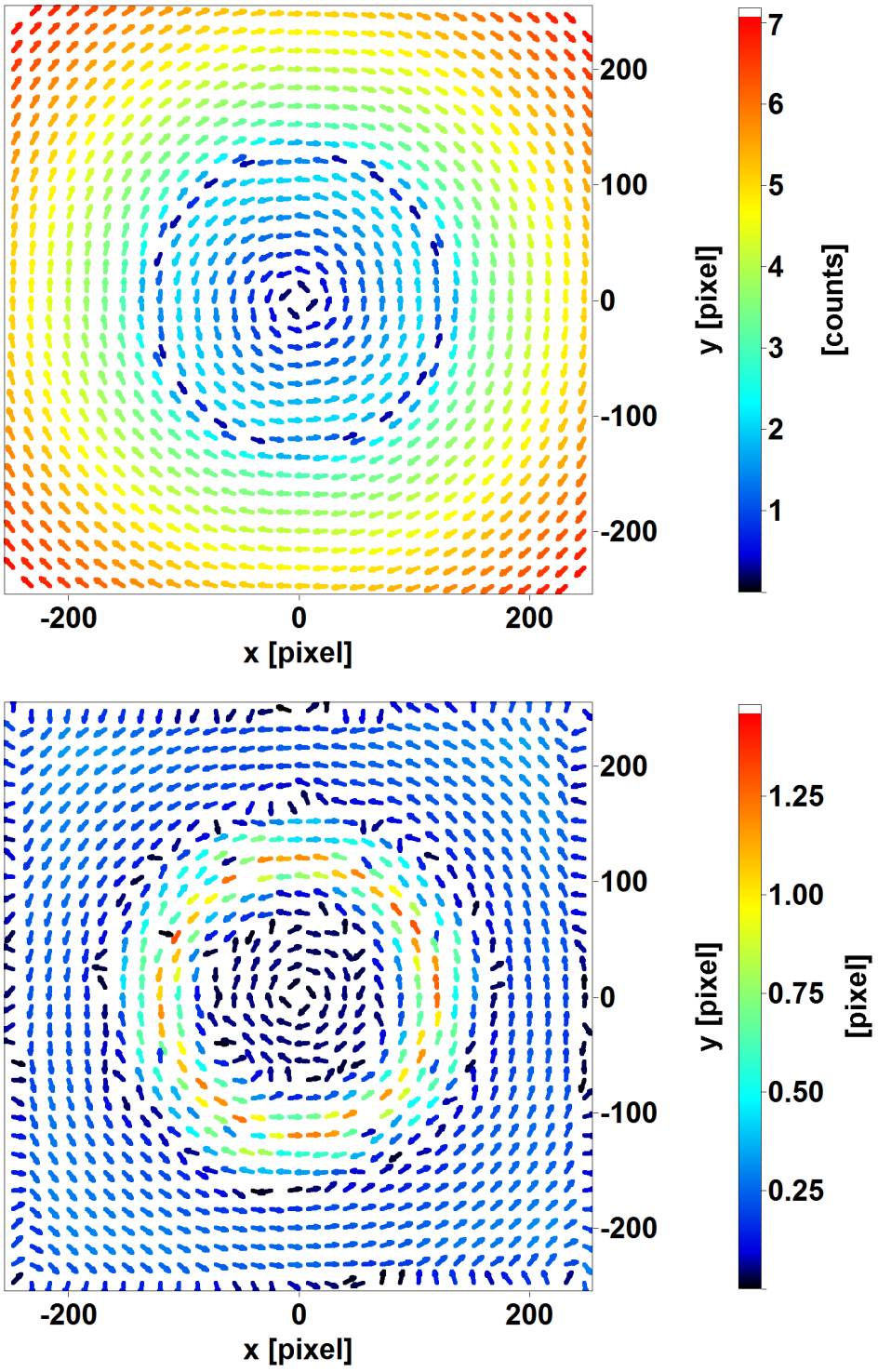

Figure 5.10: 16 pixel wide shear zone, source vectors (top), and difference from calculation (bottom).

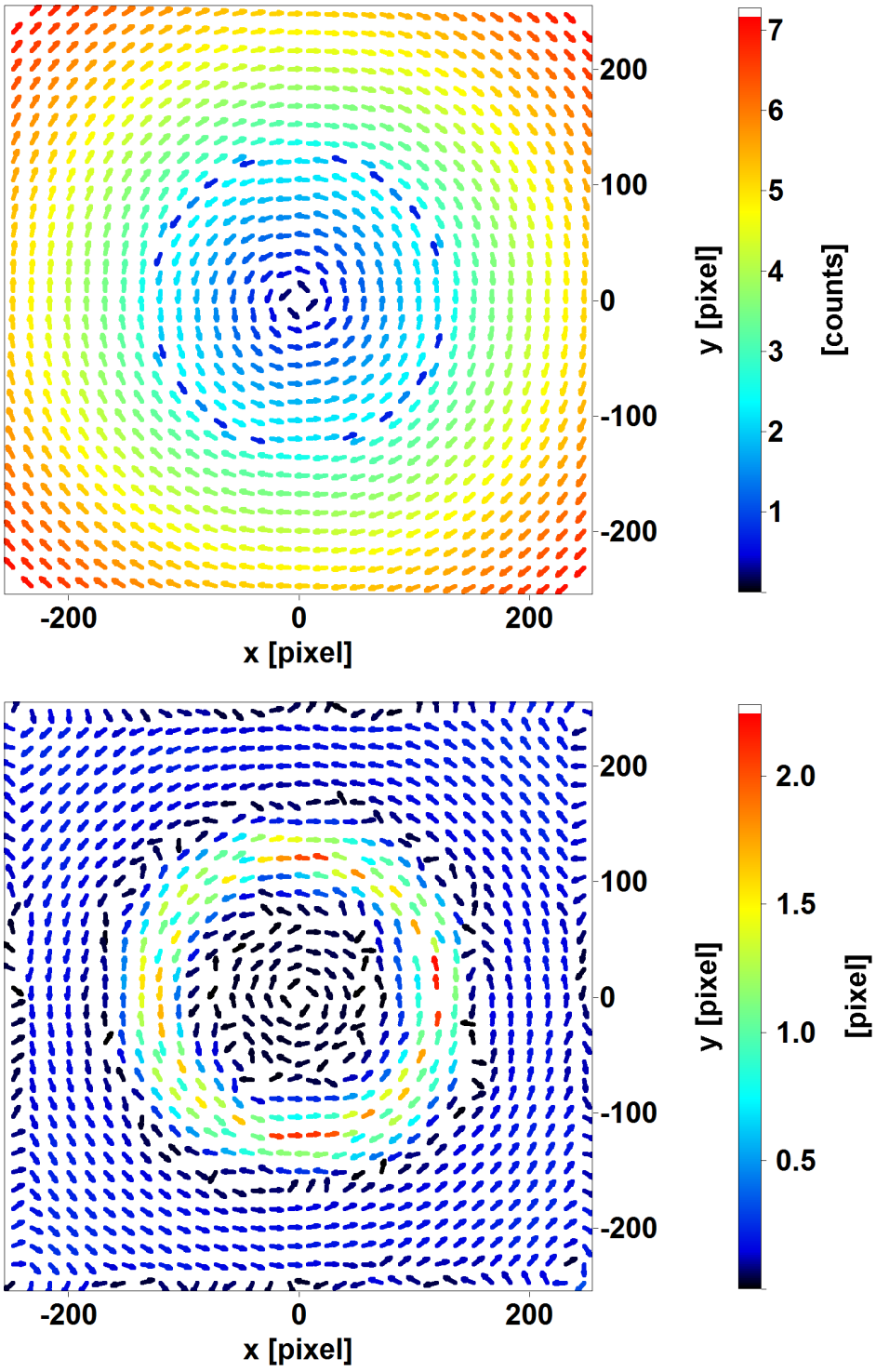

Figure 5.11: 8 pixel wide shear zone, source vectors (top), and difference from calculation (bottom).

Laminar Flow

A laminar flow case was also performed, all of the parameters were kept the same as in the circular shear zone case. The only different parameter is the location of the wall, which was placed exactly at the edge of the image so that there is a zero velocity at the edge. The peak displacement of the pixels was set ~5 pixels. The particle movement is shown in a video in Figure 5.12

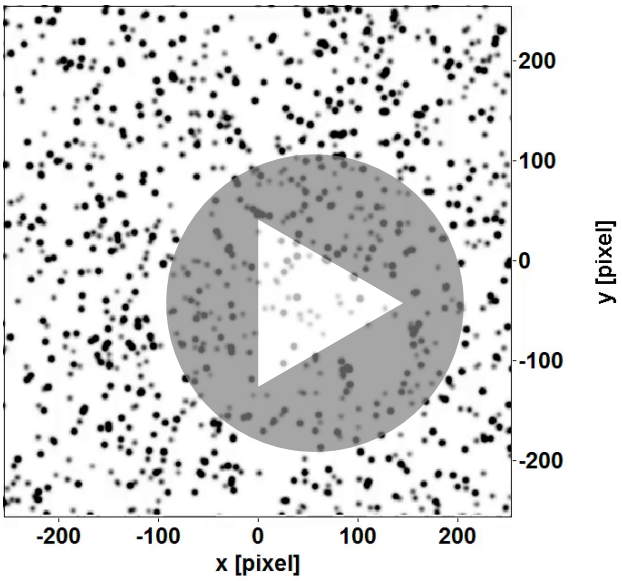

Figure 5.12: Video of synthetic image with laminar flow with a wall at the image boundary on the top and bottom, flow is going from left to right, black dots are particles.

Based on the laminar flow experiment, the circular shear zone synthetic images, and the laminar flow synthetic images, an estimate of PIV velocity uncertainty can be formulated. The error for PIV vector calculations are $\sim 1/5$ of a pixel. For particle displacements that are approaching a pixel, the error is bounded by ~5% of the full displacement (~5 pixels) as long as the shear size scales are not smaller than the interrogation window. For particle displacements of less than 1 pixel error is ~10% of full scale as long as the shear size scales are not smaller than the interrogation window.

For the laminar flow case the worst angular error was 4°, which was the vector next to the wall where the velocity error was quite large. For the higher velocities of the vectors just one interrogation window away from the wall (above 20% of the full scale), the angular error had an angular error of $<1°$, and the angular error quickly drops below 0.2°as you approach 40% of full scale velocity.

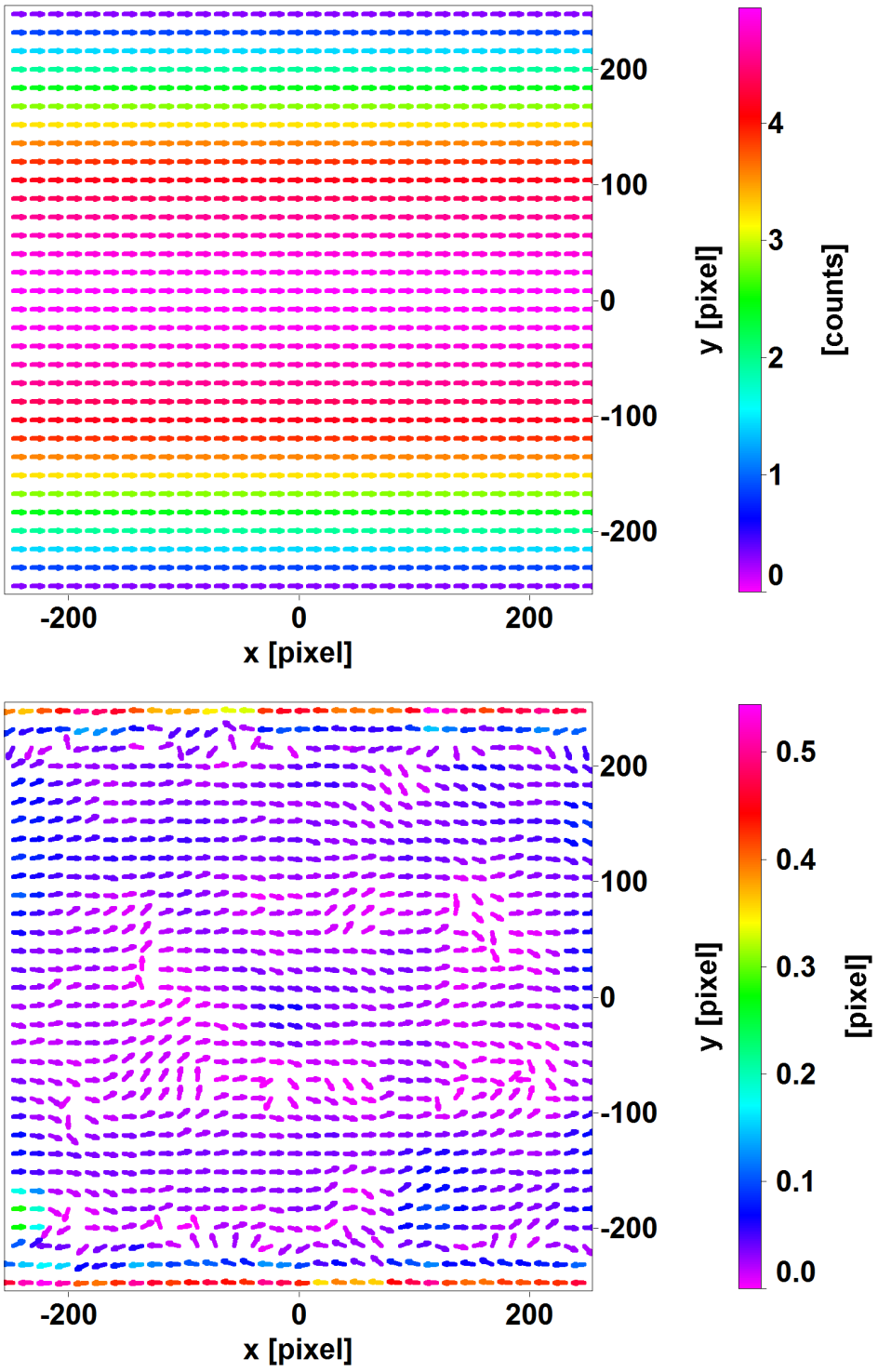

Figure 5.13: Laminar flow source vectors (top), and difference from calculation (bottom).

5.13 Uncertainty Summary

The summary of the uncertainties discussed in this chapter are summarized in Table 5.1.

Table 5.1: Summary of estimated uncertainties.

Parameter	Uncertainty
Bubble Departure Diameter	15 µm
Heat Flux	2.8%, <0.6% bias
Heat Transfer Coefficient	Varies, <12% typical
Pressure	0.035 bar
Inlet Temperature	<1.0 °C
IR Surface Temperature	<2.0 °C, ΔT <0.5 °C
Nucleation Site Density	15%
Bubble Departure Frequency	17%
Mass Flux	1.80%
Bulk Velocity	1.80%
Bubble Sliding Velocity	<9.0%, typically 3.6%
Camera Timing	<1 µs/s
Camera Synchronization PIV/IR	~300 µs
Camera Synchronization HSV/IR	~10 µs
PIV Velocities	~⅕ of a pixel, ~5% of full scale

6 Summary, Conclusions, and Recommended Future Work

6.1 Summary

A unique test section was designed that allowed for simultaneous measurement using high speed video (HSV), infrared thermography (IR), and particle image velocimetry (PIV).

Two different sets of data were developed, the first was using HSV and IR at a spatial resolution of 15 μm for HSV and 37 μm for the IR. The temporal resolution for the IR was 1250 Hz, and 1250-5000 Hz for the HSV. A large range of flow conditions was tested at 3 different subcoolings of 5, 10, and 15 °C and pressures of 1.05, 1.5, and 2.0 bars. Flow rates explored were 150-1250 kg/m^2/s and heat fluxes of 100 - 1600 kW/m^2/s. This data set allowed for the measurement of boiling curves, heat transfer coefficient, nucleation site density, nucleation frequency, bubble sliding velocity, bubble sliding temperature effect, bubble departure diameters, and the 2-D time dependent temperature profile of the heater surface.

The second set of data included synchronized PIV/HSV/IR at ONB for single bubble flow conditions. The data was taken at a higher magnification of 6.8 μm/pixel for HSV and 14.8 μm/pixel for the IR. The temporal resolution was also higher at 10,000 Hz for HSV and 2500 Hz for IR. The pressure was 1.05 bar for subcoolings of 5, 10, and 15 °C. Flow rates were nominally 150, 250, and 350 kg/m^2/s. This data allowed the measurement of bubble growth times, bubble front growth velocities, detailed wall temperatures profiles under bubbles as a function of time, as well as a 2-D velocity field for the liquid phase.

6.2 Conclusions

Bubble departure diameters measured were consistent with the trends of the mechanistic model of Sugrue [14, 34]. However, the model had too large a dependence on mass flux compared to data taken, and tended to underestimate bubble sizes at higher mass fluxes. The bubble departure diameters followed the expected trends of increasing departure diameters with increasing heat flux, decreasing mass flux, decreasing pressure and decreasing subcooling.

Nucleation site densities were found to be slightly higher than anticipated by the Kocamustafaogullari-Ishii, Lemmert-Chawla, and Hibiki-Ishii models. The Kocamustafaogullari-Ishii model greatly overpredicted the influence of mass flux on nucleation site density, which originates from the model's calculation of effective wall superheat to account for the flow. The Lemmert-Chawla model has a shape that does not represent the data or the other models. The Lemmert-Chawla model model has a very slow, almost linear, rise in nucleation site density as wall superheat increases. The effect of pressure increase had a much larger effect on the data than predicted by any of the models.

Bubble departure frequency was found to have the largest deviation from the expected values from the traditional models found in the literature. The average frequency of bubbles was found to be an order of magnitude or slower than predicted by the models. This discrepancy came from the bubble wait time. The reason for the poor fit is the lack of proper consideration of heat flux, heater properties, and heat transfer to the fluid via single phase mechanisms during the wait time between bubbles. A new mechanistic model for calculating the wait time was developed that split the wall heat flux into the component that is transferred

to the fluid, and the component that goes into the heater to increase the sensible heat of the wall. With a single fitting parameter, the model better captures the wait time for the experimental data. It should also be mentioned that bubble nucleation site density and frequency are values which should be used together and must be internally consistent. For example, if there are two nucleation sites adjacent to one another that have the same frequency, they could be counted as two sites with a frequency of f or as one site as a frequency of $2f$. Also, one site could be counted as two sites with half the frequency, thus the measurement methods of the to parameters must be internally consistent.

Bubble sliding velocity was found to be dominated by the bulk flow velocity, and bubbles slid at a velocity of 0.5 - 0.7 times the bulk fluid velocity. The expected result was to see faster sliding velocities for larger bubbles due to both the buoyancy force and drag force increasing, which both would increase the velocity of the bubble. However, the increase in the drag force due to the higher velocity dominated over these effects.

The thermal effects of bubble sliding was found to not be strongly dependent on variables such as subcooling, heat flux, mass flux, or pressure. The thermal effect was fairly constant and typically ~1-4 °C. At some point pressure will have an affect on the thermal influence of a sliding bubble as the bubble gets much smaller, the thermal effect of a single bubble will have to decrease. However, for the range of values tested here, sliding bubbles were found to have a more or less constant effect on wall superheat. The constant thermal effect of sliding bubbles was attributed to transient conduction within the substrate, because on the time scales of sliding bubbles, the conduction from the substrate reached an equilibrium with the heat removal by the bubble and prevented a further drop in wall temperature. The thermal effect also had a large variation for a single flow condition. The likely dominating factor was the thickness of the liquid film underneath the sliding bubble, which affected its local heat transfer coefficient, and in turn affects the maximum temperature drop under the bubble.

6.3 Technical Contributions

1. A large database was developed that characterized subcooled boiling using the parameters listed in Table 1.1. This data includes high quality synchronized 2-D temperature profiles of the heater surface as well as a 2-D velocity profiles of the liquid generating a unique set of data. This data is unique in that there are a large number of synchronized parameters that were measured with high accuracy for a single experiment. This database can be used by other researchers to inspire or validate mechanistic and CFD models for subcooled flow boiling heat transfer.

2. Developed methods to automatically count nucleation sites and determine bubble frequency from infrared images of a time dependent 2-D surface temperature profile.

3. Quantified the thermal effect of sliding bubbles on a surface, and found that it was insensitive to parameters such as mass flux, heat flux, pressure, and subcooling.

4. Proposed a new mechanistic model for calculating wait time based on the split of the heat flux between the flow and the substrate during a temperature transient caused by a bubble nucleation.

6.4 Future Work

6.4.1 Phase Determination

One parameter that was desired by modelers after the test section was designed was measuring the phase on the surface of the heater. This could be measured independently of temperature using a silicon wafer such as has been used in the past by Kim et al [82]. This used the ability of the IR to directly measure the

water temperature to determine which phase is on the surface, as well as see the microlayer through the interference rings created by the curvature of the microlayer.

A draft of a heater design that could be used for phase determination was created, and the 3D model is shown in Figure 6.1. The design was similar to that of the sapphire heater. It had 2 mm x 10 mm silver pads (silver) for the electrical connections and would be placed on a 5-25 Ω-cm wafer. However, to keep the actual heater area to 10 mm x 20 mm, a silicon piece of 10 mm x 20mm size would have to be used, and the rest of the heater would be made of an insulating material affixed to the silicon (black area in Figure 6.1).

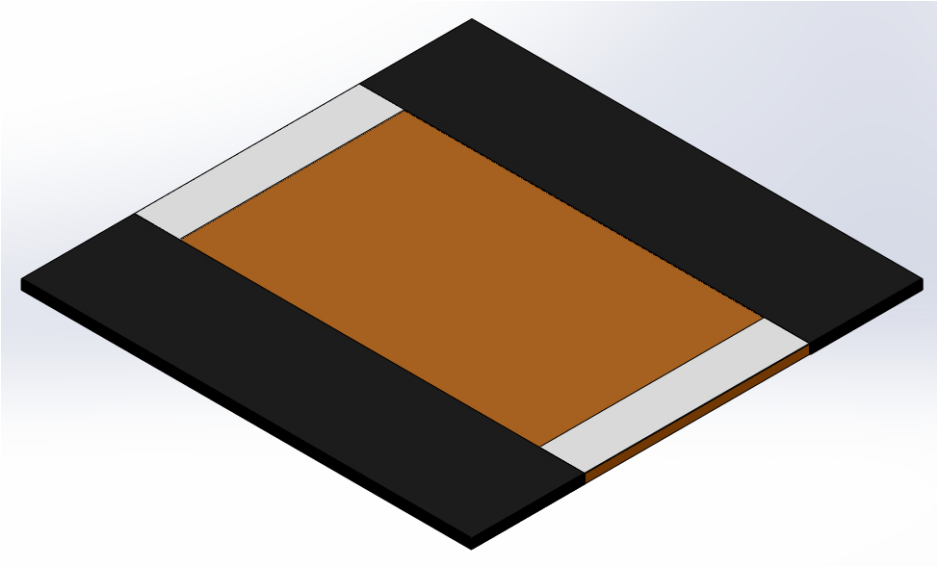

Figure 6.1: Draft model of silicon heater for phase determination. Brown is silicon, gray is silver, and black is insulating material that makes up the rest of the structure of the heater.

A single piece of conductive silicon could be used if a 20 mm x 20 mm heater was acceptable. However, if the heater area was attempted to be constrained by attaching a 20 mm x 20 mm piece of silicon to the cartridge electrodes only on a 10 mm span, the heat flux would become nonuniform. The Fourier equation for an electrically conductive media is shown in (6.1),

$$\nabla \left(\sigma \nabla \left(V \right) \right) = 0 \tag{6.1}$$

where σ is the electrical conductivity and V is the potential. This was solved in 2D, and all boundaries had a 0 current density condition except for the two 10 mm edges where the electrical pads would be. A conductivity of 10 Ohm-cm was used, which was within the range of the wafers used previously for phase determination (5-25 Ohm-cm resistance). The results showed that there would be a factor of 2 or more deviation in the heat flux over the area of the heater.

6.4.2 PIV Data Improvements

The data collected by PIV could be improved by improving the optics for the laser to decrease the laser sheet width from the current ~500 μm to give a more defined plane for the velocity profile. Higher high speed video spatial resolutions would also be desirable to get a better vector resolution. However, both of these improvements would require an even higher seeding density, which was already a challenge to keep the density at the desired value. Also increasing the spatial resolution would decrease the maximum velocity

that could be imaged because of the larger displacement of particles at the maximum frame rate of 10,000 Hz. However, even with the current setup, the flow velocity could have been increased slightly above the conservative value used as the maximum. Higher velocities also translate to smaller bubbles which make PIV more difficult.

PIV could be taken for higher heat fluxes and only investigate the liquid region outside the vapor phase region. Any details around bubbles would be lost, but could yield results for velocities near the liquid vapor interface and in the bulk flow.

The PIV data could also be coupled with laser induced fluorescence to get an estimate of the temperature within the liquid phase. This does involve using additional dyes and additives in the fluid, and could have effects on the boiling characteristics.

The selection/development of a better PIV particle for high temperature two-phase water applications would be very useful. Ideally a particle with a density close to that of water, that is stable up to 200 °C, has limited adhesion to walls, and that can doped to fluoresce from 527 nm laser light. A new particle that met these requirements would make maintaining seeding density much easier, less time consuming, and less expensive.

6.4.3 IR Improvements

The infrared data fidelity is close to the current limits of IR camera technology. The spatial resolution can only be increased further by sacrificing temporal resolution and field of view. For the PIV/IR data with a spatial resolution of 14.8 μm/pixel, which was used for single bubble analysis, the field of view was only ~1.4 mm.

If faster cameras were developed higher spatial and temporal resolution could be achieved. However, to maintain the current temperature resolution, a surface with higher emissivity would have to be developed to accommodate shorter integration times of the camera and to keep the signal to noise ratio high.

Surface temperature determination by a radiometric calculation that determines the temperature profile within the substrate would be a large improvement. This would allow for computation of local, time resolved heat flux values as well as the surface temperature.

6.4.4 Miscellaneous Future Work

The experimental database could be extended to more heat fluxes, pressures, and subcoolings to gather a larger amount of data and to see trends in some of the parameters that were not able to be distinguished, such as the influence of pressure on the temperature under a sliding bubble.

The addition of a method to measure the average void fraction at various locations of the test section would also be useful to modelers who use void fraction as a parameter to match in CFD simulations.

The heated section could be increased in size to create a longer heated wall where measurements could be taken at different axial locations to interrogate the flow development.

Additional high speed cameras would allow synchronized imaging of the flow from multiple angles, and allow for a 3-D reconstruction of bubble shapes for isolated bubbles during flow boiling.

References

[1] M. Ishii and T. Hibiki, *Thermo-Fluid Dynamics of Two-Phase Flow*. Springer, 2011.

[2] N. Kurul and M. Podowski, "Multidimensional effects in forced convection subcooled boiling," in *Proceedings of the Ninth International Heat Transfer Conference*, (Jerusalem, Israel), 1990.

[3] N. Kolev, "How accurately can we predict nucleate boiling?," in *Multiphase Flow Dynamics 3*, pp. 143–178, Springer Berlin Heidelberg, 2012.

[4] N. Dinh, "CIPS validation data plan," Tech. Rep. INL/EXT-12-25347, INL, March 2012.

[5] N. E. Todreas and M. S. Kazimi, *Nuclear Systems Volume I: Thermal Hydraulic Fundamentals*. CRC Press, 2nd ed., 2011.

[6] D. Euh, B. Ozar, T. Hibiki, M. Ishii, and C.-H. Song, "Characteristics of bubble departure frequency in a low-pressure subcooled boiling flow," *Journal of Nuclear Science and Technology*, vol. 47, no. 7, pp. 608–617, 2010.

[7] R. Situ, M. Ishii, T. Hibiki, J. Tu, G. Yeoh, and M. Mori, "Bubble departure frequency in forced convective subcooled boiling flow," *International Journal of Heat and Mass Transfer*, vol. 51, no. 25-26, pp. 6268–6282, 2008.

[8] N. Basu, G. R. Warrier, and V. K. Dhir, "Onset of nucleate boiling and active nucleation site density during subcooled flow boiling," *Journal of Heat Transfer*, vol. 124, pp. 717–728, 2002.

[9] V. H. D. Valle and D. Kenning, "Subcooled flow boiling at high heat flux," *International Journal of Heat and Mass Transfer*, vol. 28, no. 10, pp. 1907–1920, 1985.

[10] M. C. Díaz, H. Boye, I. Hapke, J. Schmidt, Y. Staate, and Z. Zhekov, "Investigation of flow boiling in narrow channels by thermographic measurement of local wall temperatures," *Microfluidics and Nanofluidics*, vol. 2, pp. 1–11, 2005.

[11] S. G. Bankoff, "Entrapment of gas in the spreading of a liquid over a rough surface," *AIChE Journal*, vol. 4, no. 1, pp. 24–26, 1958.

[12] V. P. Carey, *Liquid-Vapor Phase-Change Phenomena*. Taylor & Francis, 2nd ed., 2008.

[13] J. Klausner, R. Mei, D. Bernhard, and L. Zeng, "Vapor bubble departure in forced convection boiling," *International Journal of Heat and Mass Transfer*, vol. 36, no. 3, pp. 651–662, 1993.

[14] R. Sugrue and J. Buongiorno, "A modified force-balance model for predicting bubble departure diameter in subcooled flow boiling," in *Proceedings of The 15th International Topical Meeting on Nuclear Reactor Thermal-Hydraulics, NURETH-15*, 2013.

[15] N. E. Todreas and M. S. Kazimi, *Nuclear Systems Volume I: Thermal Hydraulic Fundamentals*. Taylor & Francis, 1st ed., 1993.

[16] L. Tong and Y. Tang, *Boiling Heat Transfer and Two-Phase Flow*. Taylor & Francis, 1997.

[17] LaVision, *Product-Manual for FlowMaster Item-Number(s): 1105011-4*, December 2007.

[18] LaVision, *DaVis 8.2 Software*, April 2014.

[19] FLIR, *ThermoVision®SC4000/SC6000 User's Guide*.

[20] L. IRCameras, *IRC800 Liquid Nitrogen Cooled Infrared Camera User's Guide*, May 2013.

[21] R. M. Podowski, D. A. Drew, R. T. L. Jr., and M. Z. Podowski, "A mechanistic model of the ebullition cycle in forced-convection subcooled boiling," in *Proceedings of the 8th International Topical Meeting on Nuclear Reactor Thermal Hydraulics (NURETH-8)*, vol. 3, (Kyoto, Japan), pp. 1530–1537, September-October 1997.

[22] M. Z. Podowski and R. M. Podowski, "Mechanistic multidimensional modeling of forced convection boiling heat transfer," *Science and Technology of Nuclear Installations*, vol. 2009, p. 387020, 2009.

[23] V. K. Dhir, "Mechanistic prediction of nucleate boiling heat transfer–achievable or a hopeless task?," *Journal of Heat Transfer*, vol. 128, pp. 1–12, 2006.

[24] R. Situ, Y. Mi, M. Ishii, and M. Mori, "Photographic study of bubble behaviors in forced convection subcooled boiling," *International Journal of Heat and Mass Transfer*, vol. 47, no. 17-18, pp. 3659–3667, 2004.

[25] N. Basu, G. R. Warrier, and V. K. Dhir, "Wall heat flux partitioning during subcooled flow boiling: Part 1-model development," *Journal of Heat Transfer*, vol. 127, pp. 131–140, February 2005.

[26] Y. Hassan, T. Blanchat, C. S. Jr, and R. Canaan, "Simultaneous velocity measurements of both components of a two-phase flow using particle image velocimetry," *International Journal of Multiphase Flow*, vol. 18, no. 3, pp. 371–395, 1992.

[27] C. Estrada-Pérez and Y. Hassan, "PTV experiments of subcooled boiling flow through a vertical rectangular channel," *International Journal of Multiphase Flow*, vol. 36, no. 9, pp. 691–706, 2010.

[28] C. E. Estrada-Pérez, "Analysis, comparison and modification of various particle image velocimetry (PIV) algorithms," Master's thesis, Texas A&M University, December 2004.

[29] G. Thorncroft, J. Klausnera, and R. Mei, "An experimental investigation of bubble growth and detachment in vertical upflow and downflow boiling," *International Journal of Heat and Mass Transfer*, vol. 41, no. 23, pp. 3857–3871, 1998.

[30] R. Ahmadi, T. Ueno, and T. Okawa, "Bubble dynamics at boiling incipience in subcooled upward flow boiling," *International Journal of Heat and Mass Transfer*, vol. 55, no. 1-3, pp. 488–497, 2012.

[31] S. Li, S. Tan, C. Xu, P. Gao, and L. Sun, "An experimental study of bubble sliding characteristics in narrow channel," *International Journal of Heat and Mass Transfer*, vol. 57, no. 1, pp. 89–99, 2013.

[32] C. Hutter, K. Sefiane, T. Karayiannis, A. Walton, R. Nelson, and D. Kenning, "Nucleation site interaction between artificial cavities during nucleate pool boiling on silicon with integrated micro-heater and temperature micro-sensors," *International Journal of Heat and Mass Transfer*, vol. 55, no. 11-12, pp. 2769 – 2778, 2012.

[33] C. Chen, W. Chang, K. Li, Y. Lie, and T. Lin, "Subcooled flow boiling heat transfer of r-407c and associated bubble characteristics in a narrow annular duct," *International Journal of Heat and Mass Transfer*, vol. 52, no. 13-14, pp. 3147–3158, 2009.

[34] R. Sugrue, T. McKrell, and J. Buongiorno, "On the effects of orientation angle, subcooling, mass flux, heat flux, and pressure on bubble departure diameter in subcooled flow boiling.," in *Proceedings of Computational Fluid Dynamics in Nuclear Reactor Safety - 4*, 2012.

[35] C. D. Gerardi, *Investigation of the Pool Boiling Heat Transfer Enhancement of Nano-Engineered Fluids by means of High-Speed Infrared Thermography*. PhD thesis, Massachusetts Institute of Technology, May 2009.

[36] T. Theofanous, J. Tu, A. Dinh, and T. Dinh, "The boiling crisis phenomenon: Part I: nucleation and nucleate boiling heat transfer," *Experimental Thermal and Fluid Science*, vol. 26, no. 6-7, pp. 775–792, 2002.

[37] T. Theofanous, T. Dinh, J. Tu, and A. Dinh, "The boiling crisis phenomenon: Part II: dryout dynamics and burnout," *Experimental Thermal and Fluid Science*, vol. 26, no. 6-7, pp. 793–810, 2002.

[38] E. Wagner and P. Stephan, "High-resolution measurements at nucleate boiling of pure FC-84 and FC-3284 and its binary mixtures," *Journal of Heat Transfer*, vol. 131, pp. 121008–1, 2009.

[39] T. H. Kim, E. Kommer, S. Dessiatoun, and J. Kim, "Measurement of two-phase flow and heat transfer parameters using infrared thermometry," *International Journal of Multiphase Flow*, vol. 40, no. 0, pp. 56–67, 2012.

[40] I. Golobic, J. Petkovsek, M. Baselj, A. Papez, and D. Kenning, "Experimental determination of transient wall temperature distributions close to growing vapor bubbles," *Heat and Mass Transfer*, vol. 45, pp. 857–866, 2009. 10.1007/s00231-007-0295-y.

[41] J. P. O'Connor and S. M. You, "A painting technique to enhance pool boiling heat transfer in saturated FC-72," *Journal of Heat Transfer*, vol. 117, pp. 387–393, 1995.

[42] S. M. You and J. P. O'Connor, "Boiling enhancement coating," *United States of America Patent*, vol. 5814392, pp. 1–13, 1998.

[43] R. Furberg, B. Palm, L. Shanghua, M. Muhammed, and M. Toprak, "Porous layer," *World Intellectual Property Organization Patent*, vol. WO 2007/100297 A1, pp. 1–56, 2007.

[44] H. Ahn, V. Sathyamurthi, N. Sinha, S. Lau, and D. Banerjee, "Boiling experiments on vertically alighned carbon nanotubes and using surface micromachined thin fill thermocouple," in *9th AIAA/ASME Joint Thermophysics and Heat Transfer Conference*, June 2006.

[45] H. S. Ahn, V. Sathyamurthi, and D. Banerjee, "Pool boiling experiments on a nano-structured surface," in *IEEE Transactions on Components and Packaging Technologies*, vol. 32, pp. 156–165, March 2009.

[46] S. Ujereh, T. Fisher, and I. Mudwar, "Effects of carbon nanotube arrays on nucleate pool boiling," *International Journal of Heat and Mass Transfer*, vol. 50, no. 19-20, pp. 4023–4038, 2007.

[47] R. Chen, M. C. Lu, V. Srinivasan, Z. Wang, H. H. Cho, and A. Majumdar, "Nanowires for enhanced boiling heat transfer," *Nano Letters*, vol. 9, no. 2, pp. 548–553, 2009.

[48] B. A. Phillips, "Nano-engineering the boiling surface for optimal heat transfer rate and critical heat flux," Master's thesis, Massachusetts Institute of Technology, 2011.

[49] M. C. Lu, *Exploring the Limits of Boiling and Evaporative Heat Transfer Using Micro/Nano Structures*. PhD thesis, University of California, Berkeley, 2010.

[50] R. Furberg, B. Palm, S. Li, M. Toprak, and M. Muhammed, "The use of a nano- and microporous surface layer to enhance boiling in a plate heat exchanger," *Journal of Heat Transfer*, vol. 131, p. 101010, 2009.

[51] A. R. Betz, J. Xu, H. Qiu, and D. Attinger, "Do surfaces with mixed hydrophilic and hydrophobic areas enhance pool boiling?," *Applied Physics Letters*, vol. 97, no. 14, p. 141909, 2010.

[52] G. L. DeWitt, *Investigation of Downward Facing Critical Heat Flux with Water-Based Nanofluids for In-Vessel Retention Applications*. PhD thesis, Massachusetts Institute of Technology, September 2011.

[53] F. P. Beer, E. R. J. Jr., and J. T. DeWolf, *Mechanics of Materials*. McGraw Hill, 3rd ed., 2002.

[54] W. C. Young and R. G. Budynas, *Roark's Formulas for Stress and Strain*. McGraw, 7th ed., 2002.

[55] Cotronics, *Duralco™ 4463 Low Expansion Adhesive & Potting*.

[56] Cotronics, *Adhesive & Casting Compound 650°F Duralco™ 4703*.

[57] B. R. Munson, D. F. Young, and T. H. Okiishi, *Fundamentals of Fluid Dynamics*. John Wiley & Sons, 4th ed., 2002.

[58] H. Schlichting, *Boundary Layer Theory*. McGraw-Hill, 7th ed., 1987.

[59] M. Ishii, *THERMALLY INDUCED FLOW INSTABILITIES IN TWO-PHASE MIXTURES IN THERMAL EQUILIBRIUM*. PhD thesis, Georgia Instittue of Technology, 1971.

[60] J. G. Collier and J. R. Thome, *Convective Boiling and Condensation*. Oxford University Press, 3rd ed., 1994.

[61] J. Hinze, *Turbulence*. McGraw-Hill, 1975.

[62] N. Zuber, "The dynamics of vapor bubbles in nonuniform temperature fields," *International Journal of Heat and Mass Transfer*, vol. 2, pp. 83–98, 1961.

[63] M. Lemmert and J. M. Chawla, "Influence of flow velocity on surface boiling heat transfer coefficient," in *Heat Transfer in Boiling* (E. Hahne and U. Grigull, eds.), Academic Press, 1977.

[64] T. Hibiki and M. Ishii, "Active nucleation site density in boiling systems," *International Journal of Heat and Mass Transfer*, vol. 46, no. 14, pp. 2587 – 2601, 2003.

[65] G. Kocamustafaogullari and M. Ishii, "Interfacial area and nucleation site density in boiling systems," *International Journal of Heat and Mass Transfer*, vol. 26, no. 9, pp. 1377 – 1387, 1983.

[66] Y.-Y. Hsu and R. W. Graham, *Transport Processes in boiling and Two-Phase Systems*. American Nuclear Society, 1986.

[67] G. H. Yeoh, S. C. P. Cheung, J. Y. Tu, and M. K. M. Ho, "Modeling vertical subcooled boiling flows at low pressures," *Journal of ASTM International*, vol. 8, no. 4, p. JAI103374, 2011.

[68] LaVison, "Glass hollow spheres," tech. rep., LaVison, 2011.

[69] X. Duan, B. Phillips, T. McKrell, and J. Buongiorno, "Synchronized high-speed video, infrared thermometry, and particle image velocimetry data for validation of interface-tracking simulations of nucleate boiling phenomena," *Experimental Heat Transfer*, vol. 26, no. 2-3, pp. 169–197, 2013.

[70] LaVision, "Fluorescent seeding particles," tech. rep., LaVision, 2011.

[71] R. Lindken and W. Merzkirch, "A novel piv technique for measurements in multiphase flows and its application to two-phase bubbly flows," *Experiments in Fluids*, vol. 33, no. 6, pp. 814–825, 2002.

[72] J. E. Castle, "The composition of metal surfaces after atmospheric exposure: An historical perspective," *The Journal of Adhesion*, vol. 84, no. 4, pp. 368–388, 2008.

[73] H. O'Hanley, "Seperate effects of surface roughness, wettability and porosity on boiling heat transfer and critical heat flux and optimization of boiling surfaces," Master's thesis, Massachusetts Institute of Technology, 2012.

[74] O. Adeyinka and G. Naterer, "Experimental uncertainty of measured entropy production with pulsed laser piv and planar laser induced fluorescence," *International Journal of Heat and Mass Transfer*, vol. 48, no. 8, pp. 1450–1461, 2005.

[75] J. D. Luff, T. Drouillard, A. M. Rompage, M. A. Linne, and J. R. Hertzberg, "Experimental uncertainties associated with particle image velocimetry (piv) based vorticity algorithms," *Experiments in Fluids*, vol. 26, no. 1, pp. 36–54, 1999. 10.1007/s003480050263.

[76] S. Beresh, "Comparison of piv data using multiple configurations and processing techniques," *Experiments in Fluids*, vol. 47, pp. 883–896, 2009. 10.1007/s00348-009-0685-7.

[77] P. Hariharan, M. Giarra, V. Reddy, S. W. Day, K. B. Manning, S. Deutsch, S. F. C. Stewart, M. R. Myers, M. R. Berman, G. W. Burgreen, E. G. Paterson, and R. A. Malinauskas, "Multilaboratory particle image velocimetry analysis of the fda benchmark nozzle model to support validation of computational fluid dynamics simulations," *Journal of Biomechanical Engineering*, vol. 133, no. 4, p. 041002, 2011.

[78] F. Scarano, "Iterative image deformation methods in piv," *Measurement Science and Technology*, vol. 1, pp. R1–R19, 2002.

[79] M. Stanislas, K. Okamoto, C. J. Kähler, and J. Westerweel, "Main results of the second international PIV challenge," *Experiments in Fluids*, vol. 39, no. 2, pp. 170–191, 2005.

[80] W. M. Rohsenow, J. P. Hartnett, and Y. I. Cho, eds., *Handbook of Heat Transfer*. McGraw-Hill, 3rd ed., 1998.

[81] S. Marco and L. Han, "A note on limiting laminar nusselt number in ducts with constant temperature gradient by analogy to thin-plate theory," *Transactions of ASME*, vol. 77, pp. 625–630, 1955.

[82] H. Kim and J. Buongiorno, "Detection of liquid-vapor-solid triple contact line in two-phase heat transfer phenomena using high-speed infrared thermometry," *International Journal of Multiphase Flow*, vol. 37, no. 2, pp. 166–172, 2011.

[83] F. Chen and H. Hagen, "A survey of interface tracking methods in multi-phase fluid visualization," *OpenAccess Series in Informatics*, vol. 19, pp. 11–19, 2010.

[84] R. V. Garimella, V. Dyadechko, B. K. Swartz, and M. J.Shashkov, *Interface Reconstruction in Multi-fluid, Multi-phase Flow Simulations*. Springer, 2005.

[85] J. Glimm, J. W. Grove, X. L. Li, K.-M. Shyue, Y. Zeng, and Q. Zhang, "Three-dimensional front tracking," *SIAM Journal of Scientific Computing*, vol. 19, no. 3, pp. 703–727, 1998.

[86] J. M. Hyman, "Numerical methods for tracking interfaces," *Physica D*, vol. 12, pp. 396–407, 1984.

[87] R. D. Richtmyer, *Difference Methods for Initial-Value Problems*. Interscience, 1957.

[88] C. W. Hirt and B. D. Nichols, "Volume of fluid (VOF) method for dynamics of free boundaries," *Journal of Computational Physics*, vol. 39, pp. 201–225, 1981.

[89] M. Rudman, "Volume-tracking methods for interfacial flow calculations," *International Journal for Numerical Methods in Fluids*, vol. 24, no. 7, pp. 671–691, 1997.

[90] S. Osher and J. A. Sethian, "Fronts propagating with curvature-dependent speed: Algorithms based on hamilton-jacobi formulations," *Journal of Computational Physics*, vol. 79, pp. 12–49, 1988.

[91] S. Osher and R. P. Fedkiw, "Level set methods: An overview and some recent results," *Journal of Computational Physics*, vol. 169, pp. 463–502, 2001.

7 Appendices

A Bubble Departure and Re-attachment

Figure A.1 shows a bubble grow, depart, and reattach and then slide. Video captured at 1000 Hz, 109 kW/m^2, G=160 kg/m^2/s, ΔT_{sat}=10 °C. Figure A.2 is the video, video is played back at 10 Hz, and slowed down 100x.

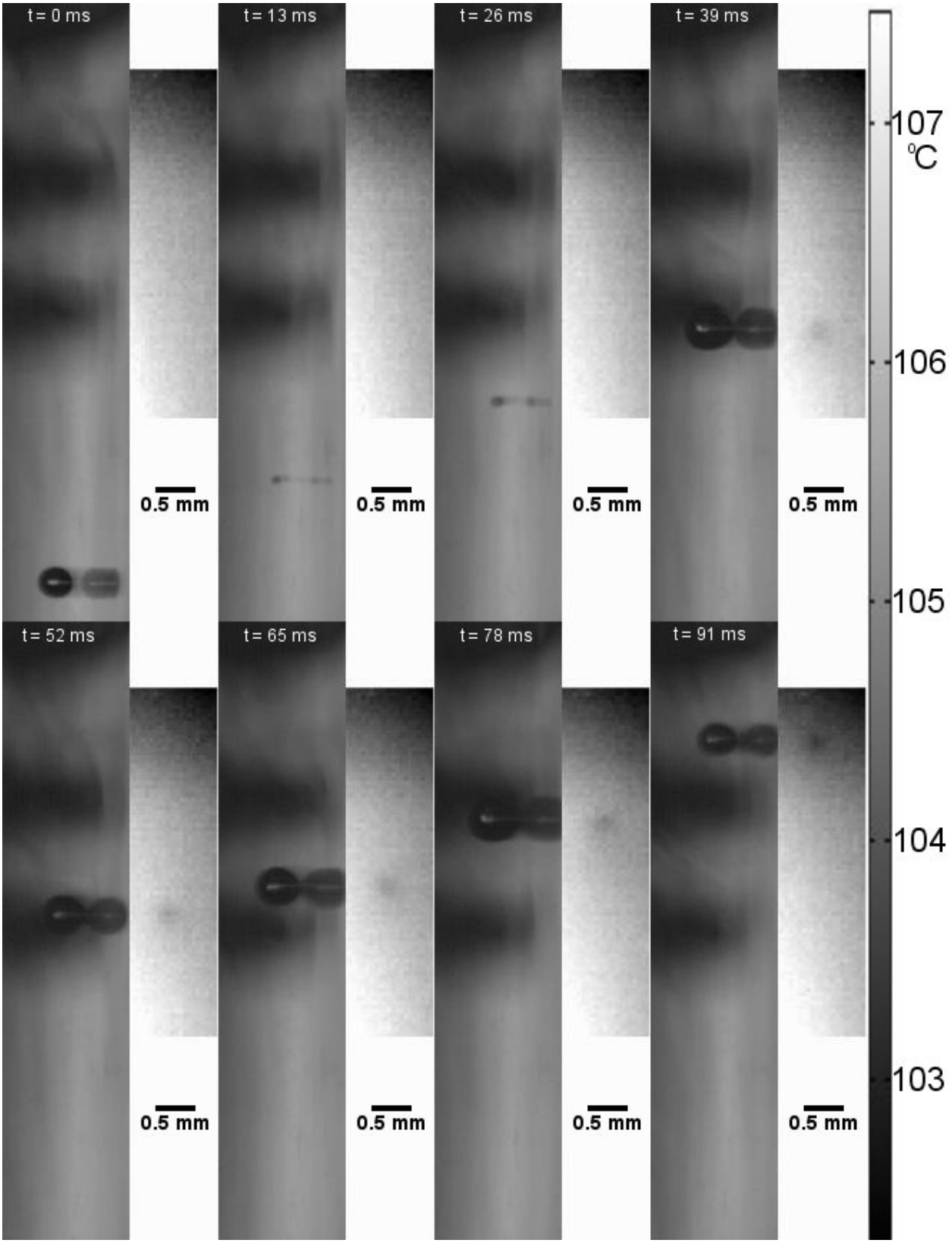

Figure A.1: HSV from side of bubble departure and reattachment. t=0 is bubble nucleation. The temperature bar is for the IR images.

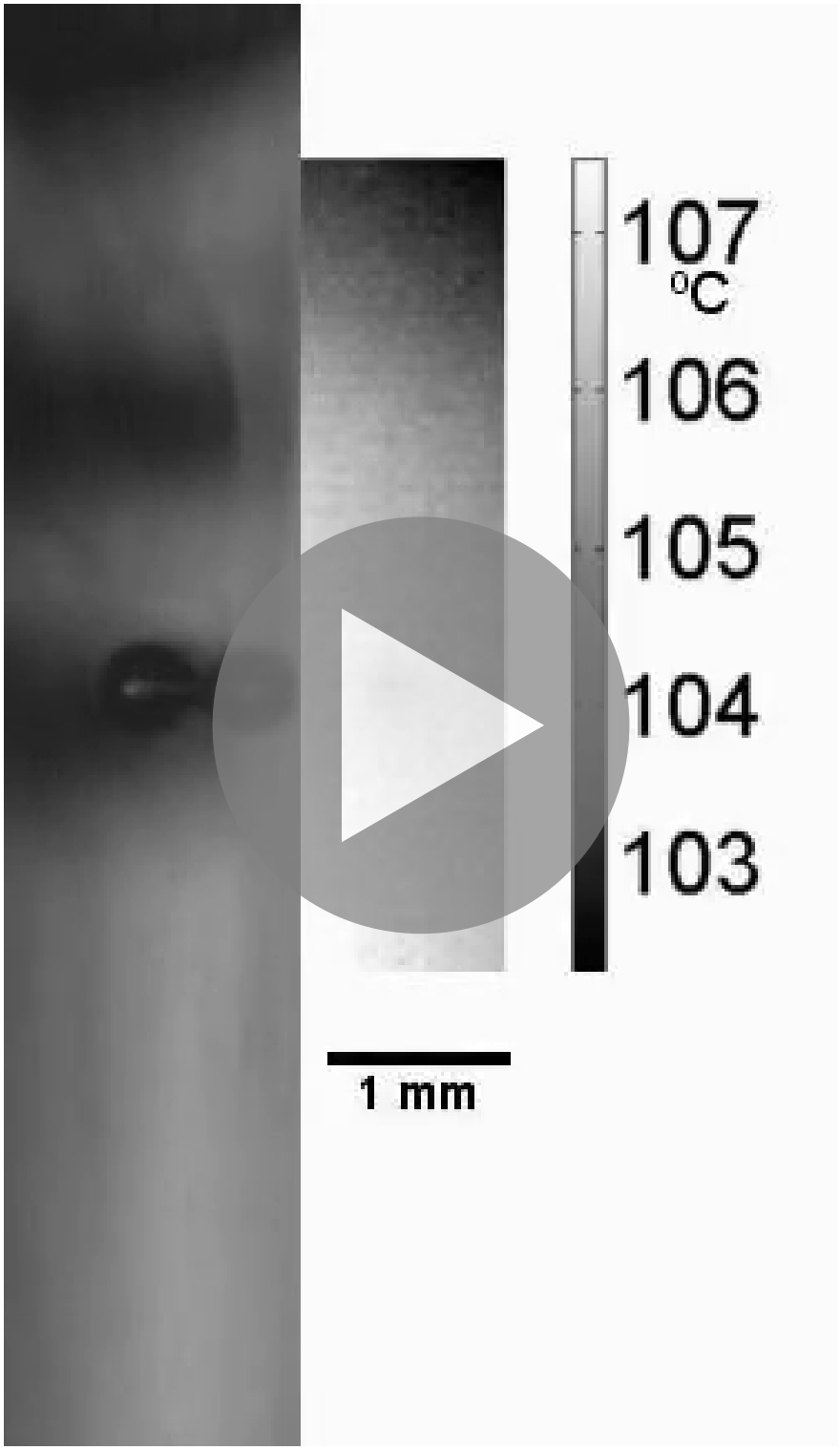

Figure A.2: Video of bubble growth departure, reattachment, and sliding, HSV from side (left) and IR (right).

B Test Section Heat Flux Determination

The point of interest for studying bubble growth and departure in subcooled boiling behavior is at and beyond the point of Z_D. Assuming the process of bubble departure is thermally controlled both Griffith (B.1) and Dix (B.2) proposed models based on balancing the heat removal from the wall with the energy necessary to bring the fluid up to saturation [15].

$$q'' = 5h_{lo}\left(T_{sat} - T_{bulk}\right) \tag{B.1}$$

$$q'' = 740.7h_{lo}\left(T_{sat} - T_{bulk}\right)\left(Re_{\ell}\right)^{-\frac{1}{2}} \tag{B.2}$$

Saha and Zuber proposed that hydrodynamic phenomena should also be considered. For low mass flow rates the heat transfer controls the bubble condensation while for high flow rates hydrodynamics are also important. Their proposal for high flow is given in (B.3) and is valid for pressures of 0.1-13.8 MPa, mass fluxes of 95-2760 $\frac{kg}{m^2 s}$ and heat fluxes of 0.28-1.89 $\frac{MW}{m^2}$ [15] [60] [12].

$$\text{For Pe}< 7\times10^4\text{:}\quad q'' = 454.5\frac{\left(T_{sat} - T_{bulk}\right)k_{\ell}}{D_e} \tag{B.3a}$$

$$\text{For Pe}> 7\times10^4\text{:}\quad q'' = \frac{\left(T_{sat} - T_{bulk}\right)Gc_{p\ell}}{154} \tag{B.3b}$$

Where the Pe number is given by (B.4).

$$Pe = \frac{Nu}{St} = \frac{GD_e c_{p\ell}}{k_{\ell}} \tag{B.4}$$

The heat flux necessary for net vapor generation versus flow velocity is plotted in Figure B.1 for water for a 2 cm equivalent diameter channel with a heated perimeter of 1 cm and 40 °C of subcooling at atmospheric pressure. This gives an estimate of the heat flux needed to obtain bubble departure, which can be used when sizing the heater for the experiments discussed in Section 2. The Dittus-Boelter correlation [15] was used for the heat transfer coefficients. This shows that the test section will need to be capable of at least 1 MW/m^2 of heat flux in order to achieve bubble departure.

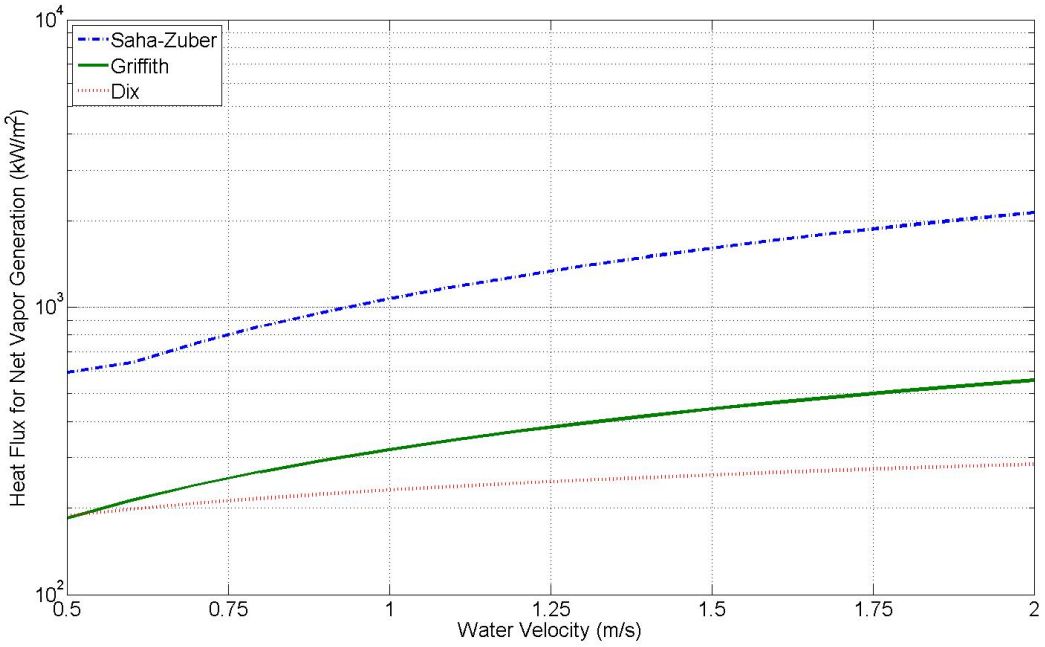

Figure B.1: Heat flux for net vapor generation versus water velocity for several different models.

C Heater Replacement Procedure

The procedure for the replacement is below and some pictures of the process are shown in Figure C.1.

1. Place the cartridge in a cold oven, and set the temperature to 100 °C.
2. After the cartridge has soaked at 100 °C for 10 minutes, increase the oven temperature to 200 °C.
3. Let the cartridge soak at 200 °C for 30 minutes.
4. Remove the cartridge from the oven and remove the heater while still hot.
5. The epoxy can be easily removed with a hobby knife. If it cools down and the epoxy gets hard to remove, it can be placed back in the oven for a few minutes to heat it back up.
6. After the cartridge has cooled to near room temperature, use acetone to clean up the dust.
7. Fit the new heater into the recess and make sure it seats without binding.
8. Cut two strips of 1/4" thick Viton® foam for the heater to sit on over the Macor®.
9. Place a flat plate that is covered in a clean room wipe over the top to make sure that everything seats properly.
10. Remove the heater and the Viton® foam strips.
11. Mix up the silver epoxy from McMaster-Carr and place a little bit along the graphite within the recess of the cartridge. The proper amount is where the epoxy forms slightly dipped surface from the edge of the graphite face down to the bottom of the the recess.
12. A small amount of Locktite 4014 should be applied to the the Macor® where the Viton® will go.
13. Place the Viton® foam strips in their location on top of the Macor®. The epoxy and Locktite will help hold them in place.
14. The top of the Viton® strip should be coated with Locktite 4014.
15. Place the heater on top of the Viton® foam, and center it properly with the silver pads pointed towards the epoxy.
16. Use the flat plate covered in a clean room wipe to press straight down on the heater and push it into place.
17. If necessary place more weight on top of the plate to balance it properly.
18. After the epoxy cures for 24 hours remove the plate and clean up any stray epoxy.
19. Seal the graphite with a thin coat of Locktite 4014 to prevent water from seeping through between the grains of the graphite.

20. Seal around the sapphire with RTV silicone to create a totally flat surface, don't get any on the active heater and let the silicone cure for at least 2 hours.

21. Reinstall the cartridge into the test section.

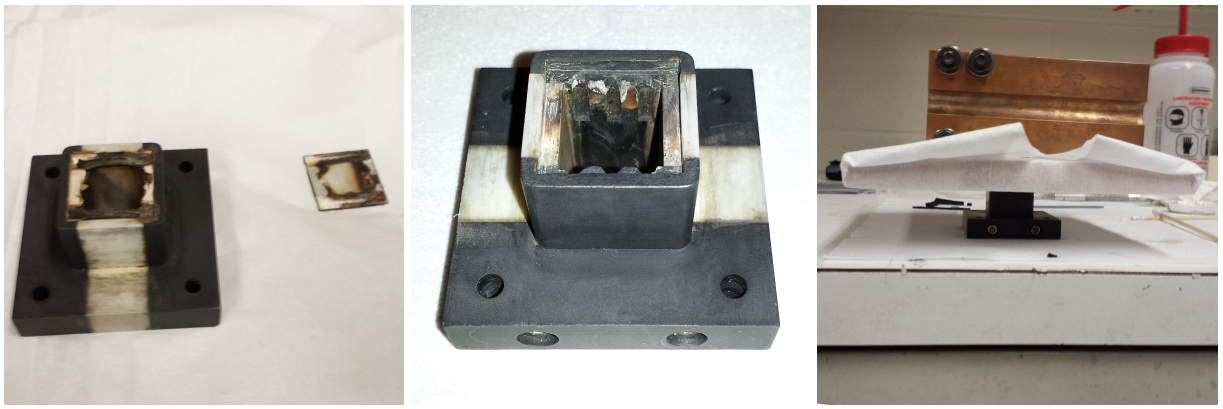

Figure C.1: Replacement of heater. Heater removed (left), heater cartridge cleaned (middle), new heater curing (right).

D Experiments without bladder

When running without the bladder, it became necessary to select a suitable cover gas. The equilibrium gas concentrations at 2 bar for several different commonly available gases are shown in Figure D.1. Nitrogen is still the best option to use even if no bladder is present.

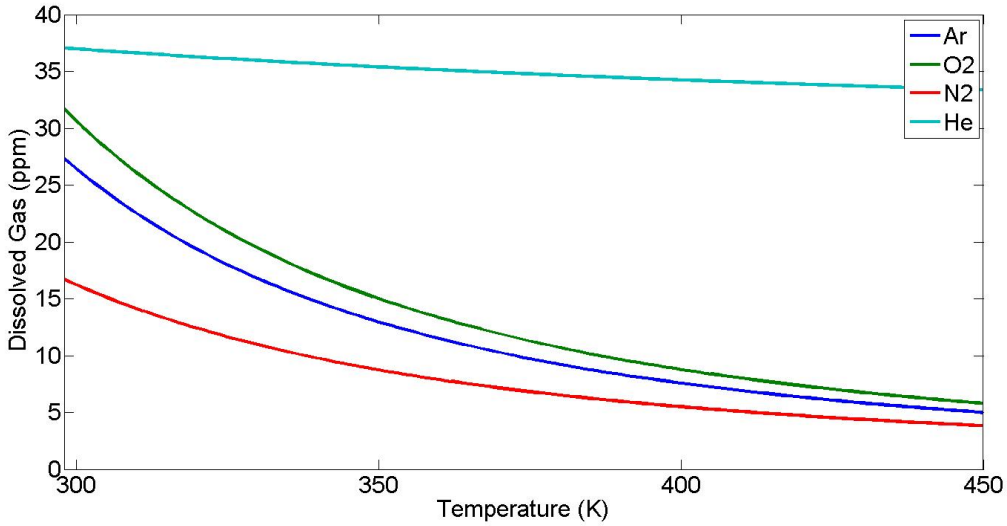

Figure D.1: Equilibrium Gas Concentration versus Temperature in water at 2 Bar.

E Overview of Interface Tracking Methods (ITM)

Interface tracking methods are techniques used to quantify the location and movement of the interfaces of phases in multi-phase flows. These techniques can be broken down into 3 distinct categories [83] [84]:

1. **Front Tracking Method** – Follows an initial given interface as the multi-phase fluid develops, each time step yields a piecewise continuous inter-facial line.

2. **Volume of Fluid Method** – Breaks the problem into sub-volumes of fluid to track the volume fraction of each phase within each sub-volume.

3. **Level Set Method** – The interface is represented by a function that stores the distance of mesh points to the interface.

E.1 Single-Phase Representation of a Multi-Phase Problem

The first concept in dealing with a multi-phase fluid is the reduction of the problem to that of a single-phase using a marker function If we choose one of the phases to be represented by Ω then the marker function χ represents the locations of each phase within a given mesh.

$$\chi = \begin{cases} 1 & \text{for } \mathbf{x} \in \Omega \\ 0 & \text{for } \mathbf{x} \notin \Omega \end{cases} \tag{E.1}$$

Thus the conservation laws can be represented by a single equation that contains the marker function, for example the conservation of mass not involving a phase change,

$$\frac{\partial \rho}{\partial t} + \nabla \cdot (\rho \mathbf{v}) = 0 \tag{E.2}$$

where ρ is given by $\rho = \rho_1 + (\rho_1 - \rho_2)\,\chi$.

E.2 Front Tracking (FT) Method

Front tracking is a numerical scheme that represents discontinuous surfaces (multi-phase interfaces) with degrees of freedom represented by an ordered set of marker points on the interface. The continuous solution is then represented by interpolating using a piecewise polynomial [85, 86]. This method was first developed by Richtmyer and Morton [87]. The points representing the front are represented by the distance from a reference surface. The interface is then evolved in time using a physical model of the phenomena involved [86]. Front tracking works well in problems where the discontinuities are important such as phase transition boundaries, flame fronts, and shock waves [85]. However, since it tracks the topology of the interface, front tracking is not ideal for multi-fluid problems involving phase changes with time [83].

E.3 Volume of Fluid (VOF) Method

This was first developed by Hirt and Nichols [88] it conserves mass and volume using a Eulerian method. The problem is broken into sub-volumes with a matrix C representing the fraction of each phase present in that volume. C is referred to as the "Color" function is defined as:

$$C = \frac{1}{V} \int_V \chi \left(\mathbf{x}, t \right) dV. \tag{E.3}$$

A value of $C = 0$ represents the cell is entirely filled by the first fluid while a value of 1 represents that the cell is completely filled with the second fluid. The interface is the region where $0 < C < 1$ and the interface line is usually taken as $C = 0.5$ where the cells volume is composed half of each phase. Problems involving M fluids are possible, but there must be $M - 1$ color functions to fully represent the cell contents. The advection equation not involving a phase change,

$$\frac{\partial C}{\partial t} + \nabla \cdot (\mathbf{v} C) = 0 \tag{E.4}$$

must be solved using a numerical method that maintains sharp interfaces [89]. Detail of how the phases are distributed within the cell is lost, the only information is the fraction of each phase [84] in the volume cell.

E.4 Level Set Method (LSM)

This was first introduced by Osher [90] and approximates the motion of inter-facial fronts. Consider an interface Γ bounding a region Ω then the level set function $\varphi \left(x, t \right)$ is defined as [91]:

$$\varphi \left(x, t \right) > 0 \quad \text{for } \mathbf{x} \in \Omega \tag{E.5a}$$

$$\varphi \left(x, t \right) < 0 \quad \text{for } \mathbf{x} \notin \Omega \tag{E.5b}$$

$$\varphi \left(x, t \right) = 0 \quad \text{for } \mathbf{x} \in \partial\Omega = \Gamma \left(t \right). \tag{E.5c}$$

$\varphi \left(x, t \right)$ is a similar marker function to that of equation (E.1), but the sign of function $\varphi \left(x, t \right)$ represents whether a given location at a given time contains the first phase (positive), the second phase (negative), or it lies on the boundary (zero). The interface movement is determined by the values of $\varphi \left(x, t \right)$ with the velocity field $\mathbf{v}$ given by equation (E.4), where $\varphi \left(x, t \right)$ is the color matrix.

The only part of the velocity that is actually needed is the component that is normal to interface. In some cases the mesh chosen may not allow for each cell to contain only one phase. In this case the interface is usually defined as the point where the void fraction is $\alpha = 0.5$. The major disadvantage of the LSM is that it does not always preserve the volume as the interface advances [84].

F HSV and IR Camera Synchronization Quantification

F.1 Synchronization Quantification Background

The synchronization offset between the IR and HSV cameras can be determined using a periodic event that occurs at a slightly different frequency than the cameras record at. The event needs to be short and well defined, and visible on both cameras at the same time. Therefore, using a traditional incandescent light is not ideal because of the thermal signature precedes the visible signal. One solution to this problem is to use two different LEDs that are driven by a single function generator that provides the signal to turn the LEDs on and off. One LED would emit in the visible range and one LED would emit in the IR range of the camera. Diodes have response times on the order of nanoseconds, which is an insignificant time scale compared to the time between frames of approximately 1ms. A diagram of a circuit to quantify the synchronization is given in Figure F.1.

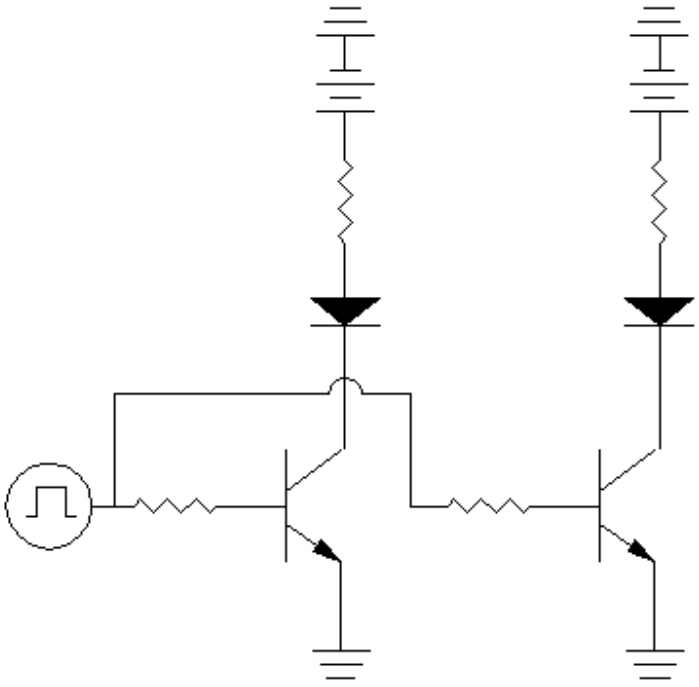

Figure F.1: HSV and IR synchronization verification circuit diagram.

Then for a given frequency for a camera of f_c, an exposure time of t_c, a strobe frequency for the diodes of f_d, and a time that the diodes remain lit t_d, an equation can be derived for the number of frames in a row where the diode being lit and the exposure of the camera will be in sync, N_s. This is given in Equation (F.1). The derivation assumes that $f_c > f_d$, $t_d < t_c$, that if the diode is lit for any amount of time during the

exposure the frame is bright, and that the frequencies are close enough that they create a single interference pattern.

$$N_s = \left(\frac{f_c}{f_c - f_d}\right) t_c f_c \left(1 + \frac{t_d}{t_c}\right) \tag{F.1}$$

The expression $\left(\frac{f_c}{f_c - f_d}\right)$ represents the total number of frames in the interference period, or the number of frames it takes for the diode pulse to return to the same point in the camera exposure. Then multiplying by t_c gives the total total time the camera is exposed in an interference period. Multiplying this expression by the frame rate of the camera, f_c, gives the total number of frames that are exposed during the interference cycle if the diode flash was an instantaneous event. Then, multiplying by $\left(1 + \frac{t_d}{t_c}\right)$ corrects for the fact that the diode will be lit for a finite amount of time.

The number of frames where the diode will be out of sync, N_{os}, with camera exposure is given by Equation (F.2). An example how the different frequencies of the camera and the diode interact combined with the effects of the exposure time of the camera and the time the diode is lit is shown in Figure F.2.

$$N_{os} = \left(\frac{f_c}{f_c - f_d}\right) \left[1 - t_c f_c \left(1 + \frac{t_d}{t_c}\right)\right] \tag{F.2}$$

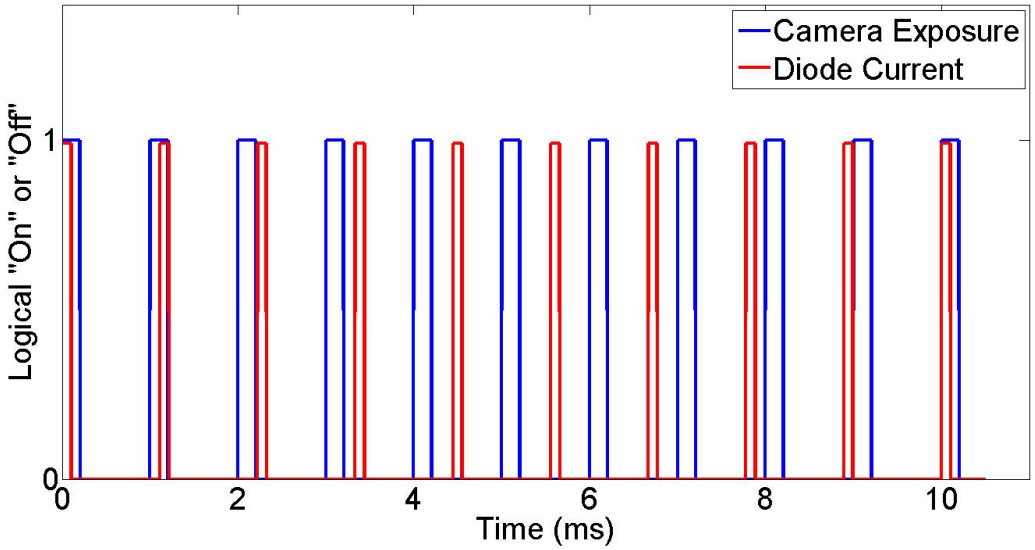

Figure F.2: Camera exposure and diode current for camera synchronization for a camera frequency of 1000 Hz, a diode flashing frequency of 900 Hz, a camera exposure time of 200 µs, and a diode current time of 100 µs.

Equations (F.1) and (F.2) can be used to do a couple of verifications on the cameras timings. First the frequency of the camera can be verified by ensuring that the correct number of light and dark frames occur in sequence. Second, the cameras synchronization can be tested to quantify how much one camera is lagging the other. This is accomplished by determining how many frames of discrepancy, N_{disc}, there are between the transition from frames where the diode is lit to frames where the diode is dark. Then the time lag of the

slow camera, t_{lag}, can be calculated by Equation (F.3).

$$t_{lag} = N_{disc}\left(\frac{1}{f_d} - \frac{1}{f_c}\right) \tag{F.3}$$

For an f_c of 2000 Hz and a f_d of 1990 Hz this leads to a time of ~3 μs per frame, so the synchronization of the cameras can be quantified down to ~3 μs.

F.2 Synchronization Quantification Results

The synchronization circuit is identical to that shown in Figure F.1. The circuit uses an IR LED that emits radiation in the wavelength range of 2.5-4.2 μm and peaks at approximately 3.6 μm while the IR camera measures in the 3-5 μm range. The visible LED is a 500 mCd Red LED with a forward operating voltage of 1.8V and operating current of 20 mA. The power transistors for each LED are identical and use an NPN rated for a CE voltage of 80V, a current of 1A, a max frequency of 3 MHz, and and a power dissipation of 30W. The response time of all of the electronic components are less than 100 ns. The transistors were switched using a HP 8116A function generator outputting a square wave 5 V in height. Its frequency accuracy for the range of interest is ±3% and its duty cycle accuracy for the setting used is 0.5 μs. Since these values have large error the actual values of the frequency (f_d and the duty cycle (t_d) were measured using an Tektronix TDS 1002B oscilloscope with 50 ppm accuracy for the time resolution, which makes the error in these values much less than the uncertainty associated with the interference pattern being incorrectly determined by 1 frame (μs). The rise and fall times of the square wave were measured and both were found to be less than 20 ns. Thus the time error on the synchronization measurements can be taken to be the equivalent to a single frame given by equation (F.3).

The test was performed by taking synchronized images with the IR and HSV camera of the pulsing diodes with the cameras set to a slightly higher frequency than that of the diode. The exposure time t_e were set to identical values for both cameras, and the IR camera was used as the master for the HSV camera for recording. The discrepancy between the interference pattern on each camera was measured. Also the number of bright frames (LEDs on) and dark frames (LEDs off) were counted to compare to the theoretical values for the camera and diode settings. A bright frame was defined as the LED being above the background range of counts, and the rest were considered dark frames. Pictures of examples of light and dark frames are shown in Figure F.3. The results are summarized in Table F.1.

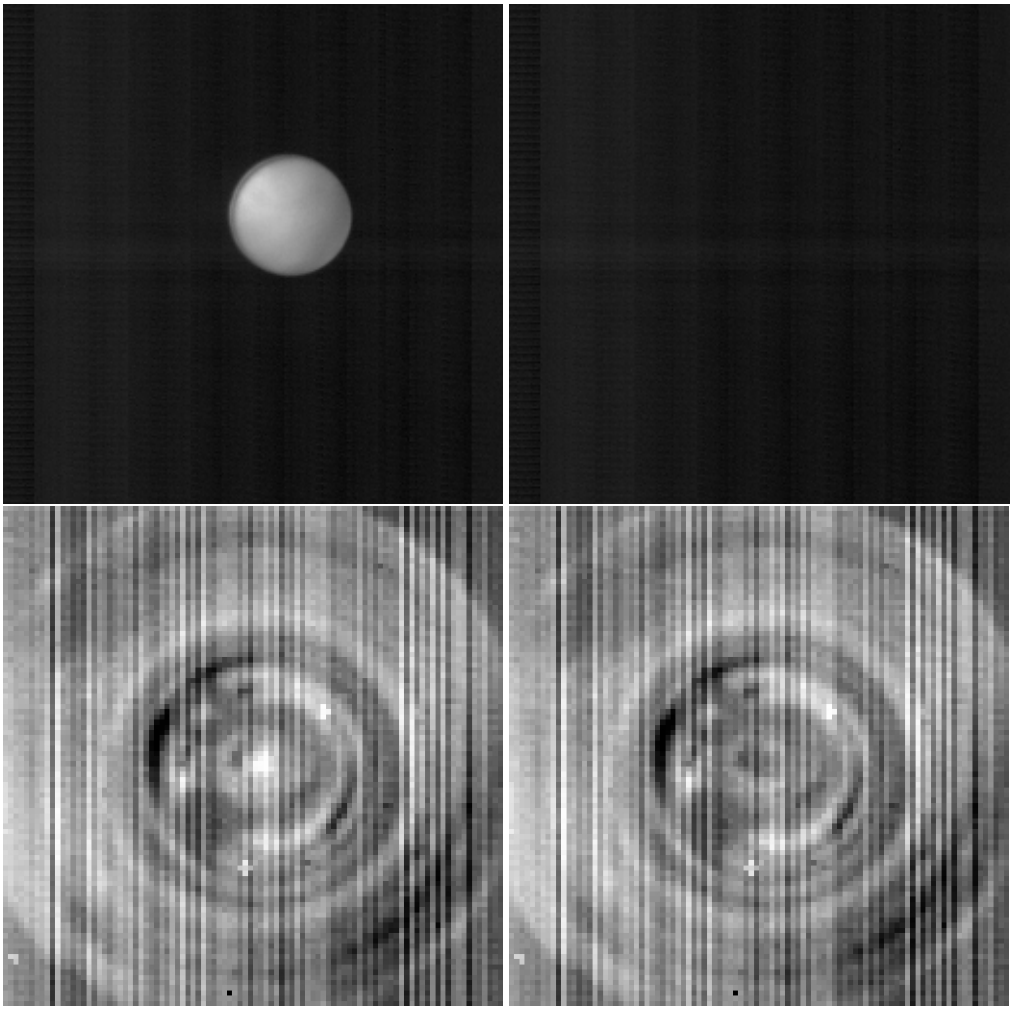

Figure F.3: Examples of bright frames (left column) and dark frames (right column) for the HSV camera (top row) and the IR camera (bottom row)

Table F.1: Summary of experimental results and theoretical calculations for IR and HSV camera synchronization. Bracketed values are measured values or theoretical values rather than the settings on the equipment.

Test Name	f_c (Hz)	t_e (µs)	f_d (Hz)	t_d (µs)	Frame Offset	Frames In Sync	Frames Out Sync	Max Camera Desync (µs)
sync1	1000	50	990	10.0	0	5	66	14.5
			[985.7]	[10.08]		[4.2]	[65.7]	
sync2	1000	50	999	10.0	0	12	177	5.3
			[994.7]	[10.08]		[11.4]	[177.8]	
sync3	2000	50	1990	10.0	0	21	148	3.0
			[1988.2]	[10.08]		[20.5]	[150.0]	
sync4	2000	50	1990	10.0	0	21	148	3.0
			[1988.2]	[10.08]		[20.5]	[150.0]	
sync5	2000	50	1990	10.0	0	21	148	3.0
			[1988.2]	[10.08]		[20.5]	[150.0]	

F.3 IR Camera and PIV System Synchronization

Xili and I performed synchronization tests between the IR camera and the PIV system. The tests were performed using the IR camera as the master and using it to trigger the PIV system. The frame rate of the IR camera for a set frame rate was measured and then this was the value set on the PIV system. The IR camera was then used to trigger the PIV system, and both cameras ran on their own internal clocks.

Table F.2: Summary of experimental results and theoretical calculations for IR and HSV camera synchronization and IR and PIV synchronization. Bracketed values are measured values or theoretical values rather than the settings on the equipment. In-sync and De-synced frame values are the values for the IR camera if there was a slight difference between the IR camera and the HSV camera.

Test Name	f_c (Hz)	t_e (µs)	f_d (Hz)	t_d (µs)	Frames In-Sync	Frames Out of Sync	Frame Offset	Time per Frame Off-set (µs)	Max De-Sync (µs)
sync1	1000	50	990 [985.7]	10.0 [10.08]	5 [4.2]	66 [65.7]	0	14.5	14.5
sync2	1000	50	999 [994.7]	10.0 [10.08]	12 [11.4]	177 [177.8]	0	5.3	5.3
sync3	2000	50	1990 [1988.2]	10.0 [10.08]	21 [20.5]	148 [150.0]	0	3.0	3.0
sync4	2000	50	1990 [1988.2]	10.0 [10.08]	21 [20.5]	148 [150.0]	0	3.0	3.0
sync5	2000	50	1990 [1988.2]	10.0 [10.08]	21 [20.5]	148 [150.0]	0	3.0	3.0
PIVsync1	2000 [2001]	50	1990 [1988.2]	10.0 [10.08]	18 [18.9]	142 [138.3]	137	3.2	438
PIVsync2	2000 [2001]	50	1990 [1988.2]	10.0 [10.08]	18 [18.9]	141 [138.3]	107	3.2	342
PIVsync3	1000 [1000.5]	50	990 [985.7]	10.0 [10.08]	5 [4.1]	65 [63.5]	20	15.0	300.4
PIVsync4	1000 [1000.5]	50	990 [985.7]	10.0 [10.08]	5 [4.1]	65 [63.5]	27	15.0	405.6
PIVsync5	1000 [1000.5]	50	980 [975.3]	10.0 [10.08]	3 [2.4]	38 [37.3]	18	25.8	465.1
PIVsync6	1000 [1000.5]	50	980 [975.3]	10.0 [10.08]	3 [2.4]	38 [37.3]	18	25.8	465.1

The PIV system consistently lagged behind the IR camera by about 400 µs. However, the lag was not constant and ranged from 300-470 µs. The PIV camera also consistently had a shorter interference pattern than the IR camera and than what was theoretically expected, which indicates the PIV camera is operating at a faster frequency. This amounted to approximately a 0.5 Hz faster capture rate than the IR camera when they were set to the same frame rate. This has the affect of the PIV camera slowly advancing on the timing

of the IR camera, and eventually passing it. Thus, the frequency of the HSV camera needs to be slightly tweaked to prevent it from getting too far out of sync with the IR camera, or the slightly faster frequency can be used to make up the initial lag of the PIV camera behind the IR camera.

F.4 Burst Sync Mode

The Phantom HSV V12.1 camera and the IRC806HS camera follows TTL pulses regardless of the frequency. Thus, they takes a picture at every pulse even if the pulses arrive in an irregular fashion. With a function generator that can operate in burst mode (sends a series of pulses for each input pulse) the IR and HSV may be "perfectly synchronized" (i.e. less than 3 μs disparity) at different frame rates. Figure F.4 shows the setup for this method to be used.

Unfortunately, this method will not work with the LaVision PIV system since it will not respond to individual pulses, but instead just a trigger pulse to start the acquisition. Therefore, on the PIV system the best that we can do is to provide the starting signal and have them operate at different frame rates using their own clocks and have the 300-400 μs discrepancy shown in F.2.

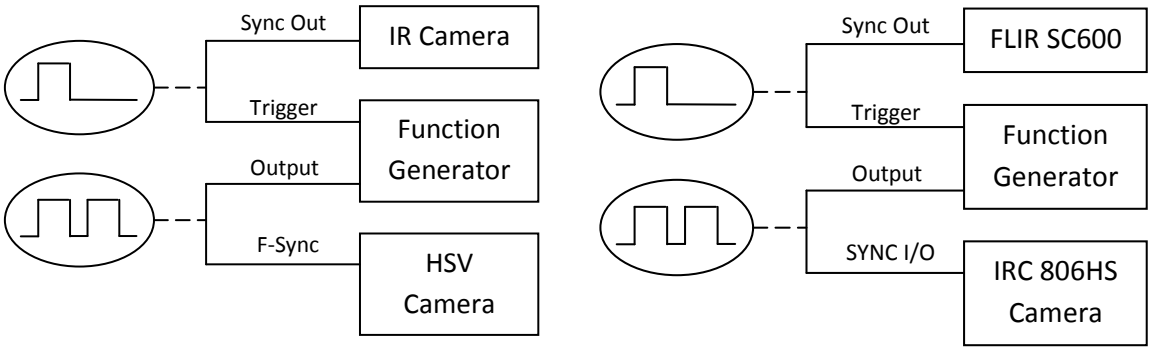

Figure F.4: Operating a function generator in burst mode to operate the FLIR SC6000 IR and Phantom V12.1 HSV cameras (left) and FLIR and IRC806HS cameras (right) at different frame rates while still maintaining frame by frame synchronization. The ovals on the left show the wave form, and the line labels show the connections on the three devices.

G IR Cameras 806HS Standard Operating Procedure

Standard Operating Procedure for IR Cameras IRC806HS High Speed IR Camera

Revision 1, May 28, 2013
For WinIRC version 4.0.12 rev K
Written by: Bren Phillips (bren@mit.edu)
Maintained by: Dr. Tom McKrell (tmckrell@mit.edu)

I. Precautions, Prerequisites, and Limitations

A. This SOP is not a replacement for reading, understanding, and following the manual for WinIRC and the IRC806HS, but is a quick reference, provides information for the specific camera/frame grabber setup, and incorporates logistics of using the camera in the lab.

B. If there are any questions on the operation or maintenance of the camera or software, contact Dr. Tom McKrell (tmckrell@MIT.EDU).

C. Only the High Speed Camera Computer on the black cart is the only computer capable of operating the camera. Take care when moving it around the lab. The computer is capable of simultaneously operating the FLIR camera and the Phantom HSV camera.

D. There is limited storage space on the High Speed Camera Computer, please remove your files at the end of each session. It is designed for high data transfer rates to the SSDs and thus space is very costly. The capture array only has 1 TB of storage.

E. The WinIRC software must be installed on the computer and the frame grabber properly configured. For information on how to do this refer to the manual. If problems arise, Dr. McKrell can contact Arn Adams (arn.adams@ircameras.com), Paul Viren (paul.viren@ircameras.com), or Elliot Rittenberg (elliott@ircameras.com) for assistance. Normally this should have already been performed.

F. Do not touch the silicon Dewar window, or any of the lenses, even with gloves on. If the lenses or Dewar window needs to be cleaned then contact Dr. McKrell.

G. If used with the PIV system or Photonics Nd-YAG laser, care must be taken to ensure that there is sufficient reduction of the secondary 1053 nm beam (IR) between the laser and the sensor. The laser and camera **should only** be used with

a filter in place which filters out the 1053 beam (currently filters 2 or 3, see Precaution Z), and there should be cylindrical optics in use on the laser (i.e. no direct beam into the camera as this could also damage the IR optics).

1. Ideally water should be between the laser and the camera to act as shielding for the 1053 nm beam.

2. The 527 nm primary beam is completely shielded by the Dewar window.

H. The camera should always be securely mounted as soon as removed from the storage case.

I. The lens shall not be attached to the camera until the camera is securely mounted.

J. The lens and camera must always be properly protected from the experiment; this includes any possible failure mechanisms.

K. Liquid nitrogen should be handled with the proper technique and PPE.

L. The liquid nitrogen funnel should always be handled by the Styrofoam insulator to prevent cryogenic burns.

1. Do not touch the stem of the funnel or the inside of the funnel to keep it clean.

2. When setting the funnel down, place it upside down with the stem sticking up.

M. The liquid nitrogen Dewar shall always be filled with the camera mounted and in an upright position.

1. The Dewar takes about 1 L of nitrogen for initial cooling, and 30 minutes to reach a stable operating temperature. It then holds about 1/3 liter total. If the Dewar is pumped down to $<2x10^{-6}$ torr, a cooled and filled Dewar will last 4-8 hours.

N. The liquid nitrogen funnel should be oriented such that the overflow channels on the funnel are pointing away from the lens of the camera.

O. When emptying the LN2 from the camera Dewar take care to not pour the nitrogen onto anyone's skin. Take special note of fingers that the nitrogen could flow over while dumping.

P. The Camera Link cables and synchronization cables shall be attached and detached from the camera while power to the camera is secured (power switch off). However, there is no need to turn off the computer when attaching cables.

Q. The Camera Link cables shall be mechanically supported so that the force and moment on the camera connections is minimized.

R. **Do Not** exceed more than +5 V pulse on the "SYNC I/O" port on the camera. A +4 V pulse is an ideal value to use. Be sure the offset on the function generator is set such that it goes from 0 V to +4 V and not -2 V to +2 V.

S. The frame grabber fan shall be set to maximum speed prior to connecting to the camera.

T. The frame grabber window must:

1. Have an area that is divisible by 2^{11} pixels (2048 pixels).
2. Have a minimum height of 8 pixels.
3. Have a minimum width of 320 pixels. When the FPA is in 4 output mode, there is no benefit to decreasing below 640 vertical lines other than to reduce the size of the stored file.
4. Be the same size or smaller than the FPA window.

U. Frame rates for various window sizes can be determined by visiting http://www.sbfp.com/fpa_selector.html. Select the "SBF 209 (digital)" as the focal plane array. Select 4 outputs at 40 MHz per output. The bits per pixel can be set as desired, the rates are higher at 13 bits, but with a lower temperature resolution. Then select the height in pixels you are interested in to see the max frame rate.

V. If you get an unstable image and can't correct it go to Setup>Camera States and load one of the saved states on the camera.

W. The frame grabber window should be 4 lines smaller than the FPA window if the counts on the pixels are less than 4000 counts.

1. If the image has less than 4000 counts in each pixel, there will be non-uniformity in the last 4 lines on the FPA.

X. Right clicking on the playback window of a stored file may crash the WINIRC program.

Y. The liquid nitrogen Dewar on the IR camera requires periodic pumping down. Refer to the camera manual for the proper procedure.

Z. The filter wheel has the following filters installed:

1. None
2. 3.0-5.0 μm band pass
3. 3.1-3.3 μm band pass (see below)

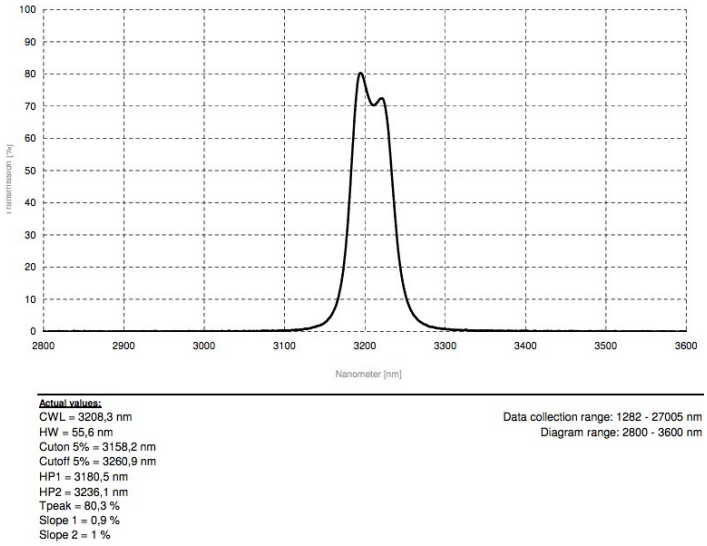

4. None

AA. The Camera Link cables should not be stepped on coiled tightly, twisted or the connectors dropped on the floor. Usually they should be loosely coiled and stored at the appropriate stowage location on the back of the computer desk.

BB. When using external synchronization from a function generator for the HSV camera and the IR camera, the offset has been measured to be about 6 µs.

CC. When setting up the camera, be aware of IR reflections which may affect the quality of your data.

DD. **Do Not** adjust the RampHi or RampLo settings on the camera unless directed to do so by IRCameras.

EE. **Do Not** adjust the number of outputs on the camera unless approved by Dr. McKrell or told to do so by IRCameras.

II. Standard Operating Procedure

A. Camera setup

1. Remove the camera from the pelican case and mount to a secure structure (tripod, optical table, etc.).

2. Remove the cap from the liquid nitrogen Dewar, and place the funnel into the camera. Fill with liquid nitrogen from a portable Dewar until the nitrogen overflows. Watch for overflowing nitrogen to avoid injury or damage to equipment.

3. The Camera Link cables can be attached and properly supported between the computer and the camera. Base 1 goes to port "0" on the frame grabber and "CAMLINK 1" on the camera. Base 2 goes to port "1" on the frame grabber and "CAMLINK 2" on the camera.

4. If desired synchronization coaxial cable may be attached to the camera.

5. After 20-30 minutes the Dewar should be topped off to where it overflows and the cap installed onto the camera Dewar.

6. After the nitrogen is topped off from the initial fill, the Dewar window cover may be removed and the desired optics attached. The large lobe of the lens goes at the top of the camera and the lens rotated clockwise until it snaps into place. Note that if an extension ring is used there will be not locking; just turn the lens until it hits a hard stop.

7. Plug in the camera power supply to a 115 VAC surge protected supply and verify all cable connections.

8. Push the top of the power rocker to power on the camera, a green light on the rocker should illuminate, the electronics cooling fan should start, and the filter wheel motor will find center.

9. It takes about 1 minute for the camera to boot up.

10. When the "Status" light on the back of the camera turns green, then load the WinIRC software.

B. Camera Operation

1. You can control the brightness and contrast of the image by holding the right mouse button and moving the mouse right and left (brightness) or up and down (contrast)

2. Go to Setup>Window Size and Position and set the parameters for the FPA and the frame grabber, observe precaution I.T-I.W. Select "OK" to approve new window

3. Go to Setup>Video Oscilloscope. Observe the FPA temperature at the top of the oscilloscope; it should be 77-80K. If it is not in this range and is not still cooling check the nitrogen level in the camera Dewar, and add as necessary.

4. Observe the electronics temperature at the top of the oscilloscope, it should be < 40°C, if the temperature is higher, secure power to the camera and inform Dr. McKrell.

5. Set the desired integration time and frame rate. The integration time needs to be set so that there is sufficient signal at the lowest temperature of interest, and that the pixels don't saturate at the highest temperature of interest (this should be observed before a NUC is applied)

6. If it is desired to enable metadata, go to Setup>Diagnostics, click the "Display" tab, look for the "Metadata" pane, set the "Overwrite Row" to the row you want to use for metadata (usually 1) and click the "Enable" box. The metadata should appear in the box at the bottom. The metadata will be saved with the file, and can be viewed by returning to this window while reviewing a saved file.

7. Go to Calibration>New NUC and set the desired settings. The NUC should be performed after the FPA is thermally stable (usually about 30 minutes after initial LN2 fill), or the settings will drift. A recommended set of settings is below. Normally a two point correction should be used with black body simulators at two different temperatures that bracket the "count range" you are interested in. Typically one around 4000 counts and one around 12000 counts works well. Follow the onscreen directions to perform the NUC. The blackbody should fill the field of view and be near out of focus. Be aware that certain numbers of frames to average will sometimes cause errors in performing a NUC.

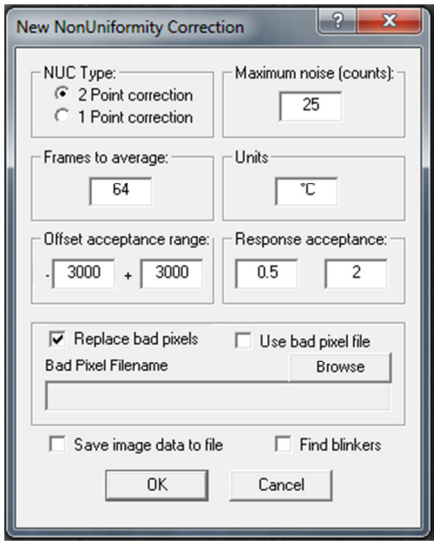

8. After the NUC is applied, go to Calibration>Save NUC to save the NUC to a file. A NUC is only valid for a given window setup, frame rate, and integration time. Changing any of these will make the NUC not valid.

9. If the camera state is one you will be using often, go to Setup>Camera States to save the state to a file to minimize setup time for the next use.

10. Alternatively to performing steps 1-9 you can go to Setup>Camera States to load a saved state and Calibration>Load NUC to load a matching NUC.

11. The count to temperature calibration needs to be performed prior to taking data. This is best performed in situ, for a given optical setup, and the method varies with various experiments. Dr. McKrell can help with your application.

12. When the settings are as desired and a calibration curve has been obtained, go to File>Video Save to capture an image sequence. You can set the filename, be sure to use the RAID array for capturing, which is drive E:\

13. Set the trigger, number of grabs, and frames per grab to the desired file. When ready click “Grab” to start the acquisition.

14. To perform a synchronized grab, select the Camera head “SyncIn for each frame” and provide a TTL input signal to the “SYNC I/O” port for each frame you want to grab.

C. Camera Shutdown

1. Close WinIRC.

2. Turn off power switch.

3. Disconnect sync and Camera Link cables.

4. Stow Camera Link cables on back of cart.

5. Remove lens and cover Dewar window with protective cover.

6. Remove the camera from the mounting and dump out the leftover liquid nitrogen.

7. Pack the camera into the pelican case along with the power cord.

8. Return the lens and blackbody simulators to the FLIR camera case.

9. Return camera in case to McKrell’s office.

10. Return tripod to McKrell’s office if necessary.

11. Return the computer to the PIV room.

III. Example window settings

A. As Configured by IRC max of ~470 fps at 640x512

FPA	
4	640
2	516
Frame grabber	
0	640
2	512

B. Max of ~1250 fps at 320x192

FPA	
160	320
160	196
Frame grabber	
0	320
0	192

C. Max of ~2403 fps at 320x96

FPA	
160	320
206	100
Frame grabber	
0	320
0	96

H Experiment Manufacturing Drawings

H.1 Test Section

Table H.1: Test Section Drawings List

Drawing Name	Description
FlowCellAssembly	Assembled quartz flow cell
Flange	Quartz Flow cell flange
FrontPlate	Quartz front plate for machined surfaces to make up FrontAssembly
FrontAssembly	Quartz front face with machined front plate epoxied to it
Front&Back	Quartz front and rear plate before additional machining
Side	Quartz side plate for HSV optical access

The "FrontAssembly" was modified slightly to correct Ferro breaking the sharp edge on the front face on the interior of the flow channel. It was ground down and re-polished to remove the broken edge. A summary of the modification is shown in Figure H.1

The inserts in the front face were actually helical coils, McMaster-Carr # 91732A204 instead of # 99362A100 as listed on "FrontPlate" and "FrontAssembly" drawing Note 1.

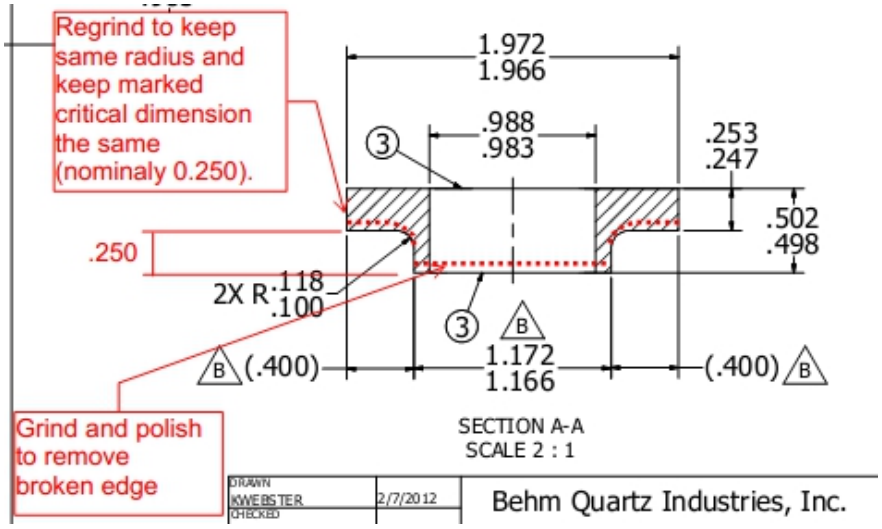

Figure H.1: Modification to the front plate to make the inner surface be totally smooth.

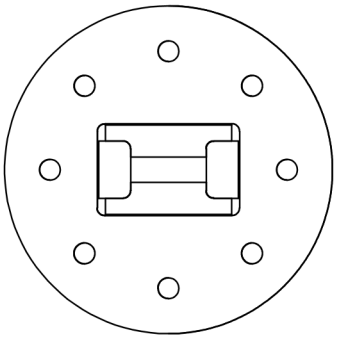

BOTTOM

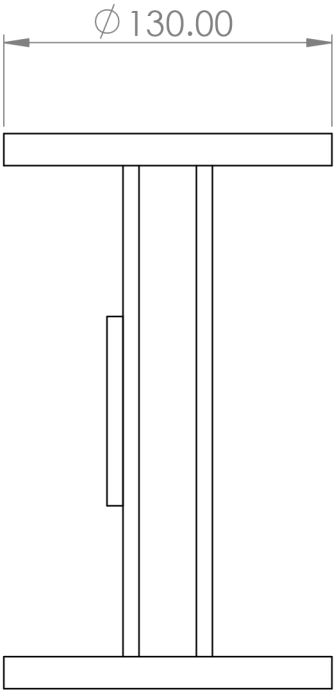

RIGHT

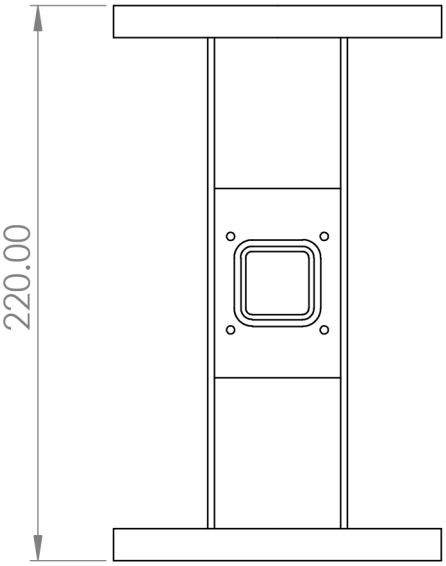

FRONT

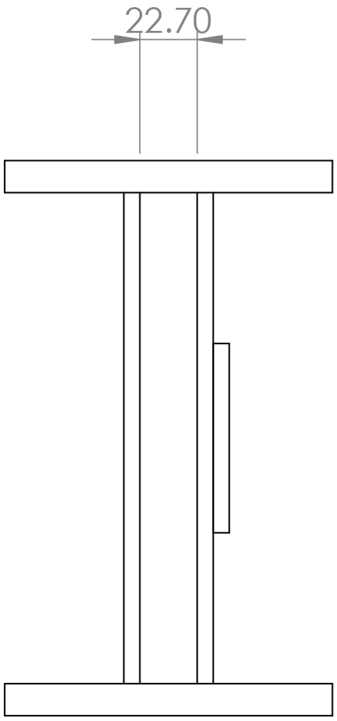

LEFT

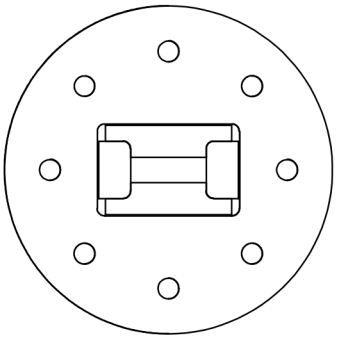

TOP

		DIMENSIONS ARE IN mm TOLERANCES ARE 0.03 mm UNLESS OTHERWISE NOTED.		NAME	DATE
			DRAWN	BAP	8/31/2011
			CHECKED		
			ENG APPR.		
			MFG APPR.		
		MATERIAL Quartz	Q.A.		
			COMMENTS:		
NEXT ASSY	USED ON	FINISH VARIOUS			
APPLICATION		DO NOT SCALE DRAWING			

MIT

138 Albany St.
NW13-239
Cambridge, MA 02139

Bren Phillips
816-258-3220

SIZE	DWG. NO.	REV.
A	FlowCellAssembly	D
SCALE:1:3	WEIGHT:	SHEET 1 OF 3

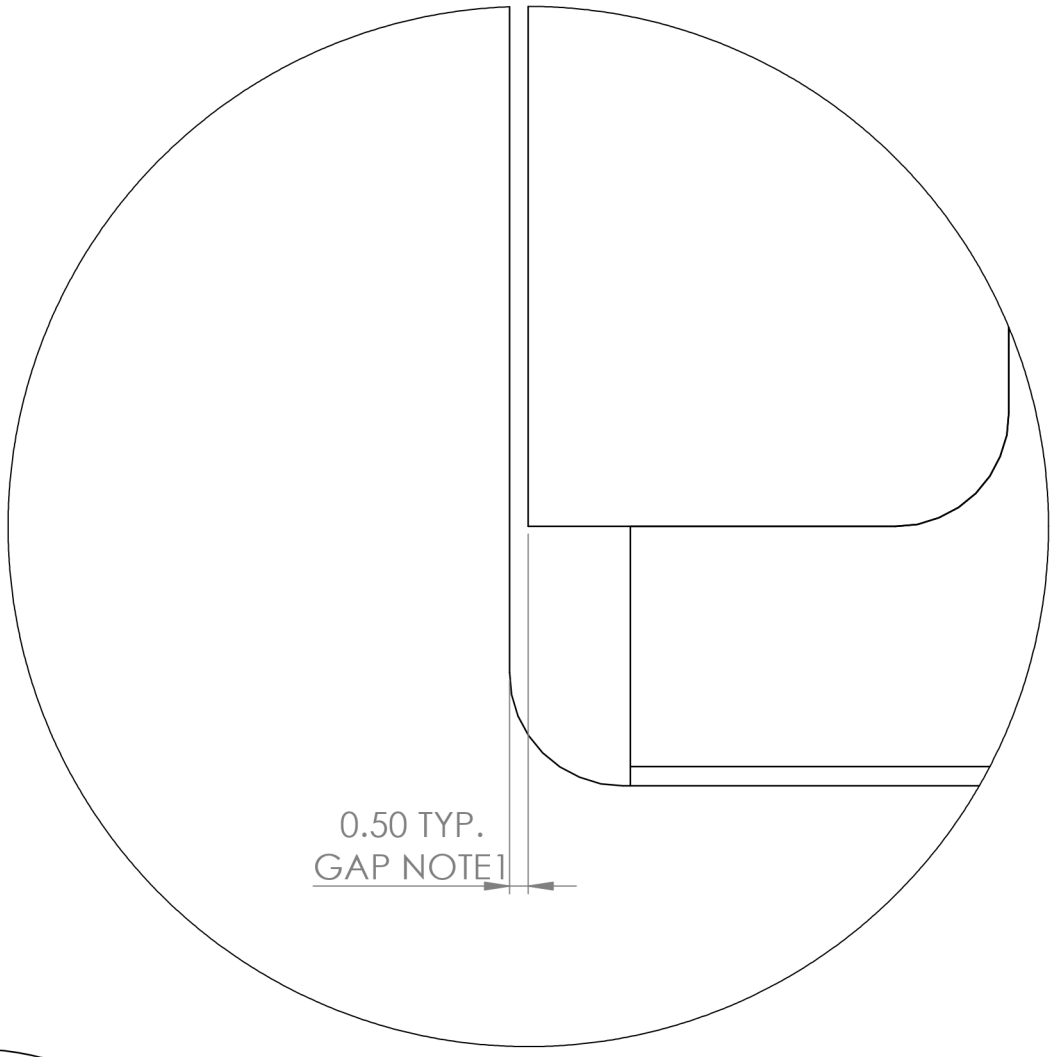

DETAIL A
SCALE 5 : 1

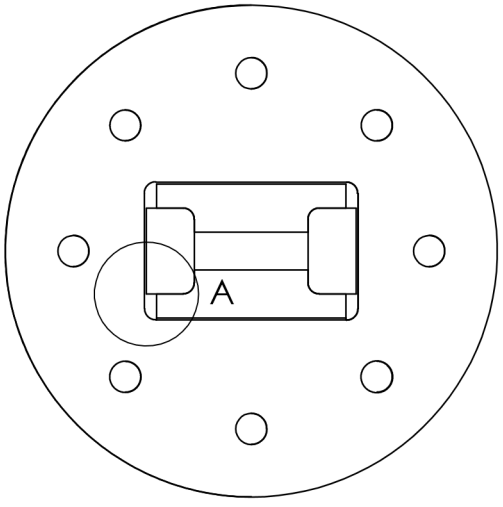

TOP

		DIMENSIONS ARE IN mm TOLERANCES ARE 0.03 mm UNLESS OTHERWISE NOTED.		NAME	DATE
			DRAWN	BAP	8/31/2011
			CHECKED		
			ENG APPR.		
			MFG APPR.		
			Q.A.		
		MATERIAL Quartz	COMMENTS: NOTE1: Bond thicknesses for Duralco 4463 epoxy should be 5-10 mils thick		
NEXT ASSY	USED ON	FINISH VARIOUS			
APPLICATION		DO NOT SCALE DRAWING			

MIT

138 Albany St.
NW13-239
Cambridge, MA 02139

Bren Phillips
816-258-3220

SIZE	DWG. NO.	REV.
A	FlowCellAssembly	D
SCALE:1:2	WEIGHT:	SHEET 2 OF 3

FRONT PLATE AND FRONTFACE COMPONENTS SHOULD BE BONDED TOGETHER WITH DURLACO 4463 EPOXY PRIOR TO MACHINING

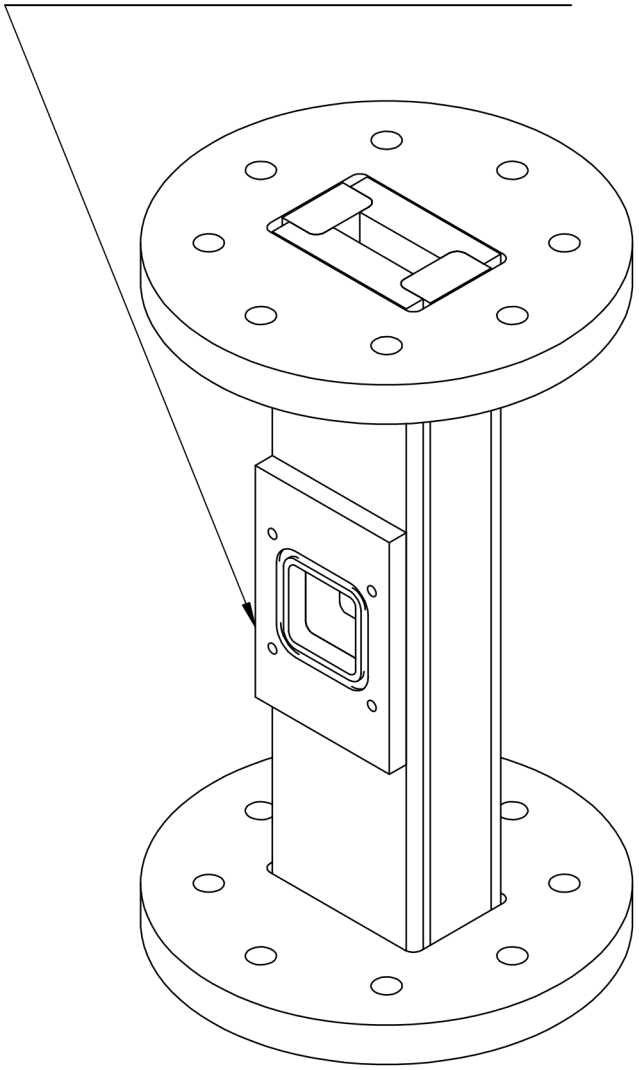

ISOMETRIC

		DIMENSIONS ARE IN mm TOLERANCES ARE 0.03 mm UNLESS OTHERWISE NOTED.		NAME	DATE
			DRAWN	BAP	8/31/2011
			CHECKED		
			ENG APPR.		
			MFG APPR.		
		MATERIAL Quartz	Q.A.		
			COMMENTS:		
NEXT ASSY	USED ON	FINISH VARIOUS			
APPLICATION		DO NOT SCALE DRAWING			

MIT

138 Albany St.
NW13-239
Cambridge, MA 02139

Bren Phillips
816-258-3220

SIZE	DWG. NO.	REV.
A	FlowCellAssembly	D
SCALE:1:2	WEIGHT:	SHEET 3 OF 3

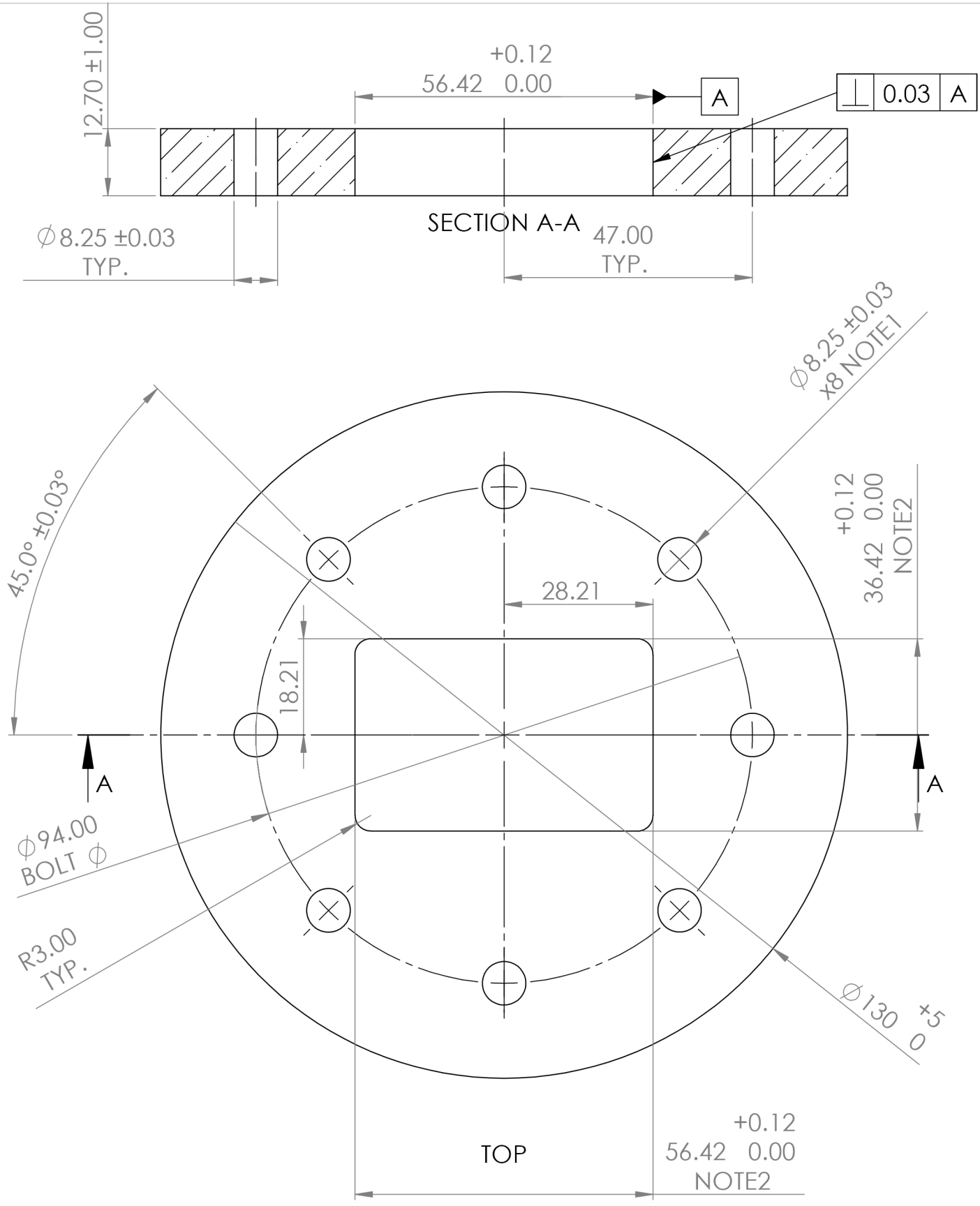

		DIMENSIONS ARE IN mm TOLERANCES ARE 0.03 mm UNLESS OTHERWISE NOTED.		NAME	DATE
			DRAWN	BAP	8/31/2011
			CHECKED		
			ENG APPR.		
			MFG APPR.		
		MATERIAL Quartz	Q.A.		
			COMMENTS:		
NEXT ASSY	USED ON	FINISH NONE	NOTE1: The 8 holes are also for alignment using AlignmentPin part. NOTE2: The center "rectangular" hole dimesnions should be adjusted based on as received quartz thickness for 0.020" clearance around the channel		
APPLICATION		DO NOT SCALE DRAWING			

MIT

138 Albany St.
NW13-239
Cambridge, MA 02139

Bren Phillips
816-258-3220

SIZE	DWG. NO.	REV.
A	Flange	D

SCALE:1:1	WEIGHT:	SHEET 1 OF 2

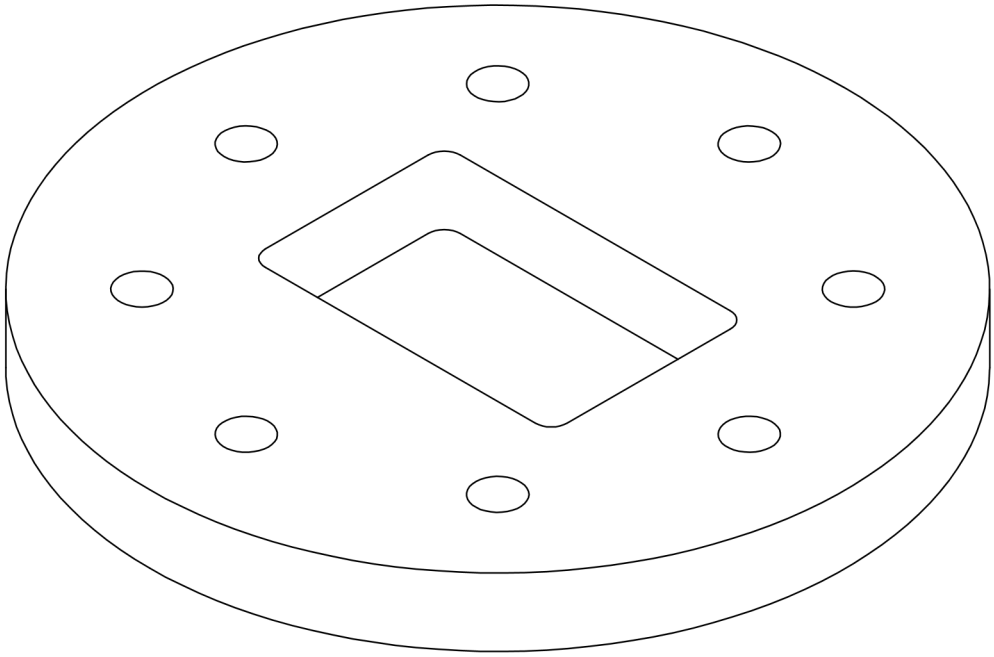

ISOMETRIC

		DIMENSIONS ARE IN mm TOLERANCES ARE 0.03 mm UNLESS OTHERWISE NOTED.		NAME	DATE
			DRAWN	BAP	8/31/2011
			CHECKED		
			ENG APPR.		
			MFG APPR.		
			Q.A.		
		MATERIAL Quartz	COMMENTS:		
			The final assembly contains 2 of this flange.		
NEXT ASSY	USED ON	FINISH NONE			
APPLICATION		DO NOT SCALE DRAWING			

MIT

138 Albany St.
NW13-239
Cambridge, MA 02139

Bren Phillips
816-258-3220

SIZE	DWG. NO.	REV.
A	Flange	D

SCALE:1:1	WEIGHT:	SHEET 2 OF 2

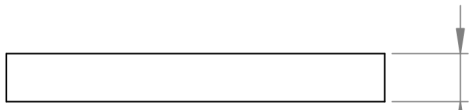

BOTTOM

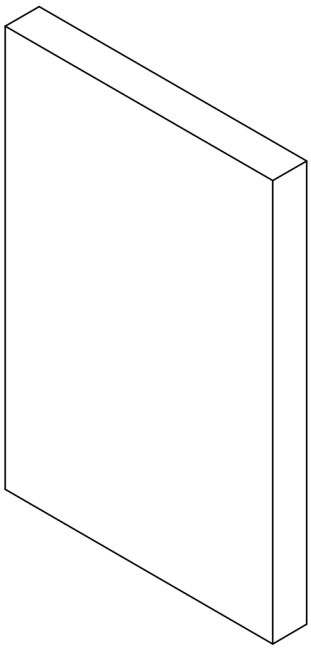

ISOMETRIC

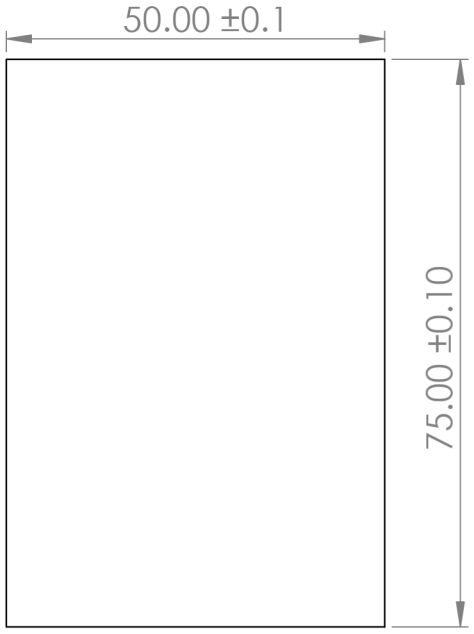

RIGHT

FRONT

LEFT

TOP

THIS PART IS JOINED WITH ONE OF FRONT&BACK USING DURALCO 4463 EPOXY. THEN FURTHER MACHINED AS SHOWN IN DRAWING FRONTASSEMBLY.

		DIMENSIONS ARE IN mm TOLERANCES ARE 0.03 mm UNLESS OTHERWISE NOTED.		NAME	DATE
			DRAWN	BAP	12/01/11
			CHECKED		
			ENG APPR.		
			MFG APPR.		
		MATERIAL Quartz	Q.A.		
			COMMENTS:		
NEXT ASSY	USED ON	FINISH NONE			
APPLICATION		DO NOT SCALE DRAWING			

MIT

138 Albany St.
NW13-239
Cambridge, MA 02139

Bren Phillips
816-258-3220

SIZE	DWG. NO.	REV.
A	FrontPlateBare	D
SCALE:1:1	WEIGHT:	SHEET 1 OF 1

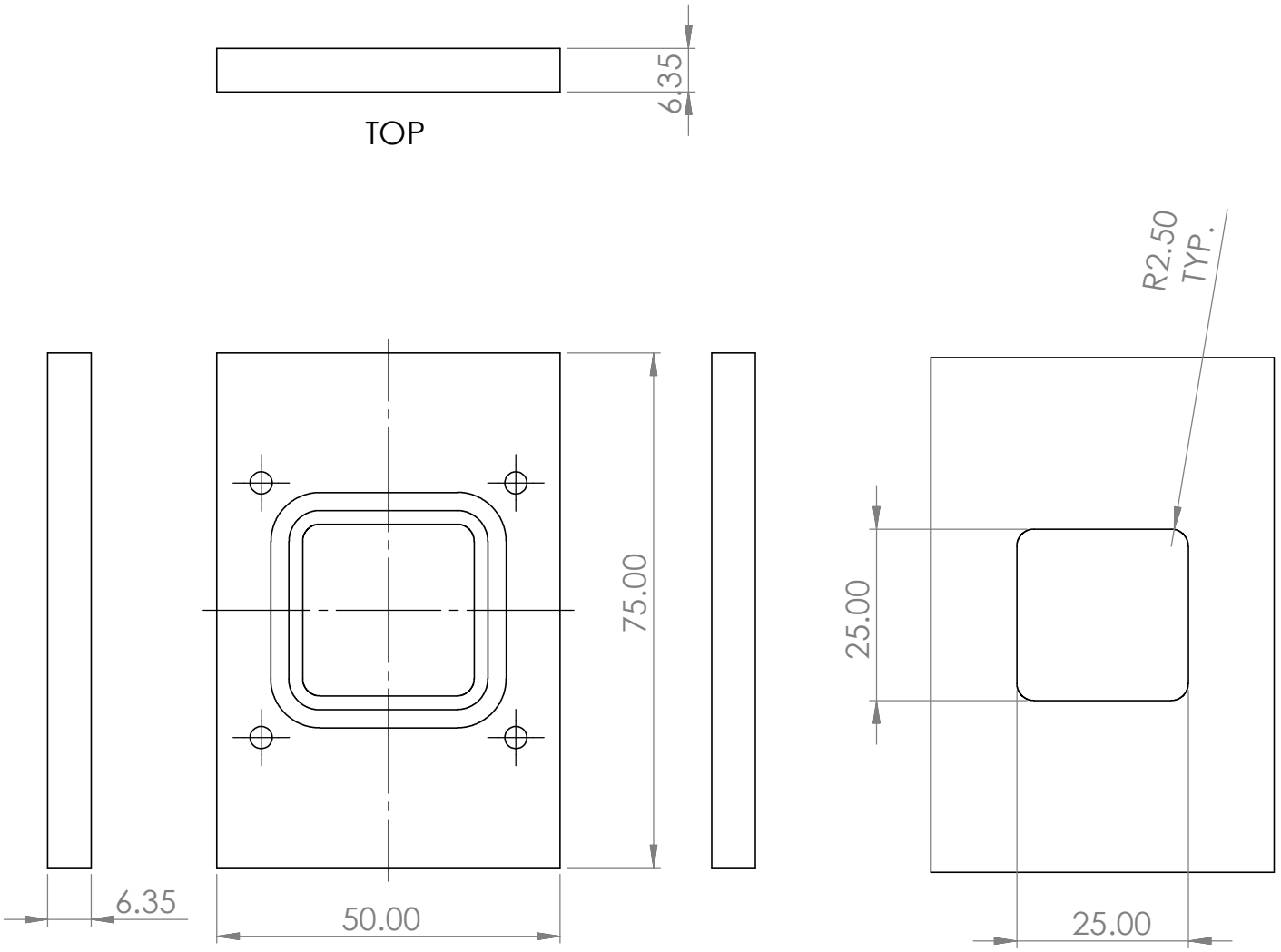

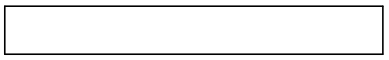

BOTTOM

		DIMENSIONS ARE IN mm TOLERANCES ARE 0.03 mm UNLESS OTHERWISE NOTED.		NAME	DATE
			DRAWN	BAP	8/31/2011
			CHECKED		
			ENG APPR.		
			MFG APPR.		
		MATERIAL Quartz	Q.A.		
			COMMENTS:		
NEXT ASSY	USED ON	FINISH NONE			
APPLICATION		DO NOT SCALE DRAWING			

MIT

138 Albany St.
NW13-239
Cambridge, MA 02139

Bren Phillips
816-258-3220

SIZE	DWG. NO.	REV.
A	FrontPlate	C
SCALE:1:1	WEIGHT:	SHEET 1 OF 3

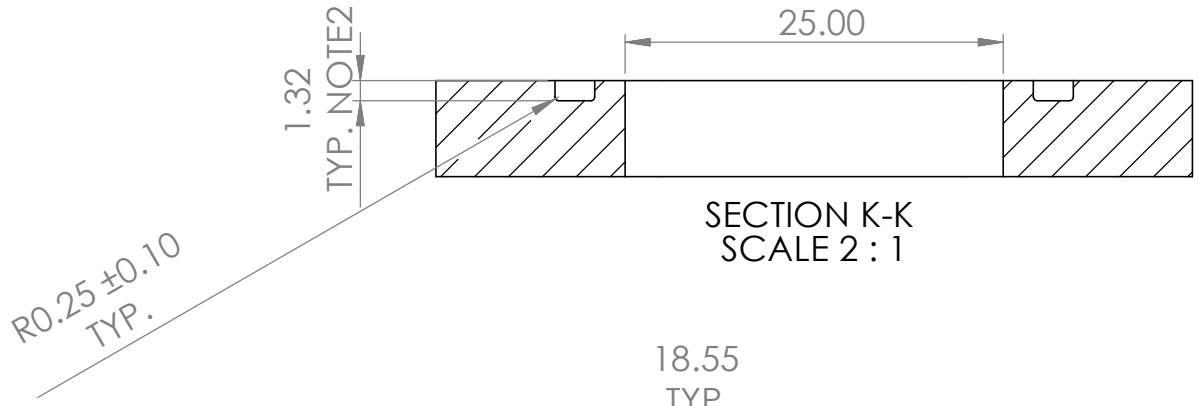

SECTION K-K
SCALE 2 : 1

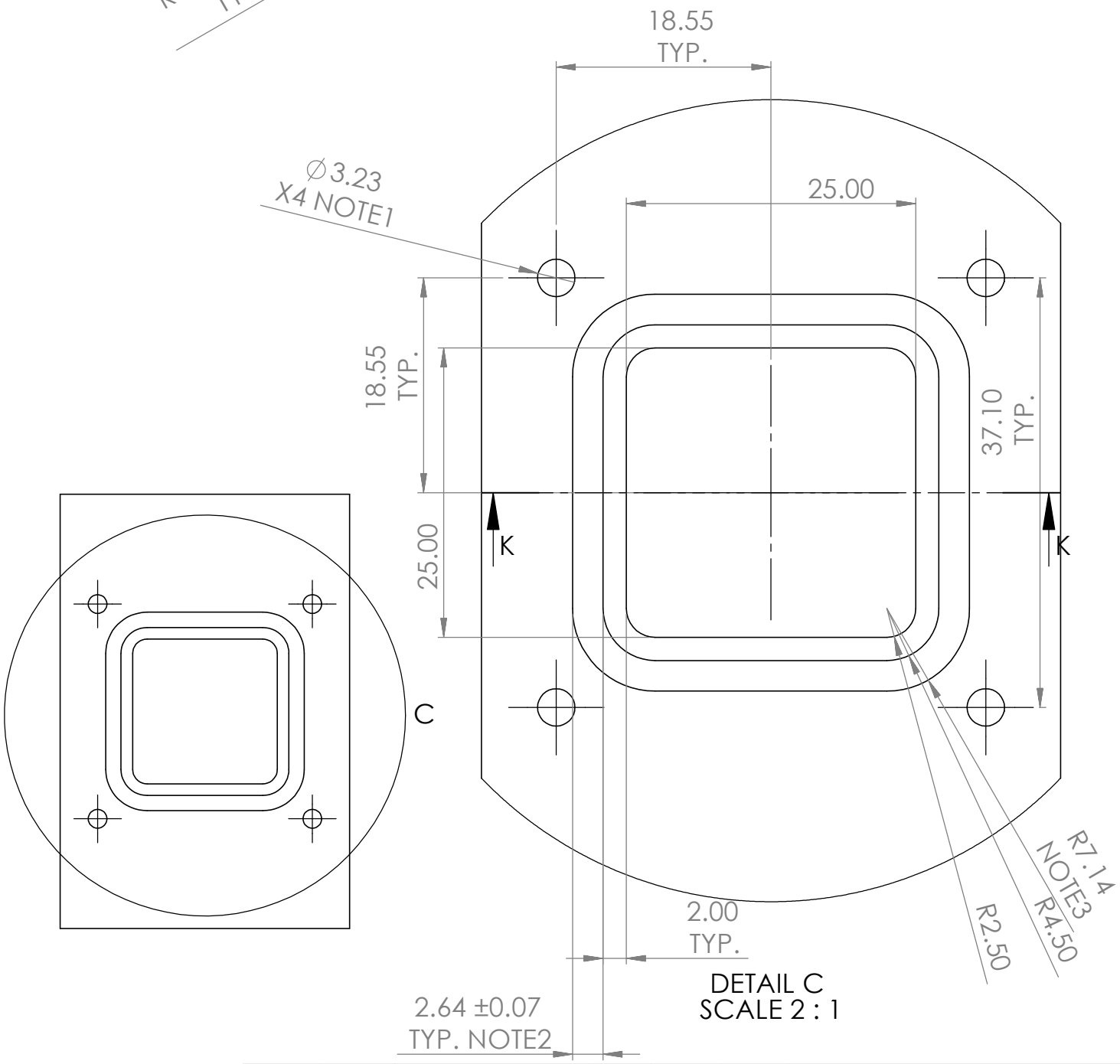

DETAIL C
SCALE 2 : 1

		DIMENSIONS ARE IN mm TOLERANCES ARE 0.03 mm UNLESS OTHERWISE NOTED.		NAME	DATE
			DRAWN	BAP	8/31/2011
			CHECKED		
			ENG APPR.		
			MFG APPR.		
			Q.A.		
		MATERIAL Quartz	COMMENTS: NOTE1: Approx 5mm deep holes for McMaster 99362A100 insert NOTE2: Groove for 1/16" O-ring NOTE3: Tolerance on fillet radiuses +/- 0.1 mm		
NEXT ASSY	USED ON	FINISH NONE			
APPLICATION		DO NOT SCALE DRAWING			

MIT

138 Albany St.
NW13-239
Cambridge, MA 02139

Bren Phillips
816-258-3220

SIZE	DWG. NO.	REV.
A	FrontPlate	C
SCALE:1:1	WEIGHT:	SHEET 2 OF 3

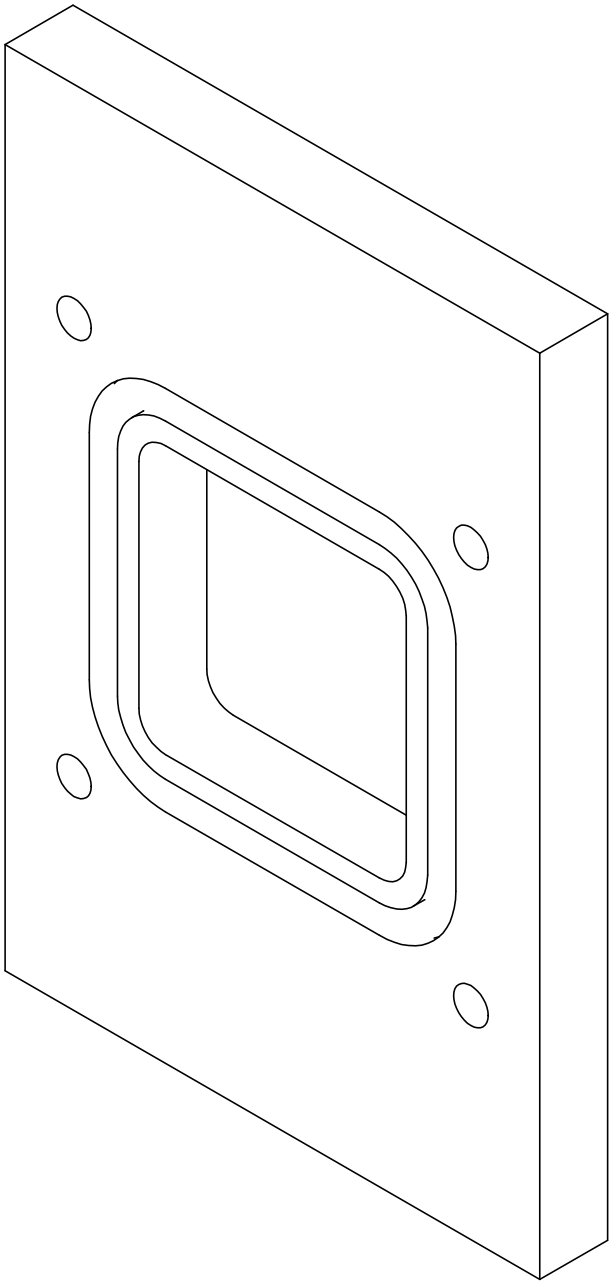

ISOMETRIC

		DIMENSIONS ARE IN mm TOLERANCES ARE 0.03 mm UNLESS OTHERWISE NOTED.		NAME	DATE
			DRAWN	BAP	8/31/2011
			CHECKED		
			ENG APPR.		
			MFG APPR.		
		MATERIAL Quartz	Q.A.		
			COMMENTS:		
NEXT ASSY	USED ON	FINISH NONE			
APPLICATION		DO NOT SCALE DRAWING			

MIT

138 Albany St.
NW13-239
Cambridge, MA 02139

Bren Phillips
816-258-3220

SIZE	DWG. NO.	REV.
A	FrontPlate	C
SCALE:2:1	WEIGHT:	SHEET 3 OF 3

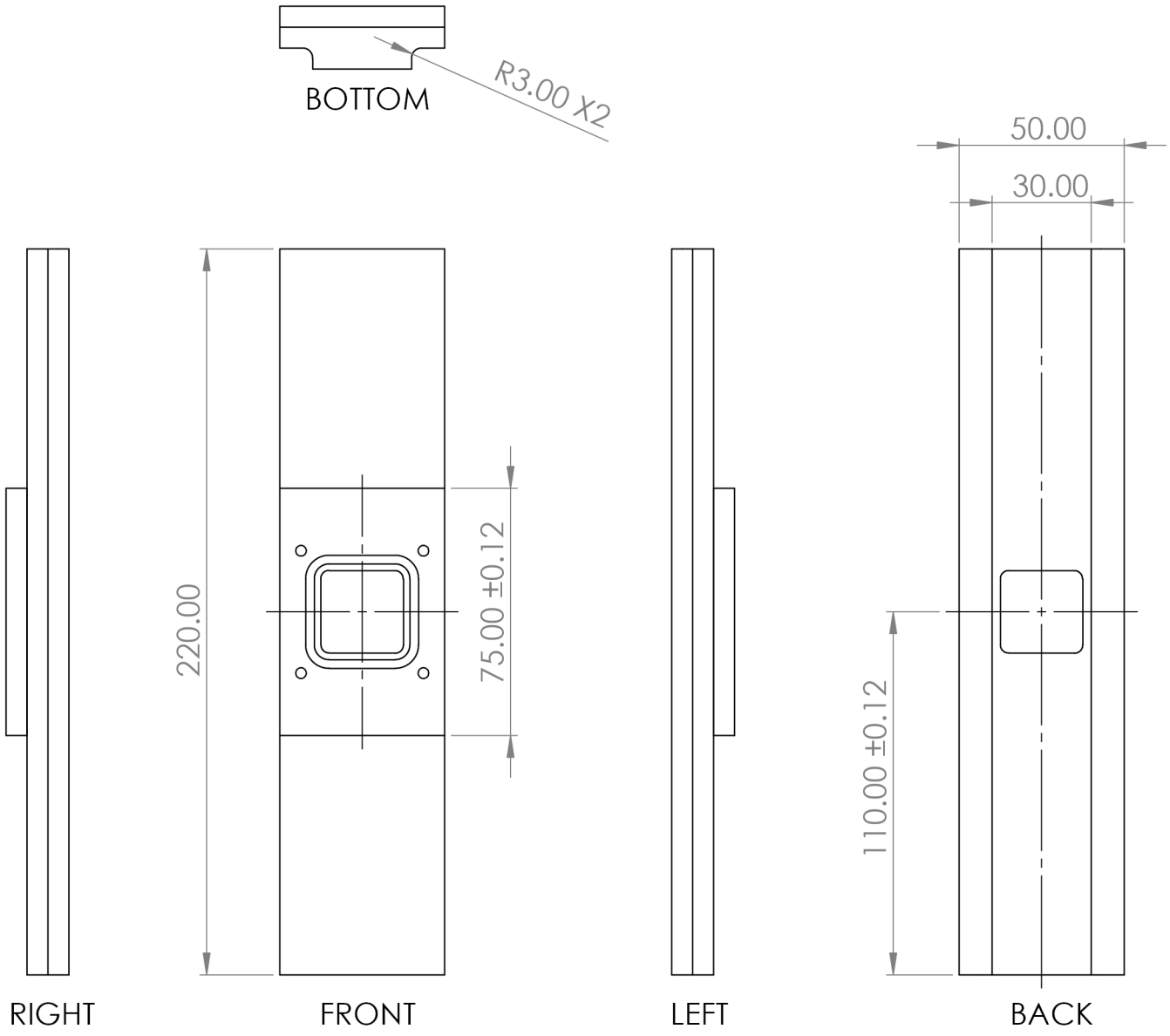

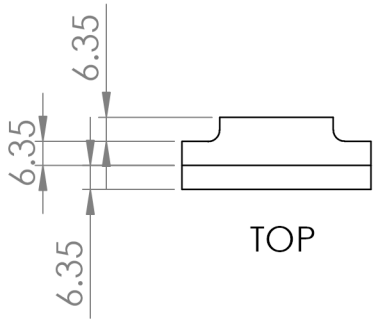

FRONTASSEMBLY IS COMPOSED OF 2 PARTS, FRONT&BACK AND FRONTPLATEBARE WHICH AFTER MACHINED AS SHOWN IN THEIR RESPECTIVE DRAWINGS SHOULD BE JOINED TOGETHER WITH DURLACO 4463 EPOXY THEN MACHINED AS SHOWN IN THIS DRAWING.

		DIMENSIONS ARE IN mm TOLERANCES ARE 0.03 mm UNLESS OTHERWISE NOTED.		NAME	DATE
			DRAWN	BAP	9/26/11
			CHECKED		
			ENG APPR.		
			MFG APPR.		
			Q.A.		
		MATERIAL Quartz	COMMENTS:		
NEXT ASSY	USED ON	FINISH POLISHED			
APPLICATION		DO NOT SCALE DRAWING			

MIT
138 Albany St.
NW13-239
Cambridge, MA 02139

Bren Phillips
816-258-3220

SIZE	DWG. NO.	REV.
A	FrontAssembly	D
SCALE:1:2	WEIGHT:	SHEET 1 OF 3

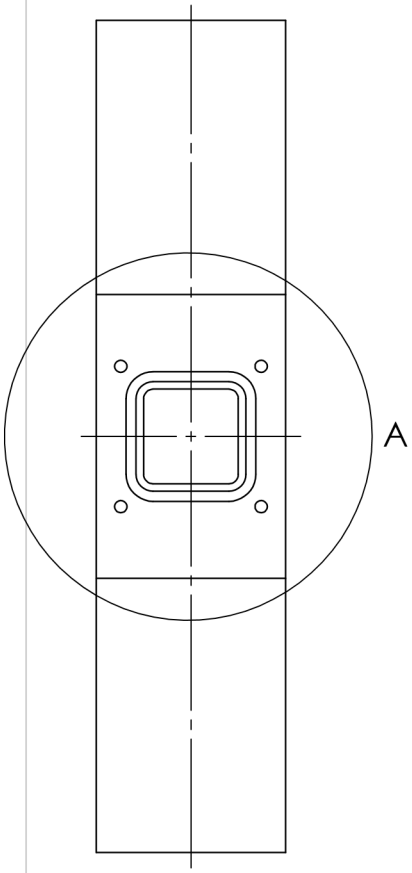

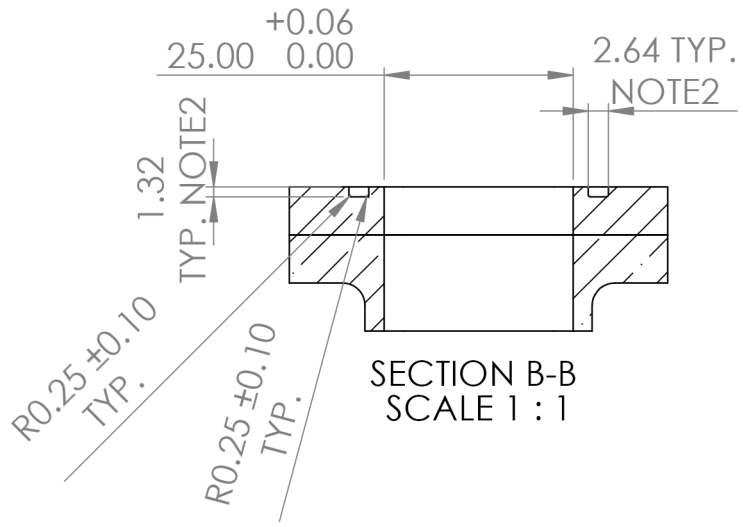

SECTION B-B
SCALE 1 : 1

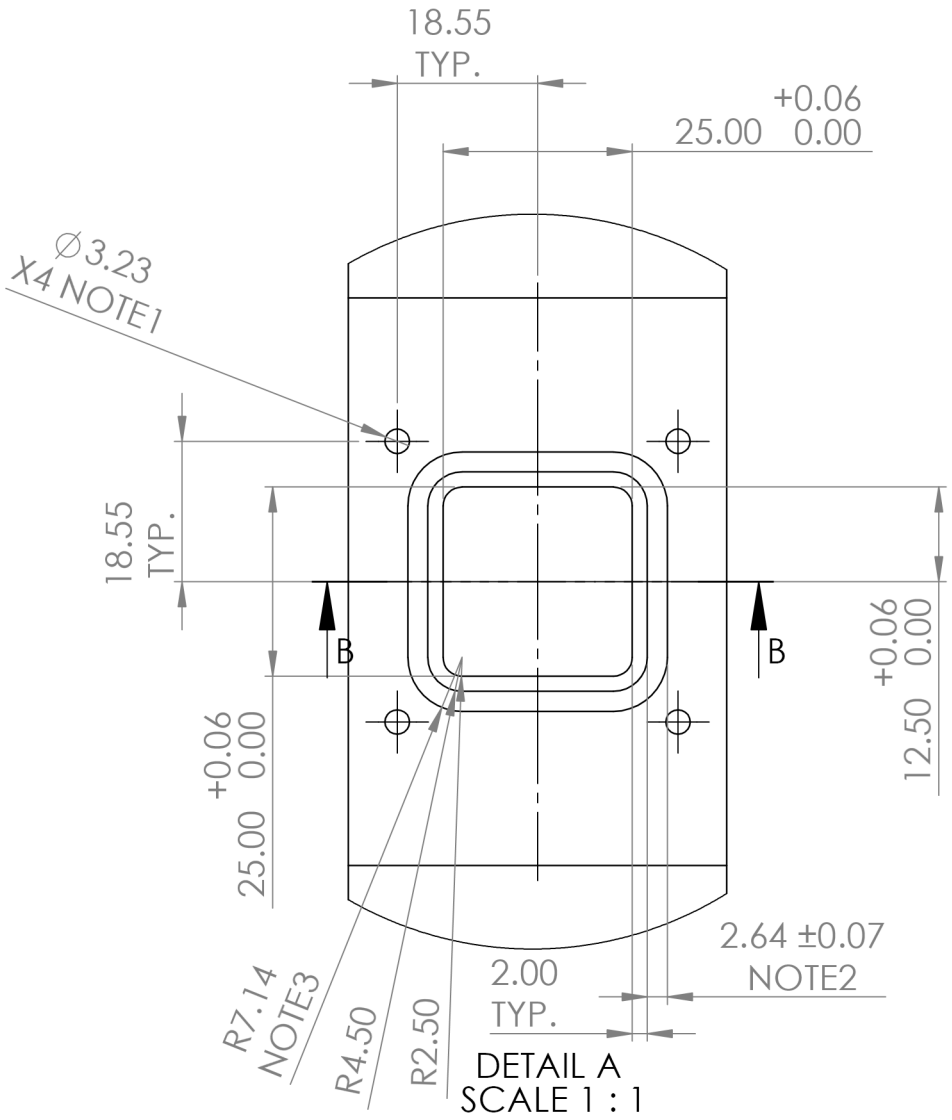

DETAIL A
SCALE 1 : 1

		DIMENSIONS ARE IN mm TOLERANCES ARE 0.03 mm UNLESS OTHERWISE NOTED.		NAME	DATE
			DRAWN	BAP	9/26/11
			CHECKED		
			ENG APPR.		
			MFG APPR.		
		MATERIAL Quartz	Q.A.		
			COMMENTS: NOTE1: Approx 5mm deep holes for McMaster 99362A100 insert. Epoxy Inserts with Durlaco 4463. NOTE2: Groove for 1/16" O-ring NOTE3: Tolerance on fillet radiuses +/- 0.1 mm		
NEXT ASSY	USED ON	FINISH POLISHED			
APPLICATION		DO NOT SCALE DRAWING			

MIT

138 Albany St.
NW13-239
Cambridge, MA 02139

Bren Phillips
816-258-3220

SIZE	DWG. NO.	REV.
A	FrontAssembly	D
SCALE:1:2	WEIGHT:	SHEET 2 OF 3

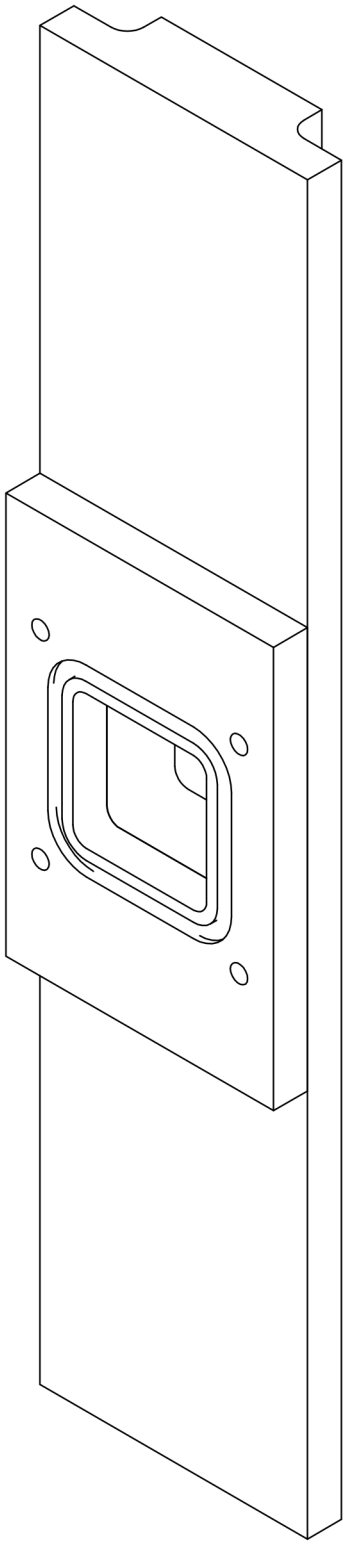

ISOMETRIC

		DIMENSIONS ARE IN mm TOLERANCES ARE 0.03 mm UNLESS OTHERWISE NOTED.		NAME	DATE
			DRAWN	BAP	9/26/11
			CHECKED		
			ENG APPR.		
			MFG APPR.		
		MATERIAL Quartz	Q.A.		
			COMMENTS:		
NEXT ASSY	USED ON	FINISH POLISHED			
APPLICATION		DO NOT SCALE DRAWING			

MIT

138 Albany St.
NW13-239
Cambridge, MA 02139

Bren Phillips
816-258-3220

SIZE	DWG. NO.	REV.
A	FrontAssembly	D

SCALE:1:1	WEIGHT:	SHEET 3 OF 3

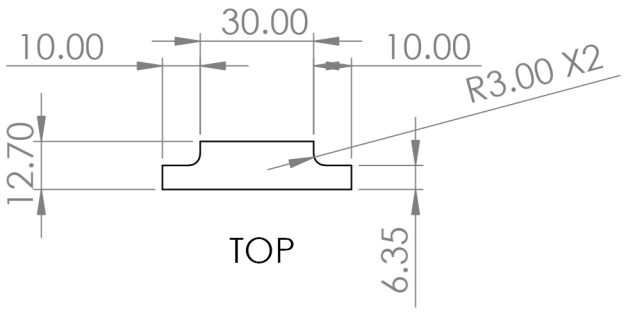

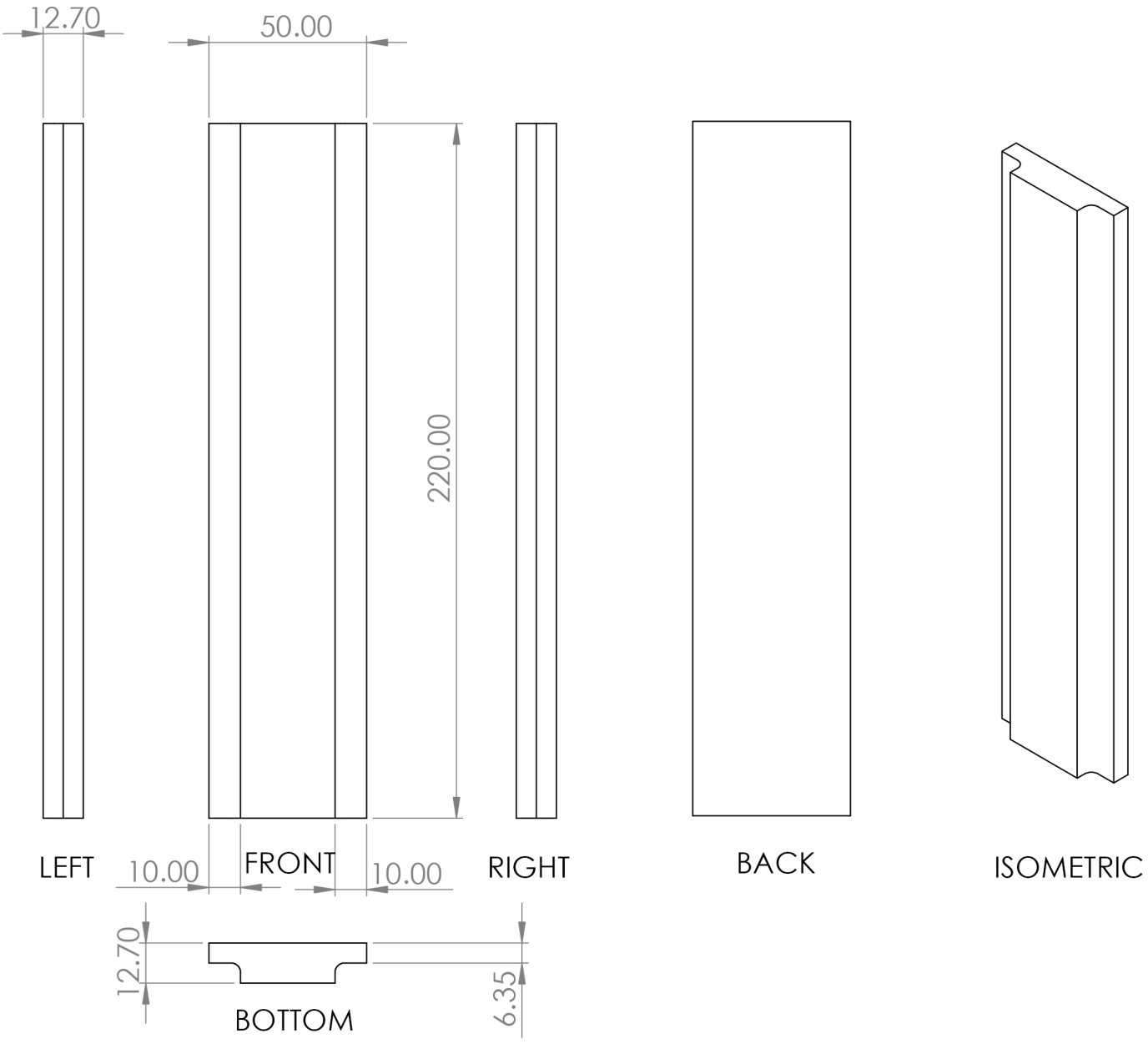

		DIMENSIONS ARE IN mm TOLERANCES ARE 0.03 mm UNLESS OTHERWISE NOTED.		NAME	DATE
			DRAWN	BAP	8/31/2011
			CHECKED		
			ENG APPR.		
			MFG APPR.		
			Q.A.		
		MATERIAL Quartz	COMMENTS: 2 Pieces. Front piece requires further machining after joined to FrontPlate as shown in DWG. FrontAssembly		
NEXT ASSY	USED ON	FINISH POLISHED			
APPLICATION		DO NOT SCALE DRAWING			

MIT
138 Albany St.
NW13-239
Cambridge, MA 02139

Bren Phillips
816-258-3220

SIZE	DWG. NO.	REV.
A	Front&Back	D
SCALE:1:2	WEIGHT:	SHEET 1 OF 1

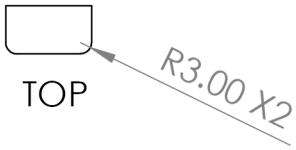

TOP

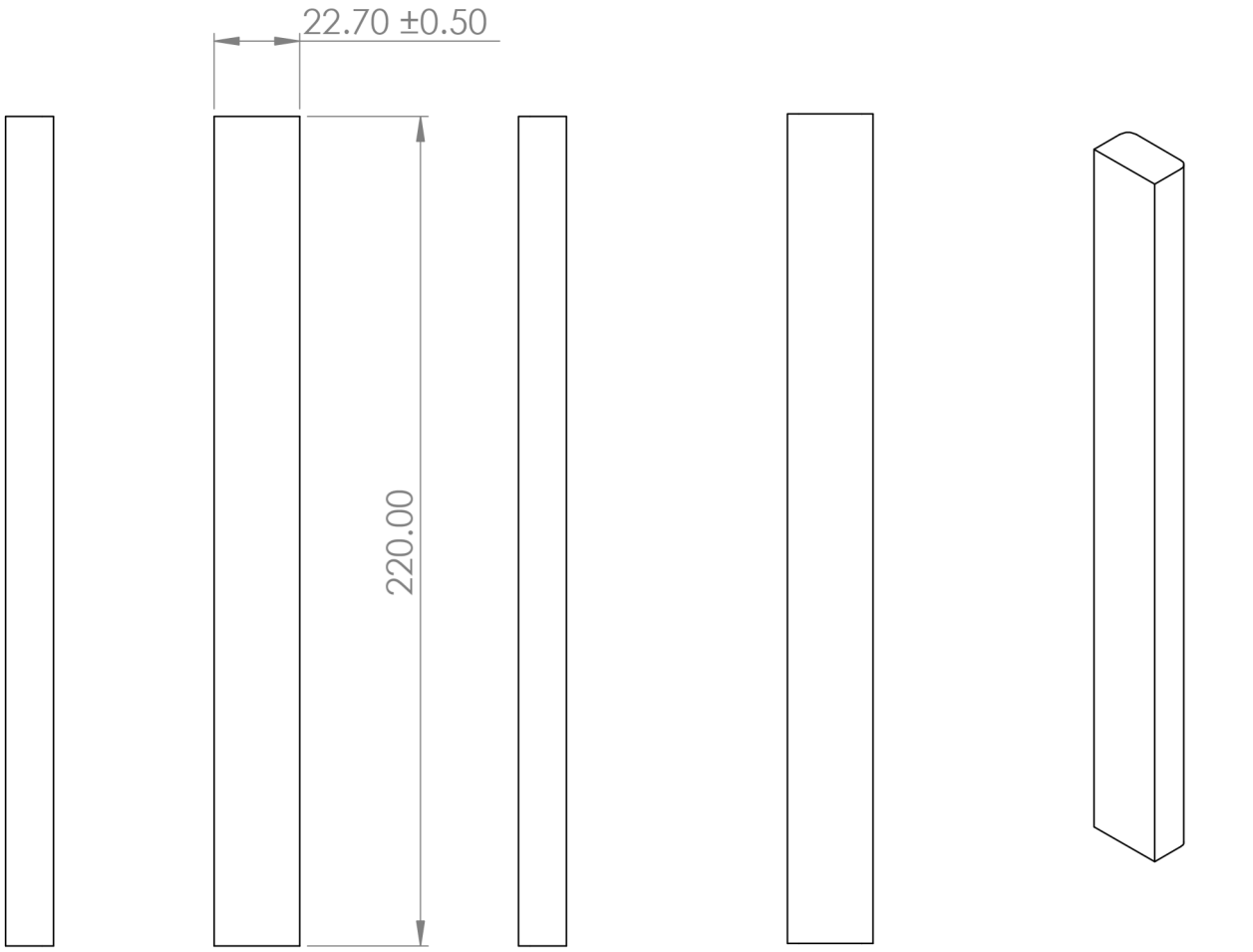

LEFT FRONT RIGHT BACK ISOMETRIC

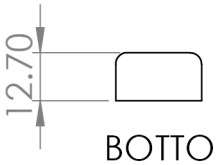

BOTTOM

		DIMENSIONS ARE IN mm TOLERANCES ARE 0.03 mm UNLESS OTHERWISE NOTED.		NAME	DATE
			DRAWN	BAP	8/31/2011
			CHECKED		
			ENG APPR.		
			MFG APPR.		
		MATERIAL Quartz	Q.A.		
			COMMENTS:		
NEXT ASSY	USED ON	FINISH POLISHED			
APPLICATION		DO NOT SCALE DRAWING			

MIT

138 Albany St.
NW13-239
Cambridge, MA 02139

Bren Phillips
816-258-3220

SIZE	DWG. NO.	REV.
A	Side	D

SCALE:1:2	WEIGHT:	SHEET 1 OF 1

H.2 Heater Cartridge and Heater

Table H.2: Heater Cartridge and Heater Drawings List

Drawing Name	Description
HeaterAssembly	Complete heater cartridge assembly
Electrode	Graphite Electrode for electrical connections to heater
Insulator	Macor® insulator to separate graphite electrodes
FilletedHeater	Sapphire and ITO heater that fits into Heater cartridge assembly

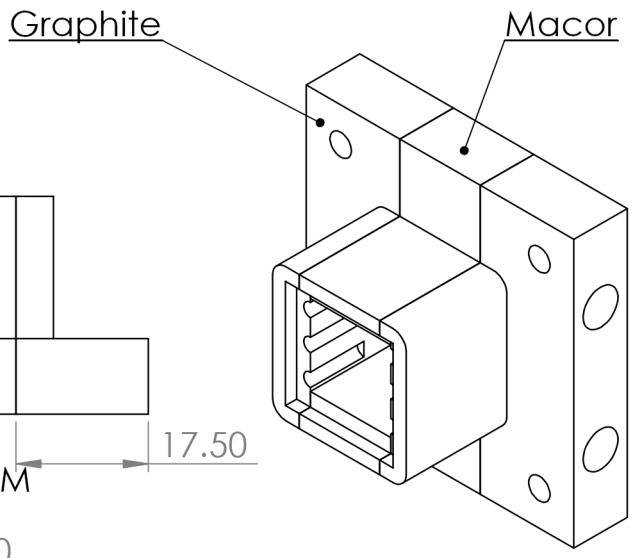

ISOMETRIC

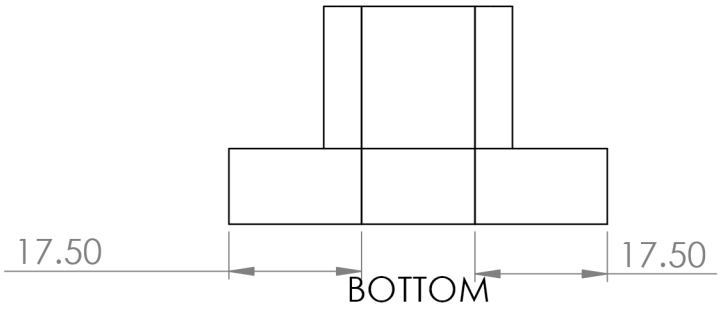

BOTTOM

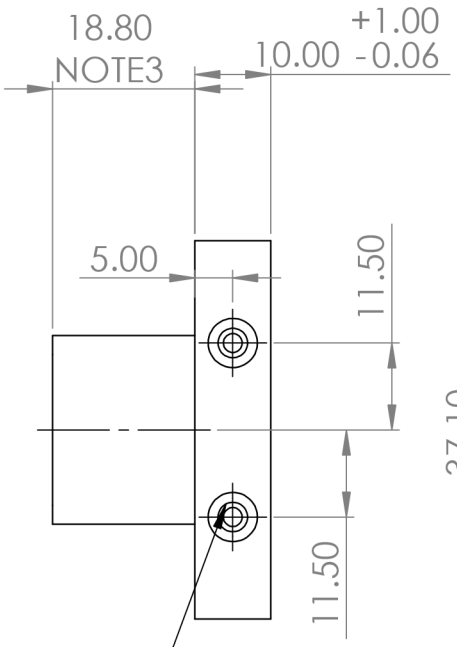

RIGHT

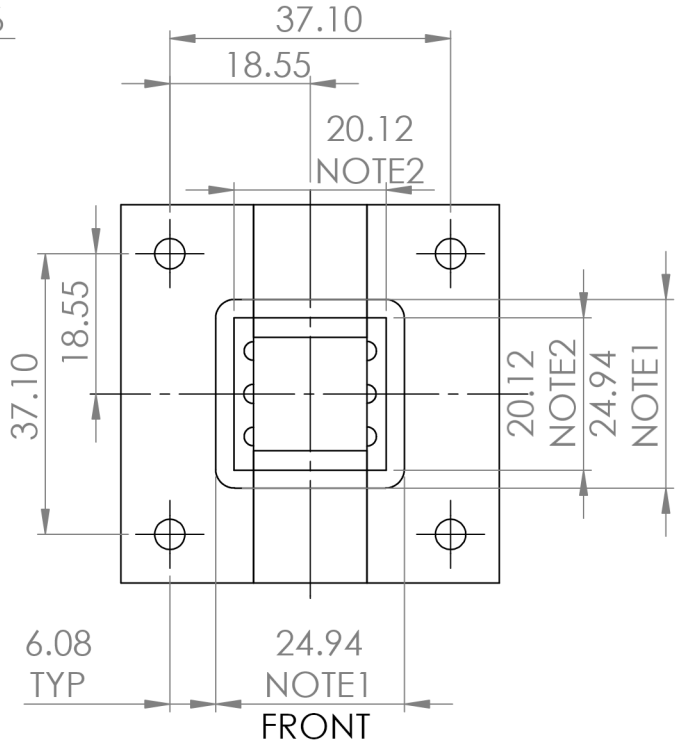

FRONT

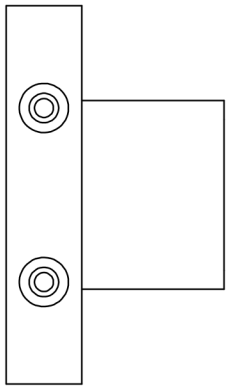

LEFT

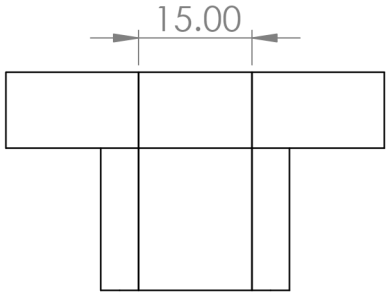

TOP

X4, MACOR THREADED FOR M3x0.5 BOLT, GRAPHITE HAS THRU HOLE

PARTS ELECTRODE AND INSULATOR SHOULD BE JOINED WITH DURLACO 4703 PRIOR TO PRECISION MACHINING. CRITICAL DIMENSIONS ARE THOSE ON THE HEATERASSEMBLY. SEE SHEET 4 FOR INSTRUCTIONS

		DIMENSIONS ARE IN mm TOLERANCES ARE 0.03 mm UNLESS OTHERWISE NOTED. NOTE1: MACHINED TO FIT SOCKET IN QUARTZ FRONT PLATE NOTE2: MACHINED TO FIT SAPPHIRE HEATER		NAME	DATE
			DRAWN	BAP	8/31/2011
			CHECKED		
			ENG APPR.		
			MFG APPR.		
			Q.A.		
		MATERIAL Various	COMMENTS: -HeaterAssembly consists of Insulator (2) and Electrode (2).		
NEXT ASSY	USED ON	FINISH NONE			
APPLICATION		DO NOT SCALE DRAWING			

MIT

138 Albany St.
NW13-239
Cambridge, MA 02139

Bren Phillips
816-258-3220

SIZE	DWG. NO.	REV.
A	HeaterAssembly	H
SCALE:1:1	WEIGHT:	SHEET 1 OF 4

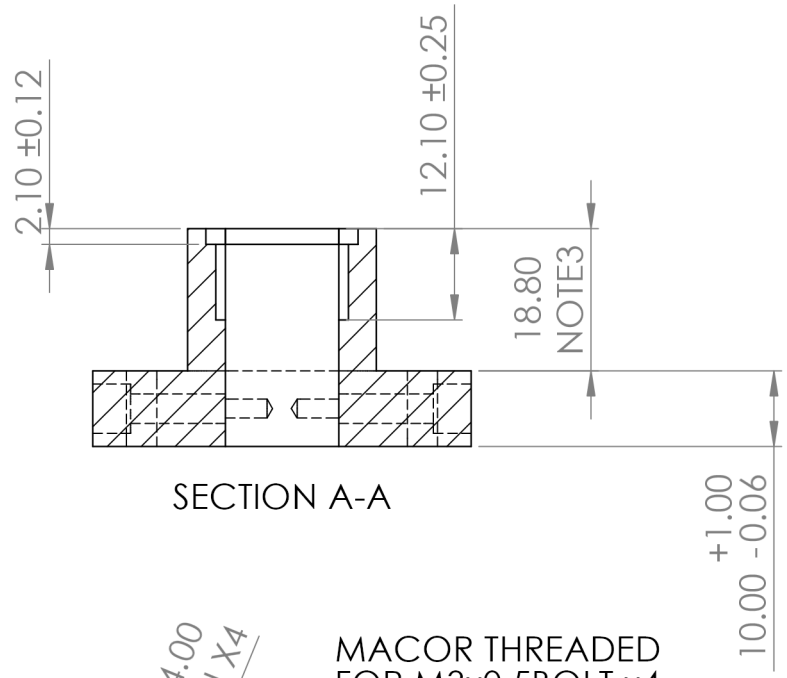

SECTION A-A

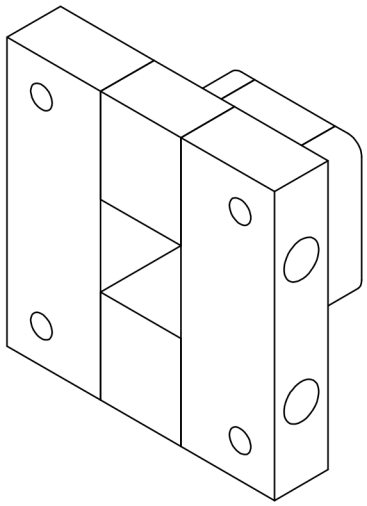

ISOMETRIC

15x15mm HOLE SIZE IS IMPORTANT DIMENSION

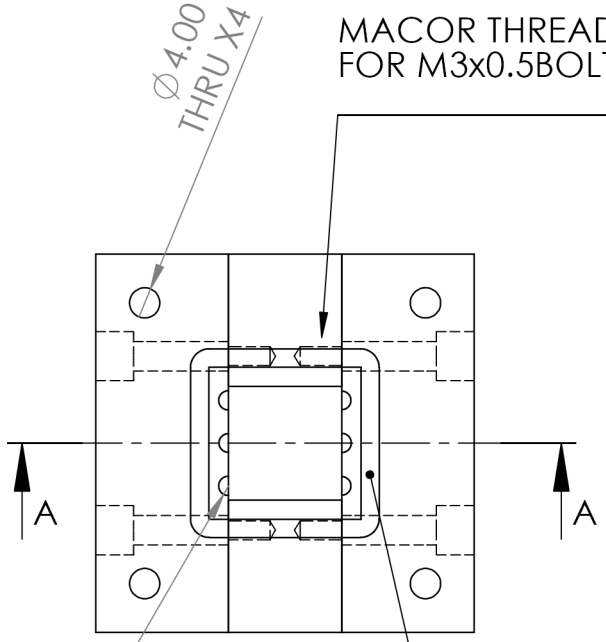

FRONT

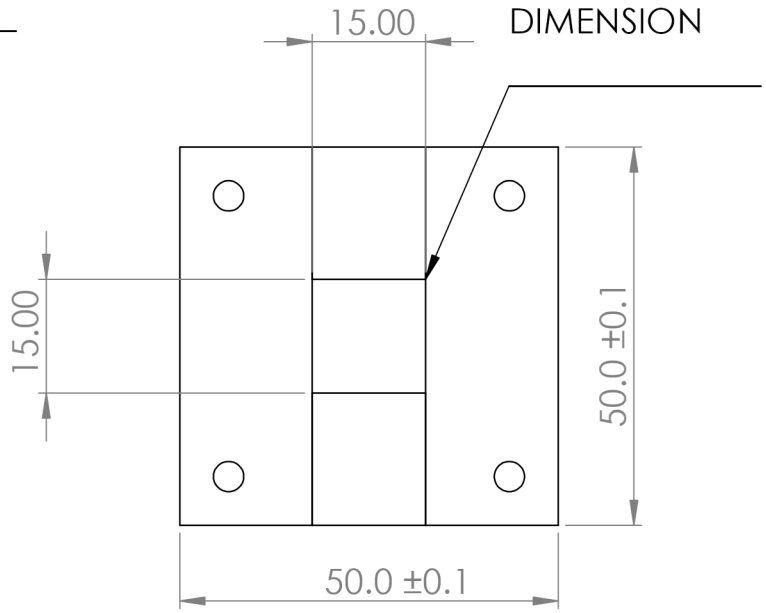

BACK

R1.25 X6

THIS FACE IS THE ONE REFERENCED IN NOTE3 TO BE MACHINED TO BE FLUSH WITH THE FACE ON THE QUARTZ

		DIMENSIONS ARE IN mm TOLERANCES ARE 0.03 mm UNLESS OTHERWISE NOTED. NOTE3: THIS DMENSION SHOULD BE ADJUSTED WHEN MACHINED TO FIT QUARTZ TO BE FLUSH WITH INSIDE FACE.		NAME	DATE
			DRAWN	BAP	8/31/2011
			CHECKED		
			ENG APPR.		
			MFG APPR.		
			Q.A.		
		MATERIAL Various	COMMENTS:		
NEXT ASSY	USED ON	FINISH NONE			
APPLICATION		DO NOT SCALE DRAWING			

MIT

138 Albany St.
NW13-239
Cambridge, MA 02139

Bren Phillips
816-258-3220

SIZE	DWG. NO.	REV.
A	HeaterAssembly	H
SCALE:1:1	WEIGHT:	SHEET 2 OF 4

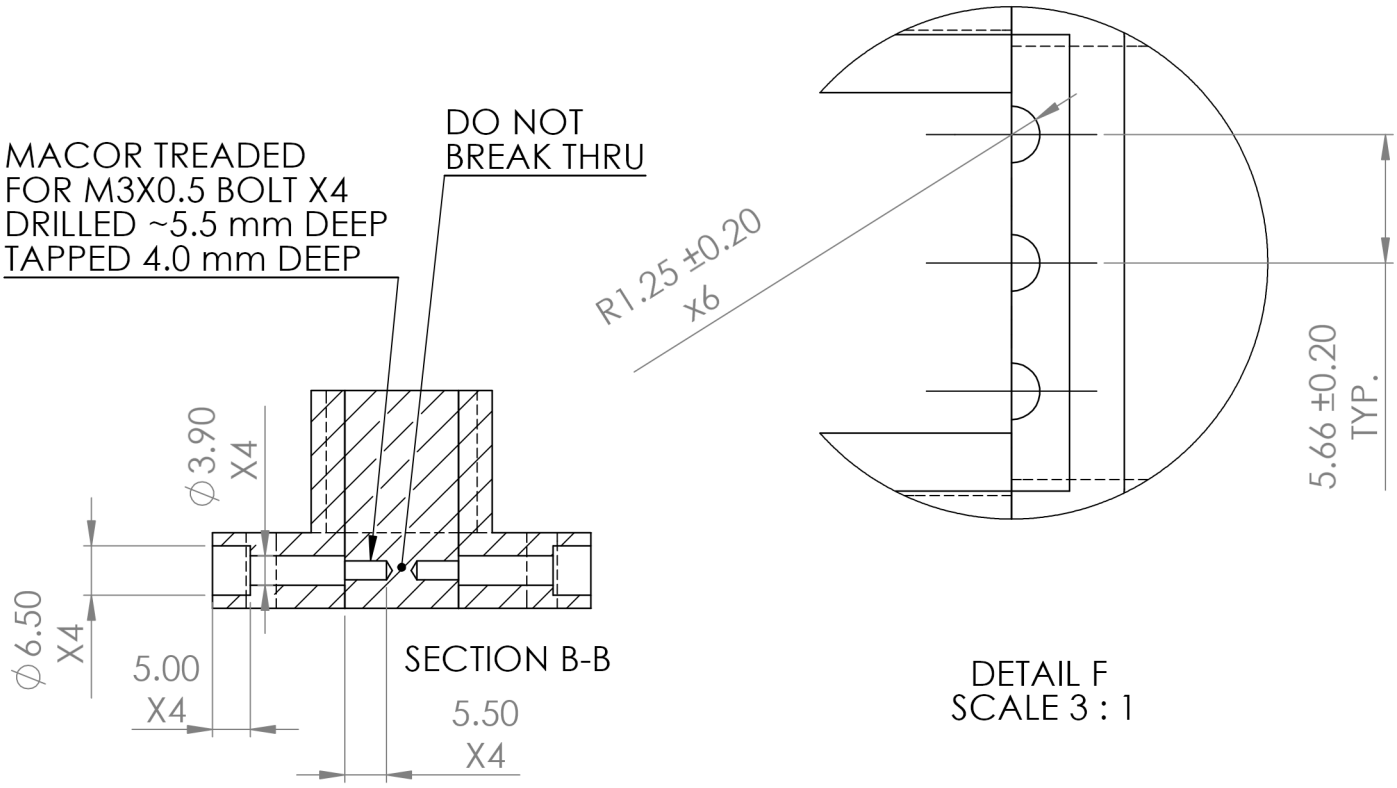

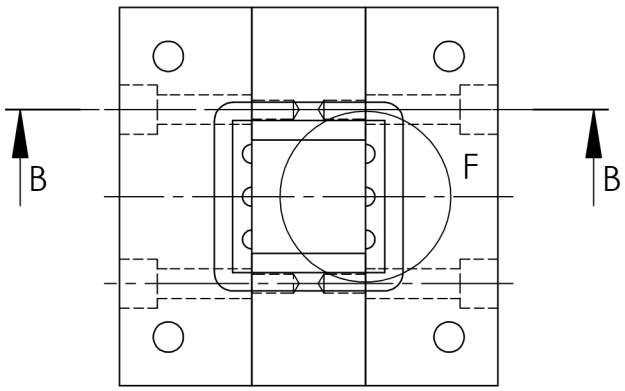

		DIMENSIONS ARE IN mm TOLERANCES ARE 0.03 mm UNLESS OTHERWISE NOTED.		NAME	DATE
			DRAWN	BAP	8/31/2011
			CHECKED		
			ENG APPR.		
			MFG APPR.		
			Q.A.		
		MATERIAL Various	COMMENTS:		
NEXT ASSY	USED ON	FINISH NONE			
APPLICATION		DO NOT SCALE DRAWING			

MIT

138 Albany St.
NW13-239
Cambridge, MA 02139

Bren Phillips
816-258-3220

SIZE	DWG. NO.	REV.
A	HeaterAssembly	H
SCALE:1:1	WEIGHT:	SHEET 3 OF 4

Please be careful with the quartz piece when handling, maintain the finish, and avoid chipping the quartz.

The Macor insulator and the graphite electrode should be joined with Durlco 4703 epoxy prior to final machining.

The critical dimensions are that the cartirdge is flush with the front face and seats with the back fce of the quartz. With as little of clearancebetween the hole in the quartz and the sides of the cartridge. The heater cartridge should be initially machined to fit and be flush with the front face and seat on the back face with the cartridge oriented as shown.

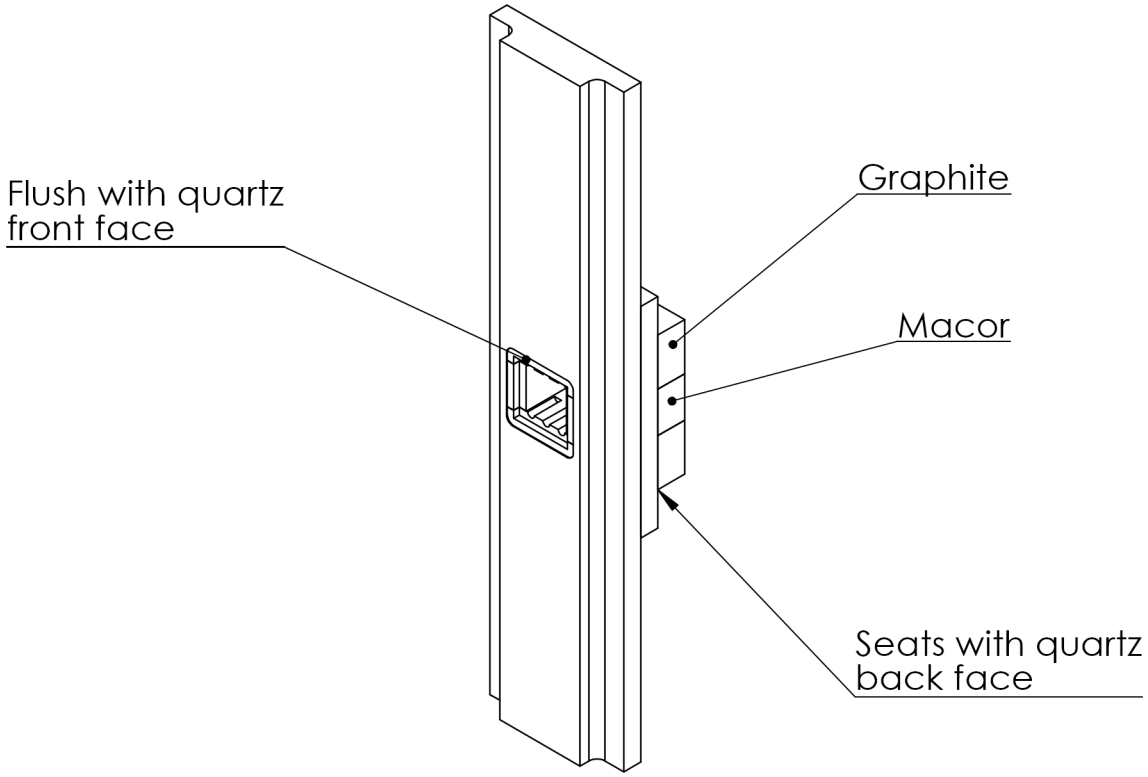

Note3 on the previous sheets denotes the dimension(s) that should be altered to get the cartridge heater flush with the front face.

		DIMENSIONS ARE IN mm TOLERANCES ARE 0.03 mm UNLESS OTHERWISE NOTED.		NAME	DATE
			DRAWN	BAP	8/31/2011
			CHECKED		
			ENG APPR.		
			MFG APPR.		
		MATERIAL Various	Q.A.		
			COMMENTS:		
NEXT ASSY	USED ON	FINISH NONE			
APPLICATION		DO NOT SCALE DRAWING			

MIT

138 Albany St.
NW13-239
Cambridge, MA 02139

Bren Phillips
816-258-3220

SIZE	DWG. NO.	REV.
A	HeaterAssembly	H
SCALE:1:2	WEIGHT:	SHEET 4 OF 4

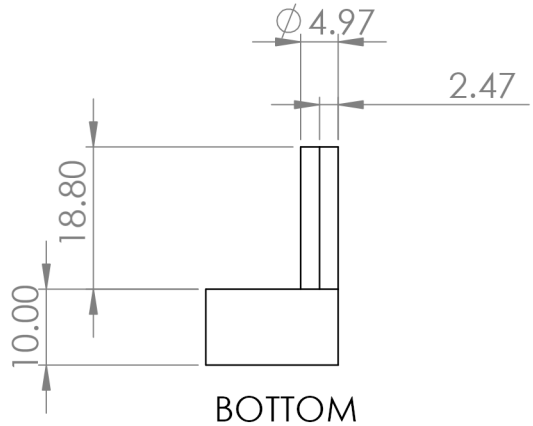

BOTTOM

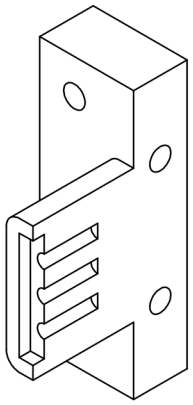

ISOMETRIC

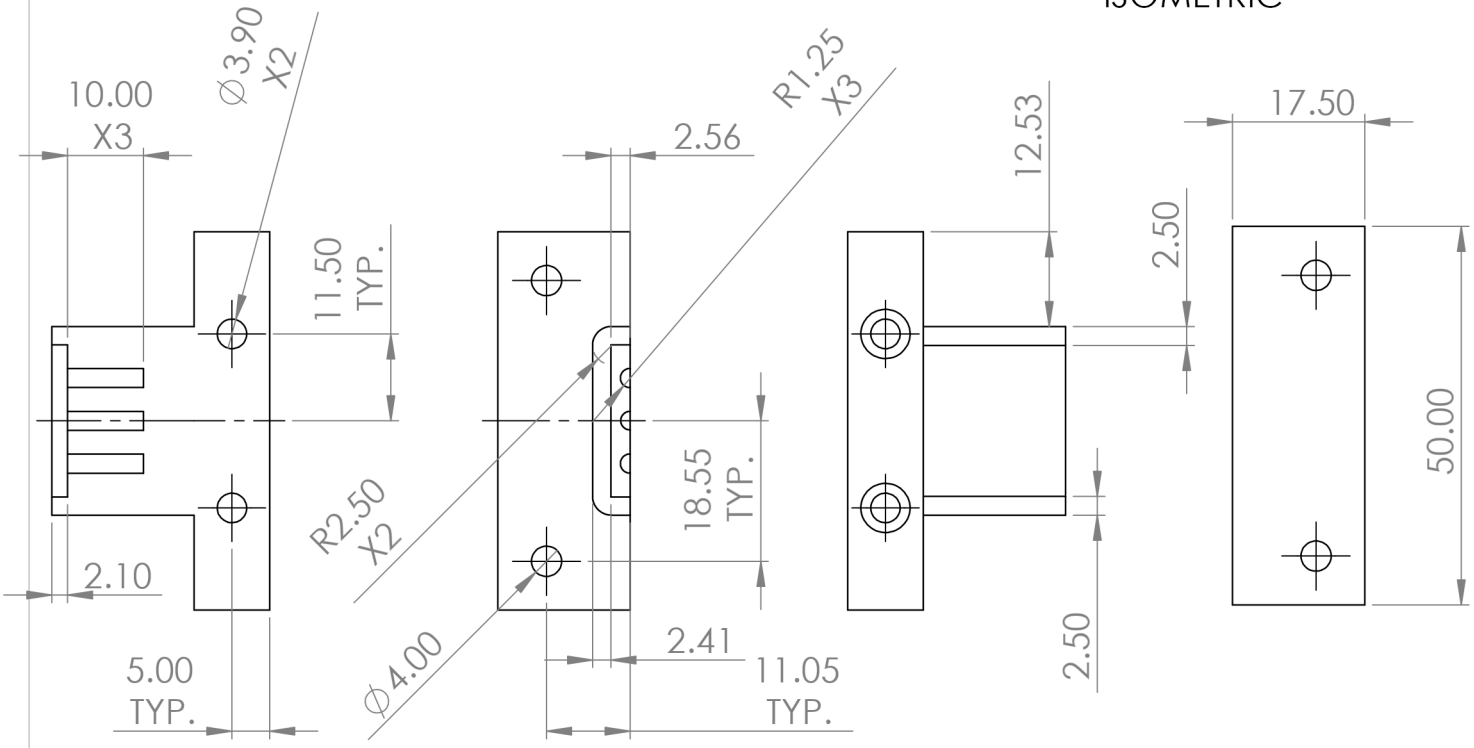

RIGHT FRONT LEFT BACK

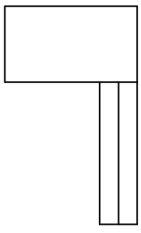

TOP

DRAWING FOR INFORMATION ONLY, CRITICAL DIMENSIONS ARE THOSE ON HEATERASSEMBLY DRAWING, WHICH IS COPOSED OF TWO OF THIS COMPONENT

		DIMENSIONS ARE IN mm TOLERANCES ARE 0.03 mm UNLESS OTHERWISE NOTED.		NAME	DATE
			DRAWN	BAP	8/31/2011
			CHECKED		
			ENG APPR.		
			MFG APPR.		
		MATERIAL Graphite	Q.A.		
			COMMENTS:		
NEXT ASSY	USED ON	FINISH NONE			
APPLICATION		DO NOT SCALE DRAWING			

MIT

138 Albany St.
NW13-239
Cambridge, MA 02139

Bren Phillips
816-258-3220

SIZE	DWG. NO.	REV.
A	Electrode	H
SCALE:1:1	WEIGHT:	SHEET 1 OF 2

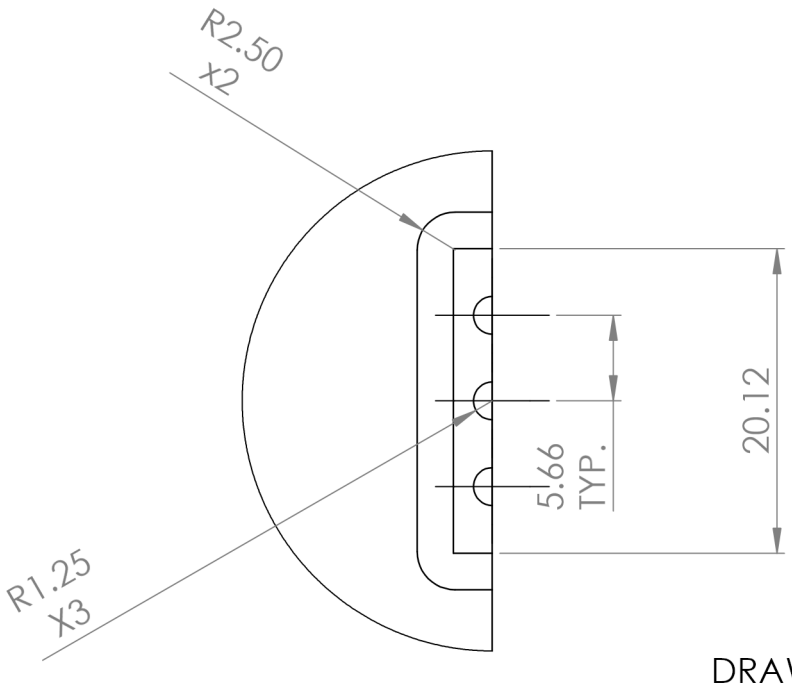

DETAIL B
SCALE 2 : 1

DRAWING FOR INFORMATION ONLY, CRITICAL DIMENSIONS ARE THOSE ON HEATERASSEMBLY DRAWING, WHICH IS COPOSED OF TWO OF THIS COMPONENT

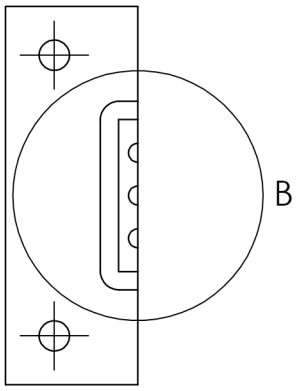

FRONT

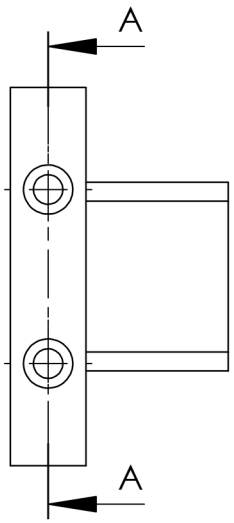

LEFT

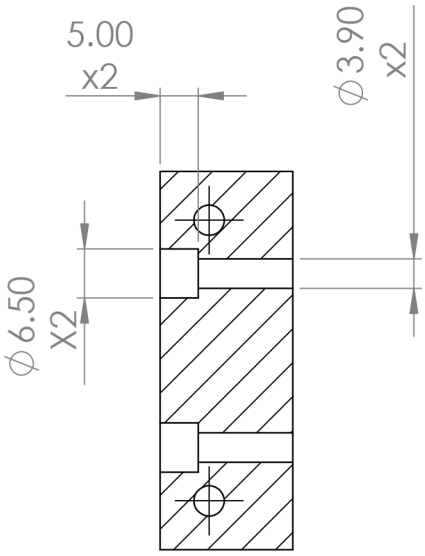

SECTION A-A

		DIMENSIONS ARE IN mm TOLERANCES ARE 0.03 mm UNLESS OTHERWISE NOTED. NOTE2: MACHINED TO FIT SAPPHIRE HEATER		NAME	DATE
			DRAWN	BAP	8/31/2011
			CHECKED		
			ENG APPR.		
			MFG APPR.		
			Q.A.		
		MATERIAL Graphite	COMMENTS:		
NEXT ASSY	USED ON	FINISH NONE			
APPLICATION		DO NOT SCALE DRAWING			

MIT

138 Albany St.
NW13-239
Cambridge, MA 02139

Bren Phillips
816-258-3220

SIZE	DWG. NO.	REV.
A	Electrode	H
SCALE:1:1	WEIGHT:	SHEET 2 OF 2

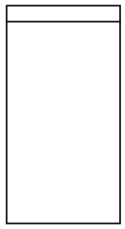

BOTTOM

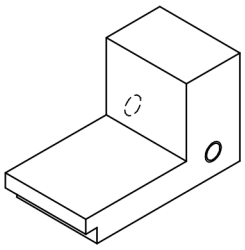

ISOMETRIC

MACOR THREADED
FOR M3x0.5BOLT x2
DRILLED 5.5 MM DEEP
TAPPED 4.0 MM DEEP

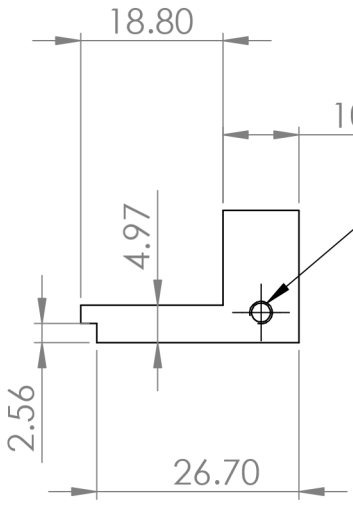

RIGHT

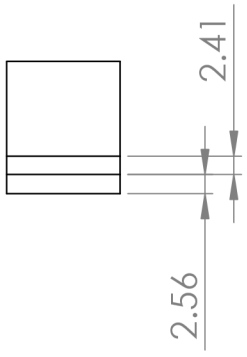

FRONT

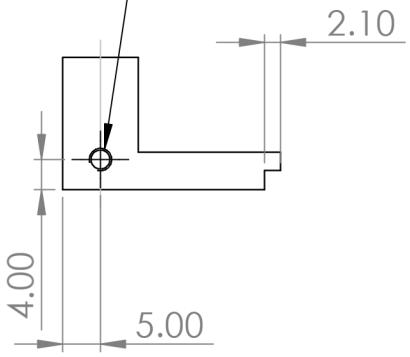

LEFT

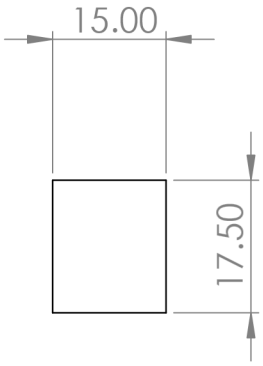

BACK

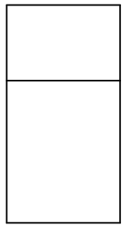

TOP

DRAWING FOR INFORMATION ONLY, CRITICAL DIMENSIONS ARE THOSE ON HEATERASSEMBLY DRAWING, WHICH IS COPOSED OF TWO OF THIS COMPONENT

		DIMENSIONS ARE IN mm TOLERANCES ARE 0.03 mm UNLESS OTHERWISE NOTED.		NAME	DATE
			DRAWN	BAP	8/31/2011
			CHECKED		
			ENG APPR.		
			MFG APPR.		
		MATERIAL Macor	Q.A.		
			COMMENTS:		
NEXT ASSY	USED ON	FINISH NONE			
APPLICATION		DO NOT SCALE DRAWING			

MIT

138 Albany St.
NW13-239
Cambridge, MA 02139

Bren Phillips
816-258-3220

SIZE	DWG. NO.	REV.
A	Insulator	H
SCALE:1:1	WEIGHT:	SHEET 1 OF 2

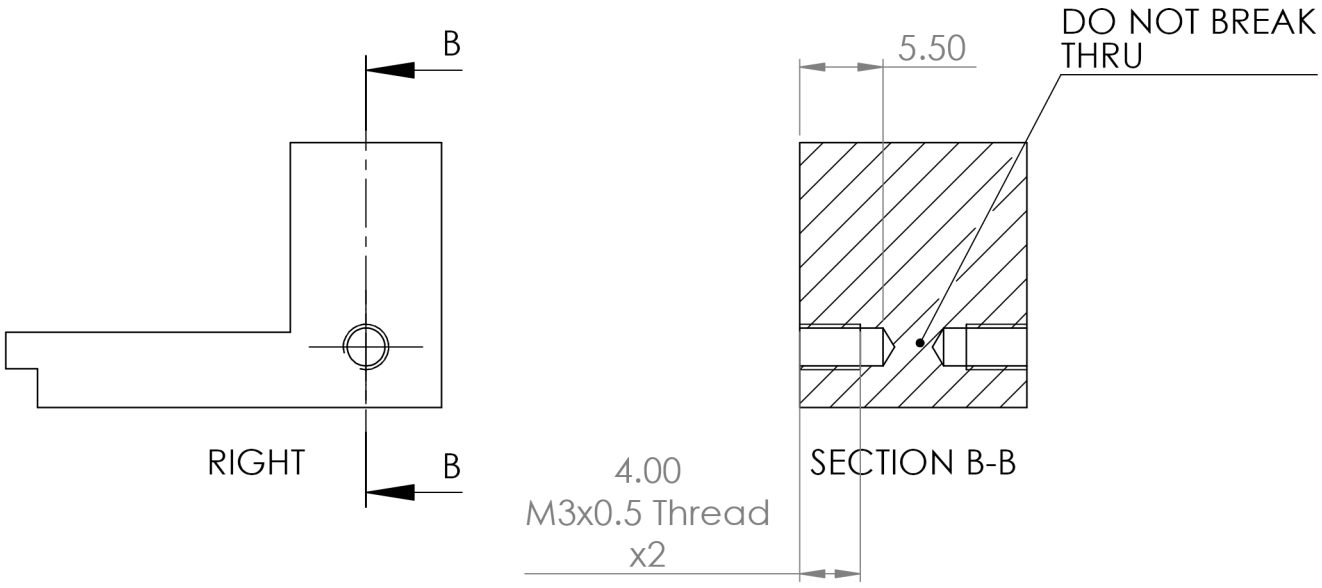

DRAWING FOR INFORMATION ONLY, CRITICAL DIMENSIONS ARE THOSE ON HEATERASSEMBLY DRAWING, WHICH IS COPOSED OF TWO OF THIS COMPONENT

		DIMENSIONS ARE IN mm TOLERANCES ARE 0.03 mm UNLESS OTHERWISE NOTED.		NAME	DATE
			DRAWN	BAP	8/31/2011
			CHECKED		
			ENG APPR.		
			MFG APPR.		
		MATERIAL Macor	Q.A.		
			COMMENTS:		
NEXT ASSY	USED ON	FINISH NONE			
APPLICATION		DO NOT SCALE DRAWING			

MIT
138 Albany St.
NW13-239
Cambridge, MA 02139

Bren Phillips
816-258-3220

SIZE	DWG. NO.	REV.
A	Insulator	H
SCALE:2:1	WEIGHT:	SHEET 2 OF 2

RADIUS TO BE SET BY DIAMOND COATINGS TO ENSURE NOMINAL RESISTANCE WHEN WRAPPING ITO AROUND THE SIDE

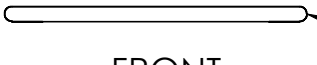

FRONT

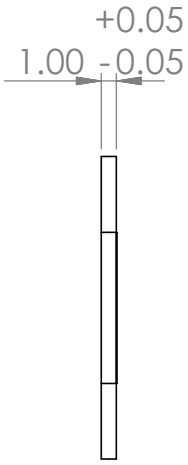

RIGHT

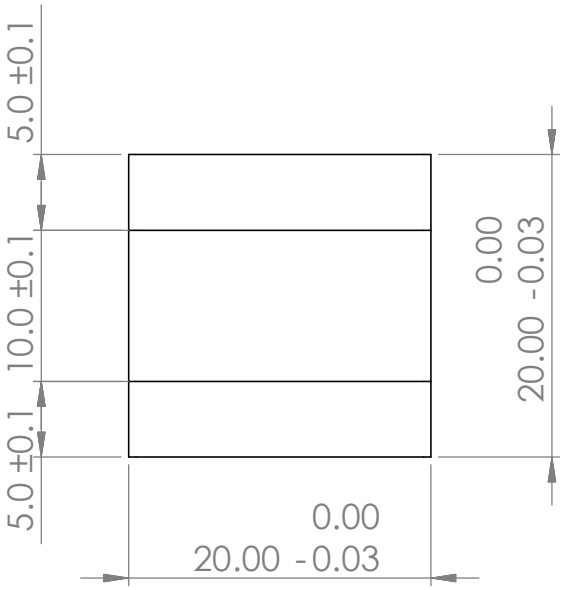

TOP

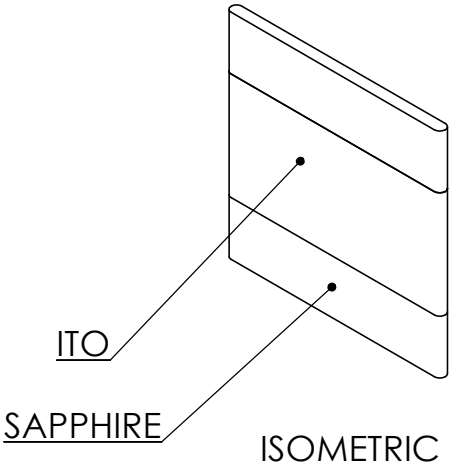

ISOMETRIC

10mm X 2mm APPROX 0.03 mm THICK SILVER ELECTRODE X2

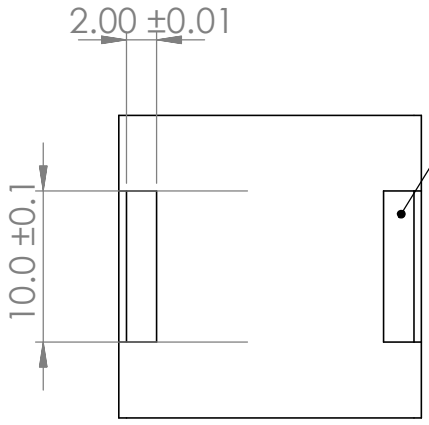

BOTTOM

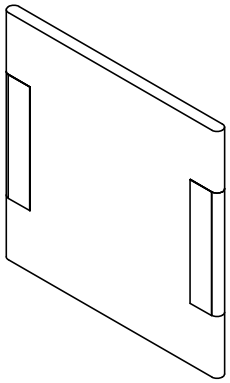

ISOMETRIC

		DIMENSIONS ARE IN mm TOLERANCES ARE 0.03 mm UNLESS OTHERWISE NOTED.		NAME	DATE
			DRAWN	BAP	10/7/11
			CHECKED	TJM	10/11/11
			ENG APPR.		
			MFG APPR.		
		MATERIAL VARIOUS	Q.A.		
			COMMENTS:		
NEXT ASSY	USED ON	FINISH AS NOTED			
APPLICATION		DO NOT SCALE DRAWING			

MIT

138 Albany St.
NW13-239
Cambridge, MA 02139

Bren Phillips
816-258-3220

SIZE	DWG. NO.	REV.
A	FilletedHeater	A
SCALE:2:1	WEIGHT:	SHEET 1 OF 2

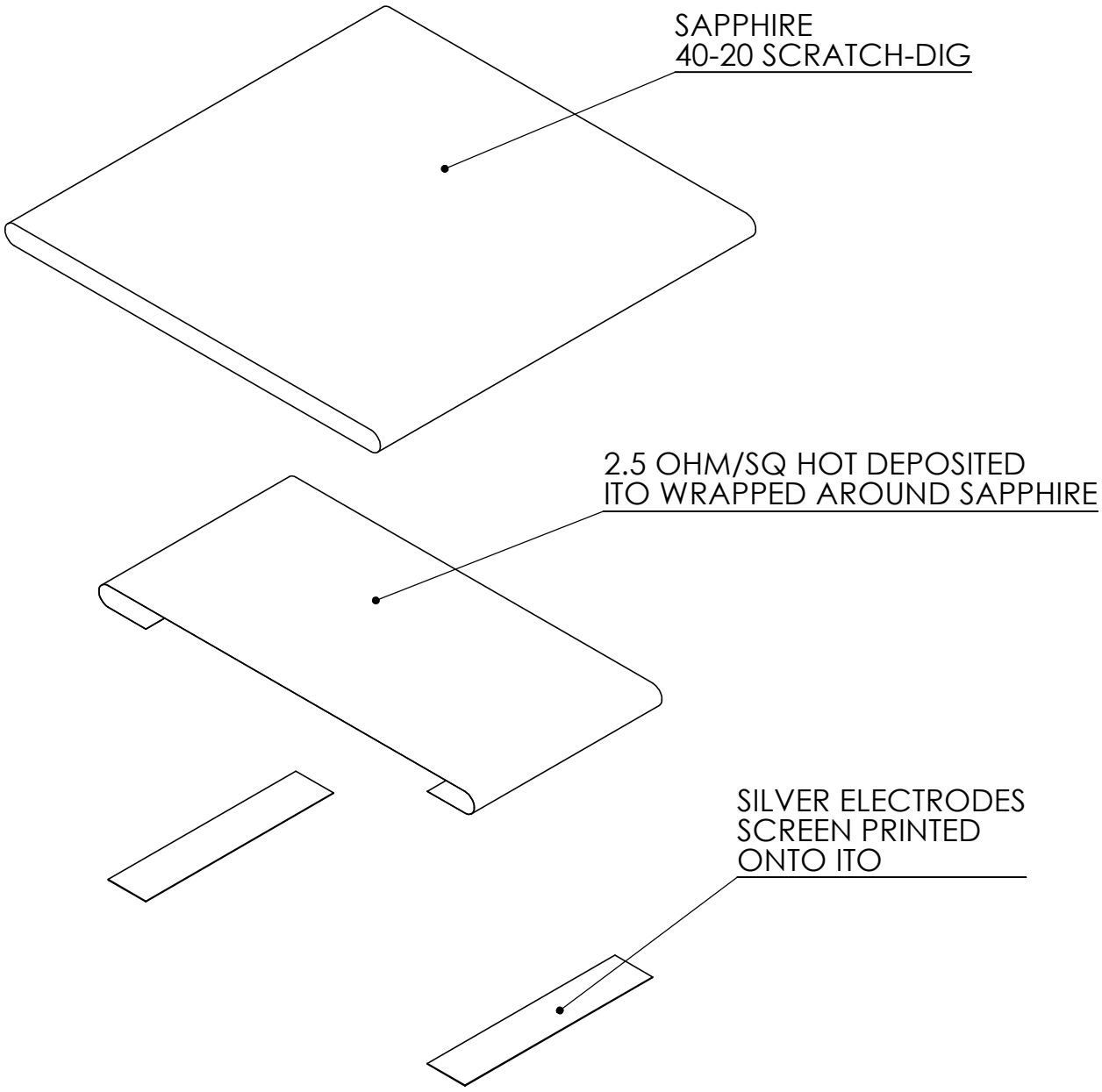

EXPLODED VIEW

		DIMENSIONS ARE IN mm TOLERANCES ARE 0.03 mm UNLESS OTHERWISE NOTED.		NAME	DATE
			DRAWN	BAP	10/7/11
			CHECKED	TJM	10/11/11
			ENG APPR.		
			MFG APPR.		
		MATERIAL VARIOUS	Q.A.		
			COMMENTS:		
NEXT ASSY	USED ON	FINISH AS NOTED			
APPLICATION		DO NOT SCALE DRAWING			

MIT

138 Albany St.
NW13-239
Cambridge, MA 02139

Bren Phillips
816-258-3220

SIZE	DWG. NO.	REV.
A	FilletedHeater	A
SCALE:4:1	WEIGHT:	SHEET 2 OF 2

H.3 Entrance Region and NPT Transition

Table H.3: Entrance region, NPT transition, and alignment pin drawing list

Drawing Name	Description
NPT_Transition	Stainless steel transition from 1 pipe thread to rectangular channel
EntranceAssembly	Stainless steel rectangular channel to match test section
AlignmentPin	Nylon alignment pin to line up entrance regions and test section

The machine shop cut the flats on the flanges for the entrance regions and the NPT transitions 45° from where they were supposed to be. The mistake on all of the parts so the flats still all match up and the parts were useable.

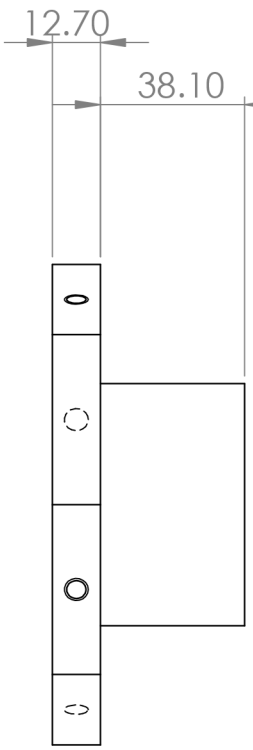

RIGHT

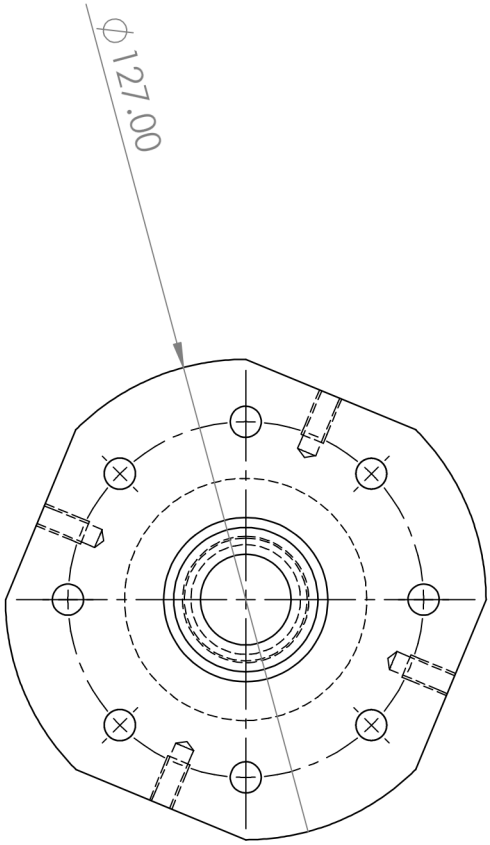

TOP

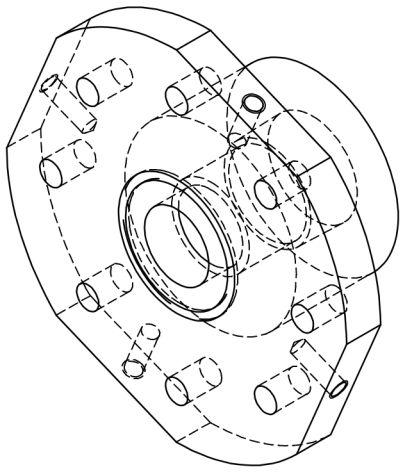

ISOMETRIC

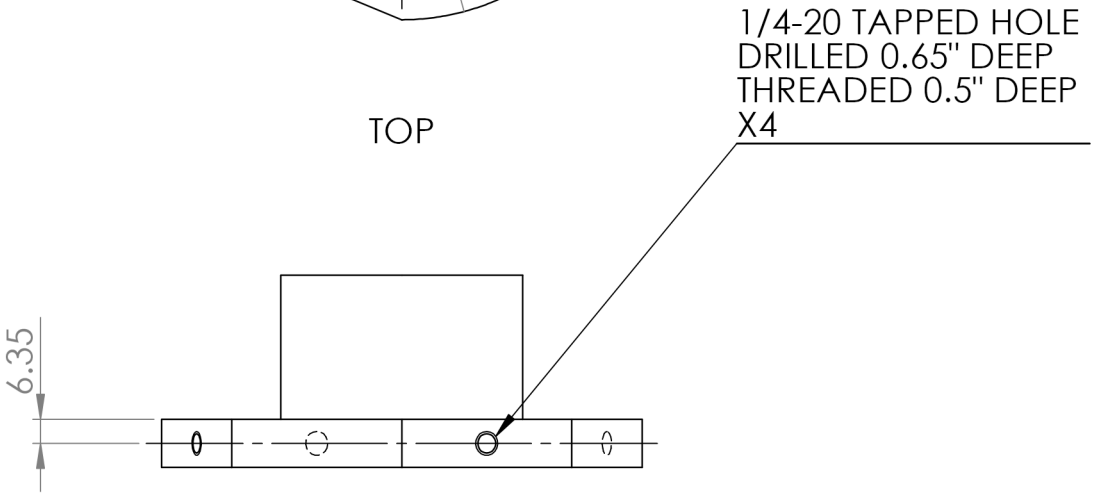

BACK

		DIMENSIONS ARE IN mm TOLERANCES ARE 0.03 mm UNLESS OTHERWISE NOTED.		NAME	DATE
			DRAWN	BAP	9/26/2011
			CHECKED		
			ENG APPR.		
			MFG APPR.		
		MATERIAL SS316L	Q.A.		
			COMMENTS:		
NEXT ASSY	USED ON	FINISH NONE			
APPLICATION		DO NOT SCALE DRAWING			

MIT

138 Albany St.
NW13-239
Cambridge, MA 02139

Bren Phillips
816-258-3220

SIZE	DWG. NO.	REV.
A	NPT_Transition	F
SCALE:1:2	WEIGHT:	SHEET 1 OF 3

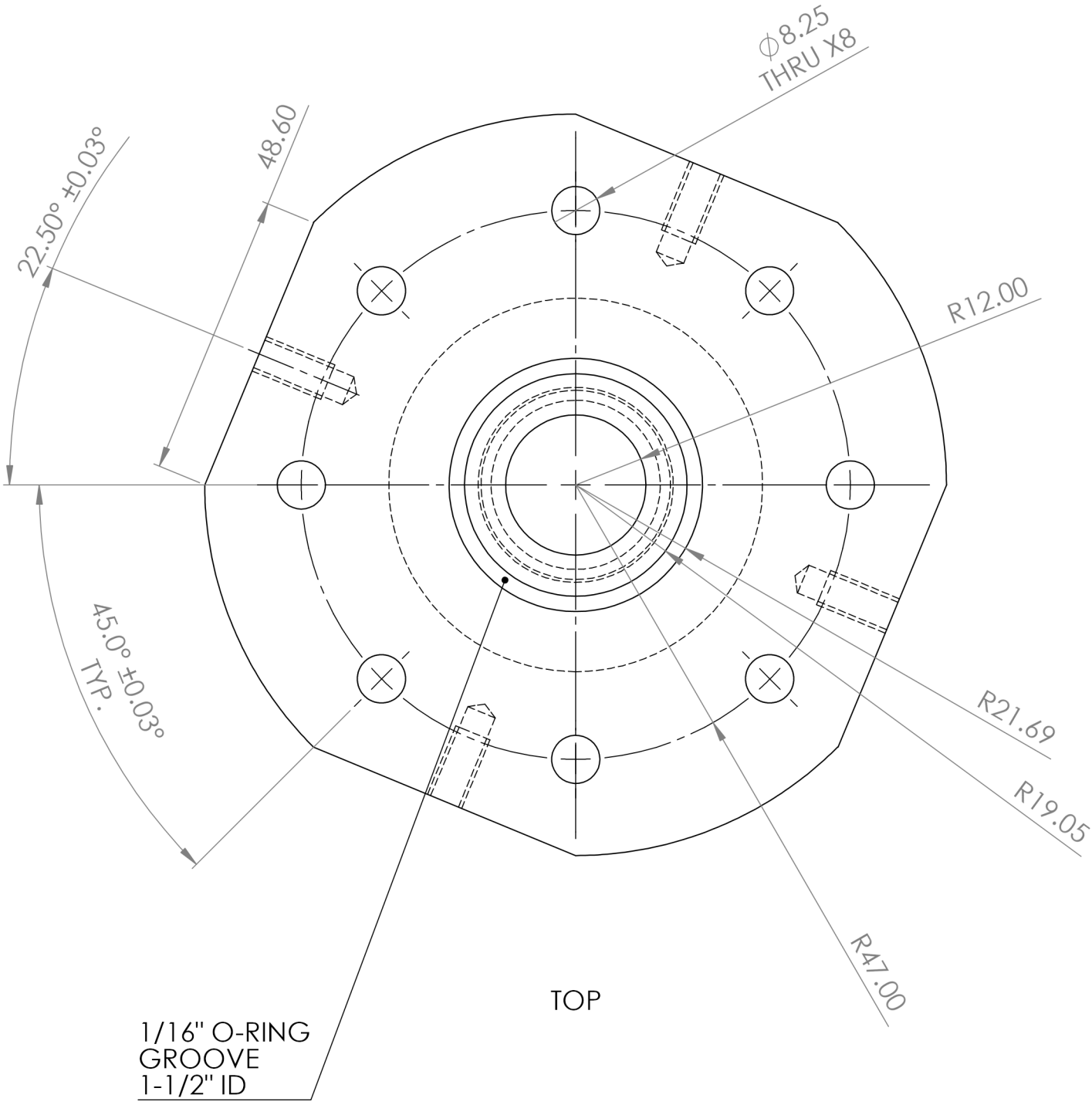

		DIMENSIONS ARE IN mm TOLERANCES ARE 0.03 mm UNLESS OTHERWISE NOTED.		NAME	DATE
			DRAWN	BAP	9/26/2011
			CHECKED		
			ENG APPR.		
			MFG APPR.		
		MATERIAL SS316L	Q.A.		
			COMMENTS:		
NEXT ASSY	USED ON	FINISH NONE			
APPLICATION		DO NOT SCALE DRAWING			

MIT

138 Albany St.
NW13-239
Cambridge, MA 02139

Bren Phillips
816-258-3220

SIZE	DWG. NO.	REV.
A	NPT_Transition	F
SCALE:1:1	WEIGHT:	SHEET 2 OF 3

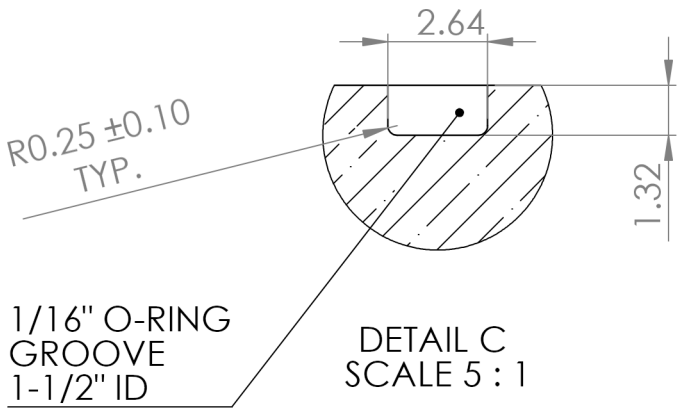

DETAIL C
SCALE 5 : 1

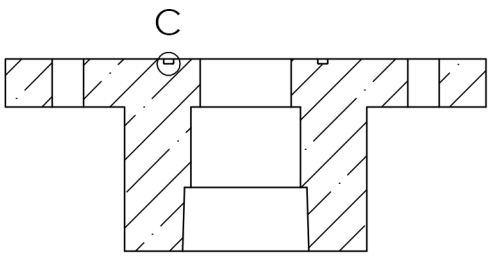

SECTION A-A

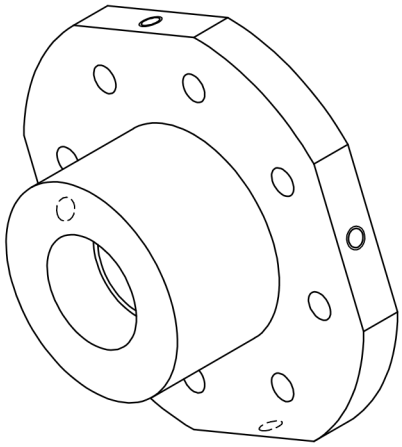

ISOMETRIC

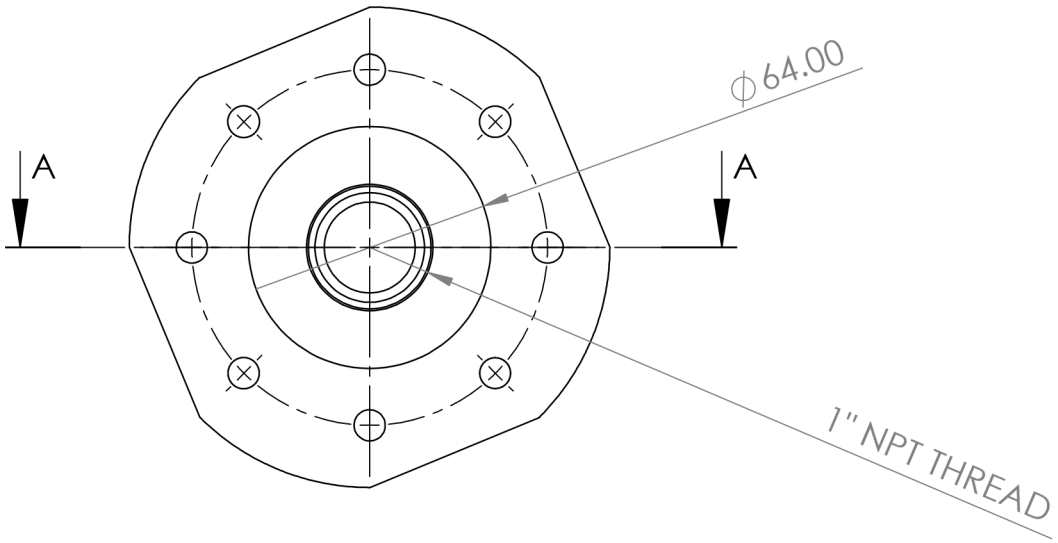

BOTTOM

		DIMENSIONS ARE IN mm TOLERANCES ARE 0.03 mm UNLESS OTHERWISE NOTED.		NAME	DATE
			DRAWN	BAP	9/26/2011
			CHECKED		
			ENG APPR.		
			MFG APPR.		
		MATERIAL SS316L	Q.A.		
			COMMENTS:		
NEXT ASSY	USED ON	FINISH NONE			
APPLICATION		DO NOT SCALE DRAWING			

MIT

138 Albany St.
NW13-239
Cambridge, MA 02139

Bren Phillips
816-258-3220

SIZE	DWG. NO.	REV.
A	NPT_Transition	F
SCALE:1:2	WEIGHT:	SHEET 3 OF 3

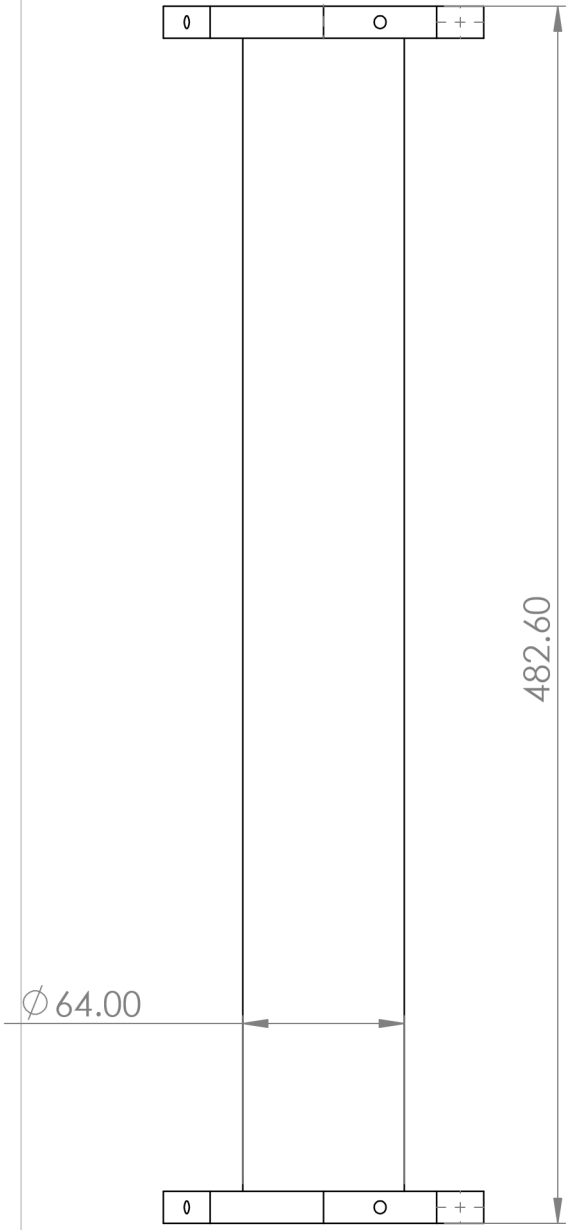

FRONT

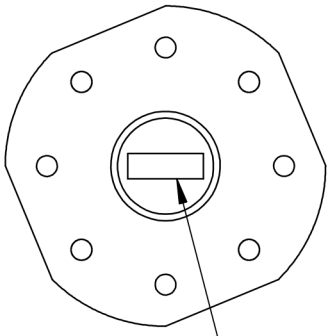

TOP

10X30 MM
CHANNEL THRU

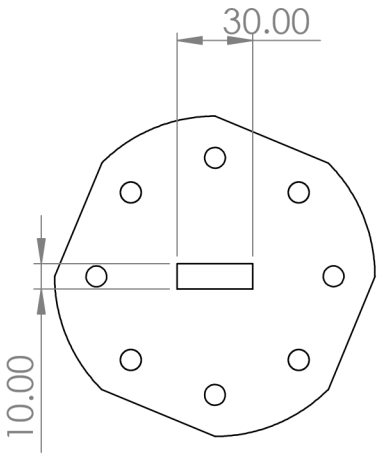

BOTTOM

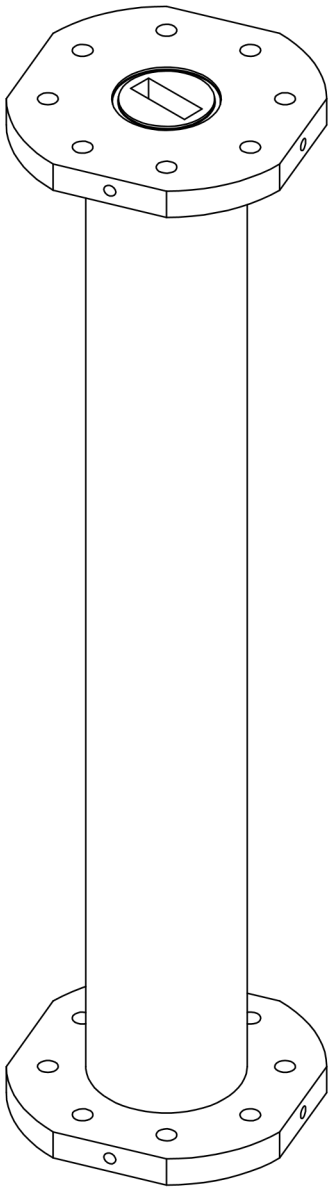

ISOMETRIC

8.25 MM BOLT HOLES FOR ONE OF THE TOP fLANGES TO BE DRILLED UPON RECEIPT OF QUARTZ SECTION TO PROPERLY ALIGN HOLES WITH QUARTZ FLANGE TO LINE UP RECTANGULAR CHANNEL.

MACHINED FROM A SINGLE PIECE OF STEEL, BUT DETAILED DRAWINGS OF THE BOTTOM FLANGE IS IN ENTRANCEFLANGE1, TOP FLANGE IN ENTRANCEFLANGE2, AND THE CHANNEL IN ENTRANCECHANNEL.

		DIMENSIONS ARE IN mm TOLERANCES ARE 0.03 mm UNLESS OTHERWISE NOTED.		NAME	DATE
			DRAWN	BAP	9/26/2011
			CHECKED		
			ENG APPR.		
			MFG APPR.		
		MATERIAL SS316L	Q.A.		
			COMMENTS:		
NEXT ASSY	USED ON	FINISH NONE			
APPLICATION		DO NOT SCALE DRAWING			

MIT

138 Albany St.
NW13-239
Cambridge, MA 02139

Bren Phillips
816-258-3220

SIZE	DWG. NO.	REV.
A	EntranceAssembly	G
SCALE:1:3	WEIGHT:	SHEET 1 OF 1

BOTTOM

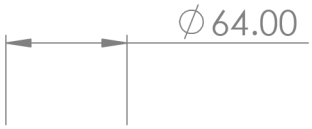

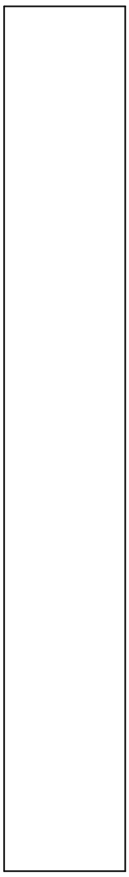

RIGHT

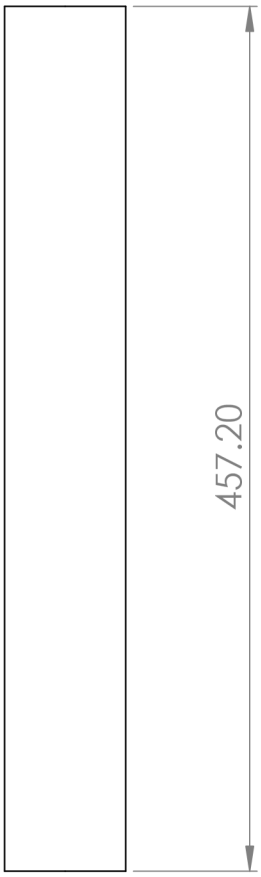

FRONT

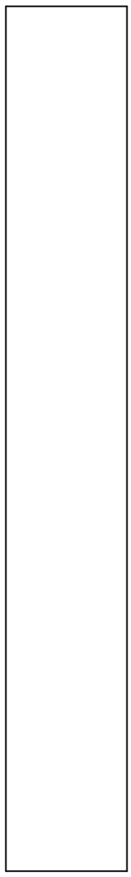

LEFT

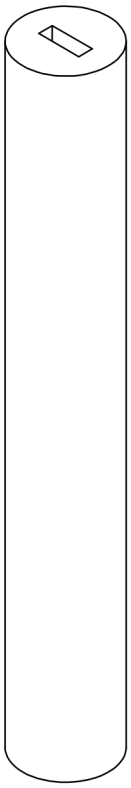

ISOMETRIC

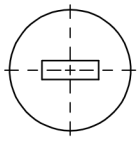

TOP

THIS IS A DETAILED DRAWING OF THE CHANNEL FOR THE ENTRANCEASSEMBLY WHICH IS MACHINED FROM A SOLID PIECE OF SS.

		DIMENSIONS ARE IN mm TOLERANCES ARE 0.03 mm UNLESS OTHERWISE NOTED.		NAME	DATE
			DRAWN	BAP	9/26/11
			CHECKED		
			ENG APPR.		
			MFG APPR.		
		MATERIAL SS316L	Q.A.		
			COMMENTS:		
NEXT ASSY	USED ON	FINISH NONE			
APPLICATION		DO NOT SCALE DRAWING			

MIT

138 Albany St.
NW13-239
Cambridge, MA 02139

Bren Phillips
816-258-3220

SIZE	DWG. NO.	REV.
A	EntranceChannel	G
SCALE:1:4	WEIGHT:	SHEET 1 OF 2

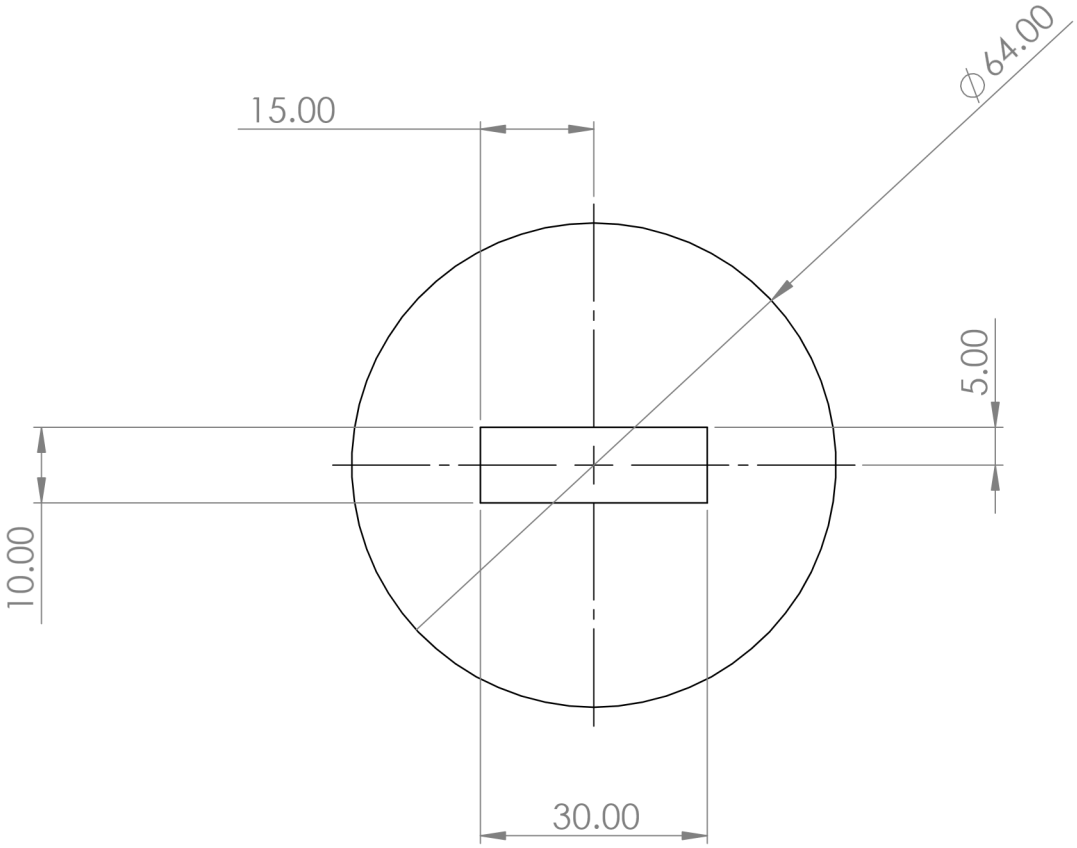

TOP

THIS IS A DETAILED DRAWING OF THE CHANNEL FOR THE ENTRANCEASSEMBLY WHICH IS MACHINED FROM A SOLID PIECE OF SS.

		DIMENSIONS ARE IN mm TOLERANCES ARE 0.03 mm UNLESS OTHERWISE NOTED.		NAME	DATE
			DRAWN	BAP	9/26/11
			CHECKED		
			ENG APPR.		
			MFG APPR.		
		MATERIAL SS316L	Q.A.		
			COMMENTS:		
NEXT ASSY	USED ON	FINISH NONE			
APPLICATION		DO NOT SCALE DRAWING			

MIT

138 Albany St.
NW13-239
Cambridge, MA 02139

Bren Phillips
816-258-3220

SIZE	DWG. NO.	REV.
A	EntranceChannel	G
SCALE:1:1	WEIGHT:	SHEET 2 OF 2

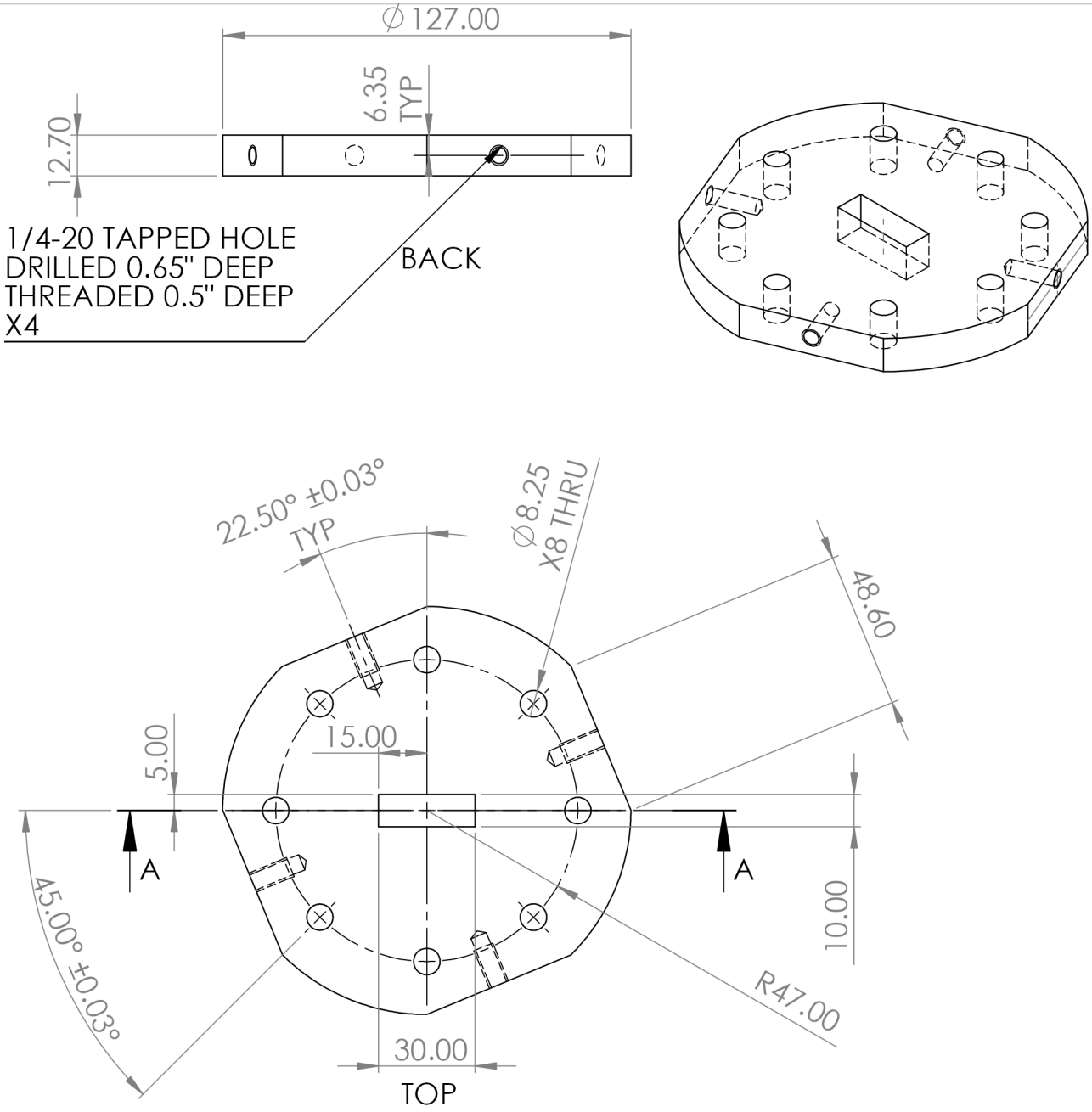

THIS IS A DETAILED DRAWING OF ONE FLANGE OF THE ENTRANCEASSEMBLY, WHICH IS MACHINED FROM ONE SOLID PIECE OF SS

		DIMENSIONS ARE IN mm TOLERANCES ARE 0.03 mm UNLESS OTHERWISE NOTED.		NAME	DATE
			DRAWN	BAP	9/26/11
			CHECKED		
			ENG APPR.		
			MFG APPR.		
		MATERIAL SS316L	Q.A.		
			COMMENTS:		
NEXT ASSY	USED ON	FINISH NONE			
APPLICATION		DO NOT SCALE DRAWING			

MIT

138 Albany St.
NW13-239
Cambridge, MA 02139

Bren Phillips
816-258-3220

SIZE	DWG. NO.	REV.
A	EntranceFlange1	G
SCALE:1:2	WEIGHT:	SHEET 1 OF 1

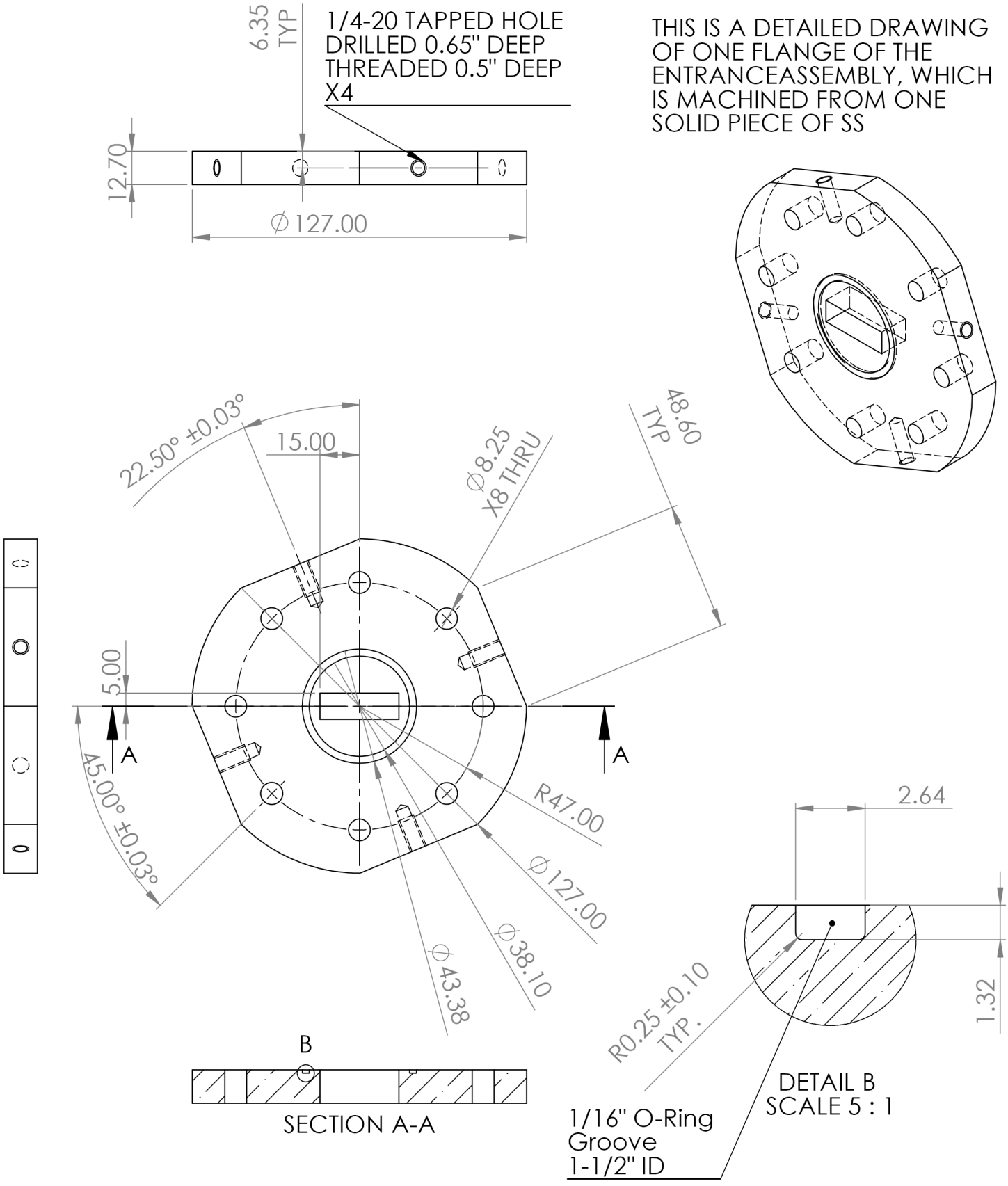

		DIMENSIONS ARE IN mm TOLERANCES ARE 0.03 mm UNLESS OTHERWISE NOTED.		NAME	DATE
			DRAWN	BAP	9/26/11
			CHECKED		
			ENG APPR.		
			MFG APPR.		
			Q.A.		
		MATERIAL SS316L	COMMENTS:		
NEXT ASSY	USED ON	FINISH NONE			
APPLICATION		DO NOT SCALE DRAWING			

MIT

138 Albany St.
NW13-239
Cambridge, MA 02139

Bren Phillips
816-258-3220

SIZE	DWG. NO.	REV.
A	EntranceFlange2	G
SCALE:1:2	WEIGHT:	SHEET 1 OF 1

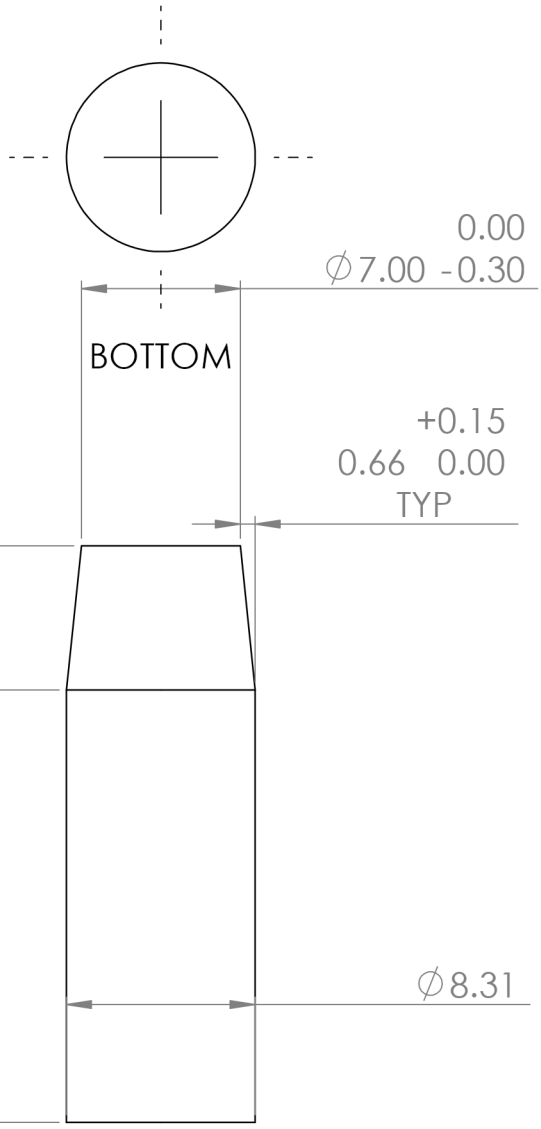

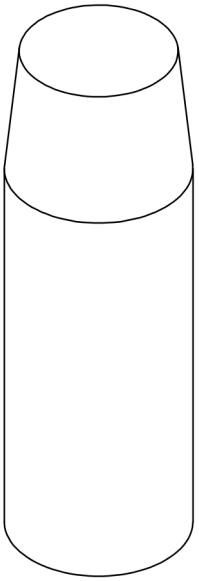

ISOMETRIC

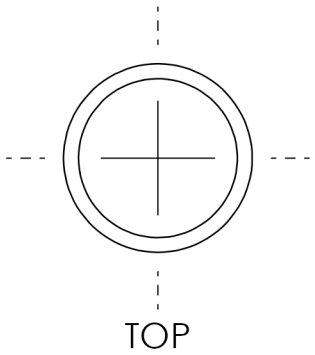

TOP

		DIMENSIONS ARE IN mm TOLERANCES ARE 0.03 mm UNLESS OTHERWISE NOTED.		NAME	DATE
			DRAWN	BAP	10/18/11
			CHECKED		
			ENG APPR.		
			MFG APPR.		
		MATERIAL NYLON	Q.A.		
			COMMENTS:		
NEXT ASSY	USED ON	FINISH NONE			
APPLICATION		DO NOT SCALE DRAWING			

MIT

138 Albany St.
NW13-239
Cambridge, MA 02139

Bren Phillips
816-258-3220

SIZE	DWG. NO.	REV.
A	AlignmentPin	D
SCALE:3:1	WEIGHT:	SHEET 1 OF 1